Title
ENGINEERING ELECTROCONDUCTIVE AND ADHESIVE HYRDOGELS FOR BIOMEDICAL APPLICATIONS

Author
Walker, Brian Wayne

Publication Date
2020

Peer reviewed|Thesis/dissertation

UNIVERSITY OF CALIFORNIA

Los Angeles

Engineering Electroconductive and Adhesive Hydrogels for Biomedical Applications

A dissertation submitted in partial satisfaction of the

requirements for the degree Doctor of Philosophy

in Chemical Engineering

by

Brian Walker

2020

ABSTRACT OF THE DISSERTATION

Engineering Electroconductive and Adhesive Hydrogels for Biomedical Applications

by

Brian Wayne Walker

Doctor of Philosophy in Chemical Engineering

University of California, Los Angeles, 2020

Professor Nasim Annabi, Chair

Bioadhesives, such as tissue sealants, hemostatic agents, and tissue sealants have gained increasing popularity for addressing wound management for traumatic and surgical injuries. This new generation of adhesive demonstrates significant advantages over traditional suturing and stapling techniques that can lead to infection, leakage of bodily fluid and gas, as well as secondary damage to tissues. Bioadhesives can be most broadly classified based on internal or external administration. While bioadhesives designed for external use are most widely used for topical application, such as wound closure, internal bioadhesives are surgically implanted and, therefore, require biocompatibility and strong adhesive ability to wet tissues. Further, hydrogel-based bioadhesives may be designed with nanoparticles or biopolymers that impart specific functionality, such as conductive or hemostatic properties. Scaffolds designed with conductive biomaterials have been extensively investigated in the field of tissue engineering based on their ability to support the function of excitable cell types, such as cardiomyocytes and neurons. Bioadhesives have also been designed to promote hemostasis for applications such as surgical sealants. In first two sections of this project, we aimed to develop conductive bioadhesives for cardiac tissue repair by combining highly biocompatible gelatin methacryloyl (GelMA), with an electrically conductive choline-

based bio ionic liquid (Bio-IL). Here, we chemically modified gelatin to form photocrosslinkable hydrogels in the presence of visible or UV light, depending on the photoinitiator used. Conductive hydrogels were fabricated with varying concentrations of GelMA and Bio-IL, which resulted in scaffolds with high biocompatibility, as well as tunable electrical conductivity, and mechanical strength. We then demonstrated the ability of Bio-IL conjugated hydrogels to transduce physicochemical stimuli and modulate the growth of primary CMs in both 2D and 3D cultures *in vitro*. In addition, we demonstrated that the engineered hydrogels were highly biodegradable and biocompatible *in vitro*, and that they did not elicit inflammatory responses when implanted *in vivo*. Our following project investigated the development of cardiopatches using electrospun GelMA conjugated with Bio-IL. The resulting cardiopatches demonstrated tunable conductive and mechanical properties by optimizing the concentration of GelMA and Bio-IL used during synthesis. GelMA/Bio-IL cardiopatches exhibited excellent adhesiveness to cardiac tissues, and biocompatibility both *in vitro* and *in vivo*. CMs and CFs seeded on the surface of cardiopatches demonstrated excellent cell attachment and proliferation, and the scaffold supported the expression of gap junction proteins indicating the cells ability to function synchronously. Taken together, these conductive bioadhesives demonstrated excellent potential to be readily tailored to cardiac tissue regenerative therapies. Lastly, our group developed a hemostatic surgical sealant with robust mechanical properties based on the biopolymers GelMA and elastin-like polypeptide (ELP). These adhesive hydrogels were rendered hemostatic by the incorporation of the synthetic clay Laponite (LA) and were rapidly photocrosslinked in the presence of UV radiation using the photoinitiator Irgacure 2959. We demonstrated the highly tunable mechanical and adhesive properties of these nanocomposite hydrogels by varying the concentrations of GelMA and ELP. Likewise, we demonstrated the excellent hemostatic performance of these scaffolds both *in vitro* and *in vivo* by

varying the concentration of LA. Our nanocomposite GelMA/ELP/LA hydrogels also showed remarkable biocompatibility both *in vitro* and *in vivo* and did not elicit an inflammatory response when implanted subcutaneously.

The dissertation of Brian Wayne Walker is approved.

Tzung Hsiai

Jun Park

Phillippe Sautet

Stephanie Seidlits

Nasim Annabi, Committee Chair

University of California, Los Angeles

2020

To my wife Tricia: thank you for all the love and support that you have given me.

I couldn't have done it without you!

Table of Contents

List of Figures

up to 5 days **(f)**. [5], Copyright 2016. Schematic for the synthesis of ECHs by adding PEDOT (red) and PEG (blue) to the surface of an electrode. Biorecognition molecules (purple) are added into the gel by attaching to -COOH groups of PEDOT. Capture of B-IFN-γ molecules (red dot) resulted in a change in the electrical signal of the ECH **(g)**. Assessment of the mechanical properties of PEG hydrogels, as well as PEDOT and PEDOT/PEG ECHs. Here the results showed that by adding PEDOT to PEG did not significantly change the elastic modulus compared to pure PEG hydrogels **(h).** However, the addition of PEDOT resulted in a significant increase in electrical conductivity **(i)**, which is necessary for application in the field of biosensors. [6], Copyright 2016.

Figure 4. Electrospinning microfabrication technique is a simple method for generating fibrous scaffolds that are suitable for many applications including tissue engineering, biosensors, and drug delivery systems. Schematic for an electrospinning set up consists of a polymer dissolved in solvent being injected out of a metal nozzle **(a)**. A high voltage power supply is connected to a metal nozzle and a metal collector creating an electrical field. A polymeric solution is then slowly pumped out of the syringe and spun onto the metal collector. Representative SEM image of a blend electrospun PELA/CNT fibrous scaffold with a 5% CNT concentration showing high alignment of fibers and 2 μm fiber diameter **(b)**. Mechanical study of electrospun PELA/CNTs demonstrated that ECHs fabricated with higher concentrations of CNTs resulted in a higher Young's modulus **(c)**. Electrical evaluation of electrospun ECHs showed that these fibrous scaffolds exhibited higher conductivity when fabricated with a higher concentration of CNTs in both blended and coaxial electrospun PELA/CNT scaffolds **(d)**. Beating rate of CMs when seeded on PELA/CNT fibrous scaffolds and cultured for 10 days. The beating rate for ECHs coaxially electrospun with a 5% CNT concentration (C5) achieved an average beating rate of 70-80 times/min, which is similar to that rate of CMs seeded on other non-conductive hydrogels **(e)**. [7], Copyright 2016.

Figure 5. 3D printing of conductive hydrogels for different biomedical applications. Pressure sensors were fabricated by 3D printing a conductive self-healing (CSH) hydrogel composed of PPy-grafted chitosan and poly(acrylic acid), and coating them with a thin layer of PDMS **(a)**. When applied to the wrist, the sensor could detect blood flow pulses in the veins below the skin in real-time **(b)** (Adapted from [8]). Hydrogel prepolymer solution containing sodium alginate, gold nanorods, and GelMA was bioprinted via a co-axial nozzle, in which the alginate prepolymer solution in the core was crosslinked by calcium ions flown in the sheath **(c)**. Lattice-like structures could be printed, and hydration was maintained by the continuous flow of the aqueous sheath solution. Cardiomyocytes printed in these structures expressed higher levels of Cxn43 cardiac junction protein and exhibited higher contraction rates compared to controls **(d)** (Adapted from [9]).

Figure 6. Micropatterning and self-assembling of ECHs for different biomedical applications. Schematic of GelMA-GNR ECHs that were photocrosslinked in the presence of UV light in a microgrooved PDMS mold. The resulting ECH was seeded with CMs, which aligned within the microgrooves **(a)**. Live/dead assay performed using CMs seeded on pure GelMA hydrogels **(b)** and GelMA-GNR ECHs **(c)**. Live cells were stained in green, while dead CMs were stained in red, confirming high cell viability after 7 days of cell culture (adapted from [10]). Schematic of supramolecular organic-inorganic composite capable of self-healing via interactions between oligomer chains (pink lines) with micro nickel and urea groups (blue and purple shapes) **(d)**. Representative stress-strain curves for ECHs containing 31% micro nickel

volume ratio under different healing conditions showing that healing efficiency was found to be a function of time **(e)** (adapted from [11]). Schematic of composite ECHs constructed with partially reduced GO using polydopamine, crosslinked with polyacrylamide **(f)** (adapted from [12]). Scale bars= 100 μm (**b, c**).

Figure 7. ECHs for tissue engineering applications. The addition of electrically conductive materials (red circles) can be used to provide conductive properties to intrinsically insulating hydrogels **(a)**. These ECHs could be used to deliver relevant biophysical stimuli to cardiomyocytes *in vitro*, such as mechanical and biological cues, or electrical stimulation/pacing. These maturation cues have been shown to trigger phenotypical changes that ultimately lead to fully mature and functional cardiomyocytes. ECHs have been used to develop conductive nerve conduits as an alternative to nerve autografts for nerve regeneration and repair (adapted from [13]) **(b)**. ECHs could provide physiological stimuli that mimic native nerve tissues and induce the differentiation of progenitor cell types to neural lineages (adapted from [14]) **(c)**. ECHs deliver biomimetic topographical and electrical cues *in vitro* to form highly oriented cellular constructs with tissue-level functionality (adapted from [10]) **(d)**. Scale bars= 100 μm (**d upper image**), 20 μm (**d lower image**).

Figure 8. Synthesis and characterization of Bio-IL functionalized GelMA hydrogels. The panels show schematics of the proposed reactions for (**a**) the acrylation of choline bicarbonate to form Bio-IL, and (**b**) the reaction between GelMA and Bio-IL in the presence of Eosin Y and visible light to form GelMA/Bio-IL hydrogel. ^{1}H-NMR analysis of (**c**) Bio-IL prepolymer, (**d**) GelMA prepolymer, and (**e**) GelMA/Bio-IL composite hydrogel. GelMA/Bio-IL hydrogels were formed by using 1% VC, 1.5% TEOA, and 0.1 mM Eosin Y at 120 s light exposure.

Figure 9. Electrical conductivity of the engineered polymer/Bio-IL hydrogels crosslinked by visible light. (**a**) Experimental set-up of the two-probe electrical station used to measure the electrical conductivity of the engineered hydrogels. Conductivity measurements of Bio-IL conjugated (**b**) GelMA and (**c**) PEGDA hydrogels at different polymer concentrations and polymer/Bio-IL ratios (1% VC, 1.5% TEOA, 0.1 mM Eosin Y, and 120 s exposure to visible light were used to form GelMA and PEGDA hydrogels). (**d**) Electrical conductivity of 15% GelMA/Bio-IL composite hydrogels at 50/50 ratio, which was stretched up to 0%, 20%, 30%, and 40% strain level demonstrating no significant changes in conductivity after stretching. (**e**) Schematic of *ex vivo* experiments performed using rat abdominal muscle tissues, connected using 15% final polymer concentration and 50/50 GelMA/Bio-IL ratio, and pure GelMA hydrogels (**f**) Threshold voltages at which contraction was achieved using 15% final polymer concentration GelMA/Bio-IL at 50/50 and 20/80 ratios, as well as pure 15% GelMA hydrogels. Error bars indicate standard error of the means, asterisks mark significance levels of $p < 0.05$ (*), $p < 0.01$ (**), and $p < 0.001$ (***).

Figure 10. Mechanical properties of Bio-IL conjugated GelMA and PEGDA hydrogels crosslinked with visible light. Compressive moduli for (**a**) GelMA/Bio-IL and (**b**) PEGDA/Bio-IL hydrogels engineered by varying polymer concentration and polymer/Bio-IL ratios. Elastic moduli for (**c**) GelMA/Bio-IL and (**d**) PEGDA/Bio-IL hydrogels with varying polymer concentration and polymer/Bio-IL ratios (1% VC, 1.5% TEOA, 0.1 mM Eosin Y, and 120 s light exposure were used to form GelMA and PEGDA hydrogels). Error bars indicate standard error of the means, asterisks mark significance levels of $p < 0.05$ (*), $p < 0.01$ (**), and $p < 0.001$ (***).

Figure 11. Ultimate stress and ultimate strain of Bio-IL functionalized GelMA and PEGDA hydrogel crosslinked with visible light. Ultimate strain values for (**a**) GelMA/Bio-IL and (**b**) PEGDA/Bio-IL hydrogels engineered by varying polymer concentration and polymer/Bio-IL ratios. Ultimate stress for (**c**) GelMA/Bio-IL and (**d**) PEGDA/Bio-IL hydrogels with varying polymer concentration and polymer/Bio-IL ratios (1% VC, 1.5% TEOA, 0.1 mM Eosin Y, and 120 s light exposure were used to form GelMA and PEGDA hydrogels). Error bars indicate standard error of the means, asterisks mark significance levels of $p < 0.05$ (*), $p < 0.01$ (**), and $p < 0.001$ (***).

Figure 12. Pore characteristics, *in vitro* swelling, and degradation of polymer/Bio-IL hydrogels Representative SEM images of (**a**) GelMA/Bio-IL and (**b**) PEGDA/Bio-IL hydrogels formed by using 100/0 and 50/50 polymer/Bio-IL ratio at 15% (w/v) polymer concentration (1% VC, 1.5% TEOA, and 0.1 mM Eosin Y at 120 s light exposure were used to form the hydrogels). Average pore sizes of (**c**) GelMA/Bio-IL and (**d**) PEGDA/Bio-IL hydrogels at varying polymer concentrations and polymer/Bio-IL ratios. Swelling ratios of (**e**) GelMA/Bio-IL and (**f**) PEGDA/Bio-IL hydrogels at 15% final polymer concentration and 50/50 polymer/Bio-IL ratio in DPBS after 4, 8 and 24 h. Degradation of (**g**) GelMA/Bio-IL and (**h**) PEGDA/Bio-IL hydrogels at 15% final polymer concentration and 50/50 polymer/Bio-IL ratio in DPBS supplemented with 10% FBS over a two-week period. Error bars indicate standard error of the means, asterisks mark significance levels of $p < 0.05$ (*), $p < 0.01$ (**), and $p < 0.001$ (***).

Figure 13. 2D *in vitro* studies using GelMA/Bio-IL hydrogels seeded with CMs. Representative live/dead images from CMs cultured on (**a**) GelMA (control) and (**b**) GelMA/Bio-IL hydrogels on days 1 and 5 (scale bar = 200 μm). Representative F-Actin/DAPI stained images from CMs seeded on (**c**) GelMA and (**d**) GelMA/Bio-IL on days 1 and 5. (**e**) Cell viability quantification of CMs cultured on the hydrogels after 1, 3, and 5 days of culture. (**f**) Quantification of metabolic activity, RFU (relative fluorescence intensity) using PrestoBlue assay, 1, 3, and 5 days after seeding with CMs. Immunofluorescent staining of sarcomeric α-actinin in CMs seeded on GelMA **(g)** and GelMA/Bio-IL **(h)** hydrogels on day 7 (scale bar = 25 μm). (**i**) Characterization of synchronous contraction in CMs seeded on GelMA and GelMA/Bio-IL hydrogels over 7 days of culture. (*$p < 0.05$, **$p < 0.01$, ***$p < 0.001$ and ****$p < 0.0001$).

Figure 14. *In vitro* 3D cell encapsulation of cardiomyocytes (CMs) and cardiac fibroblasts (CFs) in GelMA/Bio-IL hydrogels. CMs and CFs (2:1 ratio) were 3D encapsulated inside visible light-crosslinked GelMA (control) and GelMA/Bio-IL hydrogels. Representative live/dead images from CMs/CFs encapsulated in GelMA hydrogels **(a, b)** and GelMA/Bio-IL **(c, d)** at days 1 and 7 post-encapsulation. Representative F-Actin/DAPI fluorescent images of CMs/CFs encapsulated in GelMA **(e, f)** and GelMA/Bio-IL **(g, h)** hydrogels, at days 1 and 7 post-encapsulation (scale bar = 200 μm). **(i)** Quantification of cell viability for 3D-encapsulated CMs/CFs at days 1, 4, and 7 post-encapsulation. **(j)** Quantification of metabolic activity, RFU (relative fluorescence intensity) using PrestoBlue assay, at days 1, 3, and 5 post-encapsulation. **(k)** Quantification of cell proliferation based on DAPI-stained cell nuclei, at days 1, 4, and 7 post-encapsulation. **(l)** Characterization of synchronous contraction in co-cultures of CMs/CFs 3D-encapsulated in GelMA (control) and GelMA/Bio-IL hydrogels over 7 days of culture. (*$p < 0.05$, **$p < 0.01$, ***$p < 0.001$ and ****$p < 0.0001$). All hydrogels were synthesized using 15% (w/v) final polymer concentration and 50/50 polymer/Bio-IL ratio. Error bars indicate standard error of the means, asterisks mark significance levels of $p < 0.05$ (*), $p < 0.01$ (**), and $p < 0.001$ (***).

Figure 15. *In vivo* biodegradation and biocompatibility of GelMA/Bio-IL composite hydrogel using a rat subcutaneous model. (**a, b**) Evaluation of the *in vivo* degradation of GelMA/Bio-IL on days 0, 4, 14 and 28 post implantation (n = 4). (**a**) *In vivo* degradation of GelMA/Bio-IL hydrogels based on weight loss of the implants. The *in vivo* degradation profile of GelMA/Bio-IL hydrogels exhibits an approximately linear behavior during 28 days after implantation. (**b**) Images of the GelMA/Bio-IL composite hydrogels at 0, 4, 14, and 28 days after implantation. (**c-e**) Hematoxylin and eosin (H&E) staining of GelMA/Bio-IL sections after (**c**) 4 days, (**d**) 14 days, and (**e**) 28 days of implantation (scale bars = 500 μm). The H&E shows a negligible amount of inflammatory cells. (**f-h**) Fluorescent immunohistochemical analysis of subcutaneously implanted GelMA/Bio-IL hydrogels showing no significant local lymphocyte infiltration (CD3) at days (**f**) 4, (**g**) 14 and (**h**) 28 (scale bars = 200 μm), are exhibiting remarkable macrophages (CD68) only at day (**i**) 4 but significantly disappeared at days (**j**) 14 and (**k**) 28 (scale bars = 200 μm). Green, red and blue colors in (**f-k**) represent the GelMA/Bio-IL hydrogels, the immune cells, and the cell nuclei (DAPI). 1% VC, 1.5% TEOA, and 0.1 mM Eosin Y at 120 s light exposure were used to form the hydrogels. All hydrogels were synthesized using 15% final polymer concentration and 50/50 polymer/Bio-IL ratio.

Figure 16. Synthesis and physical properties of engineered cardiac patches. a) Schematic of the fabrication of GelMA/Bio-IL cardiopatches using HFIP to prepare a prepolymer solution with GelMA. Representative SEM images of GelMA/Bio-IL cardiopatches fabricated with a **b**) 0, and **c**) 33 %(v/v) concentration of Bio-IL. **d**) The electrical conductivity of cardiac patches fabricated with varying concentrations Bio-IL. **e**) The electroconductive properties of cardiopatches after incubation in DPBS at 37 °C for 2 and 4 d show no significant change in conductivity during biodegradation. The **f)** swelling ratio and **g**) degradation rate of cardiopatches following incubation in DPBS at 37 °C. **h**) The elastic modulus of cardiopatches increased when fabricated with higher concentrations of GelMA, and with higher concentrations of Bio-IL. Error bars indicate standard error of the means, asterisks mark significance levels of $p < 0.05$ (*), $p < 0.01$ (**), and $p < 0.001$ (***).

Figure 17. Mechanical properties of cardiac patches. **a**) The ultimate strain and **b**) ultimate stress exhibited by GelMA/Bio-IL cardiopatches. Error bars indicate standard error of the means, asterisks mark significance levels of $p < 0.05$ (*), $p < 0.01$ (**), and $p < 0.001$ (***).

Figure 18. Strong adhesion of cardiac patches to heart tissue, and propagation of electrical signals through patches to stimulate excitable cell types. a) Representative image demonstrating the high adhesion of cardiac patches to cardiac tissues. **b**) H&E staining of cardiac patch on rat cardiac tissue. **c**) Experimental setup of wound closure adhesion test using Instron 5944 mechanical tester conducted with excised rat cardiac tissue. **d**) Results showed that the adhesion to cardiac tissue significantly increased when cardiac patches were fabricated with a higher concentration of Bio-IL. **e**) Experimental setup of the burst pressure analysis conducted on the explanted heart of Wistar rats. **f**) There was no significant difference between the burst pressures of a healthy heart, and the heart containing a physical defect supported with GelMA/Bio-IL cardiac patches. **g**) Schematic of experimental designed used to investigate the propagation of electrical impulses across cardiac patches to stimulate explanted muscle tissue. **h**) Conductive patches fabricated with a 100% (v/v) Bio-IL concentration exhibited a lower threshold voltage to excite muscle tissue when compared with patches fabricated with 33% (v/v) Bio-IL concentration. Error bars indicate standard error of the means, asterisks mark significance levels of $p < 0.05$ (*), $p < 0.01$ (**), and $p < 0.001$ (***).

Figure 19. Characterization of the adhesion to wet tissues of cardiac patches. a) Schematic of wound closure test on cardiac patches using porcine skin. **b**) Patches displayed an increasing adhesion strength to porcine skin when fabricated with increasing concentration of Bio-IL. Additionally, these GelMA/Bio-IL cardiac patches showed a significantly higher adhesion strength when compared with commercially available tissue sealants, such as CoSEAL, and Evicel. **c**) Schematic of burst pressure set up to evaluate adhesion properties of cardiac patches on porcine intestinal tissues. **d**) Similarly, these patches exhibited an increasing burst pressure strength when fabricated with an increasing concentration of Bio-IL. The burst pressure strength of GelMA/Bio-IL cardiac patches was also greater than CoSEAL, and Evicel. Error bars indicate standard error of the means, asterisks mark significance levels of $p < 0.05$ (*), $p < 0.01$ (**), and $p < 0.001$ (***).

Figure 20. 2D co-culture of cardiomyocytes (CMs) and cardiac fibroblasts (CFs) on electrospun GelMA/Bio-IL patches. The *in vitro* cytocompatibility of the engineered patches was evaluated using 2D co-cultures of freshly isolated CMs and CFs (ratio 2:1) growing at different concentrations of Bio-IL (i.e., 0%, 33%, 66%, and 100% (v/v)). **a)** Representative Live/Dead images of CMs/CFs growing on 0% and 66% Bio-IL (v/v) at day 7 post-seeding. **b)** Representative actin/DAPI images of CMs/CFs growing on 0% and 66% Bio-IL (v/v) at day 7 post-seeding. Bar graphs showing the quantification of **c)** cell viability, **d)** cell density, and **e)** metabolic activity of 2D co-cultures of CMs/CFs at days 1, 4, and 7 post-seeding, growing at different concentrations of Bio-IL (i.e., 0%, 33%, 66%, and 100% (v/v)). Representative immunofluorescent images of CMs/CFs at day 7 post-seeding growing on the surface of **f)** 0%, and **g)** 66% Bio-IL (v/v) patches (green: sarcomeric α-actinin, red: connexin 43, blue: DAPI). **h)** Characterization of the beating frequency (beats/min) of CMs/CFs throughout 7 days of culture growing at different concentrations of Bio-IL (i.e., 0%, 33%, 66%, and 100% (v/v)). Quantification of the relative levels of expression (i.e., intensity of fluorescence) of **i)** connexin 43, and **j)** sarcomeric α-actinin in co-cultures of CMs/CFs at day 7 post-seeding.

Figure 21. *In vivo* investigation of GelMA/Bio-IL cardiac patches using a murine model of MI via permanent ligation of LAD coronary artery. a) Murine in vivo surgical procedure required cutting the skin on the left side of the chest exposing the left ventricle of the heart. Permanent ligation of the LAD coronary artery was performed. Three groups including a control (no treatment), GelMA patch, and **b)** GelMA/Bio-IL patch was used to treat infarction directly below the site of ligation. **c)** UV-irradiation was used for 300 s to crosslink cardiac patch and provide adhesion to wet tissue. **d,e)** Following 21 days post implantation, rats were sacrificed and their hearts were removed for histological evaluation. Representative images of Masson's trichrome, sarcomeric-α actinin, and connexin 43 histological analysis for **f)** control, **g)** GelMA patch, and **h)** GelMA/Bio-IL patch groups.

Figure 22. Synthesis and characterization of nanocomposite hydrogels. Gelatin methacryloyl (GelMA) (**a**), elastin-like polypeptide (ELP) (**b**), and Laponite (LA) (**c**) were utilized to engineer hemostatic hydrogels with high elasticity for application as a surgical sealant for lung tissue. (**d**) Schematic for the fabrication of these nanocomposite hydrogels by photocrosslinking prepolymer solutions in the presence of Irgacure 2959 and UV irradiation for 180 s. (**e**) The engineered hemostatic surgical sealants may be used to properly seal lung tissue following the removal of a section of tissue.

Figure 23. Mechanical characterization of hemostatic and highly elastic hydrogels for applications as surgical sealants for soft tissues. Elastic moduli for hydrogels containing (**a**) varying concentrations of GelMA and ELP, as well as for (**b**) hemostatic hydrogels containing 10% GelMA, 10% ELP, and varying concentrations of LA. Ultimate strain for hydrogels containing (**c**) varying concentrations of GelMA and ELP, as well as for (**d**) hemostatic hydrogels containing 10% GelMA, 10% ELP, and varying concentrations of LA. Compressive moduli for hydrogels containing (**e**) varying concentrations of GelMA and ELP, as well as for (**f**) hemostatic hydrogels containing varying concentrations of LA. Error bars indicate standard error of the means, asterisks mark significance levels of $p < 0.05$ (*), $p < 0.01$ (**), $p < 0.001$ (***), and $p < 0.0001$ (****).

Figure 24. *In vitro* swelling behavior and degradation rates of hemostatic and highly elastic hydrogels for applications as lung tissue sealants. Swelling ratios of highly elastic hydrogels containing (**a**) 10% GelMA and varying concentrations of ELP, as well as (**b**) 10% GelMA/10% ELP and varying concentrations of LA. Results showed that the addition of ELP into the hydrogels led to less water uptake due to the presence of hydrophobic elastin motifs. Degradation rates of elastic hydrogels containing (**c**) 10% GelMA and varying concentrations of ELP, as well as (**d**) nanocomposite hydrogels containing 10% GelMA/10% ELP and varying concentrations of LA. Our results show that the addition of ELP significantly slowed down the degradation of the engineered hydrogels after 28 d.

Figure 25. *In vitro* sealing properties of hemostatic hydrogel for application as a lung tissue sealant. (**a**) Schematic for the modified standard test method to determine adhesion strength (ASTM F2458-05) of GelMA/ELP/LA nanocomposite hydrogels. Adhesion strength for (**b**) elastic hydrogels containing varying concentrations of both GelMA and ELP, as well as for (**c**) nanocomposite hydrogels containing 10% GelMA/10% ELP and varying concentrations of LA. (**d**) Schematic of a standard lap shear test (ASTM F2255-05) to determine the shear strength of GelMA/ELP/LA nanocomposite hydrogels. Shear stress of (**e**) elastic hydrogels containing varying concentrations of GelMA and ELP, as well as (**f**) nanocomposite hydrogels containing 10% GelMA/10% ELP and varying concentrations of LA. (**g**) Schematic for the standard burst pressure test (ASTM F2392-04) to determine the burst pressure for GelMA/ELP/LA hydrogels. (**h**) Burst pressure for elastic hydrogels containing varying concentrations of both GelMA and ELP using collagen sheets as a substrate. (**i**) Burst pressure for nanocomposite hydrogels fabricated with 10% GelMA/10% ELP and varying concentrations of LA. Error bars indicate standard error of the means, asterisks mark significance levels of $p < 0.05$ (*), and $p < 0.01$ (**).

Figure 26. *In vitro* evaluation of LA on the clotting of whole blood. (**a**) Clot formation as a function of time and composition of hemostatic lung tissue sealants. (**b**) Quantitative clot time for whole blood added to nanocomposite hydrogels. (**c**) Quantitative clot mass measured at 14 mins following the addition of whole blood to hydrogels fabricated with 10% GelMA/10% ELP and varying concentrations of LA. Error bars indicate standard error of the means, asterisks mark significance levels of $p < 0.01$ (**), $p < 0.001$ (***), and $p < 0.0001$ (****).

Figure 27. *In vitro* cytocompatibility evaluation of GelMA/ELP/LA hydrogels. Representative live/dead images of human lung fibroblast cells (hLFCs) seeded on the surface of (**a**) GelMA, (**b**) GelMA/ELP, and (**c**) GelMA/ELP/LA hydrogels after 1 day post-seeding. Representative live/dead images of hLFCs seeded on the surface of (**d**) GelMA, (**e**) GelMA/ELP, and (**f**) GelMA/ELP/LA after 5 days post-seeding. Representative phalloidin (green)/DAPI (blue) stained images from hLFCs seeded on (**g**) GelMA, (**h**) GelMA/ELP, and (**i**) GelMA/ELP/LA after 1 day post-seeding. Representative phalloidin/DAPI images of hLFCs seeded on (**j**) GelMA, (**k**) GelMA/ELP, and (**l**) GelMA/ELP/LA after 5 days post seeding. (m) Quantification of cell viability for hLFCs seeded on the surface of engineered hydrogels at days 1, 4, and 7 post-seeding. (n) Quantification of cell proliferation based on DAPI-stained cell nuclei at days 1, 4, and 7

post-seeding. (o) Quantification of metabolic activity, relative fluorescence units (RFU), using a PrestoBlue assay at days 1, 4, and 7 post seeding.

Figure 28. *In vivo* biodegradation and biocompatibility of nanocomposite GelMA/ELP/LA hydrogels using a rat subcutaneous implantation model. (**a**) Representative images of GelMA, GelMA/ELP, and GelMA/ELP/LA hydrogels before implantation (day 0), and on days 7, 28, and 56 post-implantation. (**b**) *In vivo* biodegradation of the engineered hydrogels on days 0, 7, 28, and 56 post-implantation, based on weight loss of the implant (n=4). Hematoxylin and eosin (H&E) staining of 20 %(w/v) GelMA hydrogel sections (hydrogels with the surrounding tissue) after (**c**) 7, (**d**) 28, and (**e**) 56 days of implantation (scale bar = 200 μm). H&E staining of GelMA/ELP 10/10 %(w/v) hydrogel sections after (**f**) 7, (**g**), 28 and (**h**) 56 days implantation. H&E staining of GelMA/ELP/LA 10/10/2 %(w/v) hydrogel sections after (**i**) 7, (**j**), 28, and (**k**) 56 days post implantation. Hydrogels were formed using 0.5% Irgacure 2959 and 180 s UV exposure time.

Figure 29. *In vivo* evaluation of nanocomposite hydrogels as hemostats using a rat liver bleeding model. (**a**) Schematic of engineered hydrogel placement onto a lethal liver wound. Representative images of (**b**) Surgicel hemostatic patch and (**c**) GelMA/ELP/LA nanocomposite hydrogels being used to accelerate blood clotting in a rat *in vivo* liver bleeding model. (**d**) Quantification of in vivo blood loss after application of GelMA/ELP/LA nanocomposite hydrogels shows significant improvement compared to treatment with GelMA hydrogels or Surgicel hemostatic patch. Error bars indicate standard error of the means, asterisks mark significance levels of $p < 0.0001$ (****).

ACKNOWLEDGEMENT

I would like to thank the University of California – Los Angeles, particularly the Department of Chemical and Biomolecular Engineering for providing an excellent environment for doing research.

I would like to thank my research advisor, Dr. Nasim Annabi, for the encouragement and support over the last 5 years.

I would like to thank my physical chemistry undergraduate professor, Dr. Joseph Quarttucci for always inspiring and supporting me. In addition, I would also like to thank my biomaterials professor, Prof. Arthur Coury who taught me so much in the biomedical field and advised me to pursue a PhD.

Finally, I would like to acknowledge all my lab mates from both Northeastern University and UCLA. Thank you for all the support.

Part of Chapter 1 is reprinted and adapted with permission from (B. W. Walker, R. Portillo Lara, E. Mogadam, C. H. Yu, W. Kimball, N. Annabi, "Rational Design of Microfabricated Electroconductive Hydrogels for Biomedical Applications", Progress in Polymer Science, 2019, 92, 135-157. Copyright 2019 Elsevier. Co-author contributions: All the authors contributed to writing and revision of the manuscript. N. Annabi was the P.I.

Parts of Chapters 2 and 3 are reprinted and adapted with permission from (I. Noshadi*, B. W. Walker*, R. Portillo Lara, E. Shirzaei Sani, N. Gomes, M. R. Aziziyan, N. Annabi, "Engineering Biodegradable and Biocompatible Bio-ionic Liquid Conjugated Hydrogels with Tunable Conductivity and Mechanical Properties", Scientific Reports, 2017, 7, 4345. Copyright 2017 Nature. Co-author contributions: R. Portillo Lara helped with cell culture and writing, E. Shirzaei Sani helped with SEM characterization, and M. R. Aziziyan helped with conductivity quantification. N. Annabi was the P.I.

Parts of Chapters 2 and 3 are reprinted and adapted with permission from (B. W. Walker, R. Portillo Lara, C. H. Yu, E. Shirzaei Sani, W. Kimball, S. Joyce, N. Annabi, "Engineering a Naturally-derived Adhesive and Conductive Cardiopatch", Biomaterials, 2019, 207, 89-101. Copyright 2019 Elsevier. Co-author contributions: R. Portillo Lara helped with cell culture and writing, C. H. Yu helped with adhesion characterization, E. Shirzaei Sani helped with SEM characterization, and W. Kimball helped with mechanical testing. N. Annabi was the P.I.

VITA

2018-2020	Graduate Student Researcher Department of Chemical and Biomolecular Engineering, UCLA
2015-2018	Graduate Student Researcher Department of Chemical Engineering, Northeastern University
2013-2015	B.S. in Chemistry, Worcester State University

Selected Publications

Journal Articles

1. Noshadi, I.*, **B. W. Walker***, R. Portillo-Lara, E. Shirzaei Sani, N. Gomes, M. R. Aziziyan and N. Annabi (2017). "Engineering Biodegradable and Biocompatible Bio-ionic Liquid Conjugated Hydrogels with Tunable Conductivity and Mechanical Properties." Scientific Reports **7**(1): 4345. (* these authors contributed equally).
2. **Walker, B. W.**, R. P. Lara, C. H. Yu, E. S. Sani, W. Kimball, S. Joyce and N. Annabi (2019). "Engineering a naturally-derived adhesive and conductive cardiopatch." Biomaterials **207**: 89-101.
3. **Walker, B. W.**, R. P. Lara, E. Mogadam, C. H. Yu, W. Kimball and N. Annabi (2019). "Rational design of microfabricated electroconductive hydrogels for biomedical applications." Progress in Polymer Science.
4. Portillo-Lara, R., A. R. Spencer, **B. W. Walker**, E. S. Sani and N. Annabi (2019). "Biomimetic cardiovascular platforms for in vitro disease modeling and therapeutic validation." Biomaterials 198: 78-94.

5. Uehara, M., X. Li, A. Sheikhi, N. Zandi, **B. W. Walker**, B. Saleh, N. Banouni, L. Jiang, F. Ordikhani, L. Dai, M. Yonar, I. Vohra, V. Kasinath, D. P. Orgill, A. Khademhosseini, N. Annabi and R. Abdi (2019). "Anti-IL-6 eluting immunomodulatory biomaterials prolong skin allograft survival." Sci Rep 9(1): 6535.
6. Alizadeh-Ghodsi, M., M. Pourhassan-Moghaddam, A. Zavari-Nematabad, **B. W. Walker**, N. Annabi and A. Akbarzadeh (2019). "State-of-the-Art and Trends in Synthesis, Properties, and Application of Quantum Dots-Based Nanomaterials." Particle & Particle Systems Characterization 36(2): 1800302.

Introduction

Hydrogels are three dimensional (3D) networks of hydrophilic polymeric networks that can be formed through different mechanisms such as physical entanglement, electrostatic interactions, or covalent chemical crosslinking[15]. Hydrogels are remarkably suitable for a wide range of applications such as drug delivery, tissue engineering, and soft electronics for biomedical devices, due to their high hydration, tunable physical properties, and porous architecture[16, 17]. These characteristics also enable the diffusion of biomolecules, oxygen, and metabolic waste across the 3D structure of hydrogels, which is an important trait for substrates used in the physiological context[18, 19]. Hydrogels can also be tuned to mimic biochemical, mechanical, and topographical cues from the native extracellular matrix (ECM), in order to modulate physiological responses in cells and tissues[20]. Therefore, several naturally-derived and synthetic-based polymers, as well as various fabrication methods have been reported for the design and manufacture of hydrogels with different physicochemical properties[21, 22]. These polymers may be used individually or in combination with other polymers to yield composite hydrogels with increased functionality. Moreover, hydrogels may be further modified through the incorporation of chemical or biological active moieties such as growth factors, cell binding and protease-sensitive sites, or other stimuli-responsive molecules to promote their functions[23]. Although hydrogels have been demonstrated to be highly versatile platforms for different biomedical applications, their insulating nature often limits their potential for the modulation of electrically-sensitive cells and tissues such as cardiac and neural tissues[24].

In recent years, the development of advanced biomaterials and chemistries combined with micro- and nanotechnologies have improved the ability to control the properties and functionality of hydrogels for a wide range of applications (**Figure 1**)[20]. For instance, the incorporation of

inherently conductive materials to hydrogels via blending, doping or chemical modification have led to the development of new class of electroconductive hydrogels (ECHs)[25]. ECHs are composite biomaterials that combine the electroconductive capabilities of different materials with the intrinsic properties of crosslinked hydrogel networks[26]. Several strategies for the synthesis of ECHs have been reported such as the incorporation of conductive polymers (CPs) (e.g. polyaniline (PANi), polypyrrole (PPy), polythiophene (PTh), and poly(3,4-ethylenedioxythiophene) (PEDOT)) within a hydrogel network[26-30]. The organic nature of CPs greatly facilitates their chemical modification to incorporate different bioactive functional motifs into ECHs and provide them with high conductivity and processability[25]. ECHs can also be engineered by the *in situ* reduction of metal ions within the polymer network to form metallic nanoparticles (NPs)[31]. In this regard, different types of NPs have been used for the engineering of nanocomposite ECHs with tunable electrical, mechanical and optical properties[32]. For example, the incorporation of one dimensional carbon nanotubes (CNTs) and two dimensional (2D) graphene has been shown to impart high electrical conductivity and increased mechanical strength to hydrogels[33]. In addition, our group has recently demonstrated the engineering of ECHs with intrinsic electrical conductivity through the functionalization of different hydrogels with a choline-based bio-ionic liquid (Bio-IL)[34]. This diverse range of synthesis methodologies has led to the development of ECHs with distinct physical and biochemical properties, which offer unique advantages for different biomedical applications, such as tissue engineering, drug delivery, and engineering biosensors and medical devices[27]. Strategies for designing these therapeutic and diagnostic ECH-based technologies often includes electrical characteristics biomimetic to that of the native tissue (**Table 1**).

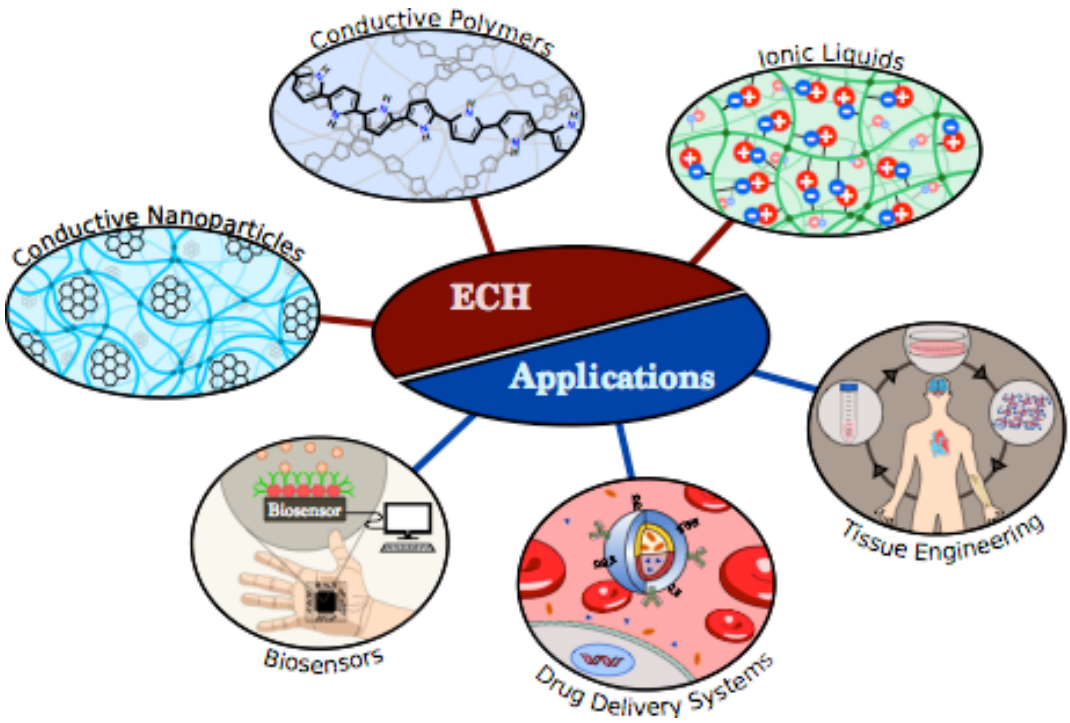

Figure 1: Synthesis and applications of ECHs. Conductive materials including conductive nanoparticles **(a)**, conductive polymers **(b)**, or ionic liquids **(c)** are incorporated into hydrogel precursors to form ECHs with high electrical conductivity. ECHs are becoming increasingly useful for many biomedical applications, including biosensors **(d)**, drug delivery systems **(e)**, and tissue engineering **(f)**.

Previous studies have demonstrated the ability of ECHs to mediate the adhesion, proliferation, migration, and differentiation of different cell types including cardiomyocytes (CMs), neurons, fibroblasts, endothelial cells, human mesenchymal stem cells (hMSCs), and preosteoblasts[35]. In addition, recent advances in hydrogel synthesis and fabrication techniques have led to the engineering of multifunctional ECHs that are able to sense and respond to different physicochemical stimuli[25]. This new class of smart ECHs have been increasingly used for a variety of applications, ranging from stimulating and recording electrodes, tissue engineered constructs, and electrically controlled drug release devices and biosensors[27]. Furthermore, the development of advanced microengineering techniques have allowed the accurate recapitulation

of the complex microarchitectural features of physiological tissues[36]. In this regard, different patterning and templating approaches have been used to fabricate micro-scale structures of ECHs using a broad range of biocompatible and biodegradable materials[37]. With the advent of microengineering techniques such as 3D printing, electrospinning, and other lithography-based approaches, it is possible to exert precise control over the composition, geometry, and spatial arrangement of cells and biomolecules within ECHs. This unprecedented degree of customization holds remarkable potential for the engineering of smart interfaces and biomimetic scaffolds for fundamental research and clinical applications.

Table 1. ECHs can be tailored to mimic the electrical properties of native tissues when used for cardiac and neural tissue engineering.

Native Tissue	Conductivity (S/cm)	Reference
Myocardium (transversely)	0.0016	[38, 39]
Myocardium (longitudinally)	5×10^{-5}	[38, 39]
Brain	0.0015 – 0.0030	[40]

Here, we review all major biomaterials used for the synthesis of ECHs. We describe the most significant conductive materials incorporated into hydrogels to impart electroconductivity. Furthermore, while recent review articles have detailed different fabrication strategies to form hydrogels with specific architectures[41-43], here we review the the advanced microfabrication technique of electrospinning, which is utilized in the fabrication of ECHs for biomedical applications.

1. CRITICAL LITERATURE REVIEW

In this section, we first review the different conductive biomaterials that have been used to develop ECHs. These conductive biomaterials have unique advantages and disadvantages to their application, as well as expected conductivity ranges for these systems (**Table 2**). We then review

the process of electrospinning and what the advantages and limitations are for implementing this technique to form cardiac patches.

1.1. Biomaterials used to impart electroconductivity to hydrogels

1.1.1. Gold nanoparticles

Metallic NPs are colloids ranging from 1 to 100 nanometers in size featuring a high surface area-to-volume ratio[44], which exhibit chemical and physical properties much different from that of bulk metals[45]. Gold NPs (AuNPs) and silver NPs (AgNPs) are of particular interest to engineer ECHs for applications requiring electroactive properties. In recent years, AuNPs have gained significant interest due to their unique conductive[46], optical[47-49], and magnetic properties[50, 51]. These characteristics have been shown to be particularly advantageous for the development of biosensors[52], and drug delivery systems[53], as well as various tissue engineering applications[54]. Apart from their ease of synthesis, their high stability[55] and biocompatibility[48-50], and tunable properties of AuNPs by varying their structural size and shape make them attractive candidates for the synthesis of ECHs for biomedical applications. Some of the drawbacks of incorporating AuNPs into ECHs is their tendency to generate reactive oxygen species (ROS). ROS are oxygen-derived small molecules that are naturally produced endogenously from several sources including through cellular respiration in the mitochondria and from an incomplete reduction of oxygen and NADPH in the plasma membrane[56]. At moderate concentrations, ROS play critical roles in the regulation of cell function, such as cell growth, migration, or apoptosis, however, high concentrations of these molecules can result in damage of proteins, lipids, and DNA potentially leading to diseases and necrosis[57, 58]. Recently, ECHs have been designed that incorporate AuNPs for the purpose of generating high concentrations of ROS in order to eradicate diseased cells[59, 60]. However, when developing ECHs for

regeneration of damaged tissues, it is important to note that due to their small size, AuNPs are capable of penetrating cell membranes and cause cellular dysfunction. Therefore, significant efforts have been conducted to determine the ideal size and shape of AuNPs, and to optimize their *in vivo* pharmacokinetics for therapeutic and clinical applications[61].

Investigations involving tissue regenerative strategies have utilized AuNPs owing to their enhanced electrical properties, which may be imparted to scaffolds and provide adequate coupling between adjacent cells[62]. ECHs formed based on AuNPs have been used for cardiac, bone, and nerve tissue engineering, due to their biocompatibility, high mechanical strength, and conductivity[63, 64]. GelMA is a photocrosslinkable biopolymer that has been widely used for tissue engineering applications as it is capable of supporting cell adhesion due to the presence of Arg-Gly-Asp (RGD) motifs[65]. A recent study conducted by Navaei *et al.* demonstrated the effectiveness of gold nanorods (GNRs) embedded in GelMA hydrogels to develop cardiac tissue constructs[50]. Hydrogels containing a larger concentration of GNRs showed lower electrical impedance, compared with control samples containing GelMA only. This lower impedance reflected the high electrical conductivity of hybrid hydrogels embedded with GNR, which in turn facilitated electrical propagation and promotes CM coupling[50]. The incorporation of GNRs also had a significant effect on the swelling ratio and the porosity of the hydrogels, which are key in the ability of a hydrogel to mediate nutrient and gas exchange[50, 66]. Furthermore, *in vitro* studies demonstrated that CMs seeded on the surface of GNR-embedded ECHs exhibited homogeneous distributions, as compared to control hydrogels without GNRs. Gold nanowires (GNWs) have also been incorporated into polymeric scaffolds for the synthesis of ECHs for tissue engineering applications. For instance, Dvir *et al.* reported the addition of GNWs to alginate scaffolds, to improve electrical communication between cells for engineering functional cardiac patches

(**Figure 2a**)[67]. By incorporating GNWs, these conductive scaffolds demonstrated increased electrical conductivity, enhancing the function of cardiac tissue constructs (**Figure 2b**). CMs and fibroblasts were also seeded onto scaffolds under static and electrically stimulated conditions before implantation. Hematoxylin and eosin staining revealed better-aligned CMs within GNW embedded scaffolds after 8 days of culture (**Figure 2c**), compared to a pure alginate matrix (**Figure 2d**)[67]. These results demonstrated the potential of GNW-loaded hydrogels in tissue engineering, for the development of materials that modulate excitable cells.

AuNPs have been used to engineer ECHs for a wide range of biomedical applications including biosensing, bioimaging, and tissue engineering owing to their high electrical conductivity, unique optical properties, low inherent toxicity, and large surface area. These properties make AuNPs a useful tool as recognition elements for detection of specific biological analytes. AuNP-incorporated ECHs have also been used to develop drug delivery systems with the capability to trigger the release of loaded molecules. Further, these versatile biomaterials have demonstrated the ability to improve cell-cell coupling in ECHs developed for cardiac and neural tissue engineering. However, challenges still exist in the fabrication of AuNP-incorporated ECHs for biomedical applications. For instance, while widely considered to be noncytotoxic, their slow rate of clearance from the physiological environment needs to be considered when designing implantable ECHs containing AuNPs. In addition, the preparation of AuNPs is time consuming and costly, and multistep reactions may result in cytotoxicity. Another consideration is that AuNPs tend to aggregate together during synthesis of ECHs due to their large surface area. Nevertheless, AuNP-incorporated ECHs have shown promise to be successfully developed into tomorrow's therapeutic and diagnostic innovations.

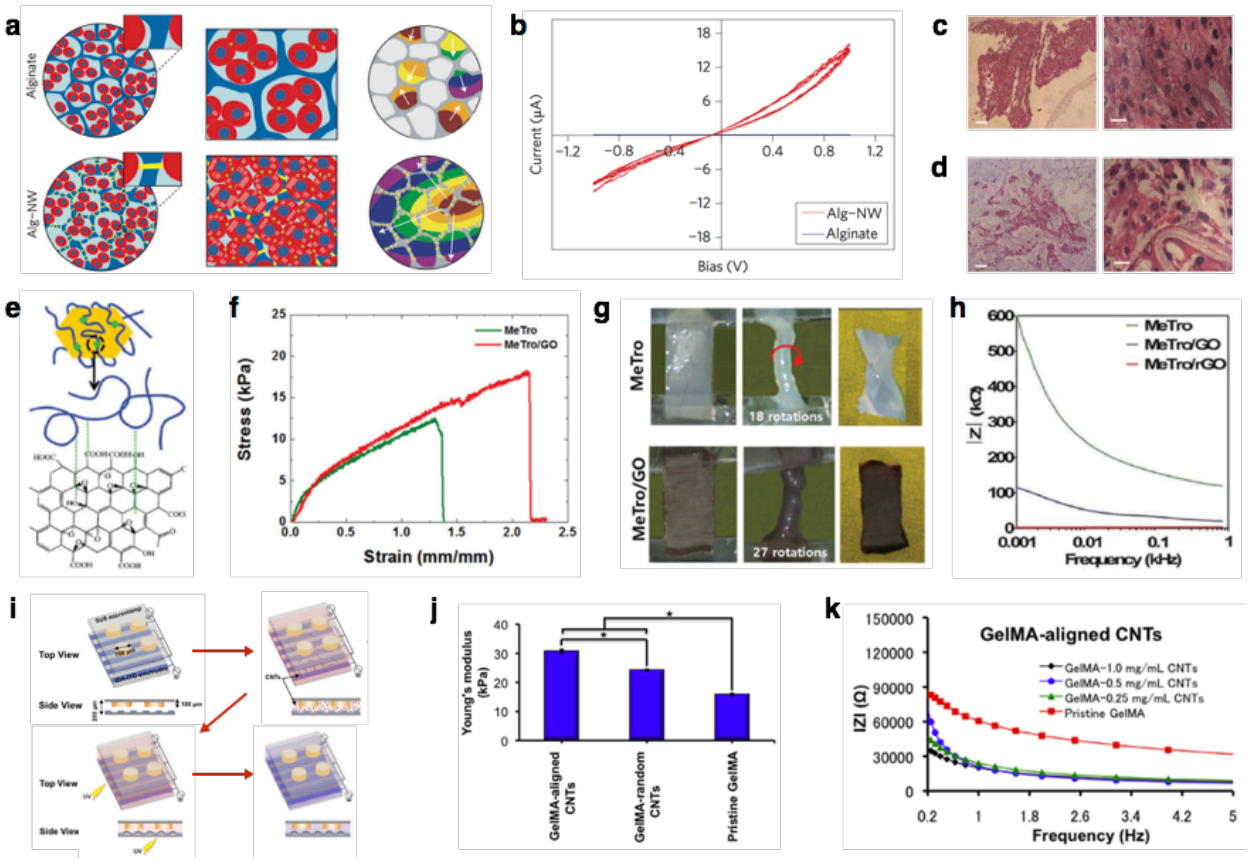

Figure 2. Synthesis and applications of ECHs formed by using conductive NPs. Schematic for the formation of alginate hydrogels and gold nanowires (NW)-alginate ECHs. Cardiomyocytes are cultured in alginate hydrogels formed small clusters and beated asynchronously. However, cardiomyocytes cultured in alginate-NW ECHs formed organized cardiac-like tissue and beat synchronously. Components of engineered cardiac tissue are shown: cardiac cells (red), alginate pore walls (blue), NW (yellow) **(a)**. Current/Potential graph of alginate hydrogels and alginate-NW ECHs showing higher electrical conductivity exhibited by the ECHs **(b)**. Hematoxylin and eosin (H&E) staining images based on *in vitro* studies showed thick tissue in the NW-alginate ECHs **(ci, cii)**, whereas the samples containing pure alginate showed non-continuous tissue separated by pore walls **(di, dii)**. [1], Copyright 2011. Synthesis of ECHs by coating graphene oxide (GO) with methacryloyl-substituted tropoelastin (MeTro) **(e)**. Elastic modulus of MeTro hydrogels and MeTro/GO ECHs demonstrating that the addition of GO significantly increases the elastic modulus **(f).** Torsion test on MeTro hydrogel and MeTro/GO ECH was conducted by twisting scaffolds for multiple rounds. Significant deformation was observed in MeTro hydrogel, however, MeTro/GO ECHs did not display any deformation **(g).** Overall impedance of MeTro hydrogels, MeTro/GO ECHs, and MeTro/reduced GO (rGO) ECHs shows that electrical resistance was the lowest for ECHs fabricated with rGO **(h)**. [2], Copyright 2016. Schematic for the fabrication of CNT-embedded GelMA ECHs using dielectrophoresis force to align CNTs in GelMA. Highly aligned CNTs were observed in under 1 min, and the GelMA prepolymer was

photocrosslinked using UV light **(i)**. Young's modulus of GelMA hydrogels, and ECHs containing GelMA and both randomly arranged and aligned CNTs. Results showed that the alignment of CNTs in GelMA-based ECHs resulted in a stiffer material as compared to ECHs fabricated with randomly dispersed CNTs **(j)**. Electrical evaluation of these ECHs demonstrated that the incorporation of CNTs into hydrogels resulted in lower impedance compared to pristine GelMA hydrogels. Further the conductivity of these ECHs could be finely tuned by adjusting the concentration of CNTs in the system **(k)**. [3], Copyright 2016. Scale bar= 200 μm (**ci, di**), 20 μm (**cii, dii**).

Table 2. Advantages and disadvantages of the incorporation of common conductive biomaterials to form ECHs and the conductivity of these systems.

Conductive materials	**Advantages**	**Disadvantages**	**Conductivity (S/cm)**	**Refs**
AuNPs/ polymer	• Tunable conductivity • Generally biocompatible	• AuNP cytotoxicity is not fully understood • Synthesis of AuNPs may be difficult depending on target particle size • Possible generation of ROS	8.0×10^{-4} – 1.0×10^{-2}	[46-49, 68, 69]
AgNPs/ polymer	• High conductivity • Highly antibacterial	• AgNPs increase brittleness of ECH • Possible generation of ROS	1.0×10^{-4} – 5.8×10^{-1}	[70-76]
Graphene/ polymer	• High conductivity • Robust mechanical strength • Generally biocompatible	• Complicated fabrication method for GO • rGO frequently aggregates during ECH synthesis • Cytotoxicity of GO, rGO is not fully understood	4.0×10^{-5} – 5.8×10^{-1}	[2, 77-80]
CNTs/ polymer	• High conductivity • Robust mechanical strength	• CNTs frequently show aggregation during ECH synthesis • CNTs increase brittleness of ECHs • Cytotoxicity not fully understood	5.0×10^{-5} – 9.0	[3, 79, 81, 82]
PANi/ polymer	• Facile synthesis • Antimicrobial • Highly conductive • Facilitates cell proliferation	• Fabrication requires harsh chemical environment	5.0×10^{-4} – 1.2×10^{-2}	[27, 83, 84]
PPy/ polymer	• Facile synthesis • Biocompatible • Environmentally Stable	• Poor solubility in polar solvents • Poor mechanical strength, brittle	1.2×10^{-3} – 1.2×10^{2}	[4, 85-87]
PEDOT/ polymer	• High conductivity	• Poor mechanical strength, brittle • Cytotoxicity not fully understood	6.7×10^{-4} – 1.0×10^{-1}	[88-92]

	• Facilitates cell proliferation • Biocompatible • High stability			
Bio-IL/ polymer	• High conductivity • Biocompatible	• Variable cytotoxicity	1.4×10^{-4} – 1.0×10^{-2}	[34, 93-96]

1.1.2. Silver nanoparticles

AgNPs have also been used in combination with several types of polymers and biomaterials to engineer ECHs with enhanced electrical conductivity, as well as antimicrobial properties. The ability to eliminate bacteria in the clinical setting is the main driving force behind the success of AgNPs in the biomedical field. The antimicrobial properties of AgNPs are mainly due to the oligodynamic effect, a biocidal effect characterized by the binding of small metal ions to reactive groups, which results in the denaturing of cellular proteins in bacteria[97]. AgNPs are highly active against many types of gram-positive and gram-negative bacteria, including antibiotic-resistant bacterial strains[72, 73, 97-99]. However, similar to AuNPs, AgNPs have the potential to generate ROS that are capable of damaging protein, lipids, and DNA [100]. Therefore, it is necessary to determine cytotoxic effects of ECHs fabricated with AgNPs.

Recently, AgNPs have also been incorporated into ECHs to impart electrical conductivity into these systems. The combination of antimicrobial and conductive properties makes AgNPs an attractive material for use in biomedical applications such as wound and burn dressings[101], coatings for surgical instruments[102], and biosensors[103]. In addition, AgNPs have also been used in a wide variety of industrial applications related to commercial sanitization, including areas of food packaging, textiles, plastics, soaps, and water treatment[104].

The incorporation of AgNPs into polymeric networks can influence the mechanical and swelling properties of ECHs. Previous studies have reported that the addition of AgNPs to

polyvinylpyrrolidone (PVP) and polyvinylalcohol (PVA) hydrogels led to increased mechanical stiffness[74].

Like AgNPs, silver nanowires (AgNWs) are another type of biocompatible material that have been used to develop ECHs for flexible bioelectronics. Recently, Ahn *et al.* developed an ECH by incorporating AgNW-based microelectrodes into a PAM-based hydrogel using a photolithographic process[105]. These materials displayed excellent electrical properties, where the conductivity could be accurately tuned by controlling the AgNW width, and spin coating speed[105]. Further, they possessed robust mechanical properties and excellent flexibility necessary for use with biological tissues. This study described a process to develop AgNW-based ECHs that are promising materials for use as flexible bioelectronic devices.

While incorporation of AgNPs and AgNWs into hydrogels is a noteworthy strategy to engineer ECHs, progress of these systems tailored for biomedical applications has been slow compared that of AuNPs. Most of the research involving AgNPs is greatly interested with their antimicrobial properties. None the less, AgNPs have been found to possess excellent conductive and optical properties, and incorporation of AgNPs into polymer-based hydrogels has little effect on their mechanical properties. Taken together, the properties of AgNP-ECHs make them suitable materials for a wide range of biomedical applications, including drug delivery systems, biosensors, and flexible electronics.

1.1.3. Graphene

Graphene is a 2D hexagonal lattice of carbon that possesses unique mechanical and conductive properties. Although pure graphene is extremely difficult to produce due to its atomic thickness, several methods have been reported for the synthesis of graphene derivatives[77-79]. One common derivative is graphene oxide (GO), where oxygen atoms form bonds with the carbon

lattice and create small imperfections in the lattice structure[77-79]. However, oxidized graphene exhibits poor electrical conductivity, and must be deoxidized to be used in the synthesis of ECHs. Oxidized graphene can be deoxidized through the repair of the sp^2 carbon bonds, which yields a conductive reduced graphene oxide (rGO)[77]. In addition, hydrothermal reduction of high concentration graphene oxide solutions can also be used to produce chemically converted graphene[78]. While graphene has been incorporated into many synthesis strategies to develop ECHs with robust electrical and mechanical properties, cytotoxicity remains to be a concern when these nanoparticles used for biomedical applications. The toxic effects demonstrated by graphene can be influenced by their size, shape, surface charge, surface area, and functional groups[106]. Future studies involving graphene nanoparticles must investigate the *in vitro* and *in vivo* biocompatibility as well as the mechanisms of cytotoxicity before seeking approval from the Food and Drug Administration (FDA).

In a recent study, GO NPs were incorporated inside a highly elastic methacryloyl-substituted tropoelastin (MeTro) hydrogel to form ECHs for cardiac tissue engineering applications[107]. The covalent bonds between polymeric chains, along with hydrophobic and electrostatic interactions between MeTro and GO yielded ECHs with excellent mechanics, electrical conductivity, and biocompatibility (**Figure 2e**)[107]. ECHs containing GO nanoparticles were similar in mechanically stiffness to control MeTro hydrogels, however these ECHs a longer elongation at their breaking point (**Figure 2f**). As a MeTro-based ECH, this material possessed robust mechanical flexibility making them ideal for various tissue engineering applications where dynamic movement is required (**Figure g**). In addition, MeTro/GO ECHs displayed excellent electrical properties with significantly lower electrical resistance compared with non-GO

hydrogels (**Figure 2h**). Furthermore, these scaffolds supported the growth and function of CMs in 2D cultures and elicited no inflammatory response when implanted in a rat model[107].

There has also been an increase in the attention GO-loaded ECHs has received for use in drug delivery systems owing primarily to their remarkable conductive[108] and magnetic[109] properties of GO. In one recent study, Servant *et al.* took advantage of these conductive properties when synthesizing stimuli-responsive hydrogels composed of poly(methacrylic acid) (PMMA) and ball-milled graphene (GBM) to control the release of small molecules *in vivo*. PMMA/GO ECHs exhibited remarkable electrical properties with bulk resistance of these materials decreasing with an increasing concentration of GBM. These smart ECHs were evaluated for their ability to control the release a small molecule drug *in vivo*, using ^{14}C-sucrose as a model drug, and subcutaneous implantation into CD-1 mice as a model. Mice were electrically stimulated using 10V for 1 min periods at 2 h intervals, a relatively low voltage and short time period. The release profile of ^{14}C-sucrose showed that PMMA/GO ECHs greatly outperformed control PMMA hydrogels with 5.5% ^{14}C-sucrose released in the blood 8 min following electrical stimulation[108]. The development of advanced drug delivery systems that are able to control the release of molecules is a vastly important biomedical field. This work demonstrates that GO can be used to develop smart ECHs which do just that.

GO-incorporated ECHs have demonstrated their potential to be developed for different tissue engineering application such as cardiac and neural tissue engineering, owing to their excellent mechanical, and conductive properties. The amphiphilic nature of GO provides it with a structure that is deemed as biocompatible, however, more *in vitro* and *in vivo* investigations are required to evaluate the reaction these materials elicit to living tissues. In addition, the superior fluorescence quenching, and surface functionalization observed by GO make them excellent

materials for use in biosensors and drug delivery systems. The unique chemical and physical properties of GO make it and excellent candidate for development into future biotechnological and biomedical applications.

1.1.4. Carbon nanotubes

CNTs are nanostructures comprised of a cylindrical lattice of carbon atoms and are characterized either as single-walled or multi-walled nanotubes. CNTs have gained significant interest due to their unique properties, including high compressive and tensile strength, as well as high electrical conductivity[79, 81, 82, 110-112]. CNTs have been shown to be useful for engineering ECHs due to their ability to reduce brittleness and significantly increase electrical conductivity. However, they can also be difficult to incorporate into ECHs due to their unique chemical structure, which is characterized by strong Van der Waals forces, high hydrophobicity, and low entropy[81]. The combination of these factors often leads to the aggregation of CNTs in solution, making homogenous mixtures difficult to produce[81].

The field of cardiac tissue engineering has also greatly benefited from the synthesis of CNT-embedded ECHs. A recent study conducted by Ahadian *et al.* used dielectrophoresis to align CNTs in a GelMA-based hydrogel (**Figure 2i**), which enhanced the cardiac differentiation of embryoid bodies cultured in the microwells of patterned ECHs[113]. CNT-loaded ECHs exhibited higher elastic moduli (**Figure 2j**), lower electrical resistance, and supported increased beating of the cells as compared to pure GelMA hydrogels (**Figure 2k**). These results demonstrated that the engineered materials could be suitable for broad applications within regenerative medicine and cell therapy where conductivity of the matrix plays an important role[113].

Incorporation of CNTs into polymeric networks to develop ECHs has become a reliable strategy to produce scaffolds with excellent conductivity and mechanical strength. These traits

make them suitable biomaterials for use in tissue engineering applications. In addition, CNTs possess excellent stability, and magnetic properties making them excellent candidates for a wide range of other biomedical applications, such as biosensors or drug delivery systems. However, the future direction of CNTs in ECHs should focus on *in vivo* models that address biocompatibility concerns, especially those that arise from health effects with the respiratory system. If CNTs can be incorporated into biocompatible ECHs without toxicological or inflammatory issues, these nanoparticles will be excellent candidates for modern biomedical applications in the future.

1.1.5. Polyaniline

PANi is an electrically conductive polymer with a conjugated backbone that has been widely used for the synthesis of ECHs due its mechanical stability, ease of fabrication, and low manufacturing costs[114-118]. Previous studies have reported the use of several derivatives of PANi, including its most reduced form (leucoemeraldine), its fully oxidized form (pernigranalline), and a partially oxidized form (emeraldine)[119, 120] for the formation of ECHs. Many natural and synthetic polymers have been used in conjunction with PANi to engineer ECHs. For instance, Xia *et al.* described the development of ECHs using PANi and polyacrylic acid (PAA), by reacting positively charged aniline monomers with the negatively charged COO^- functional groups in PAA[84]. Their results showed that the addition of PANi increased the electrical conductivity, as well as compressive and elastic moduli of the resulting ECHs. In particular, this improved electrical conductivity was likely due to PANi fibers filling in small pores of the PAA hydrogel[84]. A similar study conducted by Zhao *et al.* described the engineering of an injectable ECH using quaternized chitosan and PANi for regenerative tissue engineering applications[121]. The engineered ECH was shown to possess high antibacterial activity against Gram-negative and Gram-positive bacteria (**Figure 3a**), as well as increased electrical

conductivity (**Figure 3b**) and swellability. In addition, *in vitro* studies using C2C12 myoblasts demonstrated that ECHs containing higher concentrations of PANi showed significantly increased cell proliferation as compared to pure chitosan hydrogels grafted with oxidized dextran as a control group (**Figure 3c**). This study introduced a new class of bioactive scaffolds that may be tailored for a variety of tissue engineering applications, such as scaffolds for cardiac and nerve tissue regeneration[121].

As a conductive polymer, PANi has gained the most attention for the development of ECHs designed for biomedical related applications. This is due to the high electrical conductivity, stability, and unique redox properties found in PANi, as well as ease of synthesis and low cost[122, 123]. However, some limitations have slowed the development of PANi-incorporated ECHs for biomedical applications, such as harsh processing conditions, toxicity, and nonbiodegradability. Future investigations should evaluate PANi combined with other monomers to develop ECHs that possess high conductivity, as well as biodegradability, and biocompatibility.

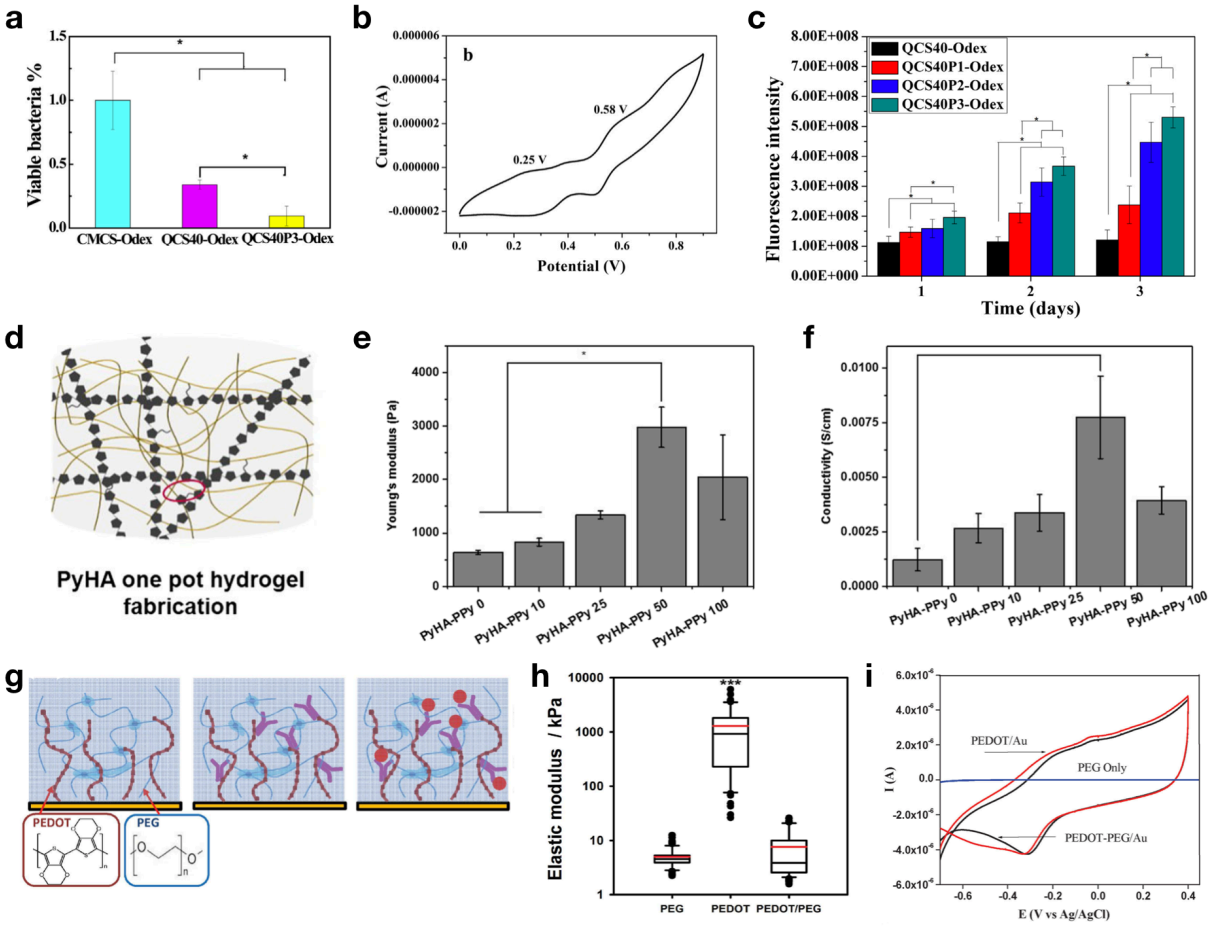

Figure 3. Structure and properties of ECHs formed by using conductive polymers. *In vivo* antibacterial activity test using hydrogels formed with carboxymethyl chitosan (CMCS-Odex), quaternized chitosan (QCS40-Odex), and quaternized chitosan with 3% (w/v) polyaniline (PANi). Oxidized dextran (Odex) was used as a crosslinker to form these ECHs. Results showed that engineered PANi-incorporated ECHs exhibited high antimicrobial properties **(a)**. PANi-incorporated ECHs also exhibited high electrical conductivity **(b)**. These ECHs demonstrated increased C2C12 cell proliferation with an increasing concentration of PANi, after 3 days of culture **(c)**. [4], Copyright 2015. ECH developed by crosslinking polypyrrole (PPy) with hyaluronic acid (HA). Mechanical testing of HA-based ECHs with varying concentrations of PPy demonstrated that higher concentrations of PPy results in higher elastic modulus **(d)**. In addition, higher concentrations of PPy increased electrical conductivity up to samples containing 50 mM **(e).** Plot of the number of attached 3T3 cells seeded on the surface of HA-based ECHs containing 50 mM PPy. These results showed that HA/PPy ECHs supported cell adhesion and the proliferation of 3T3 cells up to 5 days **(f)**. [5], Copyright 2016. Schematic for the synthesis of ECHs by adding PEDOT (red) and PEG (blue) to the surface of an electrode. Biorecognition molecules (purple) are added into the gel by attaching to -COOH groups of PEDOT. Capture of B-IFN-γ molecules (red dot) resulted in a change in the electrical signal of the ECH **(g)**.

Assessment of the mechanical properties of PEG hydrogels, as well as PEDOT and PEDOT/PEG ECHs. Here the results showed that by adding PEDOT to PEG did not significantly change the elastic modulus compared to pure PEG hydrogels **(h).** However, the addition of PEDOT resulted in a significant increase in electrical conductivity **(i)**, which is necessary for application in the field of biosensors. [6], Copyright 2016.

1.1.6. Polypyrrole

PPy is an electroconductive polymer that has been used for the synthesis of ECHs due to its facile synthesis, environmental stability, tunable mechanical properties, and biocompatibility[124-127]. PPy has also been used for other purposes, including drug delivery systems[128-130] and bio-electrodes[131, 132], as well as the engineering of cardiac tissue constructs[133, 134] and artificial muscles[135]. A recent study conducted by Yang *et al.*, reported the combination of PPy with hyaluronic acid (HA) by conjugating N-(3-aminopropyl) pyrrole onto HA polymer chains yielding ECHs with enhanced electrical conductivity (**Figure 3d**)[136]. Their results showed that the elastic modulus and electrical conductivity of the engineered ECHs increased concomitantly with increasing concentrations of PPy up to 50mM (**Figure 3e**). The highest electrical conductivity obtained by these PPy-incorporated ECHs was approximately 7.3 mS cm^{-1}, when fabricated with a 0.5 mM PPy concentration (**Figure 3f**)[136]. *In vitro* cell studies conducted by seeding 3T3 cells on PPy-ECHs showed increased cell adhesion and proliferation, as compared to pure HA hydrogels. Taken together, these results demonstrated that PPy-incorpotated ECHs could be used to develop tissue engineering scaffolds in conjunction with excitable cell types, as well as for future prosthetic devices.

The excellent redox properties of PPy have also made them attractive materials for use in the development of patterned electrodes for the skin. In a recent study, Hur *et al.* developed a PPy-incorporated smart ECH using agarose as the polymeric network[85]. This strategy yielded remarkable ECHs that were not only highly conductive, but also contained thermoplastic

properties, which enabled thermal or light-assisted healing of the network. These ECHs exhibited mechanical properties that were similar to that of human skin, with a Young's modulus of 27-46 kPa, while also possessing an electrical conductivity in the same range as other ECHs fabricated using CPs (0.35 S cm^{-1})[85]. By developing ECHs with similar mechanical flexibility and self-healing properties, as well as high electrical conductivity, these materials have demonstrated ideal physical and chemical properties for applications involving flexible electronics and biosensors.

PPy has become a very popular CP for the fabrication of ECHs suitable for biomedical applications. Importantly, these CPs exhibit good *in vitro* and *in vivo* biocompatibility and excellent stimulus-responsive properties, as well as high thermal stability[123]. These traits make them excellent biomaterials for use in biomedical related applications, such as biosensors, drug delivery, and flexible electronics. PPy may also be used for tissue engineering applications where excitable cell types are found, such as neural[137] and cardiac tissue[138]. Some challenges in fabrication of good quality PPy-incorporated ECHs is overcoming their poor solubility in polar solvents and mechanical stiffness, which can often become brittle. Future research into PPy-incorporated ECHs may focus on incorporation with natural polymers with good biodegradation profiles and cell adhesion to be used for biomedical applications.

1.1.7. Polythiophenes / PEDOT

Polythiophenes (PThs) are another innately electroconductive polymer that has been used to impart electrical conductivity to ECHs due to their solubility, high thermal stability, and excellent electrical conductivity when in a doped state[88, 139]. However, the use of PThs for biomedical applications is often limited due to the increased weight and rigidity of PThs, which can potentially decrease the mechanical and electroactive performance of resulting ECHs[88]. Unlike PThs, its derivative poly(3,4-ethylenedioxythiophene) (PEDOT) is commonly used in the

synthesis of ECHs due to its biocompatibility, cost-effectiveness[140], and electrochemical stability in aqueous solutions[141-146]. While PEDOT itself is conductive, increased electrical conductivity, as well as cationic conductivity is rendered when PEDOT is combined with poly(styrene sulfonate) (PSS)[147]. PEDOT:PSS also maintains suitable conductivity in the physiological environment, and may be cleared by the renal system, which has resulted in significant attention in a variety of biomedical-related fields, such as tissue engineering[90, 91].

Recent studies have shown that PEDOT-incorporated ECHs can be used to closely mimic the conductive and mechanical properties of certain tissues, making them suitable to use as scaffolds for tissue engineering. A study by Kim *et al.* reported that native cardiac tissue has an elastic modulus within the range of 10-100 kPa, and has a conductivity ranging from 10^{-3} S/cm to 10^{-2} S cm^{-1}. In one study, Kim *et al.* reported the formation of an ECH based on a RDG modified polyethylene glycol (PEG) containing PEDOT with an elastic modulus of 21 ± 4 kPa and a conductivity of 1.69×10^{-2} S cm^{-1}[90]. *In vitro* cell studies using electro-responsive H9C2 cells were conducted to determine the effect of PEDOT on cell attachment and proliferation. Their results showed that PEDOT-containing ECHs supported cell adhesion and proliferation without compromising the electrical and physiochemical properties of the hydrogel, and thus was found to be a promising candidate for applications such as tissue engineering of muscle and nerve tissue[148].

PEDOT has also investigated for use to develop ECHs for biosensors. Recently, Shin *et al.* developed a PEDOT/PEG-based ECH to detect specific antigen molecules in the physiological context. The outer layers of these sensors were coated in the ECH loaded with a cytokine-specific antibody, which is attached to a PEDOT-COOH group. Once these biosensors come in contact with the IFN-γin analyte, the ECHs undergo a quantifiable decrease in electrical conductivity that

would serve at the detection mechanism (**Figure 3g**). Despite the high mechanical strength of PEDOT, PEDOT/PEG ECHs exhibited an elastic modulus of 7.58 ± 0.84 kPa, which was similar to that of pure PEG hydrogels and within the range for use in many biological systems (**Figure 3h**). In contrast with non-conductive PEG hydrogels, PEDOT/PEG ECHs exhibited remarkable electrical conductivity that was highly distinguishable from control samples (**Figure 3i**). These ECHs demonstrated a system that was successfully able to transfer the detection of an analyte into an electrochemical signal. These results suggest that PEDOT is an effective material to impart electrical conductivity for future biosensor applications.

Advancements in the development of PEDOT-incorporated ECHs have led to promising innovations in areas including biosensors, implantable electrodes, and drug delivery systems. Investigators are able to take advantage of the high electrical conductivity, as well as chemical and environmental stability exhibited by PEDOT. Further, PEDOT has been widely reported as a biocompatible material with many in vitro investigations displaying no cytotoxicity. However, due to high mechanical stiffness of this material, the foreign body response may disrupt performance when PEDOT-incorporated ECHs are implanted in soft tissues, such as in the brain. While these ECHs have displayed excellent properties for biomedical applications, long term *in vitro* and *in vivo* investigations are required to determine effects of surrounding tissues before they may be transition into the clinical setting. Taken together, PEDOT-incorporated ECHs are a promising biomaterial for future biomedical related therapeutic and diagnostic strategies.

1.1.8. Ionic liquid

Ionic liquids (ILs) have been implemented in a wide range of industrial applications, including fuel cells[93], solar cells[94], batteries[95], and sensors[149] due to their many unique properties such as low volatility, non-flammability, high thermal stability, and high ionic conductivity[150-154]. ILs are liquids comprised completely of ions from salts, which have a melting point below 100°C. There are many sub-categories of ILs, including room temperature ILs, task-specific ILs, polyionic liquids, and supported IL membranes[153]. Previous studies have focused on the characterization of the physical structure and properties, nano-organization and self-assembly, and advanced chemical transformations of ILs[155]. Recently, it has been demonstrated that ECHs may be engineered by combining ILs with polymers for applications in tissue engineering, electrochemical biosensors, electro-stimulated controlled drug release systems, and neural prosthetics[156, 157].

For example, ECHs can be formed by polymerizing monomers in ILs to increase the electrical conductivity of these scaffolds. This approach was demonstrated by Liang *et al.*, using microcrystalline cellulose and PPy as polymers, to form a network in 1-butyl-3-methylimidazolium chloride (BMIMCl) IL[157]. BMIMCI was used in this study to provide a solvent that could dissolve cellulose while protecting its structure from degradation. The swelling of ECHs was found to be dependent on the microcrystalline cellulose concentration, with higher concentrations exhibiting lower swelling ratios. Furthermore, the mechanical properties were substantially improved with the incorporation of PPy, increasing from a maximum stress of 1.53 MPa for control samples, to 26.25 MPa for PPy-containing ECHs[157]. Their results also demonstrated that the composite hydrogels synthesized using ILs were suitable for the development of biological and semiconducting materials, as well as drug delivery systems and neural prosthetics[157]. In another study, Robinson *et al.* develop a synthetic sensing skin by 3D

printing two inks; one that was ionically conductive, and one that was electrically insulating[156]. For this, they used the conductive 1-decyl-3-methylimidazolium chloride IL, while the insulating material was a silicone elastomer. This approach was used to print a micropatterned material that could act as stretchable capacitive sensors. Both inks were extruded and polymerized *in situ* to form a layer of ECHs, and a layer of insulating silicone. The resulting capacitive skin demonstrated excellent adhesion to actuation chambers, as well as the ability to detect a compressive force of approximately 2 N. The combination of an ECH with the insulating silicone led to the development of the first printable skin to demonstrate enabled tactile sensing and kinesthetic feedback[156].

1.2. Microfabrication techniques used to develop ECHs

1.2.1. Electrospun fibers

The primary goal for the design of tissue engineered scaffolds is to develop materials that structurally and functionally mimic the native ECM. The ECM is a complex network of proteins, proteoglycans, and glycosaminoglycans that provides physical support for cells[158, 159]. Furthermore, the ECM is responsible for the promotion of cell adhesion and migration, as well as proliferation, and function[160]. This is achieved, in part, due to the complex nanostructure of protein fibers, such as collagen and elastin[160], and the presence of specific ligands and growth factors[161, 162]. Protein fibers may range in diameter from several tens to several hundred nanometers. In this regard, electrospinning has been increasingly used for the synthesis of polymer fibers that resemble the fibrous architecture of the ECM. Electrospinning systems are comprised of three main components; a high voltage supplier capable of generating 10-20 kV of potential, a a small diameter metal nozzle, and a metal collector (**Figure 4a**)[163-165]. The generated electrical field drives the polymer feed to the grounded metal collector in a process that is referred to as a whipping mode, which is characterized by increased acceleration and oscillation[163, 166,

167]. The solvent used in the polymer feed is mainly evaporated or solidified in the electrospinning process, and trace amounts of solvent in the fibers may be removed using vacuum after synthesis. Electrospun conductive fibrous scaffolds have been widely used in tissue engineering and biomedical applications due to the promotion of favorable cellular responses, such as increased adhesion and proliferation[168-170].

Another recent study by Malki *et al.* investigated ECHs fabricated by electrospun albumin and then absorbing AuNRs into the fibers to engineer cardiac patches capable of cardiac tissue regeneration following myocardial infarction (MI)[171]. Through the electrospinning of albumin, a porous scaffold composed of ribbon-like fibers with a thickness of 0.5 μm, was developed that closely resembled the structure of cardiac tissue[171]. Further, the incorporation of AuNRs to these cardiac patches improved electrical conductivity that would assist in the cell-cell interactions that are responsible to synchronous heart beating. The AuNR-incorporated cardiac patches were evaluated *in vitro* through cardiomyocyte encapsulation within these hybrid scaffolds to analyze the expression of the gap junction protein connexin 43 (Cxn43), which is responsible for cell-cell signaling. Their results showed that after 7 days of cell culture there was a significant expression of Cxn43, as well as pronounced actinin striation, suggesting the cells ability to contract synchronously[171]. The electrical enhancement of these electrospun scaffolds yielded cardiac patches which were able to support cardiomyocyte contraction and may be used to improve the function of cardiac tissue following MI.

In another study, Liu *et al.* developed ECHs with architecture that closely resembled the cardiac microenvironment through electrospinning poly(ethylene glycol)-poly(D,L-Lactide) (PELA) copolymers with CNTs onto a spinning mandrel[7]. Their approach investigated the efficacy of both blend electrospinning and coaxial electrospinning techniques. Blend

electrospinning involves mixing CNTs and PELA into a polymer solution. Coaxial electrospinning follows the same principles, however, two separate solutions, one containing PELA and the other CNTs, were coaxially and simultaneously electrospun through different capillary tubes into the same nozzle. Electrospinning PELA/CNT onto a rotating mandrel resulted in aligned fibers with diameters between 2-3 μm (**Figure 4b**). These blended and coaxial electrospun scaffolds demonstrated that higher CNT concentrations resulted in higher mechanical stiffness, concomitantly (**Figure 4c**). Further, scaffolds fabricated with higher concentrations of CNTs yielded higher electrical conductivity (**Figure 4d**). These electrospun scaffolds were also evaluated to determine beating strength of CMs when seeded on fibrous mats for up to 10 days. Results showed that CMs seeded on electrospun scaffolds fabricated with 5% CNTs had significantly higher average beating rates (70-80 beats/min) when compared to scaffolds fabricated with 3%, 4%, and 6% CNT concentrations (**Figure 4e**). All PELA/CNT electrospun scaffolds evaluated showed synchronous beating, except for those fabricated with 6% CNTs. The electrospinning microfabrication technique was used in this study to produce conductive patches for cardiac tissue engineering by creating fibrous scaffolds that mimic the organized cardiac muscle fibers of the heart.

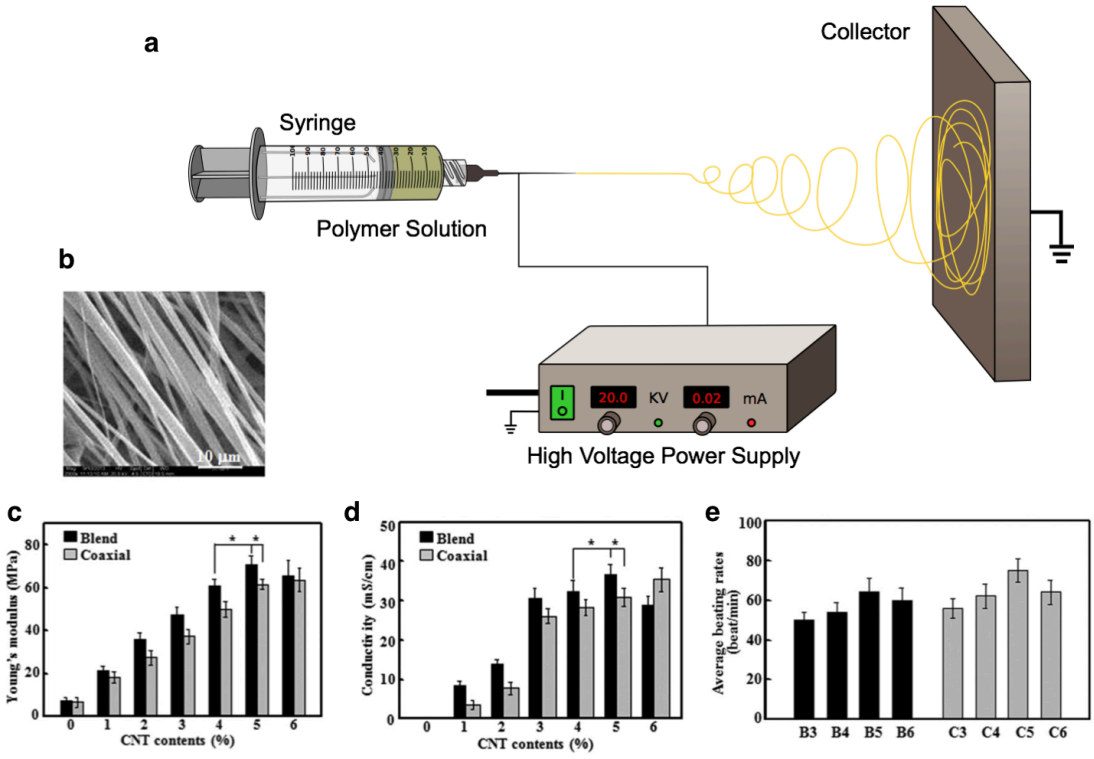

Figure 4. Electrospinning microfabrication technique is a simple method for generating fibrous scaffolds that are suitable for many applications including tissue engineering, biosensors, and drug delivery systems. Schematic for an electrospinning set up consists of a polymer dissolved in solvent being injected out of a metal nozzle **(a)**. A high voltage power supply is connected to a metal nozzle and a metal collector creating an electrical field. A polymeric solution is then slowly pumped out of the syringe and spun onto the metal collector. Representative SEM image of a blend electrospun PELA/CNT fibrous scaffold with a 5% CNT concentration showing high alignment of fibers and 2 µm fiber diameter **(b)**. Mechanical study of electrospun PELA/CNTs demonstrated that ECHs fabricated with higher concentrations of CNTs resulted in a higher Young's modulus **(c)**. Electrical evaluation of electrospun ECHs showed that these fibrous scaffolds exhibited higher conductivity when fabricated with a higher concentration of CNTs in both blended and coaxial electrospun PELA/CNT scaffolds **(d)**. Beating rate of CMs when seeded on PELA/CNT fibrous scaffolds and cultured for 10 days. The beating rate for ECHs coaxially electrospun with a 5% CNT concentration (C5) achieved an average beating rate of 70-80 times/min, which is similar to that rate of CMs seeded on other non-conductive hydrogels **(e)**. [7], Copyright 2016.

Electrospinning is a facile method that allows precise control over many parameters of the synthesis process, such as voltage applied, distance from the nozzle to collector, and flow rate. In addition, metal collectors may be static, generating randomly arranged fibers, or rotating, which

results in highly aligned fibers. By adjusting these parameters, it is possible to engineer ECHs with finely tuned fiber morphology and geometry. Using advanced electrospinning set-ups, ECHs with enhanced microarchitecture, porosity, mechanical properties, and electrical conductivity have been fabricated with exceptional properties for biomedical applications. Further, electrospinning provides a method to optimize the patterning of cells or bioactive ligands in a way that is biomimetic to the structure and morphology of natural tissues. Further characterization including *in vivo* studies, however, will be required for electrospun ECHs before they may be used for such applications as treatment of medical diseases in the clinical setting. Future electrospinning considerations should also seek to improve cost-effectiveness and increase the yield of fibrous scaffolds. Nonetheless, modern electroactive scaffolds, with excellent scalability, reproducibility, and consistency show promise for use in future biomedical applications such as cardiac and neural tissue engineering.

1.2.2. 3D printing

3D printing technology has significantly improved over the past few decades, enabling the creation of complex 3D structures that might otherwise be impossible to fabricate with traditional molding techniques or top-down milling procedures [172]. Not surprisingly, this technology has made its way into the biomedical field to form complex structures which have great potential to contribute to our understanding of healthy and diseased tissue states [173], expand our treatment options for those diseases [174], or fabricate medical devices [175]. In addition, the turnover time for these structures or devices is appreciably less than many molding or fabrication processes, which can reduce lead time and accelerate products to patient timelines.

For many biomedical applications, engineering biomaterials with biomimetic mechanical properties have been a challenge. This mechanical mismatch has inspired widespread interest in

the field of flexible electronics and electroactive tissue engineering [176]. To this end, the design of soft and conductive materials has been an emerging area of research in recent decades. Since the hydrostatic and mechanical properties of hydrogels are very similar to human tissues, they are an obvious choice as a material for fabricating complex 3D bioprinted structures for biomedical applications. In this section, we will review recent work in the field of 3D printing of ECHs and the applications targeted for the formulations and technology.

One of the common applications of 3D printed ECHs is as pressure/motion sensors or as biosensors [177]. For these applications, tuning the geometrical or chemical structure of the ECHs can modulate its electrical properties and causes a proportional response, signaling the occurrence of an event. In the case of pressure or motion sensors, the compression or extension of the hydrogel causes a corresponding change in electrical resistance and thus the generation of an electrical signal [178]. For biosensors, an analyte of interest binds to the conductive material and induces a change in its electrical properties, causing the signal to be generated [6]. Normally these sensors require advanced fabrication techniques to achieve the complex landscape for the sensor design. 3D printing can eliminate the need for costly tooling and equipment that is typically required to form these patterns and enables rapid formation of multiple designs at minimal cost and significantly reduced lead time. In some cases, elastomeric polymers, such as polydimethylsiloxane (PDMS), are utilized as printing substrates onto which the conductive hydrogel can be patterned with the printing device [179]. The PDMS helps to maintain the overall stability of the printed structure and provides a template for the sensing function of the device. While non-hydrogel conductive elastomers can be used for pressure or motion sensors [180], detection of water-soluble analytes might not be as sensitive or accurate if non-porous hydrophobic materials, such as PDMS, are used. For example, inkjet printing was used to pattern a nanostructured PANi hydrogel for

multiplex detection of glucose, lactate, and triglycerides in real time selectively and with high sensitivity [181]. The use of printing for the devices enabled them to fabricate pages of sensor arrays with 96 electrodes in minutes. In comparison, traditional photolithography patterning methods would require pre-fabrication of photomasks and careful substrate preparation and washing and cleaning steps before the device could be realized. Pressure sensors were fabricated by printing a conductive self-healing hydrogel composed of polyacrylic acid and PPy (**Figure 5a**), wherein changes in pressure caused a corresponding change in electrical resistance [182]. The devices were coated with a thin layer of PDMS to contain the conductive gel and pressed onto the wrist for taking blood pulse readings. These printed devices could be used as wearable sensors that conformed to the shape of the arm, finger, or wrist (**Figure 5b**). One group designed a photocurable conductive and elastic hydrogel that could be printed using digital light processing (DLP) stereolithography (SLA) [183]. The printed constructs were not tested for specific applications, but the formulation and printing technology combined are promising for applications where a transparent, elastic, and conductive hydrogel is required, such as for optogenetics [184]. Careful deliberation of the materials and methods will undoubtedly improve the performance and capabilities of 3D printed conductive hydrogel-based devices in the near future.

Recapitulation of complex tissues *in vitro* is becoming increasingly more possible as advanced microfabrication strategies evolve. 3D bioprinting has enabled the generation of features in an additional dimension compared to 2D patterning methods and has provided scientists with the capacity to form biomimetic tissue structures *in vitro*. Ultimately, the goal of this technology is to generate full-scale tissues or organs that can replace organ donation and transplants, thus reducing issues with donor availability and chronic organ rejection [185]. Bioprinted hydrogels with improved electrical conductivity have been shown to improve the function of electroactive

tissues, such as cardiac and neural tissue [67, 186]. For example, PEGDA hydrogels mixed with various concentrations of amine functionalized multi-walled carbon nanotubes (MWCNTs) was 3D printed into grid-like structures for nerve regeneration [187]. Results showed that neural stem cells (NSCs) proliferated more and differentiated early on scaffolds containing MWCNTs compared to controls without conductive nanotubes. In addition, exogenous electrical stimulation in the form of biphasic pulses enhanced neuronal maturity for structures containing the MWCNTs as confirmed by quantitative polymerase chain reaction (qPCR). A similar study targeting cardiac tissue utilized a bioink containing GNRs, GelMA, and sodium alginate with a co-axial printing system, where sodium alginate was used as a structural material that was rapidly crosslinked as aqueous calcium chloride was extruded through the shell of the nozzle (**Figure 5c**) [9]. CMs encapsulated in the 3D printed GelMA/GNR hydrogel structure expressed higher levels of Cxn43 cardiac junction protein and exhibited higher contraction rates than GelMA controls (**Figure 5d**). These results show promise as materials that can help us design cell-laden 3D printed structures with enhanced tissue function that may enable tissue replacement in the future.

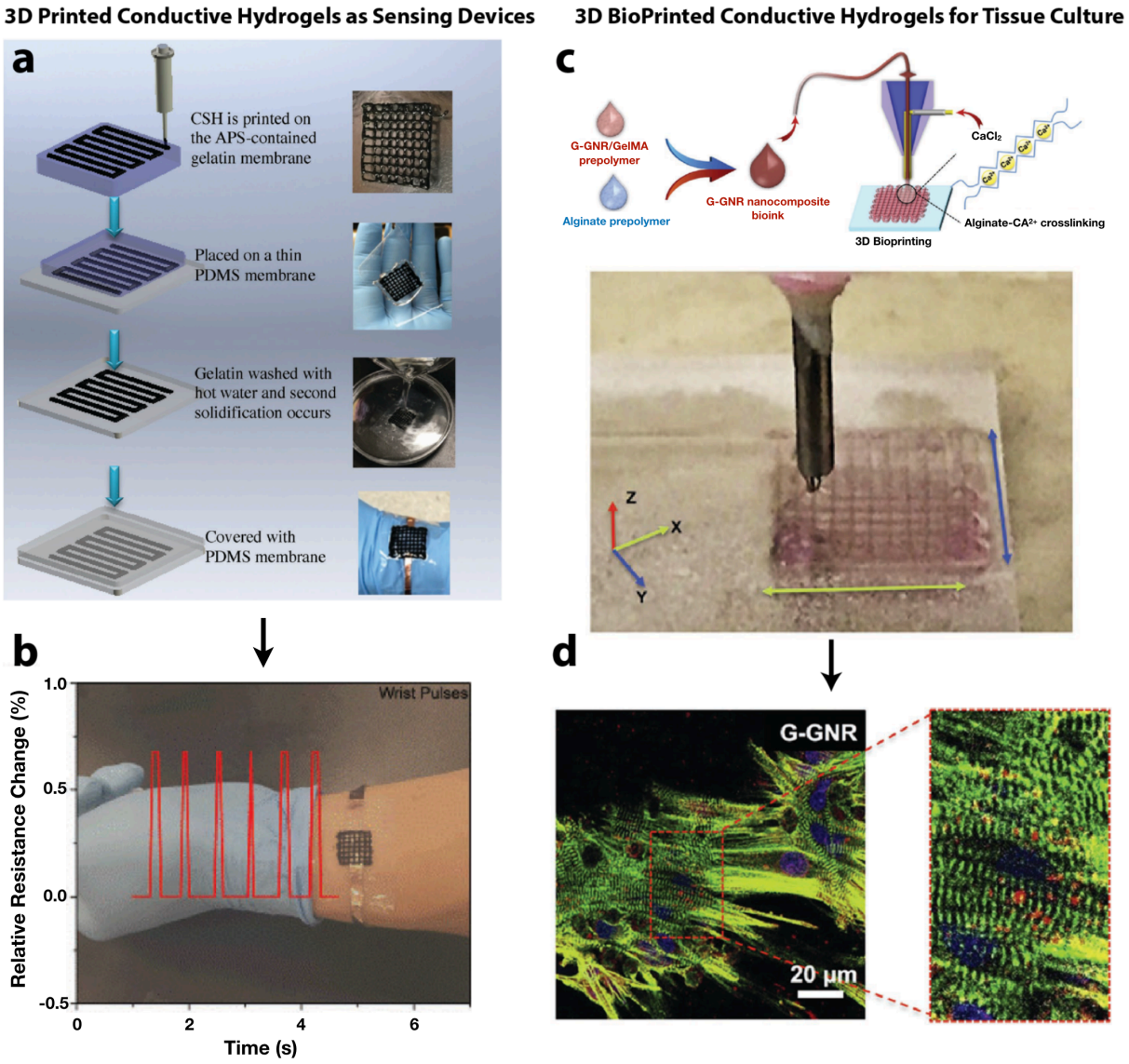

Figure 5. 3D printing of conductive hydrogels for different biomedical applications. Pressure sensors were fabricated by 3D printing a conductive self-healing (CSH) hydrogel composed of PPy-grafted chitosan and poly(acrylic acid), and coating them with a thin layer of PDMS **(a)**. When applied to the wrist, the sensor could detect blood flow pulses in the veins below the skin in real-time **(b)** (Adapted from [8]). Hydrogel prepolymer solution containing sodium alginate, gold nanorods, and GelMA was bioprinted via a co-axial nozzle, in which the alginate prepolymer solution in the core was crosslinked by calcium ions flown in the sheath **(c)**. Lattice-like structures could be printed, and hydration was maintained by the continuous flow of the aqueous sheath solution. Cardiomyocytes printed in these structures expressed higher levels of Cxn43 cardiac junction protein and exhibited higher contraction rates compared to controls **(d)** (Adapted from [9]).

3D printing has been widely used in the biomedical field. Its simplicity, low cost, minimization of waste, and ever-advancing capability have made this technique an extremely powerful tool that will revolutionize our ability to iterate designs in ways previously not possible. ECHs have proven utility for applications where an electrically active, flexible, and hydrated material is required, such as in sensing devices and for tissue culture. The combination of these approaches has provided researchers with the means to create complex structures with unprecedented speed and precision. For 3D printed conductive hydrogel motion sensors, the capabilities tested thus far were limited to simple events, such as hand or arm movement [179]. More sophisticated devices capable of sensing motion and responding could be used as medical devices, such as a film that can sense heartbeat rhythms and provide an electrical stimulation impulse if arrhythmia is detected. An ongoing challenge in biosensors is improving selectivity [188]. Hydrogel compositions could be chemically modified to improve selectivity and prevent false positive or false negative responses. For 3D bioprinting, designing ECHs bioink with biocompatibility and printability is a major limitation, especially in the case of printing complex cell-laden 3D structures. In addition, the ability to directly print integrated electrochemical probes into 3D printed devices would enable interrogation and stimulation of electroactive cells encapsulated in the structure [189]. Finally, the resolution of 3D printing is rapidly improving, and decreased feature size can shrink the overall size of devices or sensors and increase the fidelity of bioprinted structures that mimic native tissues. These improvements will enable 3D printing combined with ECHs to contribute even further to multiple facets of the biomedical field.

1.2.3. Micropatterning of ECHs

Micropatterned hydrogels have been used in a wide range of biomedical applications, such as drug delivery [190, 191], and tissue engineering [192]. Some of the most commonly used

techniques for micropatterning of hydrogels include microfluidics [193], magnetic [194] and acoustics guided hydrogel assembly [195]. However, micropatterned non-conductive hydrogels could impede electrical cell-cell coupling and lead to signal deferment inside the scaffolds [67]. This in turn could potentially limit their application in the context of physiological environments where excitable cell types are present such as nerve and cardiac tissues. Therefore, micropatterning of ECHs has gained significant attention, and different techniques have been investigated to generate unique architectures of micropatterned ECHs for biomedical applications [196]. For example, in a study by Kim *et al.*, conductive PEDOT-incorporated ECHs were patterned to develop flexible electrodes [197]. Briefly, a PEDOT film was prepared by reacting a liquid phase PEDOT monomer casting with the oxidant Fe(III) tosylate. A UV-induced photopolymerization of PEG was then performed using a photolithography technique at the PEG/PEDOT interface using a photomask. The PEG hydrogel was then peeled off removing the region of PEDOT film that was exposed to UV irradiation. Finally, a second PEG gelation step was performed on the remaining patterned PEDOT film, which left it embedded in the hydrogel. Micropatterned PEDOT-embedded ECHs exhibited high electrical conductivity coupled with flexible mechanical properties, which demonstrate their potential for biomedical applications such stimuli-responsive drug delivery systems and growth factor delivery systems [197].

In another study, Wu *et al.* reported the engineering of conductive GelMA-PANi ECHs in patterned hexagonal geometries, by utilizing digital projection stereolithography [198]. This was achieved by injecting GelMA-PANi precursor solution in a chamber and crosslinked in organized patterns using a computer-aided design-based digital mask. GelMA/PANi ECHs demonstrated remarkably lower impedance (2.9 ± 0.3 kΩ) compared to control GelMA hydrogels (6.9 ± 0.7 kΩ), at physiologically relevant frequencies. In addition, *in vitro* cell studies were used to investigate

the effect that these micropatterned ECHs on the morphology of adhered cells. This was done using C3H/10T1/2 murine mesenchymal progenitor cells (10T1/2s) cells seeded on the surface GelMA and GelMA/PANi samples and cultured for 5 days. Results showed that 10T1/2s cells seeded on GelMA/PANi ECHs demonstrated better adhesion and viability after 5 days compared to pristine GelMA [197]. Further, while 10T1/2s cells adhered exclusively to GelMA in control samples, migration between the hexagonal patterns was observed in GelMA/PANi ECHs.

More recently, Navaei *et al.* described a technique for micropatterning CMs onto ECHs by incorporating conductive GNRs into GelMA hydrogels to create microgrooved architectures [10]. Their approach utilized a micro-mold composed of PDMS with a microgrooved topography. A prepolymer solution containing GelMA and GNRs was pipetted on a 3-(Trimethoxysilyl)propyl methacrylate (TMSPMA)-coated slide, and the PDMS micromold was placed on top. (**Figure 6a**). The solution was then photopolymerized through exposure to UV irradiation. The resulting ECH constructs possessed microgrooves that were 50 μm in width. GelMA/GNR ECH constructs also exhibited significantly lower impedance (1.35 ± 0.36 kΩ) as compared with pristine GelMA (15.58 ± 9.18 kΩ) samples. In addition, cellular viability and morphology was investigated *in vitro* by seeding CMs between the microgrooves of GelMA-GNR and GelMA constructs. Their results showed there was an enhanced organization and spreading of CMs on GelMA/GNR ECHs (**Figure 6b**), when compared to pure GelMA hydrogels (**Figure 6c**) after 7 days of culture. This study demonstrated the efficacy of micropatterning techniques to fabricate ECHs with and highly organized structures that could be used to develop native-like cardiac tissues.

Micropatterning of ECHs has also been performed to enhance therapies designed to stimulate nerve tissue regeneration. In a recent study, Lee *et al.* developed an ECH composed of PED and AgNWs with parallel microridges using a standard soft lithography process [199].

Briefly, a microgrooved PDMS stamp was fabricated and placed on a polyethylene terephthalate (PET) film. A prepolymer solution containing PEG and AgNWs was then injected between the grooves of the stamp and the PET film. The prepolymer solution was then photopolymerized using UV irradiation, and the PDMS stamp was peeled from the ECH. Electrical characterization of these ECHs was conducted using Comsol Multiphysics software to simulate the current at the wall of PEG/AgNW and PEG samples when a voltage of 10 V was applied. Results of this simulation showed that PEG/AgNW exhibited a significantly higher current as compared to pure PEG hydrogels due to the higher conductivity [199]. To determine if these materials could support the differentiation of NSCs into neurons, and guide neurite outgrowth, NSCs were incubated and grown into neurospheres, then seeded on PEG/AgNW and PEG samples. Following 1 day of culture, an intermediated electrical stimulus of 5, 10, and 20 V was applied. Results showed that neurite growth was much higher in the PEG/AgNW ECHs compared to PEG hydrogels [199]. Further, the neurite growth followed the microgrooves of the ECH, while neurite growth on PEG hydrogels appeared more randomly dispersed. The combination of high conductivity, robust mechanical properties, and micropatterns that support the differentiation of NSCs into neurons suggests that these ECHs are suitable for applications involving excitable cell types, such as neuronal and cardiac tissue engineering.

Overall, micropatterning of ECHs is a facile and precise method to control the 2D arrangement in a way that mimics the ECM of natural tissues. Advanced micropatterning techniques can also be used to guide cellular interactions thus influencing the function of tissues. However, the use of micropatterning ECHs does have some limitations. For example, one challenge is determining an appropriate UV exposure time that would photocrosslink hydrogels, but not affect cellular viability. Another limitation is the inability to micropattern 3D constructs

that closely represent the microenvironment *in vivo*. However, ECHs with micropatterned surfaces shows potential in developing future 2D modeling systems that emulate human physiological functions. Taken together, micropatterned ECHs holds great potential for the development of stimuli-responsive systems for biomedical innovations, and to facilitate the development of new therapeutics aimed towards cardiac and neural tissue regeneration, as well as biosensors and drug delivery systems.

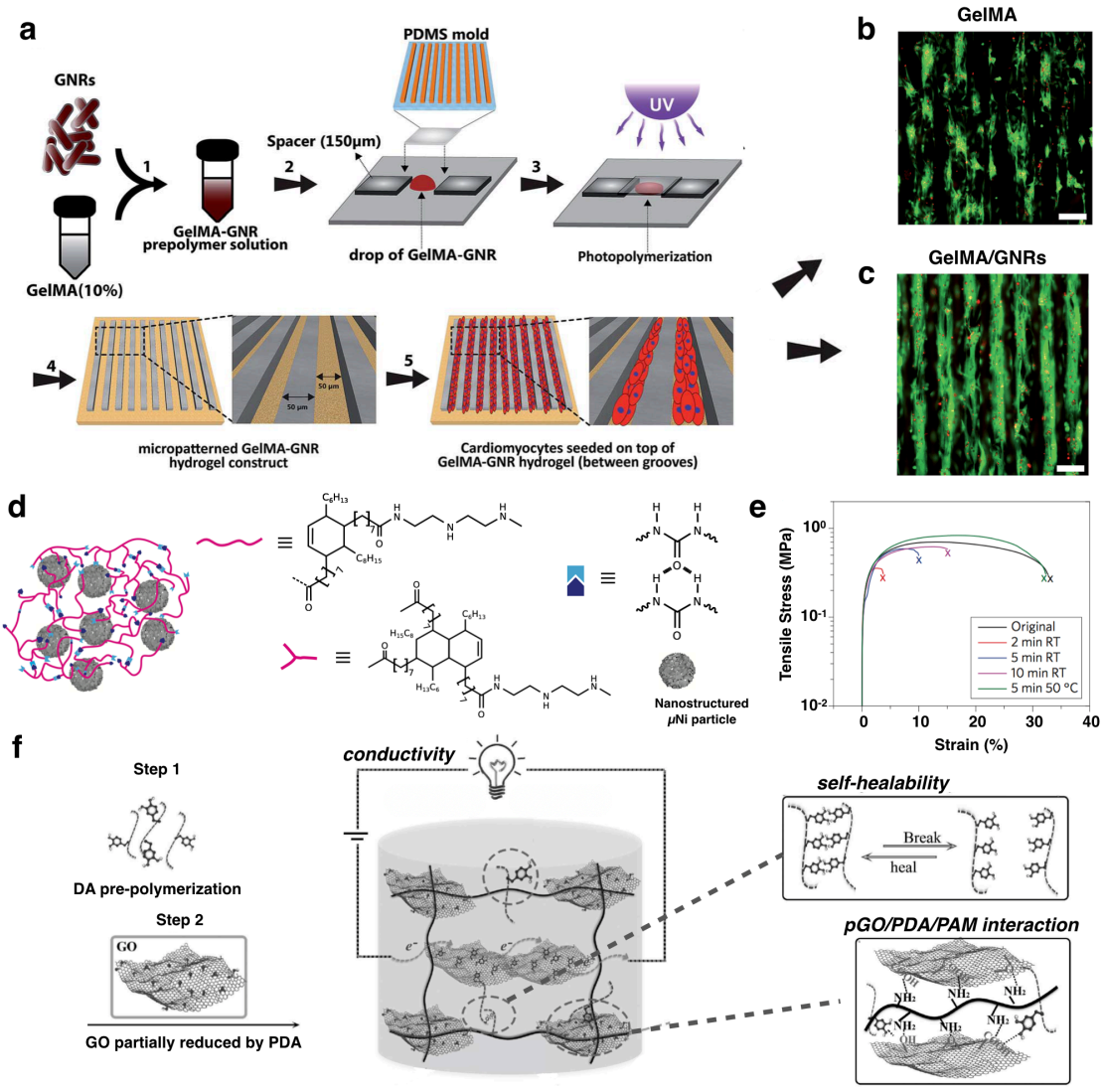

Figure 6. Micropatterning and self-assembling of ECHs for different biomedical applications. Schematic of GelMA-GNR ECHs that were photocrosslinked in the presence of UV light in a microgrooved PDMS mold. The resulting ECH was seeded with CMs, which aligned within the microgrooves **(a)**. Live/dead assay performed using CMs seeded on pure GelMA hydrogels **(b)** and GelMA-GNR ECHs **(c)**. Live cells were stained in green, while dead CMs were stained in red, confirming high cell viability after 7 days of cell culture (adapted from [10]). Schematic of supramolecular organic-inorganic composite capable of self-healing via interactions between oligomer chains (pink lines) with micro nickel and urea groups (blue and purple shapes) **(d)**. Representative stress-strain curves for ECHs containing 31% micro nickel volume ratio under different healing conditions showing that healing efficiency was found to be a function of time **(e)** (adapted from [11]). Schematic of composite ECHs constructed with partially reduced GO using polydopamine, crosslinked with polyacrylamide **(f)** (adapted from [12]). Scale bars= 100 μm (**b, c**).

1.2.4. Self-assembly / Self-healing of ECHs

Directly combining conductive components such as CPs and NPs into polymeric networks has been regarded as the most straightforward approach to synthesize ECHs [200-202]. However, conventional approaches to fabricating ECHs yields matrices with randomly suspended conducting components, which limits the ability to impart morphologies that enhance cell-material interactions [203]. To address this issue, self-assembly approaches have been introduced as an efficient strategy to develop a new class of smart materials with the ability to spontaneously form complex structures without external participation [204, 205]. Self-assembled hydrogels are characterized by the interaction of weak noncovalent bonds to form networks, such as hydrogen bonds, ionic interactions, van der Waals forces, and π-π stacking [206]. However, the absence of covalent bonds in these networks may result in weak mechanical properties making them unsuitable for biomedical applications. Therefore, it is often necessary to engineer self-assembling ECHs with either strong noncovalent bonds (e.g. ionic interactions, metal-ligand coordination), or multiple weak interaction sites (e.g. hydrogen bonds, VDW forces) [207].

Due to its unique structure, graphene has become a popular biomaterial capable of imparting self-assembling properties to ECHs. Self-assembled graphene hydrogels (SGH) have been increasingly used in multiple applications such as drug delivery systems [208], supercapacitors [209], and devices for human motion detection [210]. One study conducted by Xu *et al.*, engineered SGHs with 3D networks that were fabricated using a single-step hydrothermal approach [204]. Briefly, this was achieved by heating 2 mg/mL of a homogenous GO solution to 180 °C for 12 h using an autoclave. The effect of this treatment hydrothermally reduced GO creating graphene sheets, which self-assembled into ECHs via π-π stacking interactions. Characterization of these SGHs showed that these materials exhibited high electrical conductivity

(5×10^{-3} S cm^{-1}), high storage modulus (450-490 kPa), and high thermal stability [204]. It was therefore proposed that these self-assembling ECHs were suitable for biomedical applications, such as drug delivery systems, and tissue engineering.

ECHs with self-healing properties have also gained significant attention based on their ability to spontaneously restore the original functionality of ECHs after being damaged, which can prolong service life and avoid failure in therapeutic or diagnostic biomaterials [211]. This new class of smart material relies on dynamic and reversible noncovalent bonds, such as hydrophobic interactions, host-guest interactions, or hydrogen bonding to autonomous crosslink polymeric networks following physical, chemical, or mechanical damage to the ECHs [12]. Advanced self-healing smart materials, used for biomedical applications such as wound healing, where cuts, scratches, and breaks are common, would improve performance and lower the overall cost of these systems [211].

A study by Tee *et al.*, described the development of biomimetic electronic skin sensors with enhanced mechanical sensing and self-healing properties [11]. This composite ECH was formed by using a supramolecular polymer capable of forming hydrogen bonds with itself, coupled with micro-nickel particles with nanoscale surface modifications (**Figure 6d**) [11]. The resulting ECH was able to self-heal by forming new hydrogen bonds in response to mechanical trauma, which in turn restores the structural integrity of the hydrogel. An important feature of supramolecular polymeric networks is their glass transition below room temperature, which allows for better movement of polymer chains after damage. These ECHs exhibited high electrical conductivity (40 S cm^{-1}), and increasingly higher elastic moduli with increasing concentrations of micro nickel particles. In addition, the engineered ECHs were able to electrically heal within 15 seconds after damage occurred (**Figure 6e**), which could enable the engineering of electric skin

sensors, as well as flexible biosensors.

In another study, Han *et al.* developed a mussel-inspired self-adhesive, self-healing, stretchable ECH to be used as implantable and wearable bioelectronics [12]. These ECHs were fabricated in three steps. Briefly, dopamine was prepolymerized to form polydopamine (PDA). Next, partially reduced GO (pGO), where both GO and rGO were present, was achieved by exposure to PDA. Lastly, pGO and PDA were polymerized in the presence of acrylamide monomers, forming PDA/pGO/PAM composite ECHs (**Figure 6f**). The resulting pGO and PDA chains interacted with PAM forming hydrogen bonds and π- π stacking between catechol groups [12]. This ECH exhibited high conductivity, the ability to electronically and mechanically heal after damage, as well as high stretchability and toughness. Furthermore, the ECH possessed excellent attachment to native skin without the use of additional adhesives. Both *in vitro* studies using bone marrow stem cells and *in vivo* studies in a rabbit model demonstrated the high biocompatibility of the engineered ECHs. These studies demonstrate that self-healing ECHs hold great potential for the development of implantable and flexible bioelectronics.

Smart ECHs capable of self-assembling have been utilized as scaffolds for various biomedical applications. Further, self-healing ECHs have been engineered to autonomously adapt to dynamic environments and serve to lengthen the service life of these implantable gels. Both of these classes of materials rely on weak noncovalent bonds to assemble and repair polymeric networks. However, due to the absence of stronger covalent bonds, these self-assembling and self-healing ECHs often lack the proper mechanical stiffness necessary for use as tissue regenerative therapies or drug delivery systems. In addition, the rational design of such complex structures is often a challenge and prediction of ECHs behaviors is often based on empirical observations. Regardless, the benefits of these smart ECHs make them attractive materials for many biomedical

related applications where self-regulation and durability are required.

1.3. Biomedical applications of ECHs

1.3.1. Tissue engineering

Polymeric hydrogels have been extensively used as scaffolds to mimic biological functionality and induce the proliferation, differentiation, and migration of cells, both *in vitro* and *in vivo* (**Figure 7a**). Cells in physiological environments are exposed to various types of physicochemical cues that modulate the development and regeneration of tissues, including endogenous electric fields from excitable cell types. Therefore, ECHs have been increasingly explored for the engineering of functional tissue constructs, to control the behavior and promote the regeneration of excitable tissues [212]. To this end, the use of ECHs for the engineering of scaffolds for neural cell encapsulation, nerve conduits, and electrode coatings for neural tissue interfaces has been widely reported (**Figure 7b**). Previous studies have shown that neuroblastic PC-12 cells under electrical stimulation *in vitro* exhibit increased proliferation and differentiation [13, 213-215], as well as a higher number of neurites with a greater overall length [123]. This behavior has been mainly associated to enhanced fibronectin adsorption onto the ECHs, coupled with the direct effect of the electrical field on the integral membrane proteins of these cells [216, 217]. In a different study by Yow *et al.*, hMSCs growing on PPy-collagen hydrogels exhibited neuronal-like morphology and upregulation of noggin, MAP2, neurofilament, ß tubulin III, and nestin neural markers [218]. Using a similar approach, Yang *et al.* recently demonstrated that PPy-alginate hydrogels promoted the adhesion and growth of hMSCs, as well as overexpression of Tuj1 and MAP2 neural differentiation markers (**Figure 7c**) [14]. In addition, the engineered PPy-alginate hydrogels were shown to possess high biocompatibility *in vivo*, as demonstrated by subcutaneous implantation experiments. These studies demonstrate that ECHs are remarkably

advantageous to study the effects of electrical fields on stem cells and/or neural cells *in vitro*, and to engineer heterocellular neural tissue constructs and interfaces for *in vivo* implantation.

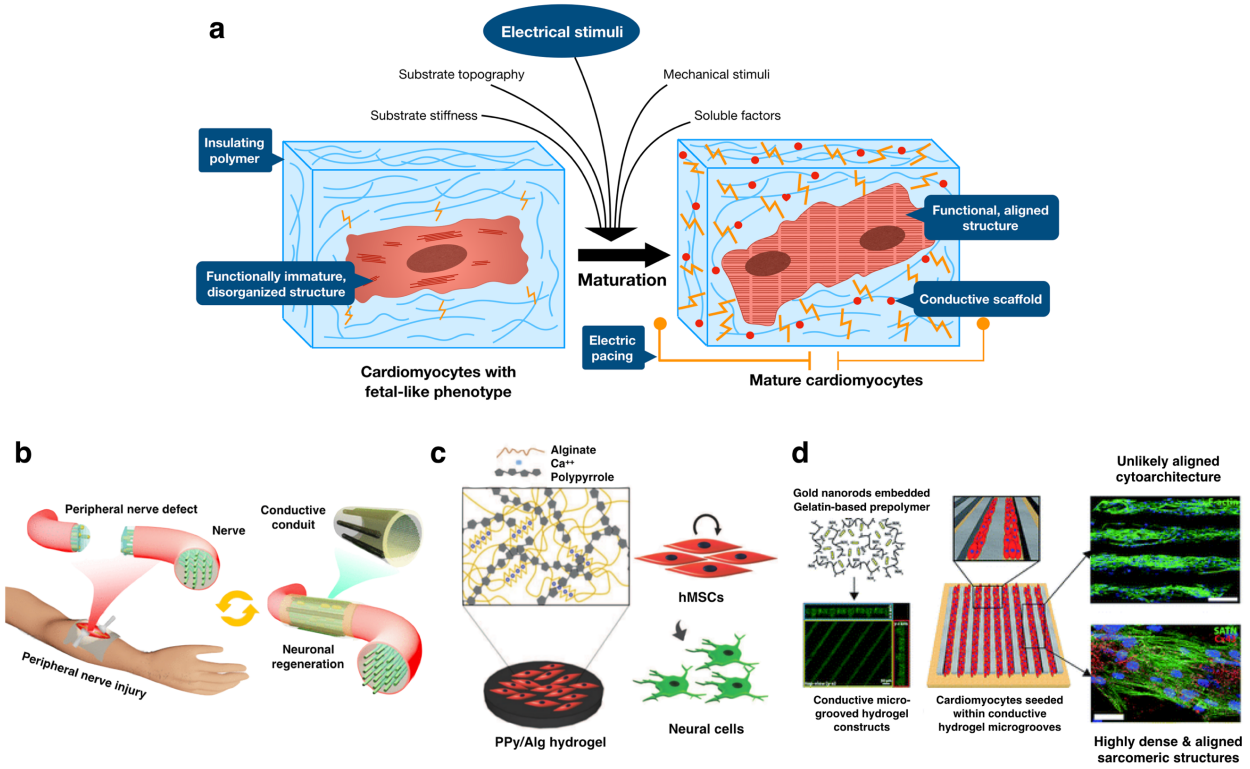

Figure 7. ECHs for tissue engineering applications. The addition of electrically conductive materials (red circles) can be used to provide conductive properties to intrinsically insulating hydrogels **(a)**. These ECHs could be used to deliver relevant biophysical stimuli to cardiomyocytes *in vitro*, such as mechanical and biological cues, or electrical stimulation/pacing. These maturation cues have been shown to trigger phenotypical changes that ultimately lead to fully mature and functional cardiomyocytes. ECHs have been used to develop conductive nerve conduits as an alternative to nerve autografts for nerve regeneration and repair (adapted from [13]) **(b)**. ECHs could provide physiological stimuli that mimic native nerve tissues and induce the differentiation of progenitor cell types to neural lineages (adapted from [14]) **(c)**. ECHs deliver biomimetic topographical and electrical cues *in vitro* to form highly oriented cellular constructs with tissue-level functionality (adapted from [10]) **(d)**. Scale bars= 100 µm (**d upper image**), 20 µm (**d lower image**).

The complex organization and microarchitecture of the myocardium, along with the electrical and mechanical coupling between CMs, are critical for the maintenance of the synchronous contractility of the heart [219, 220]. In recent years, the engineering of cardiac tissue

constructs using hydrogel-based biomaterials with biomimetic physicochemical cues have demonstrated great promise for cardiac tissue regeneration and repair [20, 221]. For instance, Dong *et al.* recently described the engineering of an injectable, self-healing ECHs based on chitosan-graft-aniline tetramer (CS-AT) and dibenzaldehyde-terminated poly(ethylene glycol) PEG-DA [222]. Their results demonstrated that the engineered ECH could be used to deliver C2C12 and H9c2 myoblasts *in vivo*, and that they possessed high biocompatibility and biodegradability. In another study by Baei *et al.,* thermosensitive chitosan-AuNPs ECHs were shown to support the proliferation, migration, and differentiation of hMSCs, as shown by the expression of the α-myosin heavy chain (α-MHC) and Nkx-2.5 cardiac markers [46]. Furthermore, in addition to electrical stimulation, the delivery of mechanical and topographical cues could also be incorporated into multifunctional ECHs. In this regard, Gelmi *et al.* recently reported the use of a PLGA-PPy hydrogel as an electromechanically active scaffold to promote the engraftment, proliferation, and differentiation of induced pluripotent stem cells (iPSCs) into CMs [223]. The mechanical actuation of the scaffold enabled individual microfiber actuation to provide encompassing, coherent physiological strain to individual cells, which mimicked the native mechanical flow and force in the heart. In another study by Navaei *et al.*, 50 μm microgrooves were incorporated into gelatin GelMA hydrogels with electrically conductive GNRs (**Figure 7d**) [10]. Fluorescent images revealed uniform, dense, and highly aligned cellular organization, as well as enhanced cytoskeletal alignment and cellular connectivity.

In addition to cardiac and neural cell types, ECHs have also been shown to modulate the proliferation and differentiation of preosteoblasts MC3T3-E1 for bone tissue engineering [224], as well as human primary skin fibroblasts for wound healing [225, 226]. However, conventional methods for engineering ECHs through the incorporation of conductive nanomaterials and

polymers are often associated with poor solubility, processability, biodegradability, and biocompatibility [227]. To address these limitations, our group recently reported a new method to engineer electroconductive materials from inherently non-conductive polymers, through the conjugation of a choline-based Bio-IL [34]. Our results demonstrated that GelMA/Bio-IL ECHs could be used to modulate the proliferation and contractile function of primary rat CMs *in vitro*. Furthermore, as current understanding of biological processes increases, and new multifunctional smart biomaterials are developed, novel applications of ECHs in tissue engineering will be explored. For instance, ECHs could be used to engineer bioactuators that transduce electrical stimuli into mechanical force, which in turn could be used as biomimetic muscle fibers [228]. ECHs could also be used to develop transparent and deformable touch sensors for emerging applications, such as bionic skin, as well as flexible/wearable biomedical devices [229].

2. EXPERIMENTAL

2.1. Synthesis of biomaterials

2.1.1. Synthesis of gelatin methacryloyl (GelMA): GelMA was synthesized as previously described[230]. Briefly, 10 g of gelatin (derived from fish or porcine sources) was dissolved in 100 mL phosphate buffered solution (DPBS) and heated to 50 °C. Then, 8 mL methacrylic anhydride (Sigma-Aldrich) was added dropwise to the gelatin solution under vigorous stirring at 50 °C to modify the lysine groups on the gelatin chains. The solution was then diluted with DPBS and dialyzed (Spectrum Laboratories, MWCO = 12-14 kDa) against deionized water at 50 °C for 5 d to remove any unreacted methacrylic anhydride. After sterile filtration using a vacuum filter (0.22 μm pore size), the solutions were subsequently lyophilized for 4 days, and the final GelMA product was stored at room temperature until experimental use.

2.1.2. Synthesis and expression of elastin-like polypeptide (ELP): The photocrosslinkable ELP sequence was expressed as previously described in our previous study[231]. This ELP sequence consists of 70 repeats of pentapeptide VPGVG, in which the first valine was replaced with an isoleucine every five pentapeptides (i.e., $([VPGVG]_4[IPGVG])_{14}$). In addition, Lys-Cys-Thr-Ser (KCTS) residues were added to both sides of the ELP sequence to render it photocrosslinkable via the formation of S-S thiol bonds. This ELP was expressed using *Escherichia coli* (*E. coli*) as a host followed by the purification of the ELP via inverse transition cycling, as previously described[232]. Briefly, the ELP solutions were alternatively equilibrated and centrifuged above and below their thermal transition temperature (T_t = 29 °C in 1% (w/v) solution). Because the ELP protein precipitates at high temperatures and is soluble at low temperatures, these temperature changes provide a way to remove contaminates resulting in pure ELP. The purified ELP solution was then dialyzed in a water bath at 4 °C against DI water, and stored at room temperature after lyophilization.

2.1.3. Synthesis of conductive hydrogels: ECHs were synthesized by mixing different ratios of methacrylated polymers and Choline acrylate (Bio-IL). Bio-IL was synthesized by mixing choline bicarbonate with acrylic acid at a 1:1 mole ratio. The mixture was reacted at 50 °C for 5 h, then purified by evaporation overnight in a vacuum at room temperature. GelMA and PEGDA were two polymers used to form ECHs with Bio-IL. GelMA was synthesized using the method previously described in literature[233]. Briefly, 10% (w/v) gelatin solution was reacted with 8 mL of methacrylic anhydride for 3 h. The solution was then dialyzed for 5 days to remove any unreacted methacrylic anhydride, and then placed in a -80 °C freezer for 24 h. The frozen acrylated polymer was then freeze-dried for 7 days. The PEGDA used for this research was purchased from Sigma Aldrich (average M_n 700). To form polymer/Bio-IL hydrogels, the

prepolymer and Bio-IL were added to distilled water at varying final polymer concentrations and polymer/Bio-IL ratios, then mixed with 1.5% TEOA, 1% VC, and 0.1 mM Eosin Y, which acted as the photoinitiator. Hydrogels were rapidly photocrosslinked in the presence of visible light at a wavelength of 475 nm for 120 s, using a LS1000 FocalSeal Xenon Light Source, manufactured by Genzyme.

2.1.4. Cardiopatch fabrication: Porcine GelMA was synthesized using the previously described method[230]. A prepolymer solution was then prepared by mixing 10, 12.5, and 15 %(w/v) of GelMA in HFIP solvent (Sigma-Aldrich), and placed in a syringe with a 27G needle (**Figure 8a**). The prepolymer solution was then pumped out of the syringe at a rate of 1 mL/h. A high voltage power source (Glassman High Voltage, Inc., Series EH) was attached to the needle of the syringe, and to a metal collector that the GelMA polymer was drawn to, creating a fibrous mat. Fibrous scaffolds were then removed from the collector plate and placed in a vacuum to remove any remaining solvent. Scaffolds were then placed in a solution bath containing 1.25 %(w/v) photoinitiator Irgacure 2959 (Sigma-Aldrich) in ethanol. Bio-IL was also synthesized using the previously discussed methodology[234]. Four concentrations of Bio-IL in water were prepared including 0, 33, 66, and 100 %(v/v). Scaffolds were placed in a refrigerator to prevent the dissolving of GelMA fibers in Bio-IL/water solution. A volume of 1 mL Bio-IL was then placed on the surface of GelMA fibrous scaffolds and immediately crosslinked using UV irradiation for 300 s on each side of the scaffold.

2.2. *In vitro* characterization of biomaterial properties

2.2.1. ^{1}H NMR characterization of GelMA/Bio-IL hydrogels: ^{1}H NMR analyses were performed to characterize GelMA/Bio-IL composite hydrogels using a Varian Inova-500 NMR spectrometer. ^{1}H-NMR spectra were obtained from choline bicarbonate, choline

acrylate (Bio-IL), GelMA prepolymer, and GelMA/Bio-IL hydrogels. Methacrylated groups were identified due to the presence of peak values at δ=5.3 and 5.7 ppm. The decreasing rate for the C=C double bond signals $\left(-\frac{\partial(C=C)}{\partial t}\right)$ in methacrylate group of GelMA was associated with the extent of crosslinking of composite hydrogel as well as conjugation of Bio-IL to GelMA. This area decrease was calculated using the following equation:

$$\textbf{Decay of methacrylate group}\ (\%) = \left(\frac{\mathbf{PA_b - PA_a}}{\mathbf{PA_b}}\right) \times \mathbf{100} \qquad \textbf{(1)}$$

Where $\boldsymbol{PA_b}$ and $\boldsymbol{PA_a}$ represent the peak areas of methacrylated groups before and after photocrosslinking, respectively. Accordingly, $\boldsymbol{PA_b - PA_a}$ corresponds to the concentration of methacrylated groups consumed in the photocrosslinking process. ACD/Spectrus NMR analysis software were used to integrate the area under the peaks and all the data was analyzed with respect to phenyl group peaks at δ=6.5-7.5 ppm.

2.2.2. Mechanical testing: Mechanical testing on engineered ECHs were performed using an Instron 5542 mechanical tester. Both the elastic and compressive modulus were analyzed for each of hydrogels with varying final polymer concentration and polymer/Bio-IL ratios. Composite hydrogels were created by using PDMS molds, which formed rectangular hydrogels (length: 12.00 mm, width: 5.00 mm, depth: 1.25 mm) for tensile test and cylindrical hydrogels (diameter: 5.5 mm, height: 4 mm) for compression test. A volume of 70 μL of prepolymer solution was used to form photocrosslinked ECHs. ECHs were allowed to swell in DPBS for 4 h at 37 °C prior to mechanical testing. At least 5 samples were tested for each condition.

For the compression test, hydrogels were placed between two compression plates, and compression was applied to each sample at a rate of 1 mm/min. Compression (mm) and load (N)

were recorded during each test using Bluehill software. Compression modulus was calculated as the tangent slope of the initial linear region of the stress-strain curve between 0 mm/mm and 0.1 mm/mm compressive strain. For the tensile tests, hydrogels were held between two tensile grips and stretched at a rate of 1 mm/min until failure. The elastic modulus was calculated as the tangent slope of the stress-strain curve. At least 5 samples were tested per condition to obtain average and standard deviation.

2.2.3. *In vitro* evaluation of electrical conductivity: ECHs with varying final polymer concentration and polymer/Bio-IL ratios were crosslinked in a rectangular PDMS mold and allowed to dry for 24 h. Once dried, conductivity analysis was performed using a two-probe electrical station connected to a Hewlett Packard 4155A Semiconductor Parameter analyzer. The dimensions of each hydrogel were measured and placed in a relaxed state where the two probes penetrated the hydrogels - one at each end (**Figure 9a**). The HP 4155A was set to measure current in the presence of an electrical stimulation ranging from -1 to 1 volt. The results were then analyzed to determine conductivity values. At least 5 samples were tested for each condition.

2.2.4. *Ex vivo* evaluation of electrical conductivity: Adult female Wistar rats were provided by the Institutional Animal Care and Use Committee (ICAUC) at Northeastern University (Boston, MA, USA). All experiments were performed in accordance with relevant guidelines and regulations. Immediately after euthanasia, the rectus abdominis muscles were dissected and cut into 10 × 10 mm pieces. The tissue samples were then transferred to a glass petri dish and placed 3 mm apart on the opposite sides of an insulating PDMS mold (**Figure 9e**). GelMA/Bio-IL hydrogels at 50/50 and 20/80 ratios, as well as pure GelMA controls were photocrosslinked *in situ* to connect the two pieces of tissue. 50 ms square pulses of direct current were applied to the tissue using an Agilent wave generator (Agilent 33220A). The electrical

stimulation was applied to the samples using short platinum wires with 0.25 mm diameter and 99.9% trace metal basis, bought from Sigma-Aldrich (MO, USA). The threshold at which contraction was achieved was determined by applying increasing voltages (1 – 10 V) at a constant frequency of 1 hertz. Muscle contraction was visually inspected at each voltage, after applying electrical stimulation to the sample on the opposite side of the mold.

2.2.5. *In vitro* degradation: ECHs were fabricated as previously explained for compression test. ECHs were then freeze-dried, weighed and were placed in 24-well plate with 1 ml of DPBS or DPBS supplemented with 10% FBS solutions at 37 ºC in an oven continuously for 2 weeks. The DPBS/FBS solutions were refreshed every 3 days to maintain constant enzyme activity. At prearranged time points (after 1, 7 and 14 days), the DPBS/FBS solutions were removed and the samples were freeze-dried for 24 h and weighed. The percentage degradation (D%) of the hydrogels was calculated using the below equation:

$$\boldsymbol{D\%} = \frac{\boldsymbol{W_i - W_t}}{\boldsymbol{W_i}} \times \mathbf{100\%}\,, \qquad \textbf{(2)}$$

where W_i is the initial dry weight of the sample and W_t is the dry weight after time t.

2.2.6. Swelling ratio measurements: The equilibrium swelling ratio of GelMA/Bio-IL and PEGDA/Bio-IL composite hydrogels were evaluated. For this purpose, cylinder-shaped hydrogels were prepared (7 mm in diameter, 2 mm in depth) as described previously. Prepared hydrogels were washed three times with DPBS. Then, they were lyophilized and weighed in dried condition. Thereafter, the samples were immersed in DPBS at 37 °C for 4, 8 and 24 h and weighed again after immersion. The swelling ratio and water uptake capacity of the samples were calculated as the ratio of the swelled sample mass to the mass of lyophilized sample.

2.2.7. SEM analysis: SEM analysis was performed to evaluate the porosity of the engineered GelMA/Bio-IL and PEGDA/Bio-IL hydrogels. The samples were prepared in a similar

procedure as described for swelling ratio test. The freeze-dried samples were then coated by gold/palladium (Au/Pd) before SEM analysis. The SEM images were acquired by using a FEI/Phillips XL30 FEG SEM (10 kV). Pore size analysis of the GelMA/Bio-IL hydrogels was performed by measuring the pore sizes of at least three images of four samples (n=50) using ImageJ software.

2.2.8. Wound closure adhesion test: Wound closure adhesion test was performed using cardiopatches on porcine skin and rat myocardium. For wound closure on porcine skin, samples of tissue were cut into 40 × 20 mm pieces with a thickness of about 5 mm. The skin was glued with a cyanoacrylate adhesive onto glass slides. Two sections of porcine skin were then butted up against each other and a section of cardiopatch was placed to the top overlapping each section of skin tissue equally. The cardiopatch was then photocrosslinked for a period of 300 s. The glass slides were then connected to an Instron 5944 mechanical tester and analyzed to determine the adhesive strength of patches on porcine skin. The same test was performed using the same protocol but using rat myocardium.

2.2.9. Burst pressure adhesion test: Burst pressure adhesion test was performed using cardiopatches on porcine intestinal tissue and cardiac tissue of female rats. Burst pressure using porcine intestinal tissue was performed by locking the tissue in a chamber connected to an air pump. A small defect in the intestinal tissue was created and covered by a cardiopatch. The cardiopatch was photocrosslinked for 300 s before the syringe pump was enabled with an infusion rate of 5 mL/min. *Ex vivo* burst pressure analysis was performed by placing a cardiopatch on the defect area of rat myocardium. Similarly, the syringe pump was set to 5 mL/min until failure of the patch.

2.2.10. Lap shear adhesion test: The shear strength of the engineered hydrogels with and without LA was evaluated using a modified ASTMF 2255-05. Two glass slides (1 cm × 3 cm) were cut and placed end to end. Each glass slide had one end coated with 20% (w/v) porcine gelatin, which was allowed to dry at room temperature. Afterwards, 20 µL of the adhesive hydrogel propolymer solution was applied on a 1 cm × 1 cm area on the gelatin of one glass slide. The second gelatin-coated glass slide was then placed over the adhesive, followed by 180 s of irradiation with UV light. The two glass slides were then placed into an Instron mechanical tester for shear testing by tensile loading with a strain rate of 1 mm/min. The shear strength of the sealant sample was determined at the point of detaching. Each tested adhesive group contained three samples.

2.2.11. *In vitro* hemostatic evaluation: Whole blood was added to a solution of 3.6% (w/v) sodium citrate in a ratio of 1:9 (citrate solution : whole blood) to prevent clotting. A volume of 630 µL of the citrated blood was then pipetted into a 1 mL Eppendorf tube. A total of 70 µL of 0.3 M calcium chloride ($CaCl_2$) was added, followed by vortexing for 10 s. Engineered hydrogels were synthesized and 100 µL of prepolymer solution was pipetted onto the bottom of the wells of a 48 well plate ensuring complete coating of the bottom surface. Then 200 µL of blood was pipetted into the sequential wells containing hydrogels with varying concentrations of LA. At selected time points, each well was washed with 0.9% (9 g/L) saline solution to halt the clotting process. The liquid was aspirated and washed repeatedly until the solution was clear to ensure the removal of soluble blood components. After a trial was complete, the clotting time was determined based on the observation of a visible clot. In addition, clots were dried and weighed to determine the clot mass clot over time.

2.2.12. Primary CM isolation: Primary rat CMs were isolated from 2-day-old neonatal Sprague Dawley pups according to the protocol approved by the ICAUC at Northeastern University. All experiments were performed in accordance with relevant guidelines and regulations. Briefly, pups were quickly decapitated with scissors after disinfecting the neck and sternum with 70% ethanol. A vertical incision was made across the sternum to excise the heart, which was placed in cold Hank's Balanced Salt Solution (HBSS) buffer. The atria and blood vessels were carefully removed and each heart was quartered and incubated overnight in a solution of 0.05% (w/v) trypsin in HBSS at 4 °C. Trypsin digestion was stopped by adding culture media, followed by shaking for 5 min at 37 °C in a water bath. The tissues were then serially digested in 0.1% collagenase type II solution in HBSS (10 min shaking incubation at 37 °C). The collagenase solution with the CMs were centrifuged at 500 xg for 5 min. Primary cells were resuspended in DMEM supplemented with 10% FBS and pre-plated for 1 h to enrich for cardiomyocytes.

2.2.13. Surface seeding (2D culture): Hydrogels were formed by placing a 7-µl drop of hydrogel precursor in a spacer with 150-µm height and covered by a glass slide coated with 3-(trimethoxysilyl) propyl methacrylate (TMSPMA, Sigma-Aldrich). Hydrogel precursor was then photocrosslinked for 20 s using a Genzyme FocalSeal LS100 xenon light source. Primary rat CMs (2.5×10^5 cells/scaffold) were seeded on the surface of the hydrogels and placed in 24-well plates with 400 µL of growth medium (DMEM supplemented with 10% fetal bovine serum (FBS, Invitrogen) and 1% penicillin/streptomycin (Invitrogen)). 2D cultures were maintained at 37 ºC in a 5% CO_2 humidified atmosphere, for 10 days and culture medium was replaced every 48 h.

2.2.14. 3D cell encapsulation: Hydrogel precursors were prepared in cell culture medium containing 1.5% TEOA, 1% VC, and 0.1 mM Eosin Y. A cell suspension containing

freshly isolated CMs and CFs in culture medium (2:1 ratio of CMs:CFs and $1.8x10^7$ cells/ml total cell density) was gently mixed with an equal volume of the precursor solution. 7-µl drops were then pipetted on 150-µm thick spacers and covered by TMSPA-coated glass slides. Hydrogels were then photocrosslinked for 120 s using a Genzyme FocalSeal LS100 xenon light source, as described before for 2D cultures. Cell-laden hydrogels were placed in 24-well plates with 400 µl of growth medium and maintained at 37 ºC in a 5% CO_2 humidified atmosphere for 10 days.

2.2.15. Cell viability: The viability of primary CMs grown on the surface of GelMA and GelMA/Bio-IL hydrogels was evaluated using a commercial live/dead viability kit (Invitrogen), according to instructions from the manufacturer. Briefly, cells were stained with 0.5 µl/ml of calcein AM and 2 µl/ml of ethidium homodimer-1 (EthD-1) in DPBS for 15 min at 37 °C. Fluorescent image acquisition was carried out at days 1, 4, and 7 post-seeding using an AxioObserver Z1 inverted microscope (Zeiss). Viable cells appeared as green and apoptotic/dead cells appeared as red. The number of live and dead cells was quantified using the ImageJ software. Cell viability was determined as the number of live cells divided by the total number of live and dead cells.

2.2.16. Metabolic activity: The metabolic activity of the cells was evaluated at days 1, 3, and 5 post-seeding, using a PrestoBlue assay (Life Technologies) according to instructions from the manufacturer. Briefly, 2D cultures of primary CMs were incubated in 400 µL of growth medium with 10% PrestoBlue reagent for 2 h at 37 °C. The resulting fluorescence was measured (excitation 530 nm; emission 590 nm) using a Synergy HT fluorescence plate reader (BioTek). Control wells without cells were used to determine the background for all experiments.

2.2.17. Cell adhesion, proliferation and spreading: CM spreading on the surface of the engineered composite hydrogels was visualized through fluorescent staining of F-actin

filaments and cell nuclei. Briefly, 2D cultures at days 1, 4, and 7 post-seeding were fixed in 4% (v/v) paraformaldehyde (Sigma) for 15 min., permeabilized in 0.1% (w/v) Triton X-100 (Sigma) for 5 min, and then blocked in 1% (w/v) bovine serum albumin (BSA, Sigma) for 30 min. Samples were then incubated with Alexa-fluor 488-labeled rhodamine-phalloidin (20/800 dilution in 0.1% BSA, Invitrogen) for 45 min. After three consecutive washes with DPBS, samples were counterstained with 1 μL/mL DAPI (4',6-diamidino-2-phenylindole, Sigma) in DPBS for 5 min. Fluorescent image acquisition was carried out using an AxioObserver Z1 inverted microscope.

2.2.18. Immunostaining of cardiac markers: Immunocytofluorescent staining was performed on 2D cultures of primary CMs in order to evaluate the expression of the cardiac differentiation marker sarcomeric α-actinin. Briefly, CMs growing on the surface of GelMA and GelMA/Bio-IL hydrogels gel were fixed in 4% paraformaldehyde for 1 h at room temperature at day 7 post-seeding. Samples were washed three times with DPBS, permeabilized in 0.1% (w/v) Triton X-100 for 30 min, and blocked in 10% (v/v) goat serum in DPBS containing 0.1% Triton x-100 for 1 h. Samples were incubated overnight with anti-sarcomeric α-actinin primary antibody (1:200 dilution) in 10% (v/v) goat serum at 4 °C. After incubation, samples were washed three times with DPBS and incubated for 2 h at room temperature with an Alexa Fluor 488-conjugated secondary antibody diluted in 10% (v/v) goat serum (1:200 dilution). Lastly, the samples were washed three times with DPBS and counterstained with DAPI (1/1000 dilution in DPBS) for 5 min at room temperature. Image acquisition was performed using an AxioObserver Z1 inverted microscope.

2.3. *In vivo* evaluation of biomaterial properties

2.3.1. *In vivo* biodegradation and biocompatibility: All animal experiments were reviewed and approved by the ICAUC (protocols 15-0521R and 15-1248R) at Northeastern

University, and all experiments were performed in accordance with relevant guidelines and regulations. Male Wistar rats (200-250 grams) were obtained from Charles River (Boston, MA, USA) and housed in the local animal care facility under conditions of circadian day–night rhythm and feeding *ad libitum*. Anesthesia was achieved by 2.0 to 2.5% isoflurane inhalation, followed by 0.02 to 0.05 mg/kg SC buprenorphine administration. After inducing anesthesia, eight 1-cm incisions were made on the posterior medio-dorsal skin, and small lateral subcutaneous pockets were by prepared blunt dissection around the incisions. GelMA/Bio-IL hydrogels (1 × 5 mm disks) were implanted into the pockets, followed by anatomical wound closure and recovery from anesthesia. Animals were euthanized by anesthesia/exsanguination at days 4, 14 and 28 post-implantation, after which the samples were retrieved with the associated tissue and placed in DPBS.

2.3.2. Histological analysis and immunofluorescent staining: Histological analyses were performed on cryosections of the explanted hydrogel samples in order to characterize the inflammatory response elicited by the implanted material. After explantation, samples were fixed in 4% paraformaldehyde for 4 hours, followed by overnight incubation in 30% sucrose at 4 ºC. Samples were then embedded in Optimal Cutting Temperature compound (OCT) and flash frozen in liquid nitrogen. Frozen samples were then sectioned using a Leica Biosystems CM3050 S Research Cryostat. 15-µm cryosections were obtained and mounted in positively charged slides using DPX mountant medium (Sigma). The slides were then processed for hematoxylin and eosin staining (Sigma) according to instructions from the manufacturer. Immunohistofluorescent staining was performed on mounted cryosections as previously reported[2]. Anti-CD3 [SP7] (ab16669) and anti-CD68 (ab125212) (Abcam) were used as primary antibodies, and an Alexa Fluor 488-conjugated secondary antibody (Invitrogen) was used for

detection. All sections were counterstained with DAPI (Invitrogen), and visualized on an AxioObserver Z1 inverted microscope (Zeiss).

2.3.3. *In vivo* liver bleeding model: A median laparotomy was performed, and the central liver lobe was exposed by retraction of skin. A standard liver laceration was created by taping a #11 scalpel 5 mm from the tip. The tip of the scalpel was used to lacerate the liver tissue up to the tape. Immediately after the injury, nanocomposite hydrogels (n = 4; 150 μL) or Surgicel was (n = 4) applied on the site of lesion. Hemostatic properties were quantified by measuring the mass of blood absorbed on filter paper after 1 minute and 10 minutes post laceration for each sample. Rats were then sacrificed by severing the aorta.

3. RESULTS AND DISCUSSION

3.1. Engineering biodegradable and biocompatible bio-ionic liquid conjugated hydrogels with tunable conductivity and mechanical properties

3.1.1. Synthesis of Bio-IL conjugated ECHs

Herein, we describe a versatile method to conjugate choline-based Bio-ILs to both natural and synthetic polymers, to yield biodegradable and biocompatible ECHs (**Figures 8**). GelMA biopolymer was synthesized according to a methodology reported previously[233]. The Bio-IL was synthesized based on the reaction between choline bicarbonate and acrylic acid (**Figure 8a**). Different ratios of GelMA and Bio-IL were then mixed at room temperature. The resulting GelMA/Bio-IL prepolymer was then crosslinked into a hydrogel via visible-light initiated

photopolymerization, using Eosin Y, vinyl caprolactone (VC), and triethanolamine (TEOA) (**Figure 8b**). Composite hydrogels were synthesized using 100/0 (control), 80/20, 50/50, and 20/80 polymer/Bio-IL ratios at 10%, 15% and 20% (w/v) final polymer concentrations.

The acrylation of choline bicarbonate was confirmed by comparing the ^{1}H NMR spectra of choline bicarbonate with that of the choline acrylate (Bio-IL). The appearance of a peak related to the hydrogen atoms in the acrylate groups at δ=5.8-6.1 ppm was indicative of the acrylation of choline bicarbonate (**Figures 8c**). In addition, the ^{1}H NMR spectra were collected for GelMA prepolymer (**Figure 8d**), and GelMA/Bio-IL composite hydrogel (**Figure 8e**) to confirm the conjugation of Bio-IL to GelMA. We used Equation 1 to calculate the continuous decrease of the C=C double bond signal in the GelMA methacrylate groups after exposure to visible light. By comparison between ^{1}H NMR spectra of GelMA prepolymer (**Figure 8d**) and GelMA/Bio-IL composite hydrogel (**Figure 8e**), it was found that 94.1 ± 4.6 % of the methacrylate groups in GelMA/Bio-IL composites disappeared after photocrosslinking. In addition, 57.4 ± 4.3 % of the peak area related to C=C double bonds of the acrylate groups in Bio-IL (**Figure 8c**) also disappeared in composite GelMA/Bio-IL hydrogels following crosslinking (**Figure 8e**). This can confirm the incorporation of both Bio-IL and GelMA in the resulting composite hydrogel. The appearance of a sharp peak at δ=3.1-3.2 ppm in composite hydrogel (**Figure 8e**), corresponded to the three hydrogen atoms of choline (ammonium ion), can also confirm the conjugation of Bio-IL to the hydrogel network. This peak was absent in the GelMA prepolymer spectrum (**Figure 8d**), but it was observed in both the Bio-IL (**Figure 8c**) and the composite GelMA/Bio-IL hydrogel (**Figure 8e**).

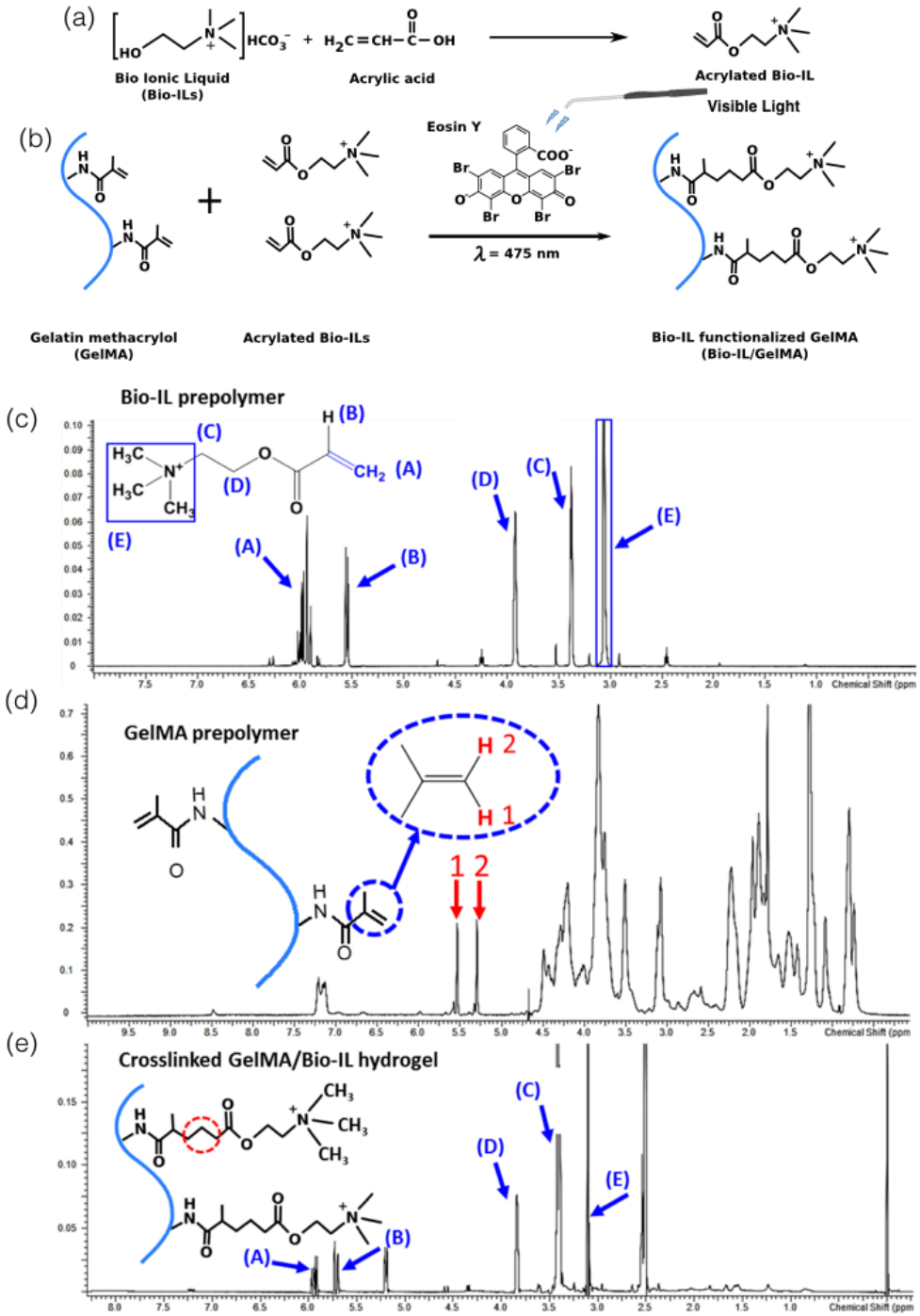

Figure 8. Synthesis and characterization of Bio-IL functionalized GelMA hydrogels. The panels show schematics of the proposed reactions for (**a**) the acrylation of choline bicarbonate to form Bio-IL, and (**b**) the reaction between GelMA and Bio-IL in the presence of Eosin Y and visible light to form GelMA/Bio-IL hydrogel. ^{1}H-NMR analysis of (**c**) Bio-IL prepolymer, (**d**) GelMA prepolymer, and (**e**) GelMA/Bio-IL composite hydrogel. GelMA/Bio-IL hydrogels were formed by using 1% VC, 1.5% TEOA, and 0.1 mM Eosin Y at 120 s light exposure.

3.1.2. Characterization of the electroconductive properties of Bio-IL conjugated ECHs

Conventional polymer-based hydrogels, including those based on GelMA and PEGDA, are intrinsically non-conductive. This characteristic limits their application for the modulation of excitable cell types, such as neurons and CMs. Therefore, we aimed to determine if the conjugation of a choline-based Bio-IL could provide electroconductive properties to polymer-based hydrogels. Briefly, Bio-IL functionalized GelMA and PEGDA hydrogels were synthesized as described before and allowed to dry for 24 h. In particular, we could not form stable hydrogels with 20/80 polymer/Bio-IL ratios at 10% final polymer concentration. This was likely due to the low concentration of polymer within the network. The partially dried hydrogels were placed in a two-probe electrical station connected to a Hewlett Packard 4155A Semiconductor Parameter analyzer to measure their conductivity (**Figure 9a**). A probe was placed at each end of the hydrogels and voltage was applied in increments of 0.05 V, from -1 to 1 V. The variations in the current were recorded, and the conductivity was calculated using Ohm's Law[141]. These results demonstrated that the use of different final polymer concentrations, as well as different polymer/Bio-IL ratios enabled the modulation of the electrical properties of the composite ECHs. For instance, the conductivity of 50/50 GelMA/Bio-IL hydrogels increased from $3.03 \times 10^{-05} \pm 0.72 \times 10^{-05}$ S/m to $4.27 \times 10^{-05} \pm 0.21 \times 10^{-05}$ S/m, and $5.03 \times 10^{-05} \pm 0.80 \times 10^{-05}$ S/m, when the final polymer concentration was increased from 10% to 15% and 20%, respectively (**Figure 9b**). Furthermore, the conductivity of 15% GelMA/Bio-IL hydrogels increased more than 63-fold, from $4.27 \times 10^{-05} \pm 0.21 \times 10^{-05}$ S/m to $272 \times 10^{-05} \pm 27.05 \times 10^{-05}$ S/m, when the GelMA/Bio-IL ratio was changed from 50/50 to 20/80 (**Figure 9b**).

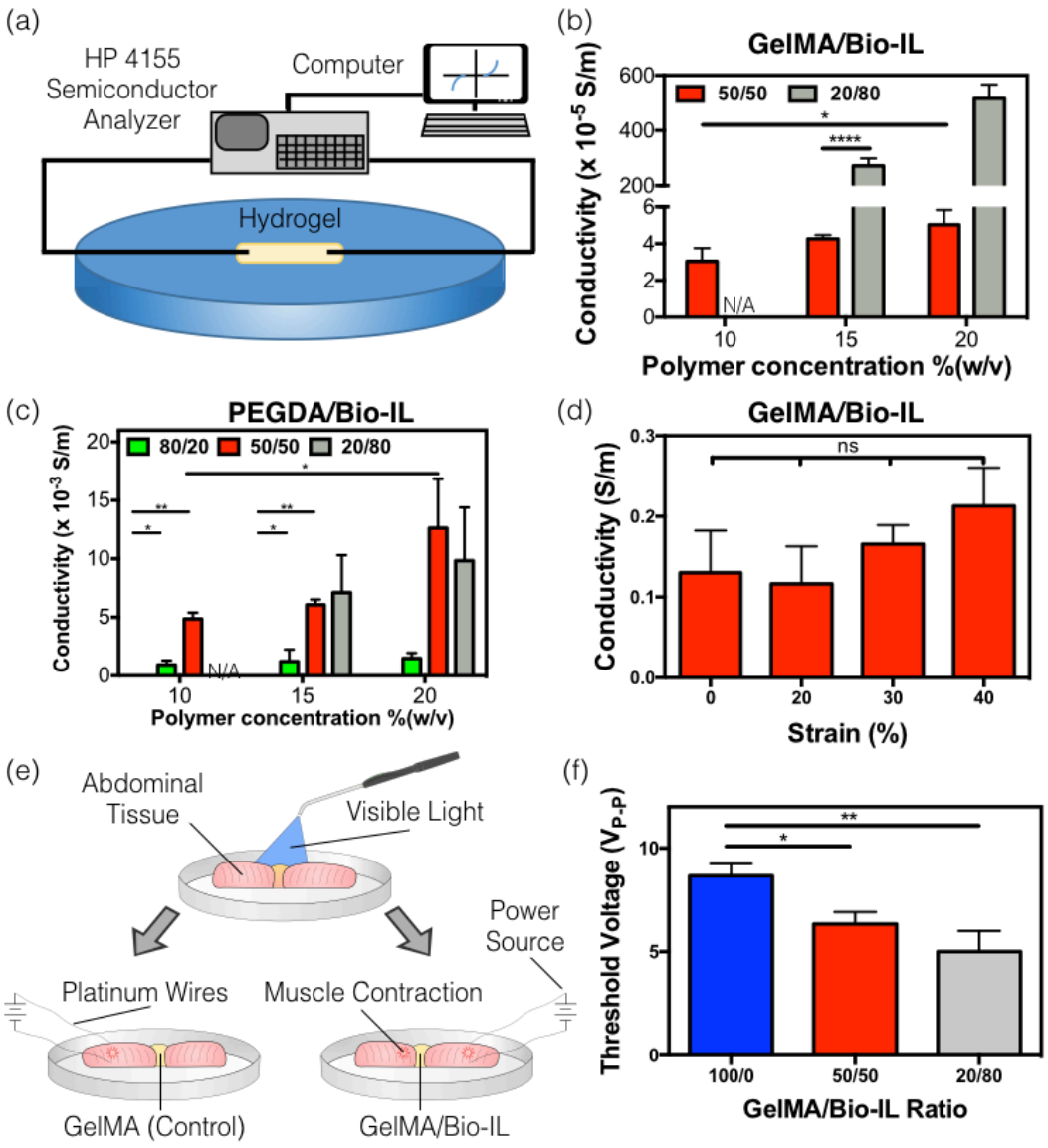

Figure 9. Electrical conductivity of the engineered polymer/Bio-IL hydrogels crosslinked by visible light. (**a**) Experimental set-up of the two-probe electrical station used to measure the electrical conductivity of the engineered hydrogels. Conductivity measurements of Bio-IL conjugated (**b**) GelMA and (**c**) PEGDA hydrogels at different polymer concentrations and polymer/Bio-IL ratios (1% VC, 1.5% TEOA, 0.1 mM Eosin Y, and 120 s exposure to visible light were used to form GelMA and PEGDA hydrogels). (**d**) Electrical conductivity of 15% GelMA/Bio-IL composite hydrogels at 50/50 ratio, which was stretched up to 0%, 20%, 30%, and 40% strain level demonstrating no significant changes in conductivity after stretching. (**e**) Schematic of *ex vivo* experiments performed using rat abdominal muscle tissues, connected using 15% final polymer concentration and 50/50 GelMA/Bio-IL ratio, and pure GelMA hydrogels (**f**) Threshold voltages at which contraction was achieved using 15% final polymer concentration GelMA/Bio-IL at 50/50 and 20/80 ratios, as well as pure 15% GelMA hydrogels. Error bars

indicate standard error of the means, asterisks mark significance levels of $p < 0.05$ (*), $p < 0.01$ (**), and $p < 0.001$ (***).

Similar to what we observed for GelMA-based hydrogels, the conductivity of 50/50 PEGDA/Bio-IL hydrogels also increased from $485 \times 10^{-05} \pm 54.93 \times 10^{-05}$ S/m to $608 \times 10^{-05} \pm 44.85 \times 10^{-05}$ S/m and $1262 \times 10^{-05} \pm 421 \times 10^{-05}$ S/m, when the final polymer concentration was increased from 10% to 15% and 20%, respectively (**Figure 9c**). In addition, the conductivity of 15% PEGDA/Bio-IL hydrogels were also increased from $121 \times 10^{-05} \pm 1.01 \times 10^{-05}$ S/m to $608 \times 10^{-05} \pm 44.85 \times 10^{-05}$ and $711 \times 10^{-05} \pm 320 \times 10^{-05}$ S/m, when the PEGDA/Bio-IL ratio was changed from 80/20 to 50/50 and 20/80, respectively (**Figure 9c**). Interestingly, hydrogels with 80/20 GelMA/Bio-IL ratios did not exhibit any apparent conductivity in our experiments (**Figure 9b**). However, PEGDA-based hydrogels with the same polymer/Bio-IL ratio did show measurable levels of conductivity, at all final polymer concentrations tested (**Figure 9c**). These observations suggest that the use of different polymer base systems could also influence the degree of conductivity of Bio-IL conjugated hydrogels. Taken together, these results demonstrated that the conductivity of the engineered ECHs increased consistently by increasing the concentrations of Bio-IL (**Figures 9b and 9c**). In particular, the maximum conductivity observed in our tests corresponded to $516 \times 10^{-05} \pm 50 \times 10^{-05}$ S/m and $1{,}262 \times 10^{-05} \pm 420 \times 10^{-05}$ S/m, for GelMA- and PEGDA-based hydrogels, respectively (**Figures 9b and 9c**). These results suggest that the 20/80 GelMA/Bio-IL formulation, which exhibited a conductivity of 516×10^{-05} S/m, could potentially be implemented in cardiac tissue engineering applications, since the conductivity of the native myocardium has been shown to be approximately 500×10^{-05} S/m[39, 235].

The engineering of elastic and conductive materials that retain their electrical properties under substantial stretch and bending, still constitutes a major technical challenge[236, 237]. Therefore, we aimed to investigate the conductivity of the Bio-IL conjugated hydrogels at different

levels of stretching. However, no conductivity measurements at different strain levels could be obtained from PEGDA/Bio-IL hydrogels, since the samples broke after applying stretch at all polymer and Bio-IL concentrations tested. Hence, we focused our analysis solely on GelMA-based hydrogels. Briefly, GelMA/Bio-IL hydrogels were dried for 2 h to retain trace amounts of moisture and maintain their flexibility. The samples were then stretched, and the conductivity was measured at different strain levels, using a two-probe electrical station. These results showed that there were no statistically significant differences between the conductivity of hydrogels at different levels of stretching (**Figure 9d**). In contrast, alternative methods to engineer ECHs, such as the incorporation of dispersed metallic nanoparticles, often suffer from a rapid and nonlinear decrease in conductivity during stretching[236, 238, 239].

One of the most widely explored applications of ECHs is their use as conductive scaffolds for engineering excitable tissue constructs. Thus, we evaluated the potential of Bio-IL conjugated polymers to restore the propagation of electrical stimuli across severed skeletal muscle tissues *ex vivo*. Briefly, the rectus abdominis muscles of female Wistar rats were explanted after euthanasia and cut into square pieces. The tissues were placed 3 mm apart, in an electrically insulated PDMS mold. GelMA/Bio-IL hydrogels, as well as pure GelMA controls were photocrosslinked *in situ*, between the two pieces of tissue (**Figure 9e**). Pulsed direct current test runs were conducted by applying 50 ms square pulses at increasing frequencies, using short platinum wires that were positioned on one of the two pieces of muscle tissue. The induction of contraction was visually inspected in the sample on the opposite end of the hydrogel, after applying electrical pulses at increasing voltages. These results demonstrated that muscle tissue samples joined together using GelMA/Bio-IL hydrogels exhibited a significantly lower excitation threshold, when compared to pure GelMA controls (**Figure 9f**). These observations suggest that Bio-IL functionalized polymers

could be used to restore functional integrity, in tissues in which electrophysiological communication has been interrupted. Previous works have demonstrated the ability of ECHs to restore electrophysiological coupling of severed skeletal muscle tissue *ex vivo*, using PPy-chitosan[240] and GO/MeTro hydrogels[2]. However, the incorporation of the PPy polymer, as well as GO nanoparticles into the hydrogel networks was associated with poorly tunable conductive properties. In contrast, Bio-IL functionalized hydrogels exhibited a wide range of electroconductive properties (**Figures 9b and 9c**).

3.1.3. Characterization of the mechanical properties of engineered ECHs

Hydrogels used in biomedical applications must provide adequate mechanical support to cells and tissues, as well as the effective transduction of physicochemical stimuli. In particular, mechanical cues are known to modulate key cellular functions such as cell proliferation, differentiation, migration, and apoptosis[241]. Here, we characterized the mechanical properties of the engineered composite hydrogels. Tensile and compression tests were performed on Bio-IL conjugated hydrogels at different polymer/Bio-IL ratios, as well as different final polymer concentrations (**Figures 10**). Bio-IL conjugated hydrogels exhibited highly tunable compressive moduli in the range of 0.60 $\pm$ 0.20 kPa to 32.07 $\pm$ 8.61 kPa (**Figure 10a**) and 1.27 $\pm$ 0.05 kPa to 178.13 $\pm$ 20.59 kPa (**Figure 10b**) for GelMA- and PEGDA-based hydrogels, respectively. In addition, results revealed that the compressive moduli for both GelMA- and PEGDA-based hydrogels increased concomitantly, by increasing the final polymer concentration as well as the ratio of polymer to Bio-IL. For instance, the compressive moduli of 15% GelMA/Bio-IL hydrogels were shown to increase from 0.60 $\pm$ 0.20 kPa to 22.10 $\pm$ 1.56 kPa, when the ratio of GelMA to Bio-IL was increased from 20/80 to 100/0, respectively (**Figure 10a**). In addition, the compressive moduli of 50/50 GelMA/Bio-IL hydrogels were also increased from 2.65 $\pm$ 1.06 kPa to 5.53 $\pm$

0.76 kPa and 8.87 ± 1.83 kPa, when the final polymer concentration was increased from 10% to 15% and 20%, respectively (**Figure 10a**). This trend was also observed for PEGDA/Bio-IL hydrogels. However, the use of PEGDA-based hydrogels yielded significantly higher compressive moduli, as compared to GelMA-based hydrogels (**Figure 10b**). For instance, the compressive moduli of 15% PEGDA/Bio-IL hydrogels were increased from 1.27 ± 0.06 kPa to 78.17 ± 12.80 kPa, when the ratio of PEGDA to Bio-IL was increased from 20/80 to 100/0, respectively (**Figure 10b**). In addition, the compressive moduli of 50/50 PEGDA/Bio-IL hydrogels were also increased from 2.17 ± 0.23 kPa to 28.73 ± 6.31 kPa and 89.83 ± 13.59 kPa, when the final polymer concentration was raised from 10% to 15% and 20%, respectively (**Figure 10b**).

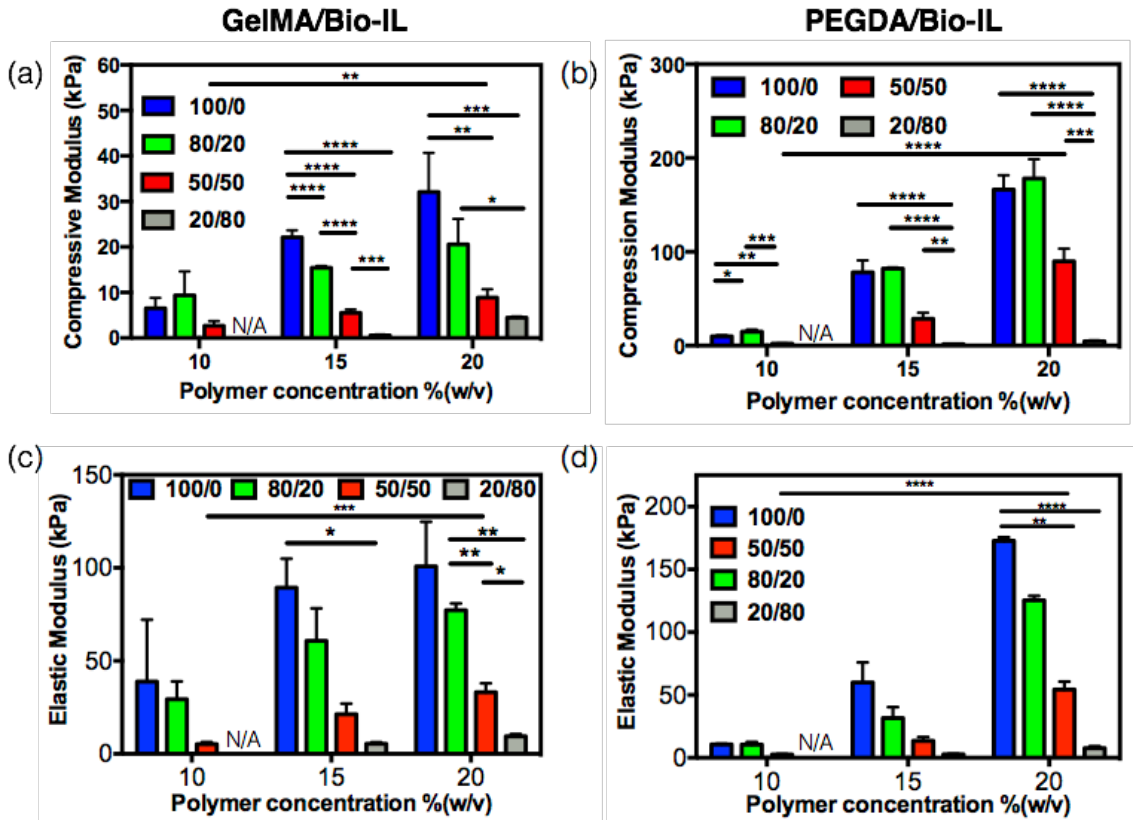

Figure 10. Mechanical properties of Bio-IL conjugated GelMA and PEGDA hydrogels crosslinked with visible light. Compressive moduli for (**a**) GelMA/Bio-IL and (**b**) PEGDA/Bio-IL hydrogels engineered by varying polymer concentration and polymer/Bio-IL ratios. Elastic moduli for (**c**) GelMA/Bio-IL and (**d**) PEGDA/Bio-IL hydrogels with varying polymer

concentration and polymer/Bio-IL ratios (1% VC, 1.5% TEOA, 0.1 mM Eosin Y, and 120 s light exposure were used to form GelMA and PEGDA hydrogels). Error bars indicate standard error of the means, asterisks mark significance levels of $p < 0.05$ (*), $p < 0.01$ (**), and $p < 0.001$ (***).

We also performed tensile tests to measure the elastic modulus of the composite hydrogels. These exhibited a wide range of elastic moduli, in the range of 5.20 ± 1.15 kPa to 100.77 ± 23.95 kPa (**Figure 10c**) and 2.60 ± 0.46 kPa to 172.70 ± 2.86 kPa (**Figure 10d**) for GelMA- and PEGDA-based hydrogels, respectively. Similar to what we observed for the compressive moduli, the elastic moduli of Bio-IL conjugated hydrogels were also dependent on the final polymer concentration, as well as the ratio of polymer to Bio-IL. For instance, the elastic moduli of 15% GelMA/Bio-IL hydrogels were shown to increase consistently from 5.40 ± 0.87 kPa to 89.30 ± 15.65 kPa, when the ratio of polymer to Bio-IL was increased from 20/80 to 100/0, respectively (**Figure 10c**). Further, the ultimate strain of GelMA/Bio-IL hydrogels were shown to increase by increasing the concentration of Bio-IL. For example, for 15% GelMA/Bio-IL hydrogels the ultimate strain increased from 13.93 ± 4.50% to 31.25 ± 5.10% when the ratio of GelMA to Bio/IL was changed from 100/0 to 20/80, respectively (**Figure 11a**). However, the ultimate stress decreased by increasing the concentration of Bio-IL. As shown in **Figure 11c** the ultimate stress decreased from 9.97 ± 1.42 kPa to 0.97 ± 0.25 kPa when the GelMA to Bio-IL ratio was changed from 100/0 to 20/80 at 15% final polymer concentration. In addition, the elastic moduli of 50/50 GelMA/Bio-IL hydrogels were also increased from 5.20 ± 1.15 kPa to 21.30 ± 5.75 kPa and 33.13 ± 4.78 kPa, when the final polymer concentration was increased from 10% to 15% and 20%, respectively (**Figure 10c**). Once again, the use of PEGDA-based hydrogels yielded significantly higher elastic moduli, as compared to GelMA-based hydrogels (**Figure 10d**). The elastic moduli of 15% PEGDA/Bio-IL hydrogels increased from 2.73 ± 0.43 kPa to 60.00 ± 15.85 kPa, when the ratio of PEGDA to Bio-IL was increased from 20/80 to 100/0, respectively (**Figure 10d**).

Similar to GelMA/Bio-IL hydrogels, the ultimate strain of 15% PEGDA/Bio-IL hydrogels were shown to increase from 9.28 ± 2.26% to 59.65 ± 11.59% when the ratio of PEGDA to Bio/IL was changed from 100/0 to 20/80, respectively (**Figure 11b**). The ultimate stress also increased from 1.53 ± 0.40 kPa for the 20/80 ratio, to 6.10 ± 3.22 kPa for the 100/0 for 15% PEGDA/Bio-IL hydrogels (**Figure 11d**). Lastly, the elastic moduli of 50/50 PEGDA/Bio-IL hydrogels were also increased from 2.60 ± 0.46 kPa to 13.43 ± 3.20 kPa and 54.37 ± 6.34 kPa, when the final polymer concentration was increased from 10% to 15% and 20%, respectively.

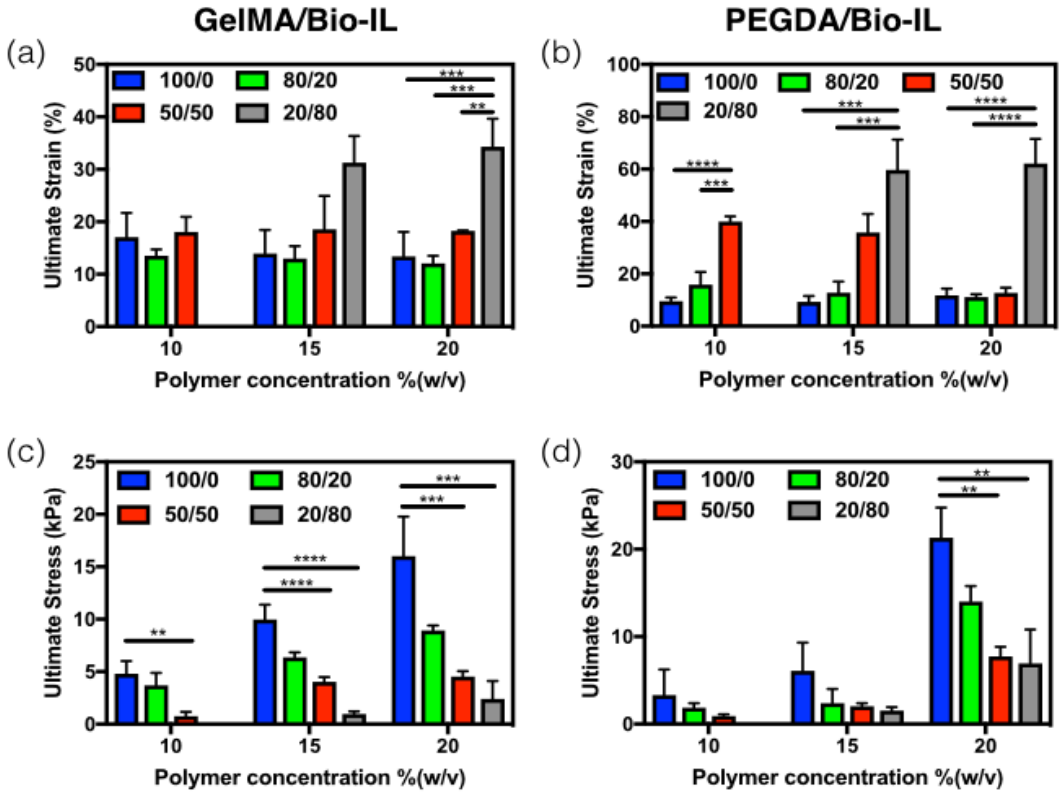

Figure 11. Ultimate stress and ultimate strain of Bio-IL functionalized GelMA and PEGDA hydrogel crosslinked with visible light. Ultimate strain values for (**a**) GelMA/Bio-IL and (**b**) PEGDA/Bio-IL hydrogels engineered by varying polymer concentration and polymer/Bio-IL ratios. Ultimate stress for (**c**) GelMA/Bio-IL and (**d**) PEGDA/Bio-IL hydrogels with varying polymer concentration and polymer/Bio-IL ratios (1% VC, 1.5% TEOA, 0.1 mM Eosin Y, and 120 s light exposure were used to form GelMA and PEGDA hydrogels). Error bars indicate standard error of the means, asterisks mark significance levels of $p < 0.05$ (*), $p < 0.01$ (**), and $p < 0.001$ (***).

Taken together, our results revealed that the mechanical properties of the composite scaffolds could be efficiently modulated by varying both the final polymer concentration, as well as the polymer/Bio-IL ratio. The enhanced mechanical properties at higher polymer concentrations could be explained in part due to the presence of a greater number of available crosslinking sites[242]. Moreover, the engineered scaffolds present several technical advantages in the context of biomedical applications. For example, previous studies have demonstrated that the stiffness of the native human myocardium ranges from 20 kPa to 100 kPa[243, 244]. Therefore, the highly versatile and tunable mechanical properties of these biomaterials could be used to generate ECHs with varying degrees of stiffness, which will mimic the mechanical properties of the native cardiac tissues.

3.1.4. Characterization of pore size, swelling ratios and *in vitro* degradation of engineered ECHs

The porosity of the hydrogels is an important factor in the modulation of cell and tissue interactions, as well as in the penetration of cells into the scaffold, in both 2D culture and 3D cell encapsulation[245]. Therefore, we aimed to characterize the porosity of GelMA/Bio-IL (**Figure 12a**) and PEGDA/Bio-IL (**Figure 12b**) hydrogels, using scanning electron microscopy (SEM). SEM image analysis determined that the average size of the pores in the GelMA/Bio-IL (**Figure 12c**) and PEGDA/Bio-IL (**Figure 12d**) hydrogels is also dependent on the final polymer concentration, as well as the polymer/Bio-IL ratio. For instance, the overall pore sizes of 50/50 GelMA/Bio-IL hydrogels decreased from 85.1 ± 18.4 μm to 61.5 ± 13.1 μm, by increasing the final polymer concentration from 10% to 20%. Similarly, the dimensions of the pores decreased from 86.4 ± 20.3 μm to 39.0 ± 7.9 μm, by increasing the ratio of GelMA to Bio-IL from 100/0 to 20/80 at 15% final polymer concentration. Although, a similar trend could be observed for

PEGDA/Bio-IL hydrogels, we were not able to observe any apparent pores in all 20/80 hydrogels, as well as 50/50 hydrogels formed at 15% and 20% final polymer concentrations (**Figure 12d**). Previous studies have shown that hydrogels with large pores allow better cell penetration, as well as new tissue formation within the microstructure of the scaffold, when compared to hydrogels with lower porosity[245, 246]. Therefore, the tunable porosity of Bio-IL conjugated hydrogels could be used to modulate the spatial distribution of cells within the scaffolds.

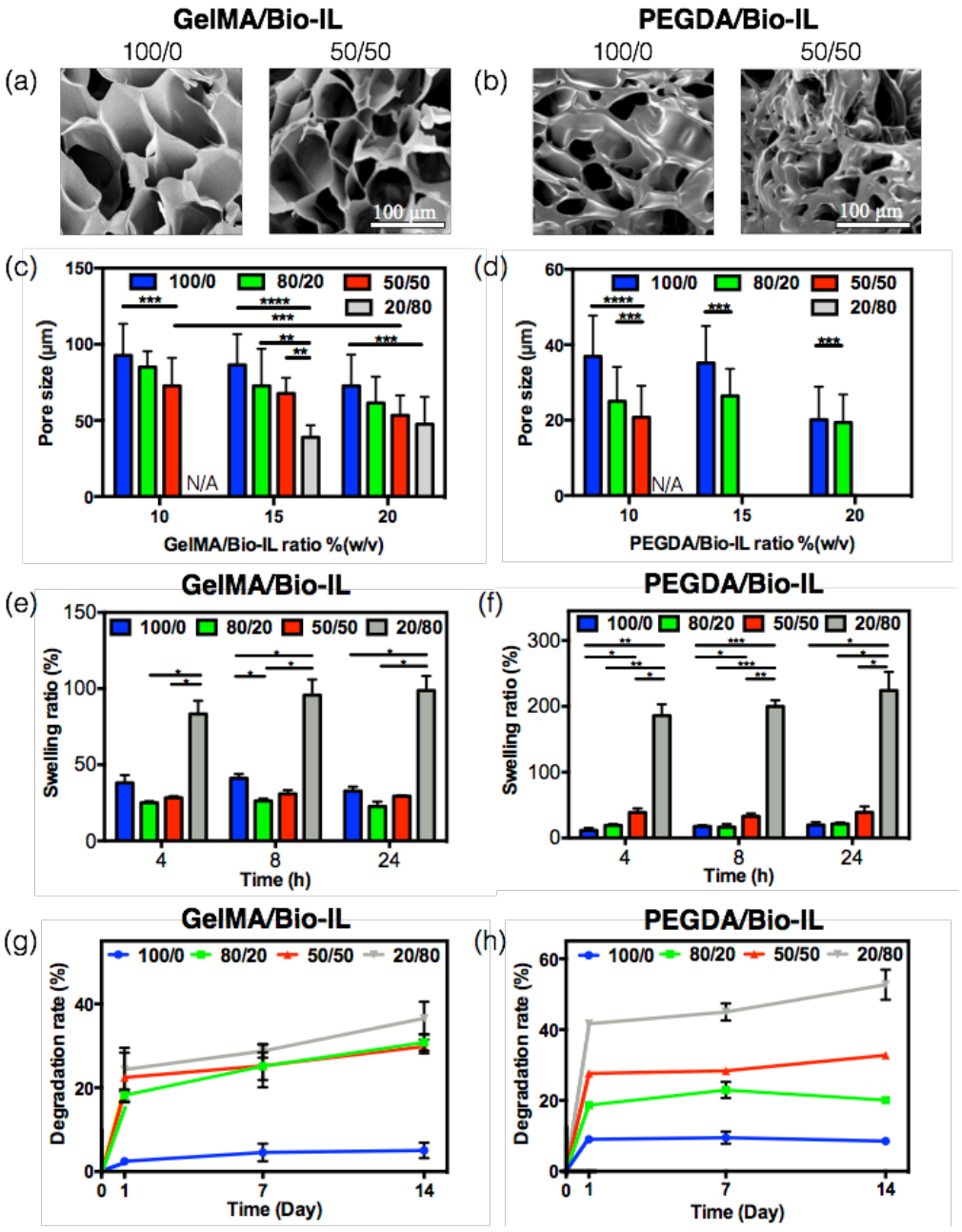

Figure 12. Pore characteristics, *in vitro* swelling, and degradation of polymer/Bio-IL hydrogels Representative SEM images of (**a**) GelMA/Bio-IL and (**b**) PEGDA/Bio-IL hydrogels formed by using 100/0 and 50/50 polymer/Bio-IL ratio at 15% (w/v) polymer concentration (1% VC, 1.5% TEOA, and 0.1 mM Eosin Y at 120 s light exposure were used to form the hydrogels). Average pore sizes of (**c**) GelMA/Bio-IL and (**d**) PEGDA/Bio-IL hydrogels at varying polymer concentrations and polymer/Bio-IL ratios. Swelling ratios of (**e**) GelMA/Bio-IL and (**f**) PEGDA/Bio-IL hydrogels at 15% final polymer concentration and 50/50 polymer/Bio-IL ratio in DPBS after 4, 8 and 24 h. Degradation of (**g**) GelMA/Bio-IL and (**h**) PEGDA/Bio-IL hydrogels at 15% final polymer concentration and 50/50 polymer/Bio-IL ratio in DPBS supplemented with

10% FBS over a two-week period. Error bars indicate standard error of the means, asterisks mark significance levels of $p < 0.05$ (*), $p < 0.01$ (**), and $p < 0.001$ (***).

In the context of tissue engineering, excessive water uptake and degradation could potentially lead to impaired mechanical and electroconductive properties. Therefore, we evaluated the water uptake ability and the *in vitro* degradation rate of the composite hydrogels. These results demonstrated that the maximum swellability was achieved after 4 h of incubation, with no further increases observed after 8 and 24 h. In addition, the swelling ratio after 4 h of incubation for 15% GelMA/Bio-IL (**Figure 12e**) and PEGDA/Bio-IL (**Figure 12f**) hydrogels, increased from 38.1% ± 5.0% to 83.3% ± 8.6%, and from 11.6% ± 3.6% to 185.7% ± 17.1%, respectively, by changing the polymer/Bio-IL ratio from 100/0 to 20/80. In general, the highest swelling ratios for GelMA/Bio-IL (**Figure 12e**) and PEGDA/Bio-IL (**Figure 12f**) hydrogels were observed in hydrogels synthesized using a polymer/Bio-IL ratio of 20/80. These observations can be explained in part due to the presence of hydroxyl (-OH) and amine ($-NH_2$) hydrophilic residues in the choline acrylate structure, which would lead to increased water uptake into the scaffold[247]. Previous studies have reported that the swellability of IL-based hydrogels is highly dependent on the concentration of IL in the system[154, 248]. In our experiments, the highest swelling ratio observed (223.7 ± 28.5) was lower than that reported for other IL conjugated polymers, such as chitosan (>400%)[249]. This characteristic is remarkably advantageous for the implementation of Bio-IL functionalized hydrogels in the context of physiological wet tissues.

Lastly, we aimed to evaluate the *in vitro* degradation of the engineered composite hydrogels. For this, we incubated Bio-IL conjugated hydrogels in Dulbecco's phosphate-buffered saline (DPBS) and DPBS with 10% fetal bovine serum (FBS), at 37 °C for 14 days. These results showed that *in vitro* degradation of 15% GelMA/Bio-IL (**Figure 12g**) and PEGDA/Bio-IL (**Figure 12h**) hydrogels occurred mainly after 24 h of incubation, for all polymer/Bio-IL ratios tested.

Furthermore, the results also showed that the rate of degradation decreased consistently, by increasing the ratio of polymer to Bio-IL. After 14 days of incubation in DPBS supplemented with 10% FBS 52.70 ± 4.24 % of 20/80 PEGDA/Bio-IL hydrogel degraded, which was considerably higher than 36.59 ± 3.95 % of 20/80 GelMA/Bio-IL hydrogel. This general trend was also observed for 10%, and 20% GelMA/Bio-IL and PEGDA/Bio-IL hydrogels at varying polymer/Bio-IL ratios, both in DPBS and DPBS supplemented with 10% FBS. In general, composite hydrogels containing lower concentrations of Bio-IL exhibited slower degradation rate after 1, 7 and 14 days of incubation. It is important to note that the due to the organic nature of this compound, the degradation of the Bio-IL functionalized hydrogels will not result in the generation of any cytotoxic byproducts[250].

Taken together, the physical characterization of Bio-IL conjugated hydrogels demonstrated that the microarchitecture, electrical conductivity, porosity, and *in vitro* degradation can be modulated by varying the final polymer concentration, as well as the polymer/Bio-IL ratio. This remarkable degree of tunability suggests that Bio-IL conjugated hydrogels could be readily tailored to different biomedical and tissue engineering applications.

3.1.5. *In vitro* 2D cell seeding on the engineered GelMA/Bio-IL hydrogels

Hydrogels with electroconductive properties possess a remarkable potential for tissue engineering since they can serve as bioactive scaffolds to modulate excitable cell types. In particular, the use of various synthetic and natural biomaterials has been investigated for the engineering of functional tissue constructs for different cardiac tissue engineering applications[251, 252]. Naturally derived polymers, such as collagen and its denatured form gelatin, have been shown to efficiently promote the attachment, proliferation, and migration of various cell types *in vitro*[253, 254]. This is mainly due to the presence of cell-binding motifs and

protease-sensitive degradation sites that modulate the attachment of cells to the ECM *in vivo*. In contrast, synthetic materials such as PEG and its acrylated form, PEGDA, exhibit no intrinsic cell-binding activity due to inert nature of PEG-based polymers[255]. Therefore, we aimed to investigate the potential of GelMA/Bio-IL conjugated hydrogels to support the growth, spreading and function of primary rat CMs in 2D cultures *in vitro*. A commercial live/dead assay was used to determine the viability of CMs growing on the surface of GelMA (**Figure 13a**) and GelMA/Bio-IL (**Figure 13b**) hydrogels, over a period of 5 days. Similarly, cell attachment and spreading on GelMA (**Figure 13c**) and GelMA/Bio-IL (**Figure 13d**) hydrogels were evaluated through F-actin/DAPI immunofluorescent staining. We also investigated the ability of GelMA/Bio-IL scaffolds to maintain the native phenotype and function of primary CMs in 2D cultures *in vitro*. For this, we evaluated the expression of the cardiac differentiation marker sarcomeric α-actinin (**Figures 13g**, and **13h**), as well as the contractile behavior (**Figure 13i**) of primary CMs seeded on the surface of 15% (w/v) GelMA and 50/50 GelMA/Bio-IL hydrogels. Our results demonstrated that the viability of CMs seeded on engineered hydrogels was not affected due to the presence of the Bio-IL (**Figure 13e**). Cells seeded on the surface of GelMA/Bio-IL hydrogels appeared to exhibit slightly lower viabilities at day one post-seeding, when compared to GelMA controls. However, there were no statistically significant differences between the composite scaffolds and the controls, at days 3 and 5 post-seeding. Furthermore, the metabolic activity of the primary cultures was shown to increase consistently throughout the duration of the culture, as shown by the commercial PrestoBlue assay (**Figure 13f**). This behavior could be explained in part due to the adaptation of the CMs to the conditions *in vitro*, as well as the proliferation of CFs that could not be removed during CM isolation. Immunofluorescent staining revealed that primary CMs on the surface of GelMA/Bio-IL hydrogels exhibited homogeneous distribution of sarcomeric α-actinin

(**Figure 13h**), compared to the intermittent pattern observed in GelMA controls (**Figure 13g**). In addition, GelMA/Bio-IL hydrogels exhibited significantly higher cell numbers than pure GelMA controls at day 5 post-seeding, as shown by quantification of DAPI-stained cell nuclei (**Figure 13j**). Taken together, these results demonstrated that the biocompatibility of GelMA/Bio-IL hydrogels was similar to that of GelMA controls, and that they could promote the growth and spreading of primary CMs *in vitro*.

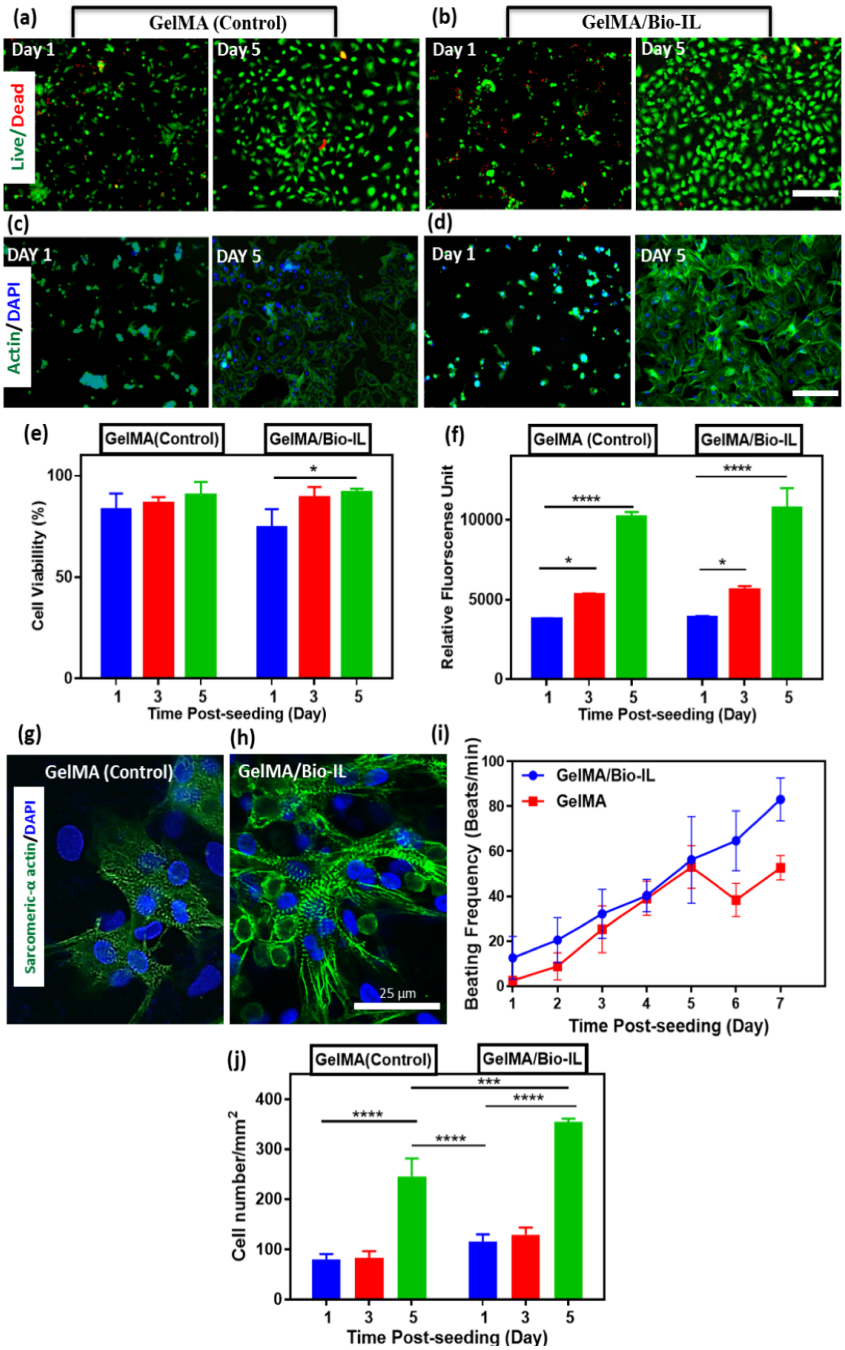

Figure 13. 2D *in vitro* studies using GelMA/Bio-IL hydrogels seeded with CMs. Representative live/dead images from CMs cultured on (**a**) GelMA (control) and (**b**) GelMA/Bio-IL hydrogels on days 1 and 5 (scale bar = 200 µm). Representative F-Actin/DAPI stained images from CMs seeded on (**c**) GelMA and (**d**) GelMA/Bio-IL on days 1 and 5. (**e**) Cell viability quantification of CMs cultured on the hydrogels after 1, 3, and 5 days of culture. (**f**) Quantification of metabolic activity, RFU (relative fluorescence intensity) using PrestoBlue assay, 1, 3, and 5 days after seeding with CMs. Immunofluorescent staining of sarcomeric α-actinin in CMs seeded on GelMA **(g)** and GelMA/Bio-IL **(h)** hydrogels on day 7 (scale bar = 25 µm). (**i**) Characterization of synchronous

contraction in CMs seeded on GelMA and GelMA/Bio-IL hydrogels over 7 days of culture. (*$p < 0.05$, **$p < 0.01$, ***$p < 0.001$ and ****$p < 0.0001$).

CMs maintained in 2D environments tend to revert to a less mature phenotype and lose the ability to respond to physiological stimuli[256]. Thus, apart from the maintenance of metabolically active cells, the preservation of the native phenotype is critical to promote the spatial and functional organization of CMs[257]. Immunofluorescent staining of the cardiac differentiation marker sarcomeric α-actinin revealed that CMs in GelMA/Bio-IL hydrogels were distributed in spatially-relevant multi-cellular organizations (**Figure 13g**). Moreover, these images also showed that CMs still exhibited characteristic cross-striations after 7 days of culture, which are indicative of the sarcomeric structures present in the native ventricular myocardium. In addition, CMs growing in GelMA/Bio-IL hydrogels exhibited a more robust and stable spontaneous contraction profile, when compared to CMs growing on GelMA controls (**Figure 13i**). For example, on day 7, the beating frequency of CMs seeded on GelMA/Bio-IL was 83.05 ± 9.54 beats/min, which was considerably higher than the beating frequency of cells seeded on pure GelMA hydrogel (52.61 ± 5.43 beats/min). These observations suggest that GelMA/Bio-IL hydrogels promoted the formation of interconnected cellular networks on the surface of the scaffolds, which in turn aided to maintain tissue-level function of primary CMs *in vitro*.

Although PEGDA/Bio-IL hydrogels could not be used for cell culture due to the intrinsic inert nature of PEGDA, previous groups have reported the modification of PEG-based hydrogels via tethering of bioactive motifs, such as the incorporation of Arg-Gly-Asp (RGD) and matrix metalloproteinase-sensitive degradation domains[258-260]. These modifications have been shown to enhance the cell-binding ability and the biodegradability of PEG-based hydrogels for tissue engineering applications. Furthermore, due to their intrinsic resistance to cell adhesion and protein adsorption, PEG-based hydrogels exhibit minimal adverse host responses and highly specific

bioactivity via the conjugation of specific bioactive agents[261]. The intrinsic differences between PEGDA and GelMA polymers clearly demonstrate the remarkable potential of Bio-IL functionalization to engineer new conductive biomaterials with a wide range of biological and physicochemical properties, which can be tailored for different biomedical applications.

3.1.6. 3D encapsulation of primary CMs/CFs inside the engineered GelMA/Bio-IL hydrogels

Biomaterials-based cardiac tissue models that rely on 2D cultures of primary CMs have been extensively reported in the literature to investigate many cellular and biochemical mechanisms relevant for cardiac physiology[251]. More recently, *in vitro* models with increased physiological relevance have been engineered to recapitulate the interactions between different cell types and the 3D architecture of native tissues[262]. However, the use of ECHs for 3D encapsulation of primary cardiac cells in highly biocompatible ECHs with tunable electroconductive and mechanical properties has not been fully explored. Here, we investigated the ability of GelMA/Bio-IL hydrogels to support the growth and function of 3D encapsulated CMs and CFs *in vitro*. Similar to 2D cultures, we used a live/dead assay, F-actin/DAPI staining, and a PrestoBlue assay to determine the viability (**Figures 14a-14d**), spreading (**Figures 14e-14h**), and metabolic activity (**Figure 14j**) of 3D encapsulated cells in 15% (w/v) 50/50 GelMA/Bio-IL hydrogels. Although the overall viability of 3D encapsulated cells was comparatively lower than that observed for 2D cultures (**Figure 14e**), cells in GelMA/Bio-IL hydrogels exhibited significantly higher viabilities compared to pure GelMA hydrogels (**Figure 14i**). In addition, these results also showed that the metabolic activity of cells encapsulated in GelMA/Bio-IL hydrogels increased consistently during the 5 days of culture (**Figure 14j**). However, no significant differences between GelMA/Bio-IL and GelMA controls were observed regarding the proliferation (cells/mm^2) of 3D encapsulated cells (**Figure 14k**). Lastly, similar to what we observe

for 2D cultures, our results demonstrated that CMs encapsulated in GelMA/Bio-IL hydrogels exhibited comparatively better contractile profiles, compared to pure GelMA controls (**Figure 14l**). Overall, *in vitro* assessment of GelMA/Bio-IL hydrogels demonstrated that the engineered ECHs are cytocompatible and promote cell growth and spreading in 3D cultures *in vitro*. Although no statistically significant differences in cell number could be observed in cell number (**Figure 14k**), the viability (**Figure 14i**) and metabolic activity (**Figure 14j**) of CMs/CFs 3D encapsulated in GelMA/Bio-IL hydrogels were higher, when compared to pure GelMA controls. The mechanism underlying the improved growth of 3D encapsulated CMs in GelMA/Bio-IL hydrogels was not investigated in this study. However, previous studies have described that electrical stimuli could influence cell fate, through the modulation of the calcium/calmodulin pathway[263, 264]. Briefly, electrical stimuli propagate across the cell membrane, raising the intracellular calcium concentration by activating voltage-gated calcium channels. Elevated intracellular calcium levels activate the cytoskeletal form of calmodulin, which results in enhanced proliferation and increased expression of vascular endothelial growth factor (VEGF), and transforming growth factor (TGF)-ß[265]. This characteristic of GelMA/Bio-IL scaffolds could be critical in the restoration of impaired electrical conductivity and tissue function in scarred peri-infarct regions.

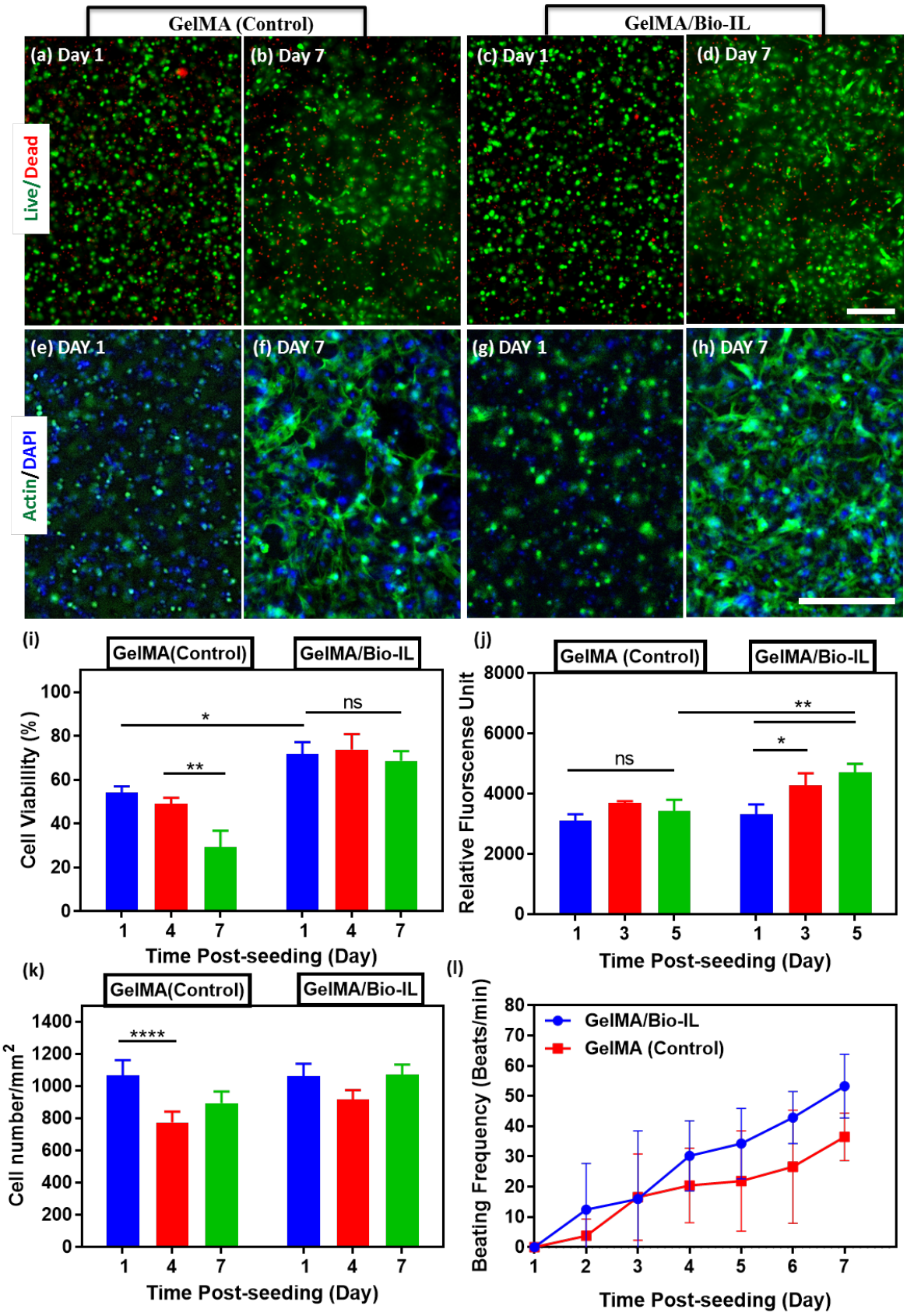
GelMA (Control)
GelMA/Bio-IL
(a) Day 1
(b) Day 7
(c) Day 1
(d) Day 7
Live/Dead
(e) DAY 1
(f) DAY 7
(g) DAY 1
(h) DAY 7
Actin/DAPI
(i)
GelMA(Control)
GelMA/Bio-IL
Cell Viability (%)
Time Post-seeding (Day)
(j)
Relative Fluorscense Unit
Time Post-seeding (Day)
(k)
Cell number/mm2
Time Post-seeding (Day)
(l)
GelMA/Bio-IL
GelMA (Control)
Beating Frequency (Beats/min)
Time Post-seeding (Day)

Figure 14. *In vitro* 3D cell encapsulation of cardiomyocytes (CMs) and cardiac fibroblasts (CFs) in GelMA/Bio-IL hydrogels. CMs and CFs (2:1 ratio) were 3D encapsulated inside visible light-crosslinked GelMA (control) and GelMA/Bio-IL hydrogels. Representative live/dead images from CMs/CFs encapsulated in GelMA hydrogels **(a, b)** and GelMA/Bio-IL **(c, d)** at days 1 and 7 post-encapsulation. Representative F-Actin/DAPI fluorescent images of CMs/CFs encapsulated in GelMA **(e, f)** and GelMA/Bio-IL **(g, h)** hydrogels, at days 1 and 7 post-encapsulation (scale bar = 200 μm). **(i)** Quantification of cell viability for 3D-encapsulated CMs/CFs at days 1, 4, and 7 post-encapsulation. **(j)** Quantification of metabolic activity, RFU (relative fluorescence intensity) using PrestoBlue assay, at days 1, 3, and 5 post-encapsulation. **(k)** Quantification of cell proliferation based on DAPI-stained cell nuclei, at days 1, 4, and 7 post-encapsulation. **(l)** Characterization of synchronous contraction in co-cultures of CMs/CFs 3D-encapsulated in GelMA (control) and GelMA/Bio-IL hydrogels over 7 days of culture. (*$p < 0.05$, **$p < 0.01$, ***$p < 0.001$ and ****$p < 0.0001$). All hydrogels were synthesized using 15% (w/v) final polymer concentration and 50/50 polymer/Bio-IL ratio. Error bars indicate standard error of the means, asterisks mark significance levels of $p < 0.05$ (*), $p < 0.01$ (**), and $p < 0.001$ (***).

In vitro 3D co-cultures of CMs and CFs are being explored to engineer myocardial tissue constructs for drug screening and tissue engineering applications[266-268]. However, the successful 3D encapsulation of CMs/CFs in highly biocompatible hydrogels with tunable mechanical and electroconductive properties has not been fully explored. Apart from material biocompatibility, the integration of physiological stimuli is critical to promote growth, survival, and the functional organization of excitable cell types, such as nerve and muscle[25, 257]. After myocardial infarction, the nonconductive nature of the resulting scar tissue leads to ventricular dysfunction, as well as the electrical uncoupling of viable CMs in the infarcted region[269]. Due to the limited regenerative potential of adult CMs, several regenerative cardiac tissue engineering approaches have been developed using two main strategies: cell-based and/or material-based scaffolds[270]. However, one of the major limitations of conventional biomaterial-based approaches is that the insulating polymeric scaffolds diminish the transfer of electrical signals between CMs, which could lead to arrhythmias after implantation[271]. Thus, ECHs could be used to engineer scaffolds that promote impulse propagation and synchronize contraction, which in turn

could help restore ventricular function by electrically coupling isolated CMs to the native tissue[240].

3.1.7. *In vivo* biodegradation and biocompatibility of GelMA/Bio-IL hydrogels

One of the limitations of conventional conductive polymers is that they are often not biodegradable *in vivo*, which could trigger a persistent inflammatory response due to their prolonged half-lives in the organism[35]. We investigated the *in vivo* degradation and interactions of GelMA-Bio-IL hydrogels with the local tissues, as well as their immunogenicity profile when implanted subcutaneously *in vivo* in an animal host. Explanted samples recovered at days 4, 14, and 28 post-implantation revealed that GelMA/Bio-IL hydrogels exhibited sustained biodegradation throughout the duration of the 28-day experiment (**Figure 15a**). This observation suggests that the engineered hydrogels were efficiently degraded *in vivo*, through enzymatic hydrolysis of the hydrogel matrix. Visual inspection of the explanted samples also revealed significant infiltration of host tissues within the hydrogels (**Figure 15b**). Although complete biodegradation of the scaffold was not observed due to the length of the study, previous works have demonstrated that GelMA-based hydrogels contain peptide sequences that facilitate cell-mediated degradation *in vivo*[230, 272, 273]. Furthermore, the conjugation of the Bio-IL to different polymers could be used to engineer ECHs with varying degrees of biodegradability. For example, biomaterials with more hydrolytically-stable backbones such as PEGDA would result ideal for long-term applications, where a more biostable implantable scaffold is needed[274].

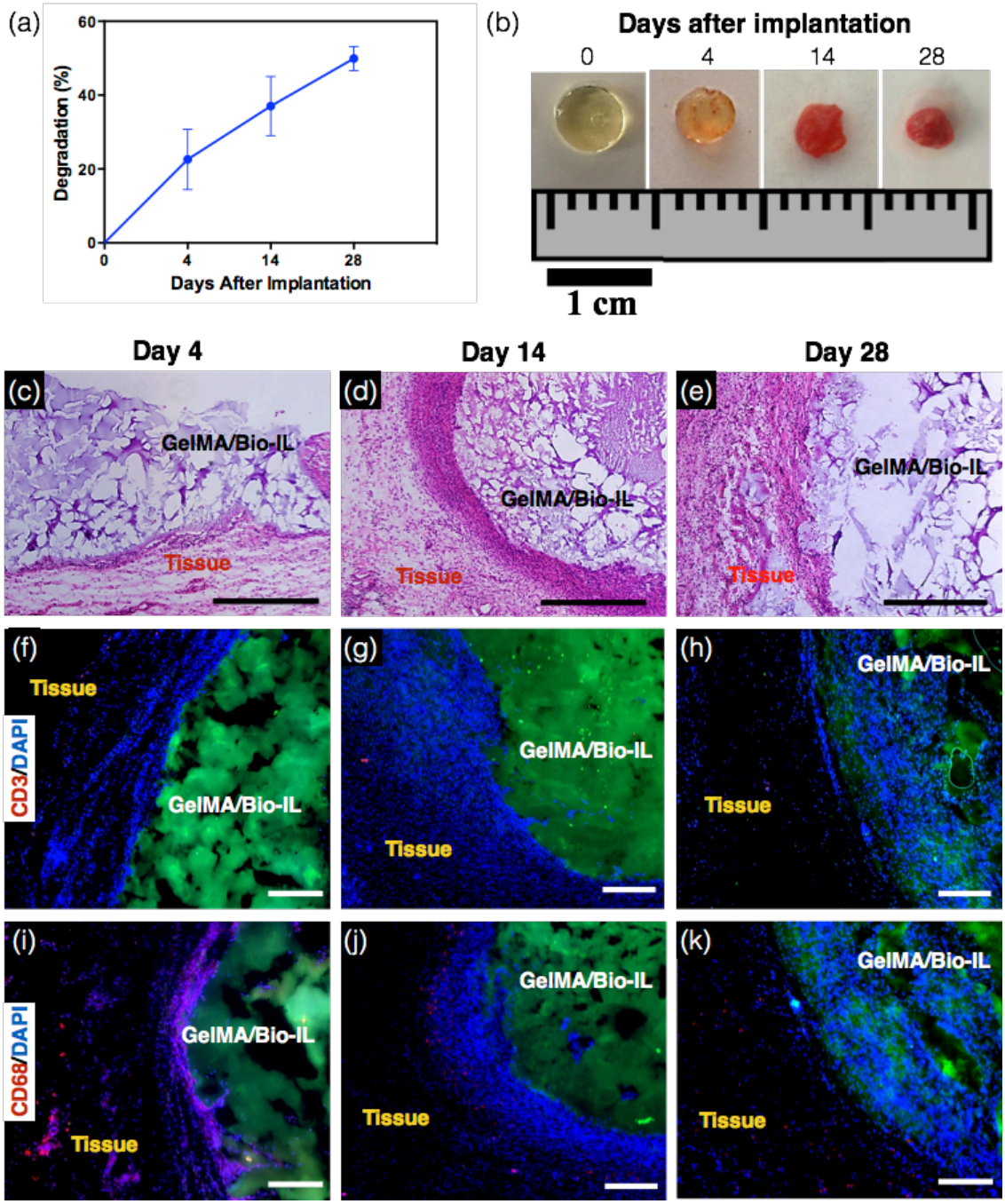

Figure 15. ***In vivo*** **biodegradation and biocompatibility of GelMA/Bio-IL composite hydrogel using a rat subcutaneous model.** (**a, b**) Evaluation of the *in vivo* degradation of GelMA/Bio-IL on days 0, 4, 14 and 28 post implantation (n = 4). (**a**) *In vivo* degradation of GelMA/Bio-IL hydrogels based on weight loss of the implants. The *in vivo* degradation profile of GelMA/Bio-IL hydrogels exhibits an approximately linear behavior during 28 days after implantation. (**b**) Images of the GelMA/Bio-IL composite hydrogels at 0, 4, 14, and 28 days after implantation. (**c-e**) Hematoxylin and eosin (H&E) staining of GelMA/Bio-IL sections after (**c**) 4 days, (**d**) 14 days, and (**e**) 28 days of implantation (scale bars = 500 μm). The H&E shows a negligible amount of

inflammatory cells. (**f-h**) Fluorescent immunohistochemical analysis of subcutaneously implanted GelMA/Bio-IL hydrogels showing no significant local lymphocyte infiltration (CD3) at days (**f**) 4, (**g**) 14 and (**h**) 28 (scale bars = 200 μm), are exhibiting remarkable macrophages (CD68) only at day (**i**) 4 but significantly disappeared at days (**j**) 14 and (**k**) 28 (scale bars = 200 μm). Green, red and blue colors in (**f-k**) represent the GelMA/Bio-IL hydrogels, the immune cells, and the cell nuclei (DAPI). 1% VC, 1.5% TEOA, and 0.1 mM Eosin Y at 120 s light exposure were used to form the hydrogels. All hydrogels were synthesized using 15% final polymer concentration and 50/50 polymer/Bio-IL ratio.

One crucial characteristic of implantable hydrogel-based scaffolds for tissue engineering is their ability to be efficiently biodegraded, in a period of time that allows the growth of new autologous tissue. Since both the mechanical and electroconductive properties of Bio-IL functionalized hydrogels rely on their physical integrity, sustained biodegradation will certainly influence the performance of the scaffolds *in vivo*. However, our results demonstrate that the degradation rate of Bio-IL hydrogels can be readily tuned by varying the final polymer concentration and the polymer/Bio-IL ratio (**Figures 12g and 12h**). As opposed to conventional methods to engineer electroconductive hydrogels, Bio-IL functionalization provides homogeneous and intrinsic electroconductive properties to the entire polymer network. This in turn suggests that the decay in the mechanical and electroconductive performance of the engineered hydrogels is directly proportional to the degradation rate. Therefore, the biodegradability of Bio-IL functionalized hydrogels could be further optimized depending on the specific application, to ensure adequate mechanical and electroconductive performance during the desired period of time. The biodegradability profile of GelMA/Bio-IL hydrogels allows for sustained cellular ingrowth, as well as the eventual replacement of the implanted sample with new autologous tissue. Accordingly, histological assessment of the explanted hydrogels revealed ingrowth of predominantly non-inflammatory tissue, as well as low deposition of a fibrous collagenous capsule (**Figures 15c-15e**). This observation was further confirmed by immunohistofluorescent analysis

of the explanted samples. Fluorescent immunostaining of the CD3 antigen revealed no sustained infiltration of pro-inflammatory leukocytes (**Figures 15f-15h**). In addition, implantation of GelMA/Bio-IL hydrogels elicited a macrophage response by expression of CD63 antigen, initially at day 4; however, they were significantly reduced by day 28 (**Figures 15i-15k**). These results demonstrated that GelMA/Bio-IL hydrogels elicit minimal inflammatory responses *in vivo*. In addition, specific physiological responses could be triggered through the use of different biopolymers. For example, previous studies have demonstrated the remarkable suitability of GelMA-based hydrogels for the induction of angiogenesis[275]. In contrast, the conjugation of Bio-IL to the bioactive polymer alginate could be used for studies involving osteogenesis, as well as other bone tissue engineering applications[276].

The physicochemical cues from the extracellular microenvironment play a key role in various physiological and pathological processes that modulate tissue function[277]. For example, after myocardial infarction, the nonconductive nature of the resulting scar tissue leads to the electrical uncoupling of the infarcted area, and eventually to ventricular dysfunction[269]. Due to the limited regenerative potential of adult CMs, several biomaterials-based tissue engineering approaches for myocardium regeneration have been developed[278]. However, the non-conductive nature of most biopolymers greatly diminishes the propagation of electrical stimuli across the scaffold[271]. Thus, biomaterials-based approaches, like the one presented in this work, could help restore ventricular function by mechanically and electrically coupling the area around the infarcted myocardium[240]. Future work will investigate mechanical and electrical recoupling of impaired myocardium using GelMA/Bio-IL composite hydrogels. Furthermore, in addition to its role in the excitation-contraction coupling, electrical stimulation of CMs is also known to modulate cell proliferation and function[279, 280]. Therefore, the ability of the GelMA/Bio-IL composite

hydrogels to efficiently transduce multiple physiological stimuli to modulate tissue function, holds a remarkable potential for cardiac tissue engineering applications.

3.2. Highly adhesive and electroconductive cardiopatches to improve cardiac function following myocardial infarction

In the next project, our group recently introduced a new method to generate electroconductive biomaterials based on the conjugation of a choline-based Bio-IL to different polymer-based systems[234]. Here, we aimed to develop electroconductive fibrous scaffolds that could adhere strongly to the native myocardium to provide mechanical support and minimize cardiac remodeling following MI. For this, we electrospun the highly biocompatible GelMA into fibrous patches that were chemically conjugated with Bio-IL. We then characterized the physical, mechanical, electroconductive, and tissue-adhesive properties of GelMA/Bio-IL cardiopatches, as well as their ability to support the growth and function of co-cultures of CMs and CFs *in vitro*. Lastly, we evaluated the feasibility of *in vivo* suture-free delivery and the cardioprotective effect of GelMA/Bio-IL cardiopatches using a murine model of MI. These intrinsically adhesive and electroconductive fibrous patches could be used to provide support to the infarcted myocardium, while also establishing a cell-supportive microenvironment that restores electromechanical coupling and minimizes cardiac remodeling following MI.

3.2.1. Physicochemical characterization of GelMA/Bio-IL cardiopatches

We first confirmed the successful conjugation of Bio-IL to the GelMA network and characterized the fiber diameter of the scaffolds. For this, fibrous patches were prepared by electrospinning different concentrations of the GelMA precursor mixed with 1,1,1,3,3,3-hexafluoro-2-propanol (HFIP), onto a static metal collector. Electrospun patches were then incubated in 1.25% (w/v) Irgacure 2959 in ethanol, followed by direct addition of Bio-IL and crosslinking via exposure to UV light (**Figure 16a**). Chemical conjugation of Bio-IL to GelMA

was first confirmed via proton nuclear magnetic resonance (^{1}H NMR) as described previously[234]. Briefly, ^{1}H NMR spectra were obtained for Bio-IL, electrospun GelMA prior to crosslinking, and GelMA/Bio-IL patches after UV exposure. We then determined the degree of consumption of C=C double bonds in methacryloyl groups during free radical polymerization, which occurs due to the crosslinking of GelMA and the conjugation of Bio-IL to GelMA. These results showed that 70.2 ± 7.8% of methacryloyl groups were consumed after photocrosslinking of GelMA/Bio-IL, which was significantly higher than that calculated for pure GelMA patches (56.7 ± 9.1%). The larger rate of decay of the C=C double bonds in GelMA/Bio-IL cardiac patch represents the chemical conjugation of acrylate groups in Bio-IL to methacryloyl groups in GelMA.

The native cardiac ECM is comprised of several structural fibrillar proteins such as collagen and elastin, which range from 10 to several hundred nanometers in diameter[281]. Fiber size also plays an important role in the physical characteristics of TE scaffolds, such as their mechanical strength, porosity, and surface area/volume ratio[282]. Hence, we aimed to characterize the fiber topology of GelMA/Bio-IL cardiopatches synthesized using different concentrations of Bio-IL via scanning electron microscopy (SEM). SEM images showed that control patches synthesized from 10% (w/v) GelMA and 0% (v/v) Bio-IL yielded scaffolds with fiber diameter of 579 ± 170 nm (**Figure 16b**). Scaffolds fabricated with 33% (v/v) Bio-IL exhibited slightly larger fiber sizes (i.e., 638 ± 160 nm) when compared to pristine GelMA controls (**Figure 16c**). However, there were no statistically significant differences in fiber diameter between all Bio-IL concentrations tested at 10% (w/v) GelMA. These results demonstrated that Bio-IL conjugation does not influence fiber diameter, which is highly advantageous to produce scaffolds with tunable conductivity without varying the microstructure of the patches.

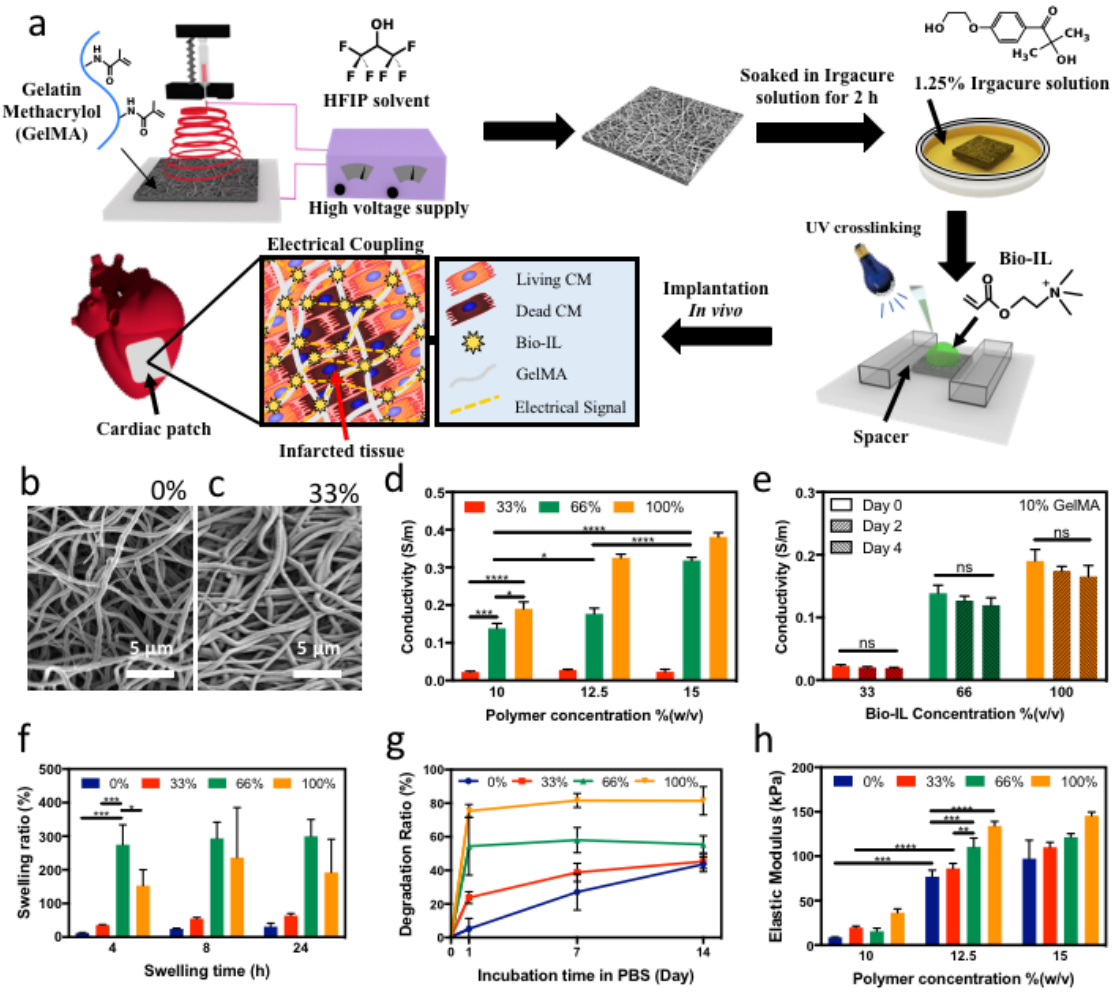

Figure 16. Synthesis and physical properties of engineered cardiopatches. a) Schematic of the fabrication of GelMA/Bio-IL cardiopatches using HFIP to prepare a prepolymer solution with GelMA. Representative SEM images of GelMA/Bio-IL cardiopatches fabricated with a **b**) 0, and **c**) 33 %(v/v) concentration of Bio-IL. **d**) The electrical conductivity of cardiac patches fabricated with varying concentrations Bio-IL. **e**) The electroconductive properties of cardiopatches after incubation in DPBS at 37 °C for 2 and 4 d show no significant change in conductivity during biodegradation. The **f)** swelling ratio and **g**) degradation rate of cardiopatches following incubation in DPBS at 37 °C. **h**) The elastic modulus of cardiopatches increased when fabricated with higher concentrations of GelMA, and with higher concentrations of Bio-IL. Error bars indicate standard error of the means, asterisks mark significance levels of $p < 0.05$ (*), $p < 0.01$ (**), and $p < 0.001$ (***).

3.2.2. Electroconductive properties of GelMA/Bio-IL cardiopatches

The conductive properties of the scaffolds were analyzed using a two-probe electrical station connected to a Hewlett Packard 4155A Semiconductor Parameter analyzer[234]. Briefly, a probe was placed at each end of the scaffolds and voltage was applied in increments of 0.05V, from -2 to 2 V. The resulting data was analyzed to determine the electrical conductivity of each sample using Ohm's Law. Our results showed that the conductivity of the scaffolds could be tuned by varying the concentrations of both GelMA and Bio-IL from $2.27 \times 10^{-2} \pm 1.85 \times 10^{-3}$ S · m^{-1} (10% (/v) GelMA and 33% (v/v) Bio-IL) to $3.81 \times 10^{-1} \pm 1.13 \times 10^{-2}$ S · m^{-1} (15% (w/v) GelMA and 100% (v/v) Bio-IL) (**Figure 16d**). For instance, the electrical conductivity of scaffolds fabricated with 10% (w/v) GelMA increased from $2.27 \times 10^{-2} \pm 1.85 \times 10^{-3}$ S · m^{-1} to $1.38 \times 10^{-1} \pm 1.27 \times 10^{-2}$ S · m^{-1}, and $1.90 \times 10^{-1} \pm 1.83 \times 10^{-2}$ S · m^{-1}, when the Bio-IL concentration was increased from 33% to 66%, and 100% (v/v), respectively. As expected, GelMA patches fabricated with 0% (v/v) Bio-IL did not demonstrate any conductivity, as GelMA itself is not inherently conductive. On the other hand, patches fabricated with 66% (v/v) Bio-IL exhibited an increase in electrical conductivity from $1.38 \times 10^{-1} \pm 0.13 \times 10^{-1}$ S/m to $1.77 \times 10^{-1} \pm 0.15 \times 10^{-1}$ S/m, and $3.18 \times 10^{-1} \pm 0.01 \times 10^{-1}$ S/m when the GelMA concentration increased from 10% to 12.5%, and 15% (w/v), respectively. Though GelMA itself is not inherently conductive, this increase in conductivity may be attributed to more functional groups available in the GelMA prepolymer at higher concentration that can react with Bio-IL. Furthermore, these values are within the range of the electrical conductivity of the native myocardium, which has been shown to be between 1.6×10^{-1} S · m^{-1} (longitudinally) and 5×10^{-3} S · m^{-1} (transversally)[38].

The conductivity of the scaffolds was also characterized after 0, 2, and 4 days of incubation in Dulbecco's phosphate buffered saline (DPBS) at 37 °C to determine the effect of scaffold

degradation on electrical conductivity. These results showed that the conductivity of GelMA/Bio-IL cardiopatches exhibited no statistically significant differences after 4 days of incubation for all conditions tested (**Figure 16e**). Furthermore, we also evaluated the conductivity of GelMA/Bio-IL cardiopatches under mechanically strained conditions to determine the effect of scaffold deformation on electrical conductivity. For this, the scaffolds were first dried for 2 h to retain trace amounts of moisture and prevent stiffening. The presence of moisture led to increased conductivity readings as compared to dried samples, however, allowed samples to be mechanically stretched without breaking. The samples were then stretched at a strain rate of 20% and 40%, and electrical conductivity was measured in the stretched state as described before. Our results showed that there were no statistically significant differences in conductivity of the GelMA/Bio-IL cardiopatches up to 40% strain, compared to static conditions. These results demonstrated that the conductivity of the scaffolds remained unaffected following degradation or stretching, which is critical to maintain a consistent supportive microenvironment for the excitable phenotypes that comprise the contractile myocardium.

3.2.3. *In vitro* swellability and degradation rates of GelMA/Bio-IL cardiopatches

Excess water intake could potentially compromise the mechanical and conductive properties of TE scaffolds. Hence, we aimed to evaluate the water uptake capacity of GelMA/Bio-IL cardiopatches. Our results showed that scaffolds fabricated with 10% (w/v) GelMA swelled rapidly after 4 hours of incubation, with no significant increases in water uptake after 8 and 24 hours for all Bio-IL concentrations (**Figure 16f**). These results also showed that scaffolds fabricated with 66% and 100% (v/v) Bio-IL underwent significantly higher swelling when compared to scaffolds with a lower Bio-IL concentration. This behavior could be explained in part due to the presence of hydroxyl (-OH) and amine ($-NH_2$) hydrophilic groups in the Bio-IL

structure, which enhances the swelling ratio. There was no statistically significant difference in the swelling ratio of cardiopatches fabricated with 66% and 100% Bio-IL after 8 h. However, we observed a decrease in swelling ratio from 66% to 100% (v/v) Bio-IL concentration after 4 h. This can be explained, in part, due to a higher percentage of Bio-IL that is not conjugated to the GelMA polymer network and is washed out in the first 4 h while submerged in DPBS. Furthermore, scaffolds fabricated with 15% (w/v) GelMA showed a similar trend, with higher swelling ratios obtained at higher concentrations of Bio-IL.

Following implantation, TE scaffolds must be able to be biodegraded enzymatically or hydrolytically into nontoxic byproducts to allow the growth of new autologous tissue[283]. Thus, we aimed to characterize the *in vitro* enzymatic degradation profile of GelMA/Bio-IL cardiopatches. Briefly, scaffolds were lyophilized and weighed, followed by incubation in DPBS and 5.0 U/mL of collagenase type II solution at 37 °C for up to 72 h. At the end of this period, the samples were lyophilized and re-weighed to determine the changes in dry mass after degradation. The collagenase solution was replaced daily. Our results showed that the degradation rate increased concomitantly when the Bio-IL concentration was increased for cardiopatches containing 10% (w/v) GelMA (**Figure 16g**). For example, our results show that following 24 h of incubation in collagenase type II solution, cardiopatches demonstrated a degradation rate of 49.65 ± 11.60% and 71.90 ± 4.55% for scaffolds fabricated with 33% (v/v) and 100% (v/v) Bio-IL, respectively. In addition, we evaluated the *in vitro* degradation profile of our cardiopatches incubated in DPBS solution. Our results showed that after 1 day of incubation, scaffolds fabricated using 10% GelMA and 33% (v/v) Bio-IL exhibited degradation rates corresponding to 25.75% ± 3.57%. At 14 days following incubation, cardiopatches containing 10% (w/v) GelMA and 33% (v/v) Bio-IL exhibited 45.32 ± 4.27% degradation. Moreover, the degradation rate increased

concomitantly when the Bio-IL concentration was increased for cardiopatches containing both 10% and 15% (w/v) GelMA. In addition, we did not observe any statistical differences between the degradation rate of the patches fabricated with 10% and 15% (w/v) GelMA after 1 and 14 days. Both degradation studies performed in DPBS as well as in a collagenase solution demonstrated that more rapid degradation occurred in cardiopatches fabricated with a higher concentration of Bio-IL. This trend could be attributed in part to higher amounts of unconjugated Bio-IL that were washed out of the hydrogel network.

3.2.4. Mechanical characterization of GelMA/Bio-IL cardiopatches

Scaffolds used for cardiac TE should possess similar mechanical properties to the native myocardium to prevent mechanical mismatches that could impair its contractile function[284, 285]. Thus, we evaluated the mechanical properties of scaffolds fabricated using varying concentrations of GelMA and Bio-IL (**Figures 16h and 17**). Our results show that the scaffolds exhibited highly tunable elastic moduli (i.e., 8.76 ± 0.42 kPa to 145.50 ± 4.10 kPa), which were in the range of the stiffness reported for the native myocardium (20 kPa to 100 kPa)[243, 244]. Our results showed that the elastic moduli increased concomitantly with higher GelMA concentrations (**Figure 16h**). For instance, the elastic moduli of scaffolds fabricated with 33% (v/v) Bio-IL increased from 19.67 ± 1.70 kPa to 86.23 ± 5.61 kPa, and 110.00 ± 5.56 kPa when the concentration of GelMA increased from 10% to 12.5%, and 15% (w/v), respectively (**Figure 16h**). These results also showed that the elastic moduli of the scaffolds could also be increased by increasing the concentration of Bio-IL. For instance, the elastic moduli of scaffolds fabricated with 12.5% (w/v) GelMA increased from 86.23 ± 5.61 kPa to 110.45 ± 9.97 kPa, and 134.06 ± 5.06 kPa when the concentration of Bio-IL was increased from 33% to 66%, and 100% (v/v), respectively (**Figure 16h**). This increase in mechanical properties of the patches may be due to the

electrostatic interactions between the positively charged groups in Bio-IL and the negatively charged functional groups present in the GelMA polymer. Ionic interactions, such as these, have previously been shown to increase mechanical strength in hydrogels [286]. In addition, there might be chemical bonding between the Bio-IL and GelMA prepolymer through photopolymerization, which can also increase the mechanical properties of the patches. Furthermore, the ultimate strain and ultimate stress of the scaffolds was also shown to vary by changing the concentrations of both Bio-IL and GelMA (**Figure 17a**). For instance, the ultimate strain of scaffolds with 10% (w/v) GelMA decreased from 84.2 ± 11.46 kPa to 54.65 ± 11.10 kPa, and 47.9 ± 8.91 kPa when the concentration of Bio-IL was increased to 33%, 66%, and 100% (v/v), respectively (**Figure 17a**). Moreover, the ultimate stress of scaffolds fabricated with 33% (v/v) Bio-IL increased to 31.31 ± 5.18 kPa, 64.59 ± 11.19 kPa, and 89.03 ± 10.41 kPa when the concentration of GelMA was increased from 10% to 12.5%, and 15% (w/v), respectively (**Figure 17b**). Taken together, these results demonstrated the remarkable mechanical tunability of GelMA/Bio-IL cardiopatches, which is highly advantageous for the engineering of electroconductive scaffolds for a variety of TE and biomedical applications.

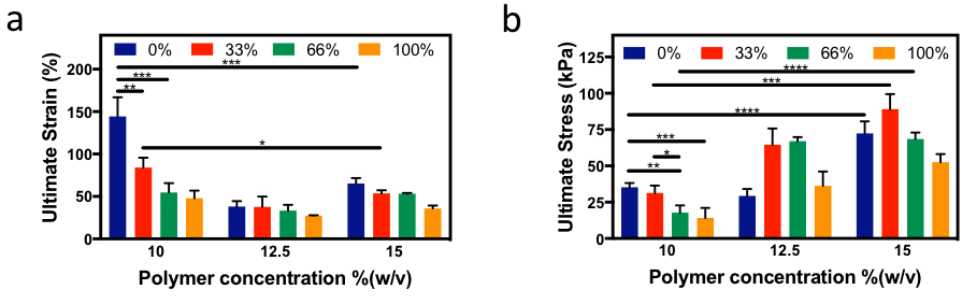

Figure 17. Mechanical properties of cardiopatches. **a**) The ultimate strain and **b**) ultimate stress exhibited by GelMA/Bio-IL cardiopatches. Error bars indicate standard error of the means, asterisks mark significance levels of $p < 0.05$ (*), $p < 0.01$ (**), and $p < 0.001$ (***).

3.2.5. GelMA/Bio-IL patches as biomimetic adhesives to cardiac tissue

Biomaterials with strong adhesive properties to wet tissues have emerged as promising strategies for sutureless wound closure following surgical procedures[287]. In this regard, in our previous studies, we demonstrated that GelMA-based hydrogels possess high adhesive strength to various physiological tissues, while also exhibiting superior mechanical performance when compared with commercially available tissue adhesives[288, 289]. Here, we aimed to evaluate the adhesive strength of GelMA/Bio-IL cardiopatches to the native myocardium to determine their potential for sutureless application following MI. We used standard wound closure and burst pressure tests from the American Society for Testing and Materials (ASTM) as well as *ex vivo* experiments using murine cardiac tissue to evaluate the adhesive properties of our engineered cardiopatches. First, wound closure experiments were carried out to evaluate the adhesive strength of the scaffolds to porcine skin (**Figure 19a-b**), and murine left ventricular myocardium (**Figures 18a-c**). Wound closure tests showed that the adhesiveness of GelMA/Bio-IL cardiopatches to porcine skin increased up to 61.97 ± 2.50 kPa by increasing the concentration of Bio-IL (**Figure 19b**). Furthermore, the adhesive strength of scaffolds synthesized using 66% and 100% (v/v) Bio-IL was shown to be significantly higher than the commercial surgical sealants such Coseal™ (19.4 ± 17.3 kPa) and Evicel® (26.3 ± 4.7 kPa) (**Figure 19b**). In addition, visual inspection revealed that scaffolds photocrosslinked on the surface of the tissue also adhered strongly to the native murine myocardium (**Figure 18a**). Similarly, wound closure tests on murine myocardium (**Figure 18b**) revealed that the adhesiveness of GelMA/Bio-IL cardiopatches increased from 5.1 ± 0.4 to 24.89 ± 2.34 kPa as the Bio-IL concentration enhanced from 0% to 100% (v/v) (**Figure 18c**). Moreover, the adhesive strength of the engineered GelMA/Bio-IL cardiopatches was significantly higher than other synthesized cardiac sealants such as poloxamine-based hydrogels (~17 kPa)[290], and

poly(glycerol sebacate)-*co*-lactic acid (24 kPa)[291], as well as commercial sealants such as Coseal™ and Evicel®. These results demonstrated that GelMA/Bio-IL cardiopatches can be readily applied to the surface of the myocardium and adhere strongly without the need for sutures or additional tissue adhesives.

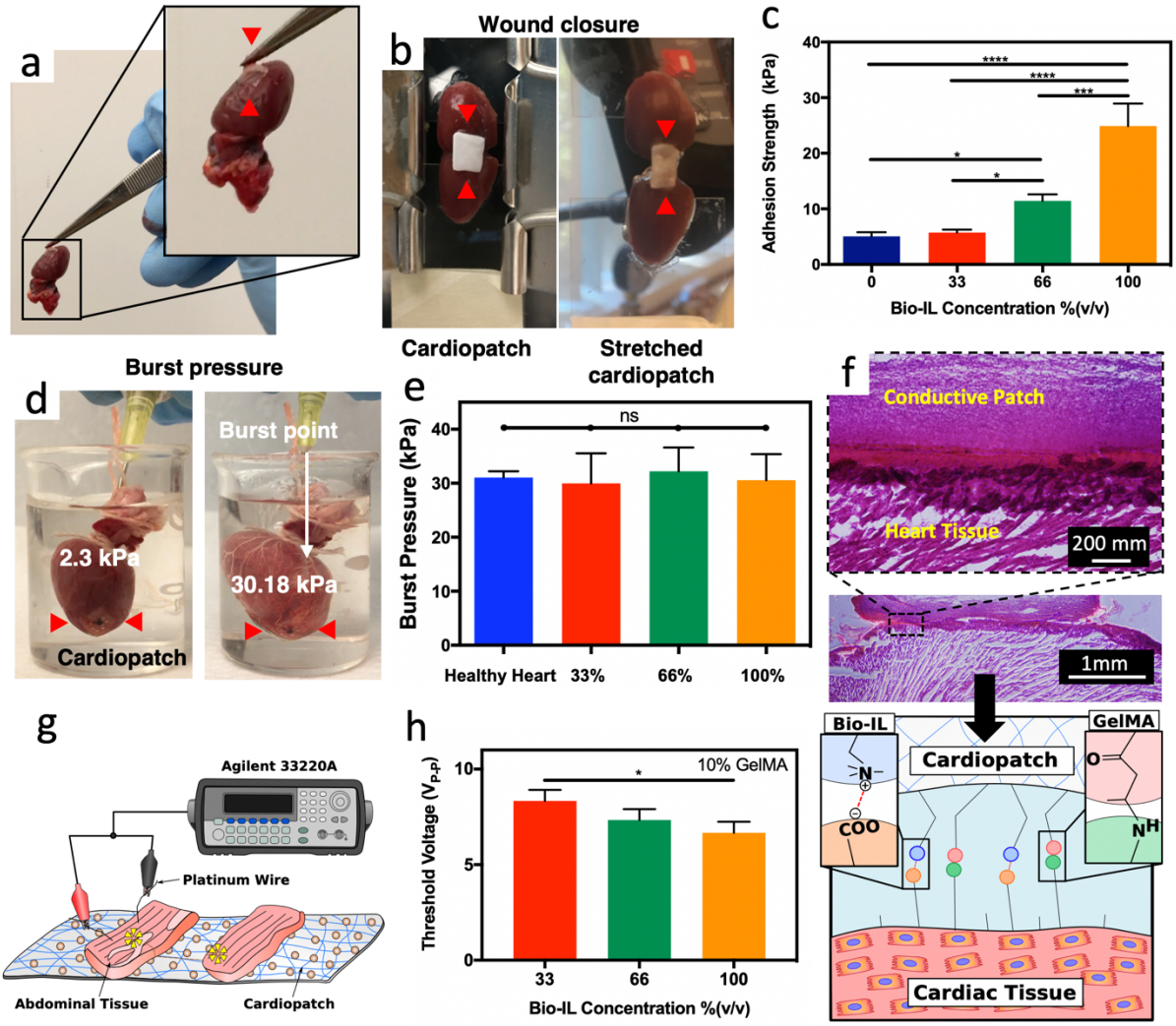

Figure 18. *Ex vivo* adhesive properties and electrical conductivity of GelMA/Bio-IL cardiopatches. a) Representative image of a GelMA/Bio-IL cardiopatch photocrosslinked on explanted rat heart demonstrating the high adhesion of the cardiopatch (red arrows) to cardiac tissues. **b**) Standard wound closure test using explanted rat heart as the biological substrate to test the adhesion strength of GelMA/Bio-IL cardiopatches. **c)** Quantification of the adhesion strength exhibited by cardiopatches fabricated with 10% (w/v) GelMA and varying concentrations of Bio-IL on explanted rat heart. Cardiopatches fabricated with higher concentrations of Bio-IL demonstrated higher adhesion strength to cardiac tissue. **d**) Representative images of GelMA/Bio-

IL cardiopatch fabricated with 10% (w/v) GelMA and 66% (v/v) Bio-IL photocrosslinked on the defect site of an explanted rat heart to measure the burst pressure. **e)** Quantification of the burst pressure of GelMA/Bio-IL cardiopatches formed with varying concentrations of Bio-IL and photocrosslinked on the defect site of rat heart showed no significant difference when compared to the burst pressure of a healthy rat heart. **f)** H&E staining of cardiopatch-tissue interfaces. The tight interface indicates a strong bonding of the GelMA/Bio-IL cardiopatch to the murine myocardium. The schematic in panel f showing the electrostatic forces between positively charged Bio-IL and negatively charged surface of cardiac muscle tissue and cells, as well as covalent bonds between methacrylate groups of GelMA and NH_2 functional groups in cardiac tissue. These two types of bonding led to strong adhesion. **g)** Schematic of *ex vivo* abdominal tissue placed adjacently on GelMA/Bio-IL cardiopatches fabricated with 10% (w/v) and varying concentrations of Bio-IL to determine the threshold voltage needed to stimulate both sections of abdominal tissue. **h)** Quantification of the threshold voltage of GelMA/Bio-IL cardiopatches significantly decreased for patches fabricated with 100% (v/v) Bio-IL compared to those fabricated with 33% (v/v) Bio-IL suggesting enhanced electrical properties with higher concentrations of Bio-IL. Error bars indicate standard error of the means, asterisks mark significance levels of $p < 0.05$ (*).

We also evaluated the ability of GelMA/Bio-IL cardiopatches to seal tissue defects under applied pressure using collagen sheets based on a standard burst pressure test[289, 292] (**Figure 19c-d**), as well as *ex vivo* explanted rat hearts (**Figures 18d-e**). For burst pressure test using collagen sheets, we first created small defects on sections of the tissue, which were then sealed by photocrosslinking the cardiopatch on top of them. We then applied increasing air pressure using a syringe pump connected to a pressure sensor until failure occurred (**Figure 19c**). Our results showed that the burst pressure of GelMA/Bio-IL cardiopatches adhered onto collagen sheets increased up to 5.36 ± 1.01 kPa by increasing the concentration of Bio-IL (**Figure 19d**). Moreover, the burst pressure of patches fabricated with 100% (v/v) Bio-IL was significantly higher than the burst pressure of both Coseal™ (1.7 ± 0.1 kPa) and Evicel® (1.5 ± 1.0 kPa) (**Figure 19d**). We also measured the *ex vivo* burst pressure of explanted rat heart sealed with our adhesive patches fabricated with 10% (w/v) GelMA and varying concentrations of Bio-IL (**Figure 18d,e**). For the *ex vivo* experiments, after sacrificing the animals, the blood vessels at the base of the heart were

sealed with clamps, and a defect was created near the apex, which was then sealed with the patch by applying the GelMA/Bio-IL scaffold and photocrosslinking for 5 min. Our results showed that failure occurred at a pressure of 29.97 ± 5.56 kPa, 32.22 ± 4.38 kPa, and 30.56 ± 4.82 kPa for the heart sealed by the engineered cardiopatch containing 33%, 66%, and 100% (v/v) Bio-IL, respectively. The burst pressure of these cardiopatch formulations were similar to the pressure at failure for the intact heart (i.e., 31.05 ± 0.67 kPa) (**Figure 18e**). Furthermore, visual inspection revealed that failure did not occur due to detachment or rupture of the adhesive patches for all formulations, but due to bursting of the myocardium distal to the defect. The strong bonding of GelMA/Bio-IL cardiopatches to the myocardium was further confirmed via histological evaluation of the interface between the patch and the tissue (**Figure 18f**). H&E stained micrographs revealed a tight interlocking between the scaffold and the myocardium, which further demonstrated the intrinsic ability of the scaffolds to adhere strongly to the native tissue.

Standard wound closure (**Figure 18c**) and burst pressure (**Figure 18e**) tests demonstrated the high adhesive strength of the scaffolds, which was superior to commercial tissue adhesives, as well as other proposed bioadhesives, such as a hydrophobic light activated heart glue[293]. These observations were further confirmed via histological evaluation, which revealed the tight interlocking at the interface between the patches and the myocardium (**Figure 18f**). GelMA has been previously reported as a suitable material to obtain strong adhesion to wet tissues[289]. This is due to the covalent bonds formed between methacrylate groups of GelMA and amine groups of tissue during photocrosslinking[294]. Thus, once photocrosslinking has been completed, the anterior side of our cardiopatches will not adhere to the pericardial sac. In addition, GelMA/Bio-IL cardiopatches demonstrated significantly stronger adhesion to cardiac tissue when fabricated with higher concentrations of Bio-IL. This can be attributed to electrostatic interactions between

the negatively charged surface of cardiac tissue (carboxyl group) and our positively charged choline-based Bio-IL[295-298]. In fact, the strong adhesion between GelMA/Bio-IL patches and tissues can be attributed to the formation of two different types of chemical bonds: covalent bonds between GelMA and tissue, and ionic bonds between Bio-IL and tissue (schematic shown in **Figure 18f**).

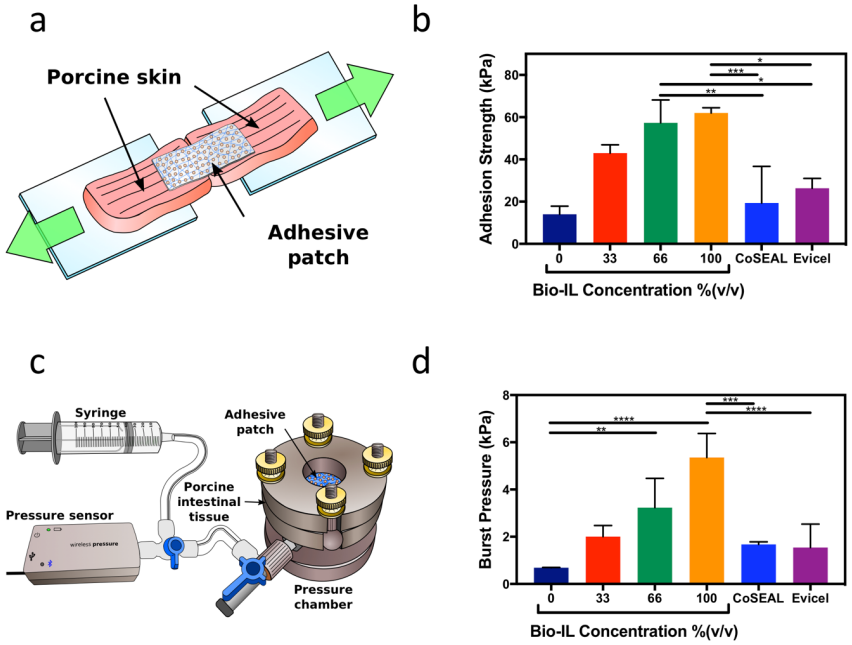

Figure 19. *In vitro* adhesion strength of GelMA/Bio-IL cardiopatches. a) Schematic of wound closure test on cardiac patches using porcine skin. **b**) Patches fabricated with 10% (w/v) GelMA and varying concentrations of Bio-IL displayed an increasing adhesion strength to porcine skin when fabricated with increasing concentration of Bio-IL. Additionally, these GelMA/Bio-IL cardiac patches showed a significantly higher adhesion strength when compared with commercially available tissue sealants, such as Coseal™, and Evicel®. **c**) Schematic of the measurement of the burst pressure of cardiac patches. **d**) Cardiopatches fabricated with 10% (w/v) GelMA and varying concentrations of Bio-IL exhibited an increasing burst pressure strength when fabricated with an increasing concentration of Bio-IL. The burst pressure strength of GelMA/Bio-IL cardiac patches was also greater than Coseal™, and Evicel®. Error bars indicate standard error of the means, asterisks mark significance levels of $p < 0.05$ (*), $p < 0.01$ (**), and $p < 0.001$ (***).

Recent studies have also reported the development of adhesive and conductive cardiac patches based on the incorporation of gold-nanorods[171] and dopamine[299] in synthetic polymer

networks. While these suture-free strategies greatly enhance the clinical translation of bioengineered cardiopatches by minimizing the risk of additional tissue damage, they may not lead to tissue repair and regeneration due to the absence of cell binding sites in the polymer network. In addition, previous groups have demonstrated the intrinsic potential of GelMA-based scaffolds to act as potent angiogenic niches[300]. Therefore, in contrast to alternative strategies, GelMA/Bio-IL cardiopatches could also act as proangiogenic patches that could help salvage the ischemic myocardium during the early stages following MI[301]. These scaffolds could also be used as a supportive layer that can minimize the risk of free wall rupture during the later stages of cardiac remodeling[302], owing to their strong tissue-adhesiveness biomimetic mechanical properties.

3.2.6. Evaluation of GelMA/Bio-IL cardiopatches capability to restore impulse propagation across severed striated muscle *ex vivo*

Electroconductive scaffolds could be used to restore electrical communication between excitable cell types to preserve the functionality of the tissue. Thus, we evaluated the ability of GelMA/Bio-IL cardiopatches to restore impulse propagation between two pieces of skeletal muscle *ex vivo*. For this, the rectus abdominis muscles of Wistar rats were explanted *post-mortem,* cut into square pieces, and placed 3 mm apart from each other on top of the scaffolds (**Figure 18g**). Pulsed direct current test runs were conducted by applying 50 ms square pulses at increasing frequencies, using short platinum wires that were placed on one of the two samples. Muscle contraction was visually assessed on the opposite sample and the threshold voltage was recorded. As expected, our results showed that scaffolds containing higher concentrations of Bio-IL exhibited comparatively lower threshold voltages as compared to GelMA patches without Bio-IL (**Figure 18h**). Therefore, the engineered GelMA/Bio-IL cardiopatches could be used to restore the

propagation of electrical impulses and preserve the functionality of excitable tissues damaged by trauma or disease.

3.2.7. Cell viability, proliferation, and phenotypic characterization of cardiomyocytes and cardiac fibroblasts seeded on electrospun GelMA/Bio-IL scaffolds

One of the most important aspects in the design of TE scaffolds is the accurate recapitulation of the different stimuli that modulate cell fate. CMs are electroactive cells that rely on electrical stimuli for maintaining tissue homeostasis and function[7]. Therefore, electroconductive scaffolds hold great potential for cardiac TE since they can promote the propagation of electrical impulses and enhance electromechanical coupling of CMs *in vitro*[251]. Here, we aimed to evaluate the ability of GelMA/Bio-IL cardiopatches to support the growth and the contractile function of co-cultures of freshly-isolated CMs and CFs. For this, primary CMs and CFs (2:1 ratio) were drop seeded on top of GelMA/Bio-IL scaffolds fabricated using different concentrations of Bio-IL. Cell viability and proliferation were evaluated using a commercial Live/Dead assay (**Figure 20a**) and fluorescent F-actin/cell nuclei staining (**Figure 20b**), respectively. The results demonstrated that the viability of CMs/CFs remained >90% up to day 7 post-seeding for all conditions tested (**Figure 20c**). In addition, quantitative analysis of fluorescent images revealed that GelMA/Bio-IL scaffolds support the proliferation of CFs, which led to increasingly higher number of cells throughout the duration of the experiment. The metabolic activity of cells growing on GelMA/Bio-IL cardiopatches was significantly higher than those growing on GelMA controls (**Figure 20d**). We also evaluated the contractile activity of CMs seeded on GelMA/Bio-IL scaffolds. For this, cell-seeded scaffolds were imaged daily using an inverted microscope equipped with a CCD camera and a temperature-controlled chamber at 37 ºC. The beating frequency (beats/min, BPM) of the CMs was calculated from digitized video-recorded

sequences using a custom MATLAB program. Our results showed that cells grown on cardiopatches containing 33% and 66% (v/v) Bio-IL exhibited a comparatively more robust contractile behavior, when compared to pristine GelMA and GelMA with 100% (v/v) Bio-IL scaffolds (**Figure 20e**). Moreover, cells grown on GelMA cardiopatches fabricated with 33% and 66% (v/v) Bio-IL exhibited observable contractility at day 7 post-seeding, and significantly higher beating frequencies (157.143 ± 1.742 BPM and 196.524 ± 1.018 BPM, respectively) than those growing on pristine GelMA patch and GelMA with 100% (v/v) Bio-IL cardiopatches (104.643± 5.845 BPM and 110.210 ± 7.360 BPM, respectively) (**Figure 20e**). The lower contractile activity of the cells grown on GelMA patches can be due to the non-conductivity of the scaffold with no Bio-IL. On the other hand, when 100% (v/v) Bio-IL was used, the excess amount of Bio-IL might cover cell binding sites available on GelMA prepolymer, leading to lower cell attachment and contractile activity. Highest beating frequency was observed for the cells cultured on cardiopatches with 66% (v/v) Bio-IL.

The contractile function of the myocardium is established by a complex network of interconnected cells that communicate via gap junction proteins termed connexin, which mediate the propagation of electrical impulses[303]. Here, we evaluated the expression of phenotypic cardiac markers in cells grown on pristine GelMA scaffolds and GelMA cardiopatches containing 66% (v/v) Bio-IL, via immunofluorescent staining (IFS) against sarcomeric α-actinin (SAA) and connexin 43 (Cxs43). Representative fluorescent images revealed that cells seeded on the scaffolds self-organized in clusters of contracting CMs, which were attached to a layer of CFs proliferating on the surface of the scaffolds (**Figure 20f and 20g**). Our results also showed that cells grown on GelMA cardiopatches with 66% (v/v) Bio-IL exhibited significantly higher levels of Cxs43 expression, located mainly between the borders of the CFs, as compared to pristine GelMA patches

(**Figure 20h**). These observations suggest that GelMA/Bio-IL cardiopatches could aid in the propagation of electrical impulses between isolated cells to enhance the tissue-level functionality and beating of cardiac constructs.

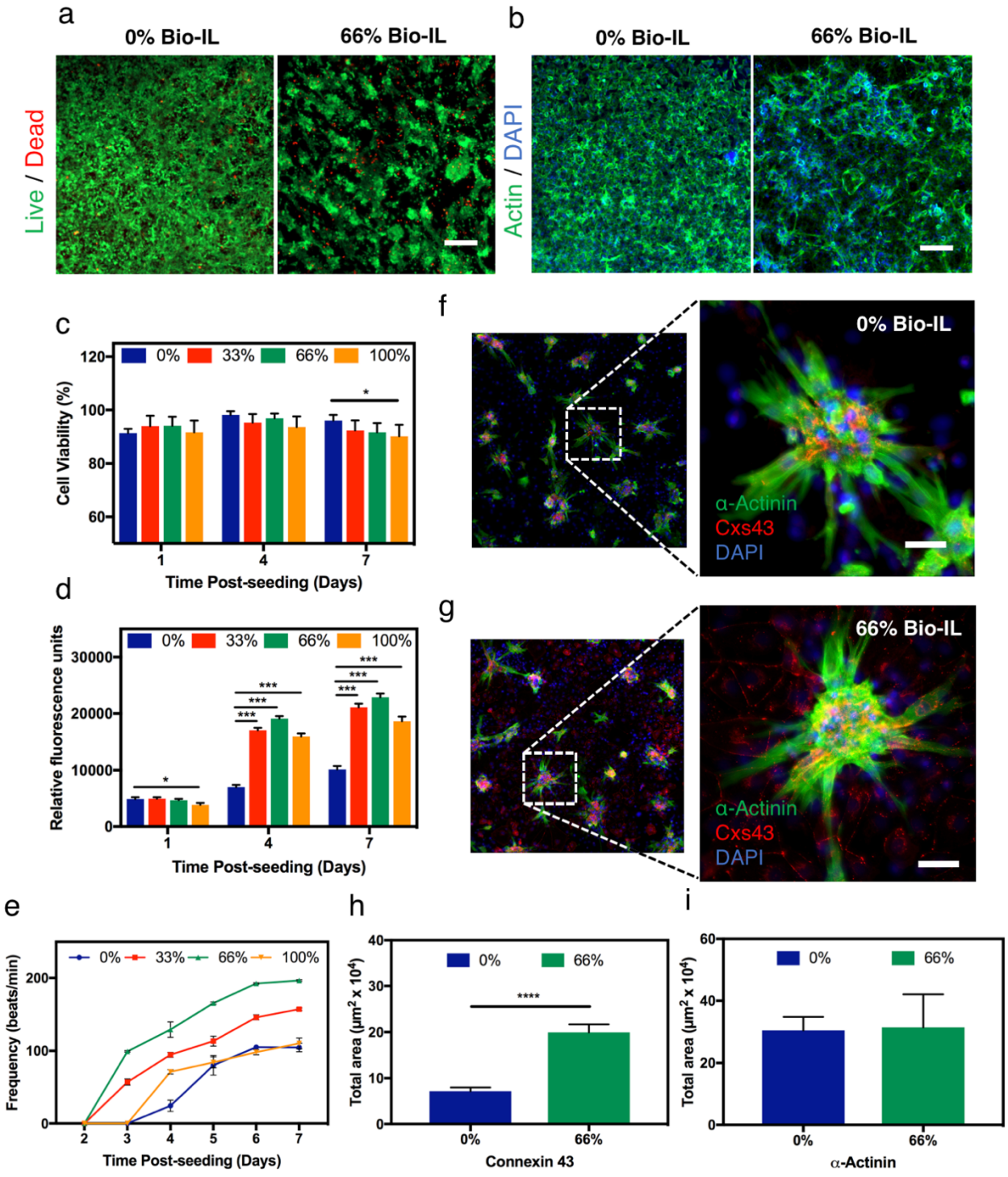

Figure 20. 2D co-cultures of CMs and CFs on GelMA/Bio-IL cardiopatches. The *in vitro* cytocompatibility of the engineered cardiopatches was evaluated using 2D co-cultures of freshly isolated CMs and CFs (ratio 2:1) growing on cardiopatches fabricated with different concentrations of Bio-IL. **a)** Representative Live/Dead images of CMs/CFs growing on patches containing 0% and 66% (v/v) Bio-IL at day 7 post-seeding. **b)** Representative actin/DAPI images of CMs/CFs growing on patches fabricated with 0% and 66% (v/v) Bio-IL at day 7 post-seeding (Scale bar = 200 μm). Bar graphs showing the quantification of **c)** cell viability, and **d)** metabolic activity of 2D co-cultures of CMs/CFs at days 1, 4, and 7 post-seeding, growing on cardiopatches engineered with different concentrations of Bio-IL. **e)** Characterization of the beating frequency (beats/min) of CMs/CFs throughout 7 days of culture growing on cardiopatches fabricated with varying concentrations of Bio-IL. Representative immunofluorescent images of CMs/CFs at day 7 post-seeding growing on the surface of patches containing **f)** 0%, and **g)** 66% (v/v) Bio-IL (green: sarcomeric α-actinin, red: connexin 43, blue: DAPI) (Scale bar = 50 μm). Quantification of the relative levels of expression (i.e., intensity of fluorescence) of **h)** connexin 43, and **i)** sarcomeric α-actinin in co-cultures of CMs/CFs on engineered patches at day 7 post-seeding.

The native myocardium is an electroactive tissue that can transfer electrical impulses that enable the synchronous contraction of the CMs, which in turn carry out the pump function of the heart. Our results demonstrated that GelMA/Bio-IL cardiopatches could effectively promote the growth and function (**Figure 20**) of co-cultures of CMs and CFs *in vitro*. Bio-IL conjugation led to a comparatively better contractile profile than pristine GelMA scaffolds, as demonstrated by the increased metabolic activity (**Figure 20d**) and enhanced beating frequency (**Figure 20e**) observed for conductive cardiopatches. In the context of cardiac electrophysiology, the propagation of electrical impulses is mediated via connexin proteins such as Cxs43, which enable heterocellular electrical coupling between CMs and CFs[304, 305]. Moreover, previous studies have showed that Cxs43-mediated CF coupling *in vitro* could enable synchronous spontaneous contraction in isolated CMs located up to 300 μm apart[306]. In this regard, IFS (**Figure 20f and 20g**) showed that CFs growing on conductive scaffolds exhibited significantly higher levels of expression of Cxs43 when compared to GelMA-controls (**Figure 20h**). Moreover, positive fluorescence against this gap junction protein was mainly located to the borders between the proliferating layer of CFs

(**Figure 20g**). These observations suggested that the conductive properties of GelMA/Bio-IL scaffolds promoted the electromechanical coupling of isolated CMs through the upregulation of Cxs43 in CFs. Furthermore, the disruption of electrical communication between cardiac cells has been shown to contribute to the generation of arrhythmias in fibrotic hearts *in vivo* and hinder the contractile function of TE cardiac constructs[306]. Therefore, Bio-IL conjugation could be used to aid in the rapid propagation of electrical impulses across heterocellular TE scaffolds, and lead to enhanced tissue-level functionality both *in vitro* and *in vivo*.

3.2.8. *In vivo* evaluation of electrospun GelMA/Bio-IL cardiopatches using a murine model of MI via permanent LAD-ligation

A series of structural and functional abnormalities occur after the onset of MI, which compromise the contractile function of the heart and could potentially lead to free wall rupture and death[307]. Electrospun fibrous patches have shown great potential to be used as cardio-supportive devices to help minimize the formation of non-contractile scar tissue and thinning of the infarcted myocardium[308, 309]. However, the delivery of conductive scaffolds to the myocardium presents several risks that could potentially lead to impaired cardiac function or fatal arrhythmias[310]. Thus, in this study, we evaluated the feasibility, safety and *in vivo* functionality of GelMA/Bio-IL cardiopatches using a murine model of MI via permanent ligation of the left anterior descending (LAD) coronary artery (**Figure 21ai-iv**). All infarcts were confirmed via blanching of the myocardium distal to the site of ligation. Following the induction of MI, animals were divided into three treatment groups: sham, GelMA control, and GelMA/Bio-IL; and followed for a period of 3 weeks to allow for cardiac remodeling. We used scaffolds fabricated with 10% (w/v) GelMA and 33% (v/v) Bio-IL for the treatment group that received conductive cardiopatches. At the end of this period, the animals were sacrificed, and the hearts were excised and processed for histological evaluation using Masson's trichrome and IFS against the cardiac markers SAA and Cxs43. Our

results showed strong adhesion of both GelMA (**Figure 21b**) and GelMA/Bio-IL (**Figure 21c**) patches to the myocardial tissue after 3 weeks. In addition, tissue ingrowth inside the scaffolds was observed for both GelMA and GelMA/Bio-IL samples. In addition, the cardiopatches were intact on the surface of the myocardium 21 days post implantation. Further, it was found that the sham controls exhibited significant thinning of the myocardium with a large aneurysmal section on the LV (**Figure 21di**). The infarcted area exhibited a marked reduction in the expression of both SAA and Cxs43, which was indicative of extensive CM death and the appearance of non-contractile scar tissue (**Figure 21dii-iii**). In contrast, the animals receiving both the GelMA (**Figure 21ei**) and GelMA/Bio-IL (**Figure 19fi**) cardiopatches showed comparatively less ventricular wall thinning and no apparent aneurysm at the site of MI after 3 weeks. Furthermore, the expression of phenotypic cardiac markers was maintained throughout the site of MI, which was indicative of the preservation of a fully functional myocardium for both hearts treated with GelMA scaffolds (**Figure 21eii-iii**) and GelMA/Bio-IL cardiopatches (**Figure 21fii-iii**). These results suggested that both GelMA-based patches could establish a cell-supportive microenvironment that prevented the remodeling of the myocardium at the site of MI and preserve normal tissue architecture. Furthermore, the expression of characteristic phenotypic markers SAA and Cxs43 was indicative of the preservation of viable myocardium and the maintenance of normal cardiac function.

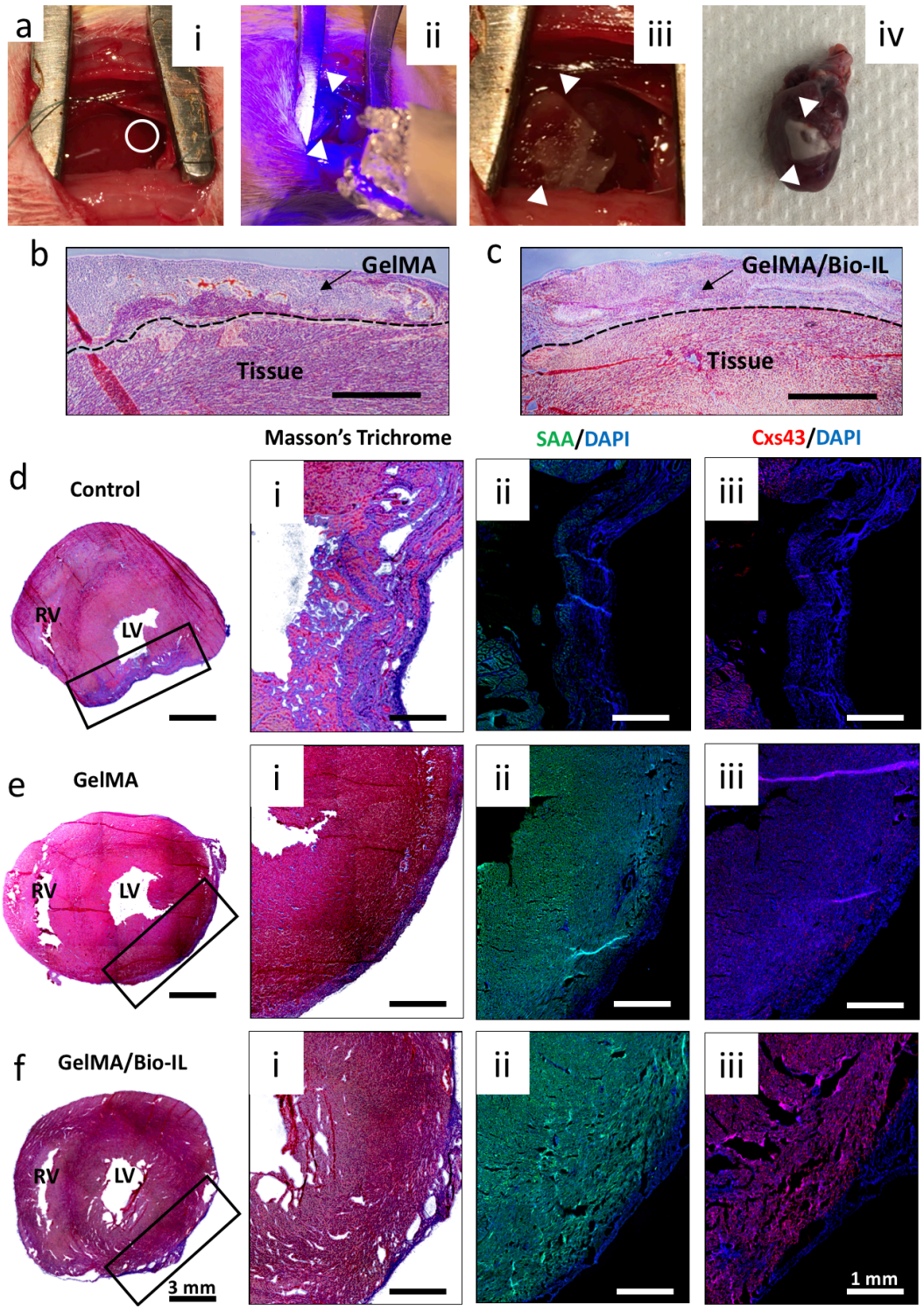

Figure 21. *In vivo* evaluation of GelMA/Bio-IL cardiopatches using a murine model of MI. Experimental MIs were induced via permanent ligation of the LAD coronary artery. **a)** Representative images showing: **a-i)** LAD ligation (white circle), **a-ii)** photocrosslinking of cardiopatches (white arrows) using UV light, **a-iii)** photocrosslinked cardiopatch on the heart, and **a-iv)** excised whole heart with cardiopatch distal to the site of LAD ligation after 21 days.

Representative Masson's trichrome stained images from the interface between **b)** GelMA and **c)** GelMA/Bio-IL cardiopatches after 21 days (Scale bar = 400 μm). Representative Masson's trichrome and fluorescent stained images of excised hearts showing the location of the MIs in **di-iii)** untreated animal (sham), and animals treated with **ei-iii)** pristine GelMA patches, and **fi-iii)** GelMA/Bio-IL cardiopatches.

Following MI, cardiac remodeling triggers a series of molecular and cellular changes that manifest clinically as changes in ventricular wall thickness and the appearance of fibrotic scar tissue[302]. In recent years, electrospun scaffolds have shown great potential to be used as cardio-supportive devices, which can help minimize the formation of non-contractile scar tissue and thinning of the ventricular wall following MI[309]. Here, we evaluated the feasibility and safety of *in vivo* delivery as well as the cardioprotective potential of GelMA/Bio-IL cardiopatches using a murine model of MI via permanent LAD ligation (**Figure 21ai-iv**). Histological evaluation revealed that the hearts treated with both GelMA and GelMA/Bio-IL patches exhibited minimal tissue remodeling and LV wall thinning, when compared to untreated animals (**Figure 21d-f)**. These observations suggested that the supportive function of both GelMA and GelMA/Bio-IL scaffolds could potentially ameliorate LV wall stress and preserve normal tissue architecture. These results were in accordance to previous studies showing that cardio-supportive devices with ECM-like properties can mediate endogenous repair mechanisms to improve heart function[311]. Moreover, these studies also showed that the attenuation of pathological cardiac remodeling occurred mainly due to architectural and compositional cues that potentiated tissue regeneration, independent of scaffold electroconductivity.

Our results suggested that GelMA/Bio-IL scaffolds yielded tissue constructs with comparatively better *in vitro* functionality, which could be due in part to enhanced electromechanical coupling via upregulation of the gap junction protein Cxs43. Moreover, *in vivo* evaluation showed that both conductive and non-conductive GelMA-based scaffolds led to the

preservation of normal tissue architecture by minimizing cardiac remodeling after MI. These observations could be explained in part due to the complex interplay of different bioactive cues that are normally present *in vivo*[312-315], which were not replicated in our experiments *in vitro*. Furthermore, these results demonstrated that cardiac remodeling could be effectively prevented using acellular scaffolds without the need for exogenous cytokines or growth factors, which is highly advantageous for the clinical translation of these scaffolds. For instance, Montgomery *et al.* recently reported a microfabricated injectable scaffold that could be used to deliver viable and functional CMs to the site of MI[316]. Although the scaffolds could be delivered through a minimally invasive procedure and significantly improved cardiac function following MI, both adult and stem cell-based strategies for the treatment of MI often shown highly heterogenous outcomes and poor clinical translation[317, 318]. Moreover, one of the most relevant characteristics of GelMA/Bio-IL cardiopatches was their high adhesive strength to the beating myocardium after photocrosslinking, even in the presence of blood (**Figure 21aiii-iv**). Recently, Lang *et al.* reported the development of blood-resistant and light-activated surgical glue that could be used to seal cardiac wall defects in large animal models[319]. Although this bioadhesive could be used by itself to form an on-demand hemostatic seal or in combination with a patch, GelMA/Bio-IL cardiopatches attached strongly to the native tissue without the need for additional adhesives or sutures. This also allowed the establishment of a tight interface and enhance the interlocking between GelMA and collagen fibers from the ECM-like fibrous patch and the myocardium, respectively, which is characteristic of strong tissue adhesives[320, 321]. In addition, cardiopatches photocrosslinked on the surface of rat hearts did not exhibit significant changes in size due to water uptake of the scaffolds (**Figure 21aiii-iv**). This demonstrates that swelling of our engineered cardiopatches would not significantly compress cardiac tissues *in vivo*.

In situ photocrosslinking of cardiopatches on the beating heart could possibly lead to systemic dissemination of unreacted components and thus, trigger toxic or inflammatory responses that could not be evaluated *in vitro*. Our preliminary *in vivo* experiments confirmed that our electroconductive patches could be safely administered on the myocardium via *in situ* photopolymerization and did not induce any cytotoxicity. In addition, the heart is a highly dynamic organ and the presence of blood and other fluids, as well as cardiac beating could greatly impair the adherence of the patches to the myocardium *in vivo*. Our *in vivo* results here demonstrated that the engineered patches exhibited high adhesion to the native murine myocardium without the need for suturing. Lastly, although the electroconductive and mechanical properties of the patches were tuned to mimic the native tissue, the delivery of a scaffold with these features to the myocardium could potentially impair cardiac function or even lead to fatal arrhythmias. Therefore, our current study aimed on evaluating the safety of *in vivo* delivery of Bio-IL functionalized patches before assessing the therapeutic effects of this strategy. Our future study will focus on evaluating heart function after applying the electroconductive patches using echocardiography, as well as studying the molecular and cellular mechanisms that could be selectively triggered by the delivery of an electroconductive scaffold to the site of MI.

3.3. Development of a highly elastic and hemostatic surgical sealant composed of GelMA, elastin-like polypeptide, and Laponite

Operations involving surgical repair, wound closure, and reconstruction of traumatized or degenerated soft tissues are common in the clinical setting. During these procedures, surgeons often rely on conventional suturing and stapling techniques to reconnect tissues that will result in low dehiscence[322, 323]. However, suturing is a very time-consuming process and may only be

used on easily accessible regions of the body[292]. Further, the repetition and quickly varying stress exerted on soft tissues during these procedures presents several drawbacks, which include high infection rate, extensive handling, risk of blood-borne disease transmission, damage to secondary tissues, and the possibility for air/fluid leakage[289, 324]. This preventable trauma can result in multiple hospital visits, high cost to the patient, slow wound recovery, and a wide range of medical complications. Therefore, researchers have investigated alternative approaches to reconnect soft tissue that may overcome the limitations associated with sutures and staples.

Currently, there are a number of commercially available sealants on the market, however, these products lack the complete efficacy desired for an implantable adhesive. For example, one of the most commonly investigated materials to develop surgical sealants have been using the naturally derived biomaterial fibrin. Fibrin glue is a material that mimics that last stage of the physiological coagulation cascade, and thus plays an active role in blood clot formation[325]. However, fibrin has also been shown to exhibit low mechanical strength and adhesion to wet tissues and, therefore, demonstrates poor performance as an adhesive material. Synthetic adhesives have also been investigated, such as cyanoacrylate. While cyanoacrylate adhesives have been shown to exhibit strong adhesion to tissue, there have been concerns regarding the biocompatibility and biodegradation of this material[325]. Recently, significant attention has been given to engineer highly elastic hydrogel-based adhesives that demonstrate ideal properties for use as a surgical sealant, such as, rapid photopolymerization *in situ*, a strong bond to wet tissue, appropriate swelling and mechanical strength, active role in blood clot formation, and biodegradation at an appropriate rate[326].

Hydrogels are a particularly attractive material class for the development of tissue adhesives owing to their high swellability and robust mechanical properties, which are similar to native soft tissue[327]. When attached to the surface of soft tissues, the elasticity of bioadhesives is an important factor, especially when used on tissues such as the lungs and blood vessels, where there is frequent expansion and contraction. Therefore, many strategies to improve the elastic properties of hydrogels have incorporated elastin-based proteins into the polymer matrices. Some of these elastin-based proteins include methacrylated tropoelastin, and elastin-like polypeptides, which are engineered with the repeating elastin pentapeptide motifs Val-Pro-Gly-Xaa-Gly, where the guest residue (Xaa) represents any amino acid except proline. In addition, hemostatic properties of surgical sealants are optimized using different strategies. One notable nanoparticle that has demonstrated excellent hemostatic performance is Laponite (LA). This highly charged nano clay promotes blood clot formation by dehydrating whole blood resulting in a higher concentration of clotting factors. Thus, in the final project of this thesis, we have engineered a nanocomposite hydrogel fabricated using GelMA to promote adhesiveness to wet tissue, and biocompatibility, ELP to improve mechanical properties and elasticity, and LA to impart hemostatic properties. These finely tuned properties resulted in a bioadhesive that is proposed to be used as a surgical sealant for soft tissue repair.

3.3.1. Synthesis of nanocomposite GelMA/ELP/LA hydrogels

Over the last decade, nanocomposite hydrogels have emerged as a new generation of biomaterials. These new materials combine biocompatible polymers with any of the various types of nanofillers, such as carbon-based nanoparticles (carbon nanotubes, graphene)[328], metal/metal-oxide nanoparticles (gold, silver, iron oxide)[329], and inorganic/ceramic nanoparticles (hydroxyapatite, silca, silicates, calcium phosphate)[330], to impart novel properties

onto the nanocomposite network. By combining nanofillers into polymeric networks, it is possible to engineer 3D scaffolds which exhibit unique properties. These nanocomposite hydrogels may be tailored to meet the needs required for various biomedical applications, such as tissue engineering, drug delivery, and biosensors.

One such nanofiller, Laponite (LA), is a synthetic nanoclay smectite with highly positively charged surfaces, and negatively charged ends (**Figure 22c**). LA is capable to form many different interactions with organic molecules and biopolymers, such as hydrogen bonding, cation linking, hydrophobic interactions, and anion interchange[331]. This unique characteristic, along with its demonstrated high biocompatibility, anisotropic and plate-like morphology, and great surface area make it a suitable material to improve hemostatic and physical properties to nanocomposite hydrogels[332]. Of particular interest is the ability for LA to significantly improve clotting time *in vivo*. These hemostatic properties are primarily due to the thin plate-like structure and anisotropic distribution of surface charge. As a result of their small size and high charge, LA rapidly absorbs water when exposed to whole blood, which leads to an increase in the concentration of cells and clotting factors that promote blood coagulation[333]. For these attributes, nanocomposite hydrogels containing LA shows excellent potential to be developed as a surgical sealant for soft tissues.

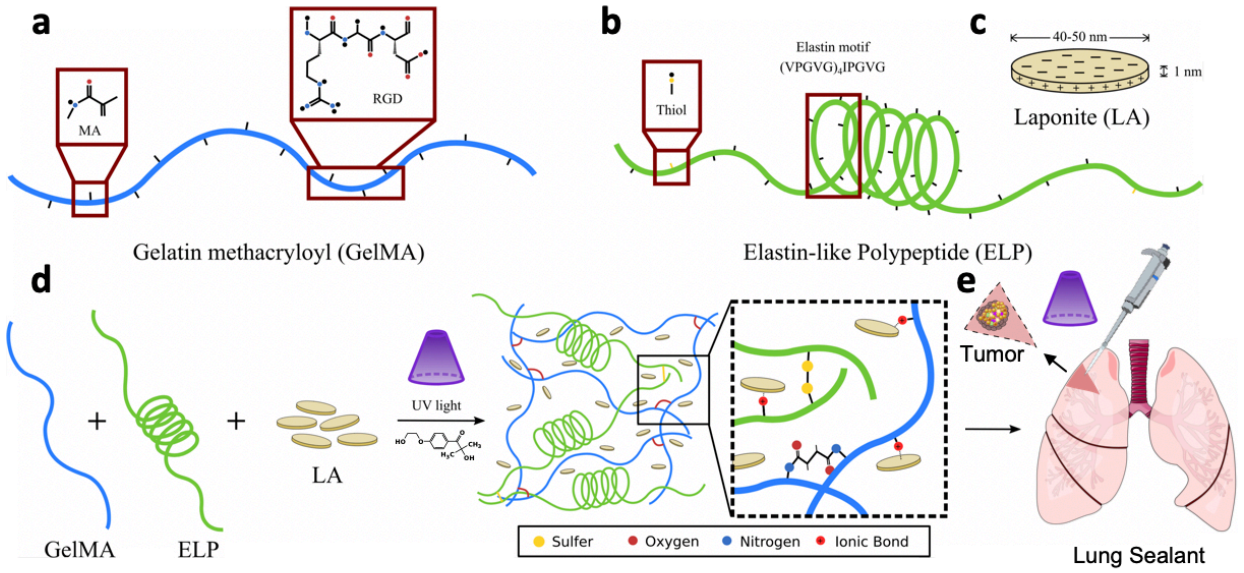

Figure 22. Synthesis and characterization of nanocomposite hydrogels. Gelatin methacryloyl (GelMA) (**a**), elastin-like polypeptide (ELP) (**b**), and Laponite (LA) (**c**) were utilized to engineer hemostatic hydrogels with high elasticity for application as a surgical sealant for lung tissue. (**d**) Schematic for the fabrication of these nanocomposite hydrogels by photocrosslinking prepolymer solutions in the presence of Irgacure 2959 and UV irradiation for 180 s. (**e**) The engineered hemostatic surgical sealants may be used to properly seal lung tissue following the removal of a section of tissue.

In contrast to hydrogels engineered with a single polymer network, composite hydrogels are a simple and efficient approach that may include multiple functionalities[74]. Thus, the blending of biopolymers to form composite hydrogels has been shown to more closely mimic the nature of the native physiological environment[334]. Various hydrogel-based biomaterials have been widely investigated for application as a surgical sealant, due to their ability to be used for 3D cell encapsulation, as well as their ease of modification, swellability, biodegradability, and biocompatibility[335]. Gelatin methacryloyl (GelMA) is a widely characterized biopolymer that has previously demonstrated appropriate cytocompatibility both *in vitro* and *in vivo*, and exhibits robust mechanical properties, and high cell adhesion due to the RGD motif (**Figure 22a**)[289]. In addition, elastin-like polypeptides (ELPs) consist of another family of widely characterized

biopolymers that are based on the recurrent hydrophobic domains observed in human tropoelastin, the soluble precursor to the ECM protein elastin (**Figure 22b**). Elastin is known for providing elasticity in tissues/organs where stretchability is of the main importance, such as lungs, blood vessels, ligaments, and skin[336]. Thus, ELPs have gained significant attention for applications in tissue engineering, such as soft-tissue repair, vascular grafts, cartilage regeneration, nerve guidance conduits, and more[231, 334, 337, 338]. This elastic motif of ELP consists of the repeating pentapeptide Val-Pro-Gly-Xaa-Gly, where the guest residue (Xaa) represents any amino acid except Pro[339]. Different types of ELPs have been investigated for applications as a surgical sealant for soft tissues owing to their tunable mechanical properties, high extensibility, and cytocompatibility.

Our ELPs possess a sequence that has been shown to contain robust mechanical properties with high stretchability and has demonstrated high biocompatibility. In addition, this protein sequence was designed with a cysteine residue at each end to allow for rapid photocrosslinking by incorporating the photoinitiator Irgacure 2959 and exposure to UV radiation. GelMA/ELP hydrogels were synthesized by combining different concentrations of GelMA (5-25% (w/v)), and ELP (0-20% (w/v)) with a 0.5% (w/v) solution of Irgacure 2959 (**Figure 22d**). Exposure to 180 s of UV radiation immediately led to rapid photocrosslinking and the formation of a 3D hydrogel network. GelMA/ELP/LA nanocomposite hydrogels were subsequently formed using 10% GelMA and 10% ELP (w/v) and varying concentrations of LA. These nanocomposite hydrogels were synthesized by combining 20% GelMA and 20% ELP in a solution containing 1% Irgacure 2959. A separate solution was prepared by mixing varying concentrations of LA (0, 1, 2, 4% (w/v)) in a 4 °C solution of deionized water. The solution was vortexed for 20 m to ensure homogeneous dispersion (**Figure 22d**). The GelMA/ELP and LA solutions were thoroughly mixed at 4 °C at a

1:1 ratio. Nanocomposite hydrogels were then formed upon exposure to 180 s UV radiation resulting in 3D hydrogel networks. These highly hemostatic and mechanically robust nanocomposite hydrogels were designed to be used as a surgical sealant. These hemostatic biomaterials show potential to be readily photocrosslinked *in situ* following the removal of a section of tissue to promote hemostasis and aid in the repair and regrowth of new tissues (**Figure 22e**).

3.3.2. Mechanical properties of nanocomposite GelMA/ELP/LA hydrogels

Cells perceive their microenvironment through physical, chemical, and mechanical cues of the ECM matrix and respond appropriately through mechanotransduction pathways that mediate tissue homeostasis, morphogenesis, cell growth, contractility, and differentiation[340, 341]. With new insights into the influence of mechanical properties on cell behavior, we aimed to characterize the mechanical properties of the engineered hydrogels synthesized with varying concentrations of GelMA, ELP, and LA. Therefore, the mechanical properties of GelMA/ELP hydrogels and GelMA/ELP/LA nanocomposite hydrogels were evaluated by performing tensile and compression tests. Tensile tests on GelMA/ELP hydrogels demonstrated that the elastic modulus and ultimate strain of the engineered hydrogels could be tuned by varying the concentrations of GelMA and ELP (**Figure 23a**). GelMA/ELP hydrogels were fabricated with between 0-25% (w/v) GelMA and 5-20% (w/v) ELP. Our results showed that the elastic modulus of the GelMA/ELP hydrogels increased with an increasing concentration of GelMA and/or ELP. For example, hydrogels containing a fixed concentration of 10% (w/v) ELP exhibited an elastic modulus of 7.3 ± 0.08 kPa, 33.9 ± 2.14 kPa, 80.6 ± 13.80 kPa, 270.2 ± 5.57 kPa, and 503.7 ± 20.36 kPa when fabricated with a GelMA concentration of 5, 7.5, 10, 20, and 25% (w/v), respectively (**Figure 23a**). Further, when hydrogels were fabricated containing a fixed concentration of 10% (w/v) GelMA, they exhibited

an elastic modulus of 25.9 ± 4.00 kPa, 27.1 ± 4.55 kPa, 80.6 ± 13.80 kPa, and 112.5 ± 3.43 kPa when fabricated with an ELP concentration of 0, 5, 10, and 20% (w/v), respectively (**Figure 23a**). The mechanical properties of hydrogels fabricated for tissue engineering applications may be manipulated by controlling the type of crosslinking used, the crosslinking density, or polymer concentration. Increasing polymer molecular weight has also shown to increase mechanical strength[342]. In addition, crosslinking density can be achieved via crosslinking molecule concentration and reaction time. Here, we are able to tune the mechanical properties of GelMA/ELP hydrogels by varying the concentration of GelMA and ELP used during synthesis. Through varying the polymer concentration of GelMA and ELP, we are able to control polymer density and crosslinking density within the polymer matrix. The increase in elastic modulus of GelMA/ELP hydrogels is expected to result due to an increase in the number of crosslinking sites in the 3D polymetric network. Our results showed that the tunability of our hydrogels was primarily achieved through adjusting the concentration of GelMA polymer in the hydrogel matrix. This is in contrast to varying the concentration of ELP, which our results showed has a less significant impact on tuning the stiffness of the resulting gels. This may be due in part to the many crosslinking sites present in the molecular structure of GelMA. By increasing the concentration of GelMA, we increase the number of functional groups responsible for rapid photocrosslinking in the presence of UV radiation necessary to hold the polymer matrix together. ELP, however, was engineered to possess only two crosslinking sites, which limits its impact on the elastic modulus. This is consistent with previous studies using the same genetically engineered form of ELP, which showed that hydrogels fabricated only with ELP demonstrated significantly lower elastic moduli than compared with our GelMA/ELP hydrogels[231]. The relationship between crosslinking density and mechanical properties for hydrogels fabricated for tissue engineering applications has

also been reported. These studies show that an increase in polymer crosslinking tends to result in improved mechanical strength[343, 344]. This is important because the crosslinking density of hydrogels plays a critical role in the physical properties of the scaffold, such as mechanical stiffness and pore size[345]. These physical properties, in turn, greatly impact cell adhesion, metabolism, migration, and proliferation[346, 347].

The mechanical properties of nanocomposite GelMA/ELP/LA hydrogels were also examined for mechanical stiffness. Nanocomposite hydrogels were fabricated with 10% GelMA and 10% ELP with varying concentrations of LA up to 2% (w/v). Our results showed that the incorporation of LA into the nanocomposite hydrogels did not significantly change the mechanical stiffness when added up to 2% (w/v). The engineered hydrogels exhibited an elastic modulus of 79.3 ± 11.41 kPa, 91.1 ± 11.61 kPa, 116.2 ± 15.15 kPa, and 119.27 ± 26.24 kPa when fabricated with a LA concentration of 0, 0.5, 1, and 2% (w/v), respectively (**Figure 23b**). This is consistent with other investigations which showed that hydrogels fabricated with high concentrations (>5% (w/v)) of LA exhibited markedly higher mechanical stiffness due to electrostatic interaction, however, no significant changes in mechanical properties was observed for hydrogels fabricated with lower concentrations (<2.5% (w/v) of LA[332, 348, 349]. The elastic modulus exhibited by our hydrogels fabricated with 10% (w/v) GelMA, 10% (w/v) ELP, and 2% (w/v) LA was similar to that of recently reported hydrogel scaffolds for surgical sealing of soft tissue applications[350-352].

Mechanical characterization of GelMA/ELP hydrogels demonstrated significantly higher extensibility when fabricated with higher concentrations of ELP with a maximum strain reaching 150%. For example, hydrogels containing a fixed 10% (w/v) GelMA concentration exhibited ultimate strain values of 31.5 ± 0.95, 44.0 ± 2.50, 59.9 ± 8.11, and 72.6 ± 5.85%, when fabricated

with 0, 5, 10, and 20% (w/v) ELP, respectively (**Figure 23c**). By incorporating higher concentrations of ELP in the polymer matrix, the resulting hydrogels were concomitantly imparted with elasticity. There have been a number of theories to explain the mechanism behind the elasticity of the elastin protein. One theory states that as the polymer is extended, the hydrophobic groups in the chain are exposed on the outside. This extension of the protein increases the overall energy of the system and enthalpic forces serve as the driving force to recoil elastin. Other theories which attempt to explain the mechanism of elasticity in elastin focus on the relationship between the hydrophobic and hydrophilic groups[353]. In contrast, GelMA/ELP hydrogels fabricated with higher GelMA concentrations resulted lower extensibility up to the failure point of hydrogels, as expected due to the increase in crosslinking sites. Our results showed that hydrogels containing a fixed 10% (w/v) ELP concentration exhibited ultimate strain values of 105.2 ± 11.27, 75.2 ± 8.16, 59.9 ± 8.11, 24.9 ± 2.30, and 23.5 ± 0.74% when fabricated with 5, 7.5, 10, 20, and 25% (w/v) GelMA, respectively (**Figure 23c**). We then evaluated the maximum mechanical strain observed for nanocomposite hydrogels containing 10% GelMA and 10% ELP and varying concentrations of LA. The extensibility of these GelMA/ELP hydrogels was found to be 59.9 ± 8.1, 57.3 ± 11.3, 56.1 ± 9.4, and 53.8 ± 9.6 kPa when fabricated with a LA concentration of 0, 0.5, 1, and 2% (w/v), respectively. Our results showed that the addition of LA did not exhibit significantly different extensibility when fabricated with varying concentrations of LA, up to 2% (w/v) (**Figure 23d**). In addition, the ultimate strain of these GelMA/ELP/LA nanocomposite hydrogels was found to be similar to recently reported hydrogel sealants for reconnection of soft tissue[290, 354].

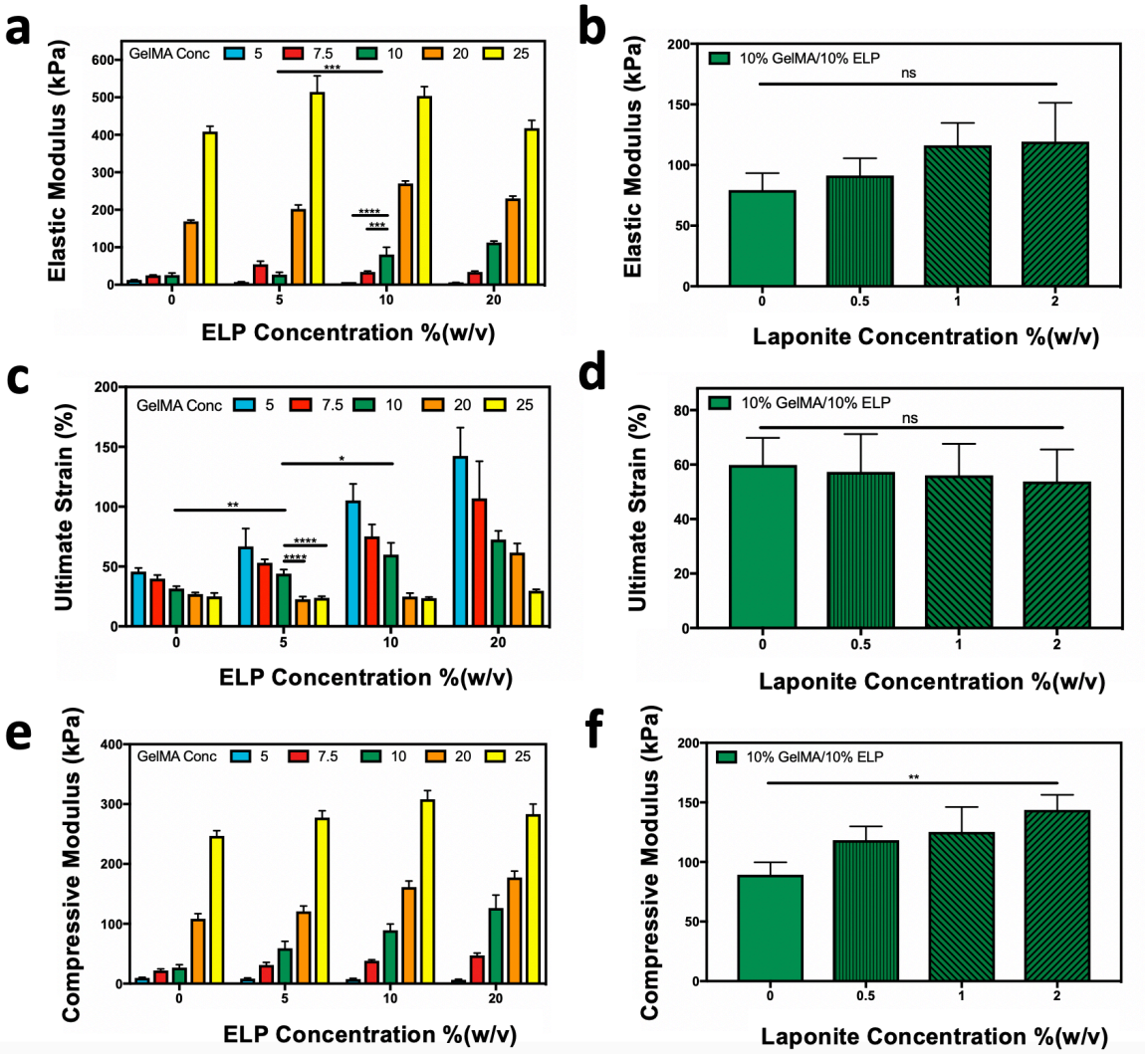

Figure 23. Mechanical characterization of hemostatic and highly elastic hydrogels for applications as surgical sealants for soft tissues. Elastic moduli for hydrogels containing (**a**) varying concentrations of GelMA and ELP, as well as for (**b**) hemostatic hydrogels containing 10% GelMA, 10% ELP, and varying concentrations of LA. Ultimate strain for hydrogels containing (**c**) varying concentrations of GelMA and ELP, as well as for (**d**) hemostatic hydrogels containing 10% GelMA, 10% ELP, and varying concentrations of LA. Compressive moduli for hydrogels containing (**e**) varying concentrations of GelMA and ELP, as well as for (**f**) hemostatic hydrogels containing varying concentrations of LA. Error bars indicate standard error of the means, asterisks mark significance levels of $p < 0.05$ (*), $p < 0.01$ (**), $p < 0.001$ (***), and $p < 0.0001$ (****).

We also evaluated the compressive modulus of GelMA/ELP hydrogels, which was shown to be tunable based on the concentration of the biopolymers. Our results show that the compressive

moduli of the engineered hydrogels increased concomitantly by increasing either GelMA or ELP. For example, hydrogels synthesized with a fixed 10% (w/v) ELP concentration exhibited compressive moduli of 7.6 ± 1.11, 38.4 ± 1.27, 89.3 ± 8.48, 161.5 ± 8.27, and 308.2 ± 11.91 kPa when fabricated with 5, 7.5, 10, 20, 25% (w/v) GelMA, respectively (**Figure 23e**). Further, hydrogels synthesized with a fixed 10% (w/v) GelMA concentration exhibited compressive moduli of 26.7 ± 3.95, 59.2 ± 9.48, 89.3 ± 8.48, and 126.5 ± 17.67 kPa when fabricated with 0, 5, 10, and 20% (w/v) ELP, respectively (**Figure 23e**). These results demonstrate that the addition of either polymer into the gel matrix resulted in higher stiffness when compressed.

In addition, GelMA/ELP hydrogels fabricated with 2% (w/v) LA demonstrated significantly higher compressive moduli compared to hydrogels containing the same concentration of biopolymers, but without LA. Our results show that nanocomposite GelMA/ELP/LA hydrogels exhibited compressive moduli of 89.3 ± 8.48, 118.4 ± 9.38, 125.3 ± 17.01, and 143.7 ± 10.32 kPa when fabricated with 0, 0.5, 1, and 2% (w/v) LA, respectively (**Figure 23f**). This increase in mechanical strength may be a direct result of the additional biopolymer-nanoparticle interactions that exist within the polymer matrix. Silicate nanoparticles have been shown to strengthen nanocomposite hydrogel suggesting that these nanoparticles can act as a pseudo crosslinker to mechanically reinforce the polymer network[355]. This strengthening of hydrogels due to the addition of silicate nanoparticles may be explained by an increase in hydrogen bonding, Van der Waals interactions, and ionic coupling[356, 357]. However, it has also been reported that silicate nanoparticles at high concentrations (~5%) can have adverse effects on the mechanical toughness of hydrogels. Recent studies have shown that the addition of 5% (w/v) silicate nanoparticles into nanocomposite hydrogels led to a decrease in elastic and compressive modulus. This may be due to large aggregates of nanoparticles interfering with photocrosslinking and thus leading to less

covalent crosslinks in the polymer network[358-360]. Taken together, these results show that our GelMA/ELP/LA nanocomposite hydrogels demonstrate robust mechanical properties ideal for tissue engineering applications involving reconnecting soft tissue.

3.3.3. *In vitro* swelling behavior and degradation rates of nanocomposite GelMA/ELP/LA hydrogels

Hydrogels are composed mainly of water due to their high hydrophilic properties, however, excessive water uptake could potentially compromise the mechanical properties of the engineered scaffolds. Furthermore, unusually high swelling rates of implanted scaffolds could cause significant morphological changes and risks compression of nerves and other tissues. Hence, we aimed to evaluate the water uptake capacity of GelMA/ELP hydrogels and GelMA/ELP/LA nanocomposite hydrogels. Previously, the swelling behavior for hydrophilic GelMA hydrogels has been widely characterized to show high water uptake capacity. Generally, higher concentrations of GelMA results in a lower swelling ratio and smaller pore size[361]. Here, we evaluated the swelling of GelMA/ELP hydrogels with a fixed GelMA concentration of 10% (w/v) and varying ELP concentrations to determine the effect ELP on swelling properties. Our results showed that all groups swelled rapidly after 8 h of incubation, with no significant increases in water uptake after 8 h up to 24 h for all samples tested (**Figure 24a**). Further, hydrogels with a higher ELP concentration underwent significantly lower swelling when compared to scaffolds fabricated with lower ELP concentrations. This is likely due to the highly hydrophobic repeating motifs ($[[VPGVG]_4IPGVG]_{14}$) present in the chemical structure of ELP[362]. In addition to the hydrophobic interactions, the increase in ELP may lead to an increase in crosslinking density, which would also contribute to decreased swelling ratios[231]. In addition, we also characterized the swelling behavior of nanocomposite hydrogels fabricated with 10% GelMA, 10% ELP, and varying concentrations of LA. Our results showed that nanocomposites fabricated with a higher

concentration of LA exhibited significantly lower water uptake compared to hydrogels synthesized with only GelMA and ELP (**Figure 24b**). This decrease in water uptake due to the incorporation of LA may be explained by interactions such as hydrogen bonding, and electrostatic interactions that served to reinforce the polymeric network[363]. Thus, the polymer network is held together tighter preventing fluid from entering the matrix. Taken together, these hydrophilic GelMA/ELP/LA nanocomposite hydrogels demonstrate ideal swelling behavior for use as a surgical adhesive.

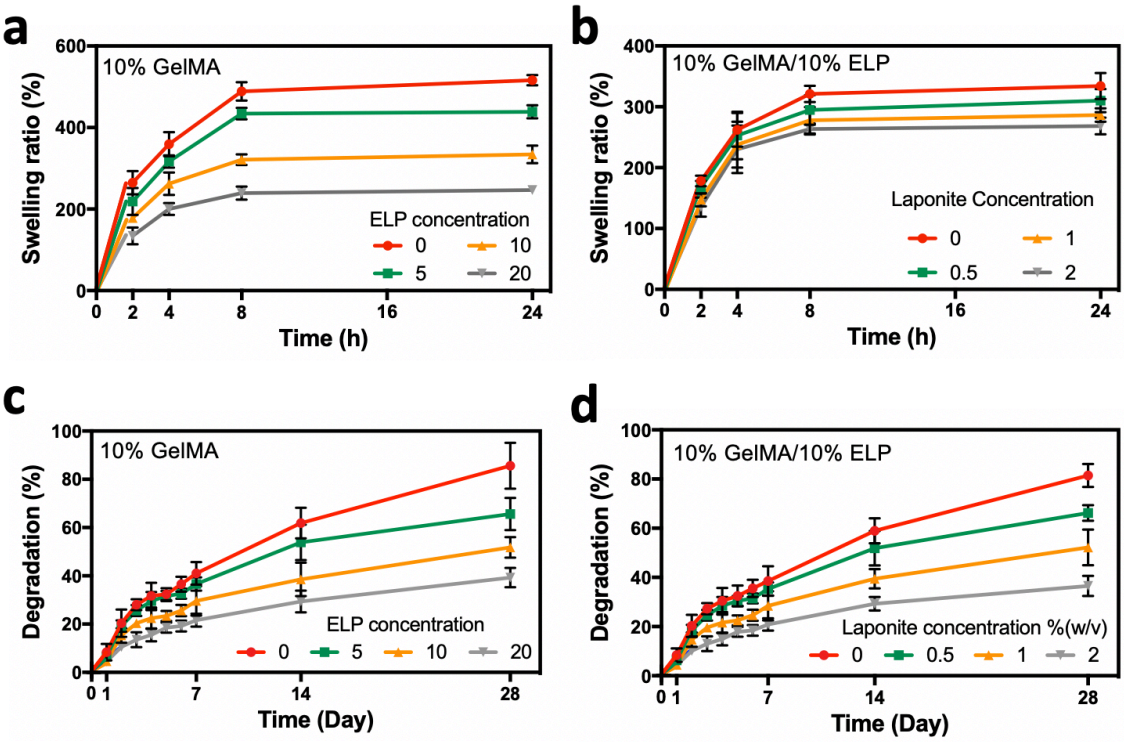

Figure 24. *In vitro* swelling behavior and degradation rates of hemostatic and highly elastic hydrogels for applications as lung tissue sealants. Swelling ratios of highly elastic hydrogels containing (**a**) 10% GelMA and varying concentrations of ELP, as well as (**b**) 10% GelMA/10% ELP and varying concentrations of LA. Results showed that the addition of ELP into the hydrogels led to less water uptake due to the presence of hydrophobic elastin motifs. Degradation rates of elastic hydrogels containing (**c**) 10% GelMA and varying concentrations of ELP, as well as (**d**) nanocomposite hydrogels containing 10% GelMA/10% ELP and varying concentrations of LA. Our results show that the addition of ELP significantly slowed down the degradation of the engineered hydrogels after 28 d.

Following the reconnecting or sealing of tissues using nanocomposite hydrogel in the clinical setting, the polymeric network should biodegrade into non-toxic byproducts, as it is no longer needed, to allow for the regrowth of new autologous tissue[364]. Thus, we aimed to characterize the *in vitro* degradation profile of these nanocomposite GelMA/ELP/LA hydrogels. Briefly, hydrogels were lyophilized, weighed, and incubated in DPBS at 37 °C for up to 28 d. At the end of given timepoints, the samples were rinsed, lyophilized, and re-weighed to determine the changes in dry mass after degradation. GelMA/ELP hydrogels were fabricated with a 10% (w/v) GelMA concentration and varying concentration of ELP. Our results demonstrated that *in vitro* degradation rates of the engineered hydrogels were significantly slower when fabricated with higher concentrations of ELP. For example, at day 28, scaffolds were 85.6 ± 7.75, 65.7 ± 5.48, 51.8 ± 3.50, and 39.3 ± 3.30% degraded when hydrogels were fabricated with an ELP concentration of 0, 5, 10, and 20% (w/v) respectively (**Figure 24c**). These biopolymer-based hydrogels are expected to degrade hydrolytically - a process where water cleaves the bonds of functional groups[365]. Degradation via hydrolysis occurs relatively faster in highly hydrophilic proteins. By increasing the concentration of ELP, we postulate that the combination of hydrophobic groups along with higher concentrations of polymer in the hydrogel matrix resulted in the hinderance of enzymatic solution into the scaffold. This would explain the slower degradation rates of GelMA/ELP hydrogels compared to pure GelMA hydrogels.

The enzymatic degradation profile of nanocomposite GelMA/ELP/LA hydrogels was then investigated by incubating samples in a 5.0 U/mL collagenase in DPBS at 37 °C. For *in vitro* enzymatic degradation, we chose to use collagenase for its known ability to degrade biopolymers *in vivo*[366]. Our results showed that *in vitro* hydrolytic degradation rates further decreased with an increasing LA concentration (**Figure 24d**). This decrease in degradation rates could be

attributed to stronger cohesion forces in the polymeric network as LA acts as an additional crosslinker forming hydrogen bonding and ionic interactions between biopolymers[367]. This increase in crosslinking sites may further prevent hydrolyzing medium from being absorbed by the scaffold. In addition, previous studies investigating nanocomposite hydrogels using silicate nanoparticles have reported similar degradation profiles for hydrogels with an increasing clay concentration[363, 368]. The decreased in degradation rate may further ensure that there is adequate time for tissue regeneration to occur as scaffold byproducts are removed. Taken together, these results suggest that GelMA/ELP/LA nanocomposite hydrogels are capable of controlled degradation and removal from the physiological environment following implantation.

3.3.4. *In vitro* adhesive properties of nanocomposite GelMA/ELP/LA hydrogels

There is a growing need for new concepts in surgical closure and treatment of tissue defects. Currently, wound closure is primarily achieved using sutures and staples, however, several drawbacks of these techniques, such as high infection rate, risk of blood-borne disease transmission, leakage of bodily fluid or air, and secondary tissue damage remains a challenge in the clinical setting[369, 370]. For these reasons, significant attention has been given toward the development of injectable protein-based adhesives and sealants that may replace the need for classical suturing techniques. Therefore, we used ASTM standard *in vitro* tests, including adhesion strength, shear strength, and wound closure to evaluate the adhesive properties of the nanocomposite GelMA/ELP/LA hydrogels.

The adhesive strength of GelMA/ELP hydrogels was also evaluated using a standard ASTM F2458-05 wound closure test. Briefly, a small section of porcine skin was glued to two glass slides at each end. The porcine skin was then severed in the center and glued together using adhesive GelMA/ELP hydrogels (**Figure 25a**). The adhesive strength of the engineered hydrogels

was then determined by carefully placing the glass slides into an Instron mechanical tester used for tensile loading. Our results demonstrated tunable and robust adhesive properties to wet tissue. Further, it was demonstrated that the adhesive strength increased concomitantly with an increasing concentration of GelMA. For example, when the engineered hydrogels were fabricated with a fixed 10% (w/v) ELP concentration, the adhesion strength of the engineered hydrogels exhibited adhesive strength of 9.1 ± 1.23, 12.3 ± 4.32, 27.2 ± 5.18, 42.8 ± 3.98, and 46.9 ± 3.29 kPa with a GelMA concentration of 5, 7.5, 10, 20, and 25% (w/v), respectively (**Figure 25b**). This is likely due to the many crosslinking sites present in the biopolymer which was able to form covalent bonds to the functional groups of soft tissue. In contrast, the addition of ELP did not elicit a significant change of the adhesive properties of the engineered hydrogels. Further, the adhesive strength of nanocomposite hydrogels fabricated with 10% GelMA, 10% ELP, and varying concentrations of LA was evaluated. Our results showed that there was no significant change in adhesive strength with the addition of LA up to 2% (w/v) (**Figure 25c**).

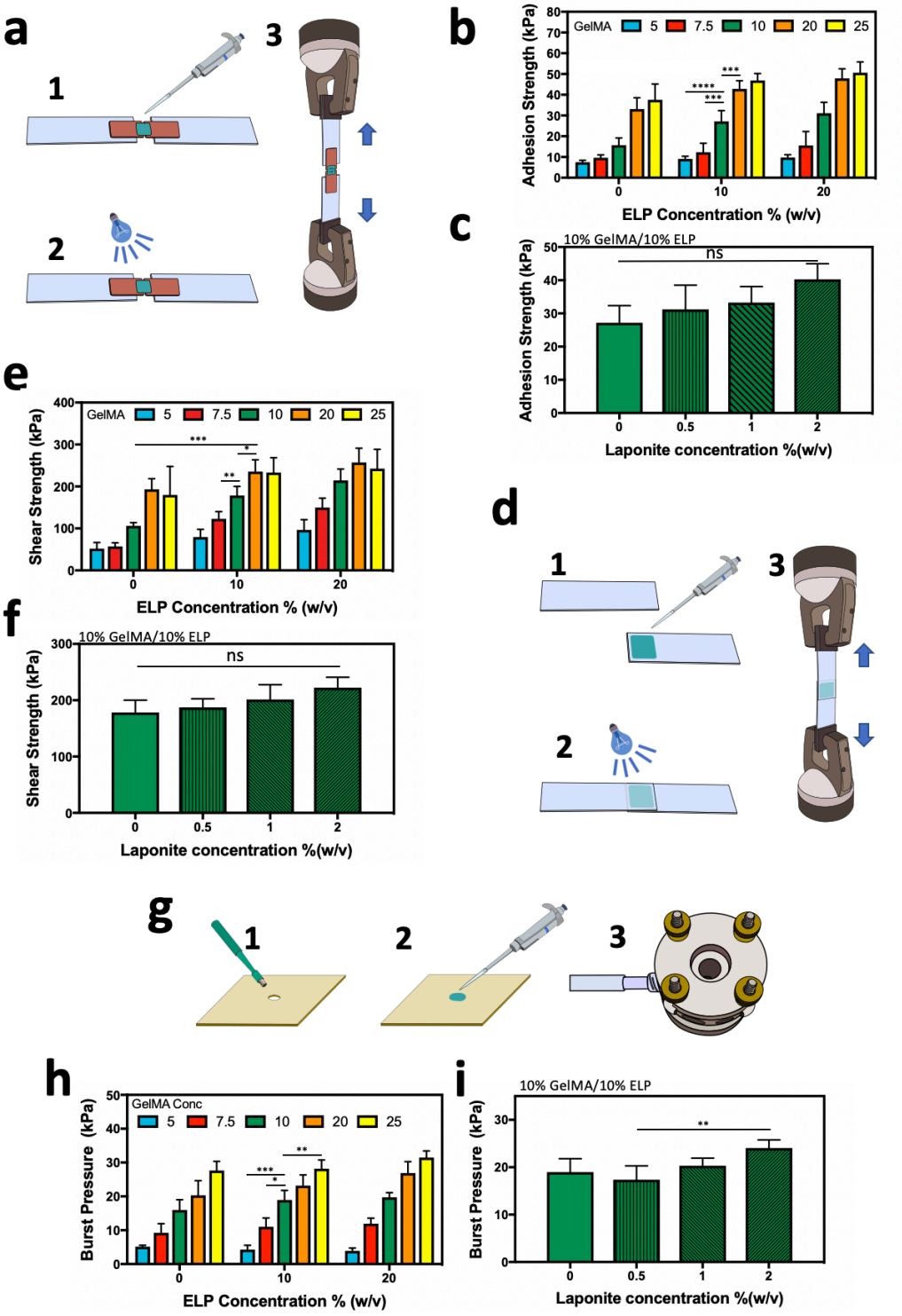

Figure 25. ***In vitro*** **sealing properties of hemostatic hydrogel for application as a lung tissue sealant.** (**a**) Schematic for the modified standard test method to determine adhesion strength (ASTM F2458-05) of GelMA/ELP/LA nanocomposite hydrogels. Adhesion strength for (**b**) elastic hydrogels containing varying concentrations of both GelMA and ELP, as well as for (**c**) nanocomposite hydrogels containing 10% GelMA/10% ELP and varying concentrations of LA.

(**d**) Schematic of a standard lap shear test (ASTM F2255-05) to determine the shear strength of GelMA/ELP/LA nanocomposite hydrogels. Shear stress of (**e**) elastic hydrogels containing varying concentrations of GelMA and ELP, as well as (**f**) nanocomposite hydrogels containing 10% GelMA/10% ELP and varying concentrations of LA. (**g**) Schematic for the standard burst pressure test (ASTM F2392-04) to determine the burst pressure for GelMA/ELP/LA hydrogels. (**h**) Burst pressure for elastic hydrogels containing varying concentrations of both GelMA and ELP using collagen sheets as a substrate. (**i**) Burst pressure for nanocomposite hydrogels fabricated with 10% GelMA/10% ELP and varying concentrations of LA. Error bars indicate standard error of the means, asterisks mark significance levels of $p < 0.05$ (*), and $p < 0.01$ (**).

The shear strength of the GelMA/ELP hydrogels was also measured using the ASTM F2255-05 method where two gelatin-coated glass slides are attached together using the engineered hydrogels as an adhesive. The two glass slides are placed into an Instron and evaluated under tensile loading (**Figure 25d**). Our results showed that shear strength increased concomitantly with an increase in both GelMA and ELP concentrations. When the GelMA concentration was fixed at 10% (w/v) the lap shear strength of the GelMA/ELP hydrogels increased from 106.0 ± 7.94, to 178.4 ± 21.73 and 214.4 ± 27.27 kPa with increasing ELP concentrations of 0, 10, and 20% (w/v), respectively (**Figure 25e**). Further, when the ELP concentration was fixed at 10% (w/v), shear strength increased concomitantly with an increasing concentration of GelMA up to 20% (w/v). Additionally, the shear strength of nanocomposite GelMA/ELP/LA hydrogels was measured using 10% GelMA, 10% ELP and a varying concentration of LA. The incorporation of LA up to 2% (w/v) into nanocomposite hydrogels did not result in significantly different shear strength (**Figure 25f**). These results are consistent with other groups who have recently investigated the effect of silica nanoparticles on the adhesive properties to wet tissues[371, 372]. Further, LA has previously demonstrated poor adhesion to wet tissues when incorporated in synthetic polymer-based hydrogels[373]. Alternative strategies to develop nanocomposite hydrogels with strong adhesive strength to wet tissues include the combination of LA with dopamine, a catecholic moiety that has

shown to have strong intermolecular crosslinking ability[374-376]. Further, an understanding at the molecular level is required to improve LA-polymer interactions that vary widely depending on the polymer structure, molecular weight, temperature, and hydrophilicity, as well as the size and dispersion of the silica nanoparticles.

Lastly, we evaluated *in vitro* adhesive properties using a standard ASTM F2392-04 burst pressure test. Briefly, a small circular defect was created in the center of moist collagen sheets, and the defect was covered with adhesive hydrogel prepolymer followed by photocrosslinking via exposure to UV radiation. The collagen sheets were then placed in a burst pressure testing chamber that slowly increased air pressure until failure of the hydrogel was observed (**Figure 25g**). Here, our results showed that the burst pressure of GelMA/ELP hydrogels increased concomitantly with an increasing concentration of GelMA. For example, when ELP concentrations were fixed at 10% (w/v), the engineered hydrogels exhibited a burst pressure of 4.3 ± 1.29, 11.0 ± 2.59, 19.0 ± 2.82, 23.2 ± 3.18, and 28.2 ± 2.57 kPa with a GelMA concentration of 0, 5, 7.5, 10, 20, and 25% (w/v), respectively (**Figure 25h**). This is likely due to the formation of covalent bonds between methacrylate groups of GelMA and -NH_2 functional groups present in the collagen sheets[294]. Further, evaluation of nanocomposite GelMA/ELP/LA hydrogels synthesized with 10% GelMA, 10% ELP, and a varying concentration of LA showed an increase in burst pressure strength when LA was increased up to 2% (w/v) (**Figure 25i**). The addition of LA into the nanocomposite hydrogels demonstrated that there was improved cohesive and adhesive strength, which may be attributed to its strong binding affinity to various nucleophiles in the hydrogel network.

These results together demonstrate the tunable adhesive properties of GelMA/ELP/LA nanocomposite hydrogels to various biological substrates. Further, these engineered nanocomposite hydrogels exhibited significantly superior adhesive properties than what has

recently been reported for several commercially available sealants, including Evicel™, Coseal™, and fibrin glue[288, 292, 377]. Our results demonstrated competitive results with biomaterial-based hydrogel networks, such as those composed of methacrylated tropoelastin and GelMA[288], and enhanced with mussel-inspired catechol groups[368, 378, 379]. We propose that the strong adhesive properties of the nanocomposite hydrogels to wet tissues can be attributed to the covalent bonding of GelMA with the amine functional groups of wet tissue substrates created during photocrosslinking[380], hydrogel-tissue interlocking[381], and hydrogen bonding at the GelMA and biological interface[382]. These results strongly suggest that nanocomposite GelMA/ELP/LA hydrogels may be used as a surgical gel for the reconnection of tissues during surgery without the need for additional suturing or stapling.

3.3.5. *In vitro* evaluation of LA on the clotting of whole blood

The formation of blood clots or hemostasis is of critical importance to prevent major blood loss in the clinical setting to prevent hemorrhagic shock or death related to excessive blood loss. Although there is currently a wide variety of commercially available hemostatic products on the market, such as SurgiSeal, TISSEEL, and CoSeal, there have been concerns related to biocompatibility, hemostatic efficiency, and high cost[383]. Therefore, several approaches have been investigated to develop a biomaterial-based hemostatic surgical sealant that may be easy to apply, prevent infection, control bleeding, and is cost effective. Hydrogels composed of nanoparticles, including silica, TiO_2 nanotubes, and carbon nanotubes, have gained significant attention due to their hemostatic properties. Further, silicate nanoparticles in particular have been reported to demonstrate excellent biocompatibility and degrade into no toxic byproducts[384, 385]. Nanocomposite hydrogels fabricated with LA initiate hemostasis when in contact with whole blood by absorbing water thus increasing the concentration of clotting factors[333]. This is in

contrast to other systems that take advantage of mechanical sealing to promote hemostasis. Recently, silicate nanoparticles have demonstrated improvements in hemostatic performance when incorporated in nanocomposite hydrogels. Thus, we aimed to evaluate the hemostatic properties of our engineered nanocomposite GelMA/ELP/LA hydrogels as a function of time. Briefly, hydrogels fabricated with 10% GelMA, 10% ELP, and varying concentration of LA were

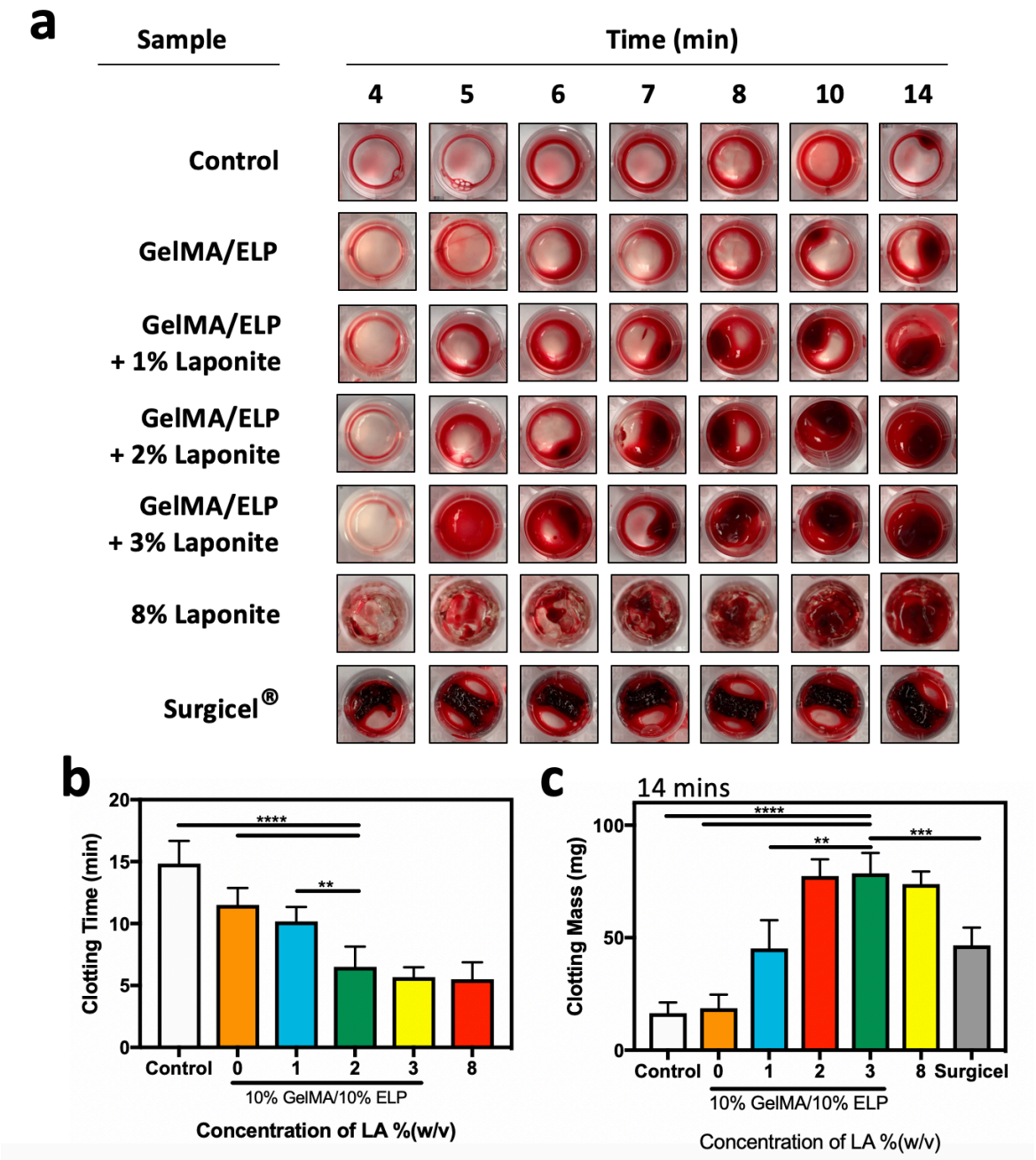

Figure 26. *In vitro* evaluation of LA on the clotting of whole blood. (**a**) Clot formation as a function of time and composition of hemostatic lung tissue sealants. (**b**) Quantitative clot time for whole blood added to nanocomposite hydrogels. (**c**) Quantitative clot mass measured at 14 mins following the addition of whole blood to hydrogels fabricated with 10% GelMA/10% ELP and varying concentrations of LA. Error bars indicate standard error of the means, asterisks mark significance levels of $p < 0.01$ (**), $p < 0.001$ (***), and $p < 0.0001$ (****).

photocrosslinked at the bottom of a 48 well plate. Fresh whole blood from a human source was then added to the surface of the hydrogels. At selected time points, saline was added to well to halt blood clotting. Resulting blood clots were then dried and weighed to determine the hemostatic efficacy of the nanocomposite hydrogels. The representative images of wells at selected time points show that hemostasis was achieved at a significantly faster rate when whole blood was applied to hydrogels containing higher concentrations of LA (**Figure 26a**). For example, a visible clot was observed at 11.5 ± 1.25, 10.2 ± 1.07, and 6.5 ± 1.50 min when whole blood was added to the surface of hydrogels containing a LA concentration of 0, 1, and 2% (w/v), respectively (**Figure 26b**). Additionally, it was shown that at a time point of 14 min, blood clots formed on the surface of nanocomposite hydrogels containing a higher concentration of LA exhibited a significantly higher weight (**Figure 26c**). These results suggest the addition of negatively charged LA played a critical role in denaturing fibrinogen and activating clot formation. The blood thrombogenic chemical cascade is a complex process resulting in clot formation[332]. Studies have shown that when negatively charged nanoparticles come in contact with whole blood, the intrinsic pathway of thrombogenesis is initiated, which triggers the formation of clotting factors, such as FXII, as well as thrombin[386]. Thrombin then converts plasma fibrinogen into fibrin monomers, which are able to polymerize into a fibrous mesh that results in a clot[387]. Therefore, the addition of LA into nanocomposite hydrogels may significantly decrease blood clotting times when exposed to whole

blood by initiating the formation of blood clotting factors. In addition, it has been shown that hydrophilic polymers coupled with charged nanoparticles show strong fluid uptake and thus may rapidly absorb the water when in contact with blood, resulting in the increase of clotting factor concentration in whole blood. It is clear that nanocomposite hydrogels formed with 10% GelMA/10% ELP demonstrated a significantly improved hemostatic performance when fabricated with a LA concentration of 2% (w/v). Therefore, these results suggest that this biocompatible nanocomposite hydrogel would be a good candidate to be used as a hemostatic agent to reduce bleeding during surgical procedures.

3.3.6. *In vitro* evaluation of the cytocompatibility of nanocomposite GelMA/ELP/LA hydrogels

To evaluate cytocompatibility of the nanocomposite GelMA/ELP/LA hydrogels, we evaluated the in vitro viability, spreading, and metabolic activity of human-derived lung fibroblast cells using surface seeding (2D cultures). Cell viability and spreading were evaluated using a commercial live/dead kit and Actin/DAPI staining, respectively. In addition, metabolic activity was assessed using PrestoBlue assays. Hydrogels fabricated with pure 20% GelMA, 10% GelMA/10% ELP, and 10% GelMA/10% ELP/2% LA (w/v) were evaluated for cytocompatibility. 2D cell studies revealed that all three hydrogel variations showed excellent cell survival up to 7 days post-seeding (**Figure 27a-f**) with >90% cell viability (**Figure 27m**). Furthermore, quantitative analysis of fluorescent images (**Figure 27g-l**) revealed that nanocomposite GelMA/ELP/LA hydrogels support cell proliferation with significantly higher number of cells throughout the duration of the experiment (**Figure 27n**). Lastly, the metabolic activity increased rapidly up to 4 days post-seeding as cells reached maturity (**Figure 27o**). Taken together, these results suggest that these nanocomposite GelMA/ELP/LA hydrogels demonstrate excellent biocompatibility and would be suitable to support tissue repair *in vivo*.

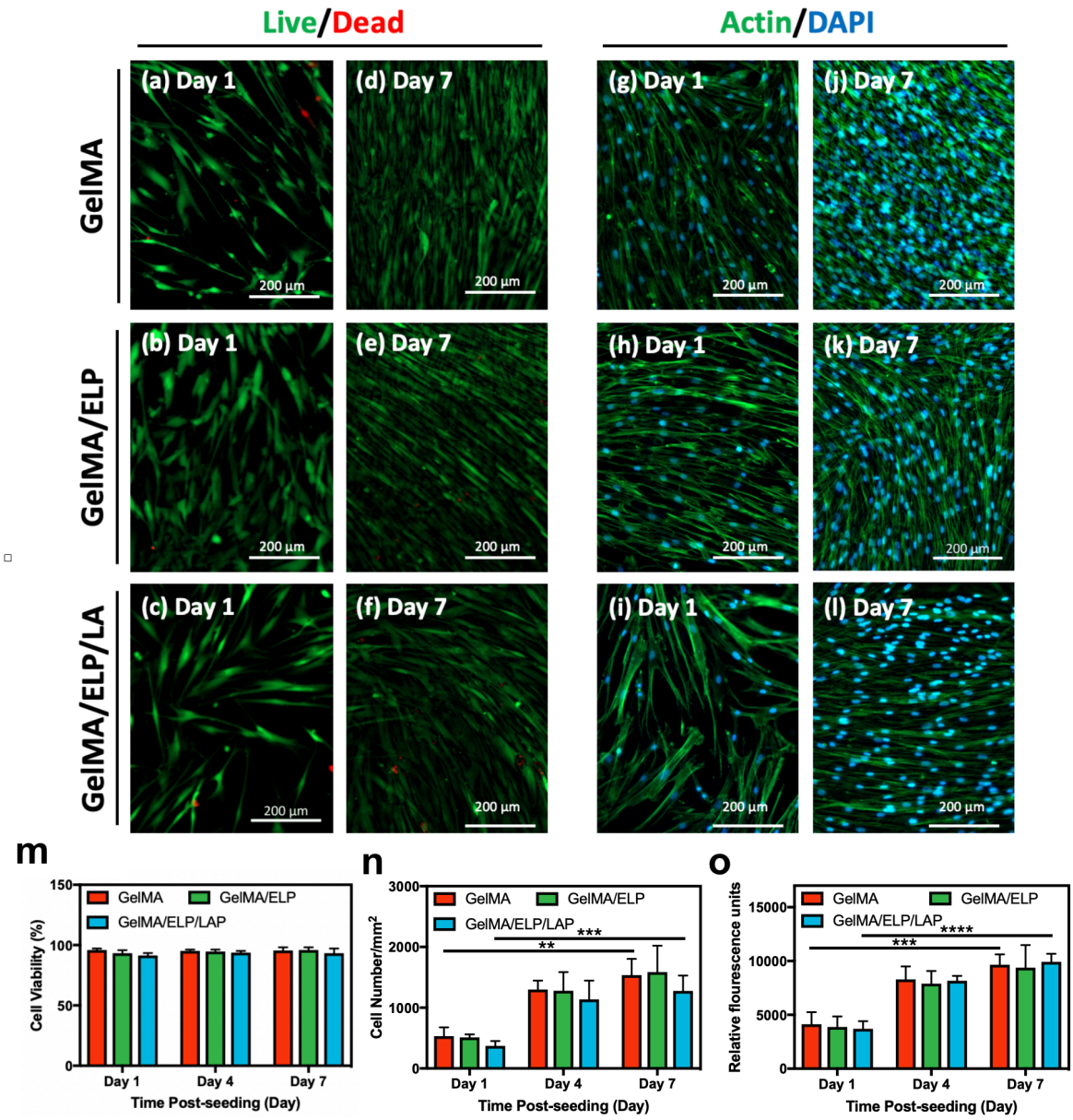

Figure 27. *In vitro* cytocompatibility evaluation of GelMA/ELP/LA hydrogels. Representative live/dead images of human lung fibroblast cells (hLFCs) seeded on the surface of (**a**) GelMA, (**b**) GelMA/ELP, and (**c**) GelMA/ELP/LA hydrogels after 1 day post-seeding. Representative live/dead images of hLFCs seeded on the surface of (**d**) GelMA, (**e**) GelMA/ELP, and (**f**) GelMA/ELP/LA after 5 days post-seeding. Representative phalloidin (green)/DAPI (blue) stained images from hLFCs seeded on (**g**) GelMA, (**h**) GelMA/ELP, and (**i**) GelMA/ELP/LA after 1 day post-seeding. Representative phalloidin/DAPI images of hLFCs seeded on (**j**) GelMA, (**k**) GelMA/ELP, and (**l**) GelMA/ELP/LA after 5 days post seeding. (m) Quantification of cell viability for hLFCs seeded on the surface of engineered hydrogels at days 1, 4, and 7 post-seeding. (n) Quantification of cell proliferation based on DAPI-stained cell nuclei at days 1, 4, and 7 post-seeding. (o) Quantification of metabolic activity, relative fluorescence units (RFU), using a PrestoBlue assay at days 1, 4, and 7 post seeding.

3.3.7. *In vivo* biodegradation of nanocomposite GelMA/ELP/LA hydrogels using a rat subcutaneous implantation model

We next aimed to investigate the *in vivo* biodegradation of our nanocomposite GelMA/ELP.LA hydrogels via a rat subcutaneous implantation model. Hydrogels fabricated with 20% pure GelMA, 10% GelMA/10% ELP, and 10% GelMA/10% ELP/2% LA (w/v) were evaluated in this study. The scaffolds were implanted in subcutaneous pockets prepared along the dorsomedial skin of male Wistar rats. Harvesting of samples at time points 7, 28, and 56 days revealed that the implanted hydrogels maintained their shape over 56 days suggesting excessive biodegradation did not occur (**Figure 28a**). A slight decrease in the size of implanted hydrogels was observed, along with change in pigment, which suggests that tissue ingrowth occurred as biodegradation took place. The incorporation of LA into nanocomposites did not significantly affect biodegradation. Our results showed that while samples fabricated with GelMA/ELP degraded by, 60.2 ± 6.28%, nanocomposite GelMA/ELP/LA hydrogels degraded by 55.4 ± 7.81% after 56 days post implantation (**Figure 28b**). Further, hematoxylin and eosin staining of implanted hydrogels shows early stage tissue ingrowth into the samples suggesting biocompatibility and integration by the host (**Figure 28c-g**). These results suggest that nanocomposite GelMA/ELP/LA hydrogels do not elicit a cytotoxic response when implanted *in vivo*. Additionally, degraded byproducts of the engineered scaffold are slowly cleared and replaced by new tissue further suggesting that these biomaterials show promise to be further developed into surgical sealants for soft tissue repair.

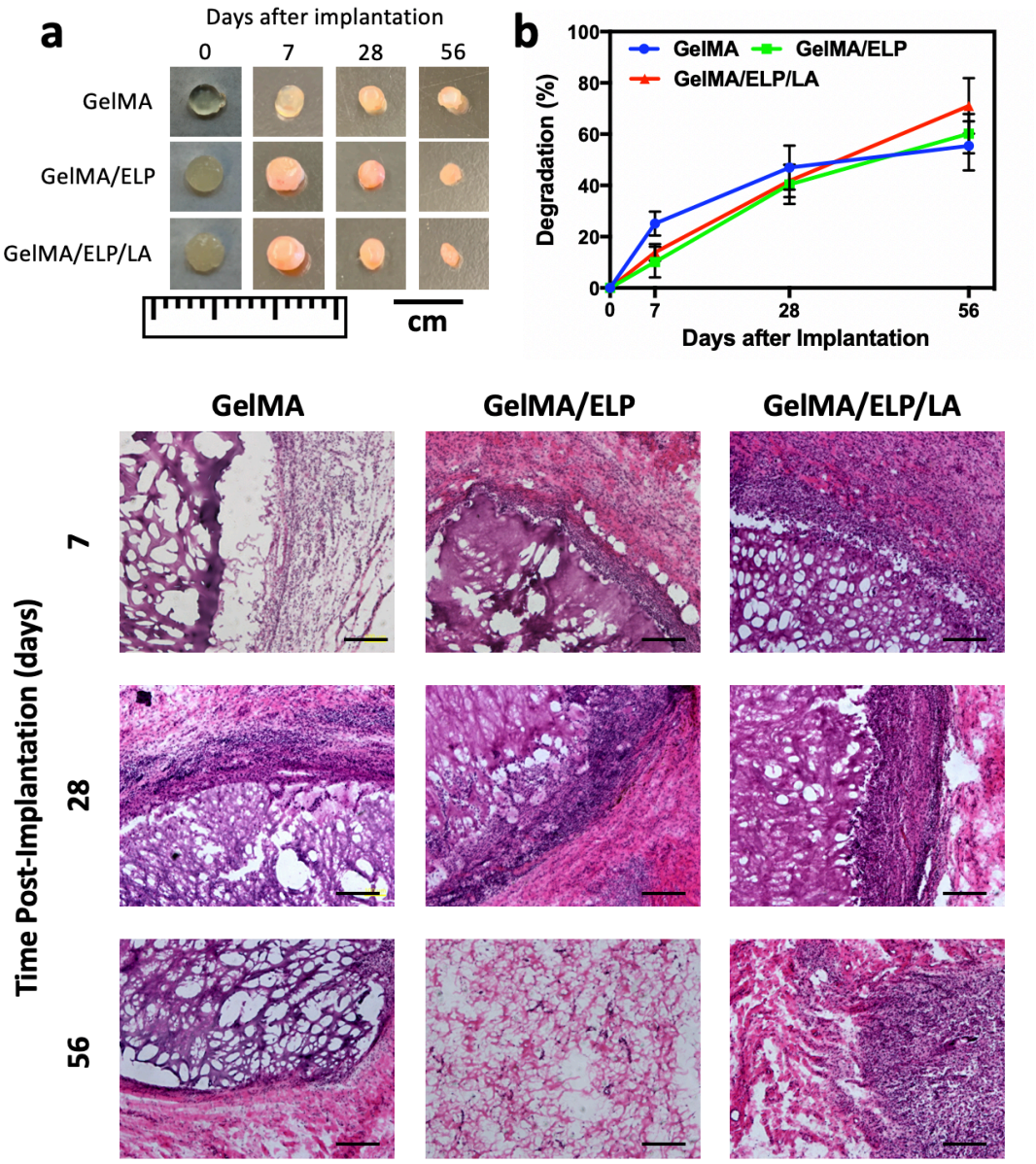

Figure 28. *In vivo* biodegradation and biocompatibility of nanocomposite GelMA/ELP/LA hydrogels using a rat subcutaneous implantation model. (**a**) Representative images of GelMA, GelMA/ELP, and GelMA/ELP/LA hydrogels before implantation (day 0), and on days 7, 28, and 56 post-implantation. (**b**) *In vivo* biodegradation of the engineered hydrogels on days 0, 7, 28, and 56 post-implantation, based on weight loss of the implant (n=4). Hematoxylin and eosin (H&E) staining of 20 %(w/v) GelMA hydrogel sections (hydrogels with the surrounding tissue) after (**c**) 7, (**d**) 28, and (**e**) 56 days of implantation (scale bar = 200 µm). H&E staining of GelMA/ELP 10/10 %(w/v) hydrogel sections after (**f**) 7, (**g**), 28 and (**h**) 56 days implantation. H&E staining of GelMA/ELP/LA 10/10/2 %(w/v) hydrogel sections after (**i**) 7, (**j**), 28, and (**k**) 56 days post implantation. Hydrogels were formed using 0.5% Irgacure 2959 and 180 s UV exposure time.

3.3.8. *In vivo* evaluation of nanocomposite hydrogels as hemostats using a rat liver bleeding model

In vivo hemostatic performance of our nanocomposite GelMA/ELP/LA hydrogels was investigated using a rat liver bleeding model via 1 cm incisions. The hemostatic treatment was immediately administered directly to the injury site and blood was collected using filter paper (**Figure 29a**). The mass of blood collected was recorded at time points of 1 and 10 minutes after creating the defect in liver tissue. Commercially available Surgicel (**Figure 29b**), nanocomposite GelMA/ELP/LA hydrogels (**Figure 29c**), and pure GelMA hydrogels were evaluated in this experiment. Our results showed that there was a significantly higher amount of blood collected at 10 minutes compared to blood collected at 1 minute for pure GelMA hydrogel and Surgicel treatments suggesting that these materials failed to adequately promote blood coagulation (**Figure 29d**). In contrast, bleeding discontinued within 1 minute for livers treated with nanocomposite GelMA/ELP/LA hydrogels. The incorporation of LA into nanocomposite hydrogels demonstrated remarkable hemostatic properties *in vivo* and show excellent potential to be utilized for vascular or soft tissue injuries to promote rapid blood clotting.

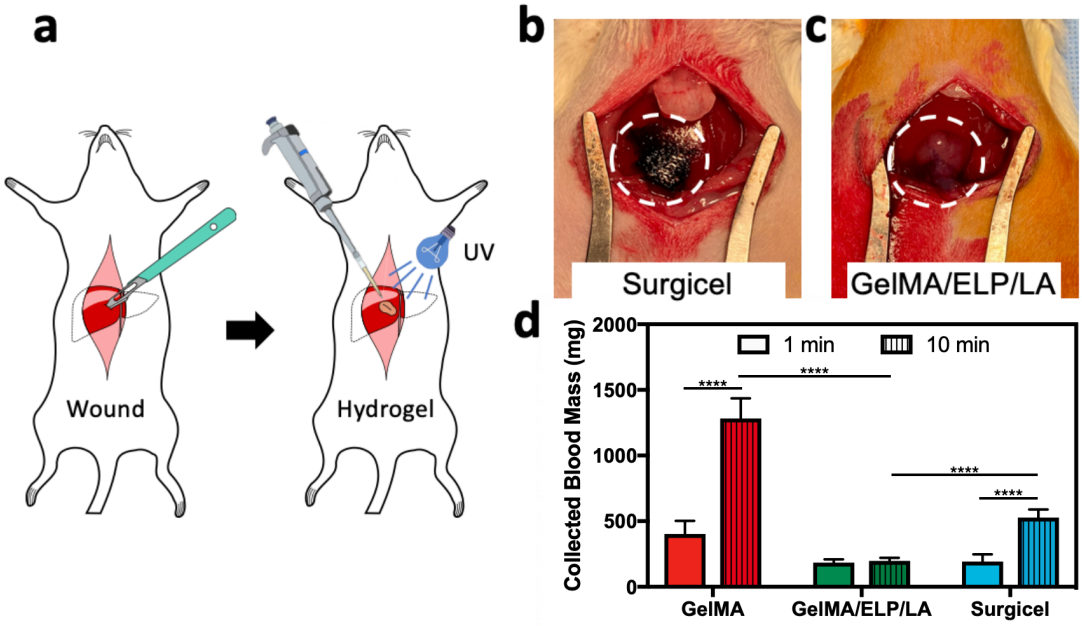

Figure 29. *In vivo* evaluation of nanocomposite hydrogels as hemostats using a rat liver bleeding model. (**a**) Schematic of engineered hydrogel placement onto a lethal liver wound. Representative images of (**b**) Surgicel hemostatic patch and (**c**) GelMA/ELP/LA nanocomposite hydrogels being used to accelerate blood clotting in a rat *in vivo* liver bleeding model. (**d**) Quantification of in vivo blood loss after application of GelMA/ELP/LA nanocomposite hydrogels shows significant improvement compared to treatment with GelMA hydrogels or Surgicel hemostatic patch. Error bars indicate standard error of the means, asterisks mark significance levels of $p < 0.0001$ (****).

4. CONCLUSION

We introduced a new method to generate electroconductive polymer-based biomaterials through the conjugation of a choline-based Bio-IL to different polymers. We demonstrated that the mechanical properties, porosity, degradability, and swellability of the engineered hydrogels could be finely tuned by varying the final polymer concentration, as well as the ratio of polymer to Bio-IL. We also investigated the ability of Bio-IL conjugated hydrogels to transduce physicochemical stimuli and modulate the growth of primary CMs in both 2D and 3D cultures *in vitro*. We demonstrated that the engineered hydrogels are highly biodegradable and biocompatible *in vitro*, and that they do not elicit inflammatory responses when implanted *in vivo*. Taken together,

our results suggest that Bio-IL conjugated hydrogels could be implemented and readily tailored to different biomedical and tissue engineering applications. Further, we demonstrated the ability to engineer cardiopatches with conductivity and mechanical properties that are finely tunable by optimizing the concentration of GelMA and Bio-IL. GelMA/Bio-IL cardiopatches demonstrated excellent adhesiveness to cardiac tissues, and biocompatibility *in vitro*. CMs and CFs seeded on the surface of cardiac patches demonstrated excellent cell attachment and proliferation, and the scaffold supported the expression of gap junction proteins indicating the cells ability to function synchronously. Furthermore, histological assessment was indicative of comparatively lower thinning of the ventricular wall 3 weeks after induction of experimental MI. However, further experiments focusing on the evaluation of cardiac function following MI are needed to elucidate the cardioprotective efficacy of this strategy. In addition, the long-term effects of the epicardial application of the cardiopatches and the potential development of co-morbidities such as constrictive pericarditis, arrhythmias and other systemic syndromes should also be evaluated. GelMA/Bio-IL cardiopatches hold great potential to be used as scaffolds to provide mechanical stabilization to the injured myocardium and to restore electromechanical coupling at the site of MI. In addition, our group developed a rapidly photocrosslinkable hemostatic surgical sealant with robust mechanical properties based on the biopolymers GelMA and elastin-like polypeptide (ELP). Our nanocomposite hydrogels were made hemostatic by the incorporation of LA. We demonstrated the finely tunable mechanical and adhesive properties of these nanocomposite hydrogels by varying the concentrations of GelMA and ELP. We also investigated how varying the concentrations of GelMA, ELP, and LA affect the swellability and degradation of the nanocomposite hydrogels. The excellent hemostatic performance of these scaffolds were displayed both *in vitro* and *in vivo* by increasing the concentration of LA. Our nanocomposite

GelMA/ELP/LA hydrogels also showed remarkable biocompatibility both *in vitro* and *in vivo* and did not elicit an inflammatory response when implanted subcutaneously. Taken together, these nanocomposite GelMA/ELP/LA hydrogels demonstrate remarkable potential to be used as surgical sealants for soft tissue.

5. REFERENCES

1. Dvir, T., et al., *Nanowired three-dimensional cardiac patches.* Nat Nanotechnol, 2011. **6**(11): p. 720-5.
2. Annabi, N., et al., *Highly Elastic and Conductive Human-Based Protein Hybrid Hydrogels.* Adv Mater, 2016. **28**(1): p. 40-9.
3. Ahadian, S., et al., *Hybrid hydrogel-aligned carbon nanotube scaffolds to enhance cardiac differentiation of embryoid bodies.* Acta Biomater, 2016. **31**: p. 134-143.
4. Zhao, X., et al., *Antibacterial and conductive injectable hydrogels based on quaternized chitosan-graft-polyaniline/oxidized dextran for tissue engineering.* Acta Biomater, 2015. **26**: p. 236-48.
5. Yang, J., et al., *Polypyrrole-incorporated conductive hyaluronic acid hydrogels.* Biomater Res, 2016. **20**(1): p. 31.
6. Shin, D.S., et al., *Sensing Conductive Hydrogels for Rapid Detection of Cytokines in Blood.* Adv Healthc Mater, 2016. **5**(6): p. 659-64, 627.
7. Liu, Y., et al., *Tuning the conductivity and inner structure of electrospun fibers to promote cardiomyocyte elongation and synchronous beating.* Mater Sci Eng C Mater Biol Appl, 2016. **69**: p. 865-74.
8. Darabi, M.A., et al., *Skin-Inspired Multifunctional Autonomic-Intrinsic Conductive Self-Healing Hydrogels with Pressure Sensitivity, Stretchability, and 3D Printability.* Adv Mater, 2018. **30**(4).
9. Zhu, K., et al., *Gold Nanocomposite Bioink for Printing 3D Cardiac Constructs.* Adv Funct Mater, 2017. **27**(12).
10. Navaei, A., et al., *Electrically conductive hydrogel-based micro-topographies for the development of organized cardiac tissues.* Rsc Advances, 2017. **7**(6): p. 3302-3312.
11. Tee, B.C.K., et al., *An electrically and mechanically self-healing composite with pressure- and flexion-sensitive properties for electronic skin applications.* Nature Nanotechnology, 2012. **7**(12): p. 825-832.
12. Han, L., et al., *A Mussel-Inspired Conductive, Self-Adhesive, and Self-Healable Tough Hydrogel as Cell Stimulators and Implantable Bioelectronics.* Small, 2017. **13**(2).
13. Liu, X., et al., *Functionalized Carbon Nanotube and Graphene Oxide Embedded Electrically Conductive Hydrogel Synergistically Stimulates Nerve Cell Differentiation.* ACS Appl Mater Interfaces, 2017. **9**(17): p. 14677-14690.
14. Yang, S., et al., *Polypyrrole/Alginate Hybrid Hydrogels: Electrically Conductive and Soft Biomaterials for Human Mesenchymal Stem Cell Culture and Potential Neural Tissue Engineering Applications.* Macromol Biosci, 2016. **16**(11): p. 1653-1661.
15. Li, W., et al., *Electrospun H4SiW12O40/cellulose acetate composite nanofibrous membrane for photocatalytic degradation of tetracycline and methyl orange with different mechanism.* Carbohydr Polym, 2017. **168**: p. 153-162.
16. Caló, E. and V.V. Khutoryanskiy, *Biomedical applications of hydrogels: A review of patents and commercial products.* European Polymer Journal, 2015. **65**: p. 252-267.

17. Ullah, F., et al., *Classification, processing and application of hydrogels: A review.* Mater Sci Eng C Mater Biol Appl, 2015. **57**: p. 414-33.
18. Jen, A.C., M.C. Wake, and A.G. Mikos, *Review: Hydrogels for cell immobilization.* Biotechnol Bioeng, 1996. **50**(4): p. 357-64.
19. Ahmed, E.M., *Hydrogel: Preparation, characterization, and applications: A review.* J Adv Res, 2015. **6**(2): p. 105-21.
20. Guan, X., et al., *Development of hydrogels for regenerative engineering.* Biotechnol J, 2017. **12**(5).
21. Buwalda, S.J., et al., *Hydrogels in a historical perspective: from simple networks to smart materials.* J Control Release, 2014. **190**: p. 254-73.
22. Annabi, N., et al., *25th anniversary article: Rational design and applications of hydrogels in regenerative medicine.* Adv Mater, 2014. **26**(1): p. 85-123.
23. Sood, N., et al., *Stimuli-responsive hydrogels in drug delivery and tissue engineering.* Drug Deliv, 2016. **23**(3): p. 758-80.
24. Green, R.A., et al., *Conductive hydrogels: mechanically robust hybrids for use as biomaterials.* Macromol Biosci, 2012. **12**(4): p. 494-501.
25. Mawad, D., A. Lauto, and G.G. Wallace, *Conductive Polymer Hydrogels.* Polymeric Hydrogels as Smart Biomaterials, 2016: p. 19-44.
26. Shi, Z., et al., *Electroconductive natural polymer-based hydrogels.* Biomaterials, 2016. **111**: p. 40-54.
27. Guiseppi-Elie, A., *Electroconductive hydrogels: synthesis, characterization and biomedical applications.* Biomaterials, 2010. **31**(10): p. 2701-16.
28. Green, R.A., et al., *Conducting polymer-hydrogels for medical electrode applications.* Sci Technol Adv Mater, 2010. **11**(1): p. 014107.
29. Hardy, J.G., J.Y. Lee, and C.E. Schmidt, *Biomimetic conducting polymer-based tissue scaffolds.* Curr Opin Biotechnol, 2013. **24**(5): p. 847-54.
30. Guo, B., L. Glavas, and A.-C. Albertsson, *Biodegradable and electrically conducting polymers for biomedical applications.* Progress in Polymer Science, 2013. **38**(9): p. 1263-1286.
31. Das, S., et al., *Enhancement of Energy Storage and Photoresponse Properties of Folic Acid-Polyaniline Hybrid Hydrogel by in Situ Growth of Ag Nanoparticles.* ACS Appl Mater Interfaces, 2016.
32. Zare, Y. and I. Shabani, *Polymer/metal nanocomposites for biomedical applications.* Mater Sci Eng C Mater Biol Appl, 2016. **60**: p. 195-203.
33. Kong, L. and W. Chen, *Carbon nanotube and graphene-based bioinspired electrochemical actuators.* Adv Mater, 2014. **26**(7): p. 1025-43.
34. Noshadi, I., et al., *Engineering Biodegradable and Biocompatible Bio-ionic Liquid Conjugated Hydrogels with Tunable Conductivity and Mechanical Properties.* Scientific Reports, 2017. **7**(1): p. 4345.
35. Wang, Q., Q. Wang, and W. Teng, *Injectable, degradable, electroactive nanocomposite hydrogels containing conductive polymer nanoparticles for biomedical applications.* Int J Nanomedicine, 2016. **11**: p. 131-44.
36. Li, Y. and K.A. Kilian, *Bridging the Gap: From 2D Cell Culture to 3D Microengineered Extracellular Matrices.* Adv Healthc Mater, 2015. **4**(18): p. 2780-96.

37. Lee, G.H., et al., *Bottom-Up Engineering of Well-Defined 3D Microtissues Using Microplatforms and Biomedical Applications.* Adv Healthc Mater, 2016. **5**(1): p. 56-74.
38. Qazi, T.H., et al., *Development and characterization of novel electrically conductive PANI-PGS composites for cardiac tissue engineering applications.* Acta Biomater, 2014. **10**(6): p. 2434-45.
39. Stout, D.A., et al., *Mechanisms of greater cardiomyocyte functions on conductive nanoengineered composites for cardiovascular application.* Int J Nanomedicine, 2012. **7**: p. 5653-69.
40. Brocker, D.T. and W.M. Grill, *Principles of electrical stimulation of neural tissue.* Handb Clin Neurol, 2013. **116**: p. 3-18.
41. Duan, B., *State-of-the-Art Review of 3D Bioprinting for Cardiovascular Tissue Engineering.* Ann Biomed Eng, 2017. **45**(1): p. 195-209.
42. Al-Enizi, A.M., M.M. Zagho, and A.A. Elzatahry, *Polymer-Based Electrospun Nanofibers for Biomedical Applications.* Nanomaterials (Basel), 2018. **8**(4).
43. Li, J., K. Zhang, and N. Huang, *Engineering Cardiovascular Implant Surfaces to Create a Vascular Endothelial Growth Microenvironment.* Biotechnol J, 2017. **12**(12).
44. Thomas, V., et al., *Review on polymer, hydrogel and microgel metal nanocomposites: A facile nanotechnological approach.* Journal of Macromolecular Science Part a-Pure and Applied Chemistry, 2008. **45**(1): p. 107-119.
45. Li, F.Y., et al., *Dynamic Nanoparticle Assemblies for Biomedical Applications.* Advanced Materials, 2017. **29**(14).
46. Baei, P., et al., *Electrically conductive gold nanoparticle-chitosan thermosensitive hydrogels for cardiac tissue engineering.* Mater Sci Eng C Mater Biol Appl, 2016. **63**: p. 131-41.
47. Kim, J.H. and T.R. Lee, *Hydrogel-templated growth of large gold nanoparticles: synthesis of thermally responsive hydrogel-nanoparticle composites.* Langmuir, 2007. **23**(12): p. 6504-9.
48. Jiang, X.M., et al., *Gold nanomaterials: preparation, chemical modification, biomedical applications and potential risk assessment.* Appl Biochem Biotechnol, 2012. **166**(6): p. 1533-51.
49. Cobley, C.M., et al., *Gold nanostructures: a class of multifunctional materials for biomedical applications.* Chem Soc Rev, 2011. **40**(1): p. 44-56.
50. Navaei, A., et al., *Gold nanorod-incorporated gelatin-based conductive hydrogels for engineering cardiac tissue constructs.* Acta Biomater, 2016. **41**: p. 133-46.
51. Shevach, M., et al., *Nanoengineering gold particle composite fibers for cardiac tissue engineering.* Journal of Materials Chemistry B, 2013. **1**(39): p. 5210-5217.
52. Saha, K., et al., *Gold Nanoparticles in Chemical and Biological Sensing.* Chemical Reviews, 2012. **112**(5): p. 2739-2779.
53. Culver, H.R., J.R. Clegg, and N.A. Peppas, *Analyte-Responsive Hydrogels: Intelligent Materials for Biosensing and Drug Delivery.* Accounts of Chemical Research, 2017. **50**(2): p. 170-178.
54. Vial, S., R.L. Reis, and J.M. Oliveira, *Recent advances using gold nanoparticles as a promising multimodal tool for tissue engineering and regenerative medicine.* Current Opinion in Solid State & Materials Science, 2017. **21**(2): p. 92-112.

55. Saha, K., et al., *Gold nanoparticles in chemical and biological sensing.* Chem Rev, 2012. **112**(5): p. 2739-79.
56. Kim, K.S., et al., *Reactive oxygen species-activated nanomaterials as theranostic agents.* Nanomedicine (Lond), 2015. **10**(17): p. 2709-23.
57. Atashi, F., A. Modarressi, and M.S. Pepper, *The role of reactive oxygen species in mesenchymal stem cell adipogenic and osteogenic differentiation: a review.* Stem Cells Dev, 2015. **24**(10): p. 1150-63.
58. Xu, Q., et al., *Reactive Oxygen Species (ROS) Responsive Polymers for Biomedical Applications.* Macromol Biosci, 2016. **16**(5): p. 635-46.
59. Khaing Oo, M.K., et al., *Gold nanoparticle-enhanced and size-dependent generation of reactive oxygen species from protoporphyrin IX.* ACS Nano, 2012. **6**(3): p. 1939-47.
60. Fu, P.P., et al., *Mechanisms of nanotoxicity: generation of reactive oxygen species.* J Food Drug Anal, 2014. **22**(1): p. 64-75.
61. Khlebtsov, N. and L. Dykman, *Biodistribution and toxicity of engineered gold nanoparticles: a review of in vitro and in vivo studies.* Chem Soc Rev, 2011. **40**(3): p. 1647-71.
62. Baei, P., et al., *Electrically conductive gold nanoparticle-chitosan thermosensitive hydrogels for cardiac tissue engineering.* Materials Science & Engineering C-Materials for Biological Applications, 2016. **63**: p. 131-141.
63. Zhu, Q., et al., *3D Graphene hydrogel - gold nanoparticles nanocomposite modified glassy carbon electrode for the simultaneous determination of ascorbic acid, dopamine and uric acid.* Sensors and Actuators B-Chemical, 2017. **238**: p. 1316-1323.
64. Bodelon, G., et al., *Gold nanoparticles for regulation of cell function and behavior.* Nano Today, 2017. **13**: p. 40-60.
65. Yue, K., et al., *Synthesis, properties, and biomedical applications of gelatin methacryloyl (GelMA) hydrogels.* Biomaterials, 2015. **73**: p. 254-271.
66. Nikkhah, M., et al., *Directed endothelial cell morphogenesis in micropatterned gelatin methacrylate hydrogels.* Biomaterials, 2012. **33**(35): p. 9009-18.
67. Dvir, T., et al., *Nanowired three-dimensional cardiac patches.* Nature Nanotechnology, 2011. **6**(11): p. 720-725.
68. Pan, Y., M. Bartneck, and W. Jahnen-Dechent, *Chapter eleven - Cytotoxicity of Gold Nanoparticles*, in *Methods in Enzymology*, N. Düzgüneş, Editor. 2012, Academic Press. p. 225-242.
69. Zhao, X., et al., *Thermoswitchable electronic properties of a gold nanoparticle/hydrogel composite.* Macromolecular rapid communications, 2005. **26**(22): p. 1784-1787.
70. Thoniyot, P., et al., *Nanoparticle-Hydrogel Composites: Concept, Design, and Applications of These Promising, Multi-Functional Materials.* Adv Sci (Weinh), 2015. **2**(1-2): p. 1400010.
71. Varaprasad, K., et al., *Hydrogel-silver nanoparticle composites: A new generation of antimicrobials.* Journal of Applied Polymer Science, 2010. **115**(2): p. 1199-1207.
72. Reithofer, M.R., et al., *In situ synthesis of size-controlled, stable silver nanoparticles within ultrashort peptide hydrogels and their anti-bacterial properties.* Biomaterials, 2014. **35**(26): p. 7535-42.

73. Varaprasad, K., et al., *Synthesis and characterization of hydrogel-silver nanoparticle-curcumin composites for wound dressing and antibacterial application.* Journal of Applied Polymer Science, 2011. **121**(2): p. 784-796.
74. Zhao, F., et al., *Composites of Polymer Hydrogels and Nanoparticulate Systems for Biomedical and Pharmaceutical Applications.* Nanomaterials (Basel), 2015. **5**(4): p. 2054-2130.
75. Lee, W.-F. and K.-T. Tsao, *Preparation and properties of nanocomposite hydrogels containing silver nanoparticles by ex situ polymerization.* Journal of Applied Polymer Science, 2006. **100**(5): p. 3653-3661.
76. Devaki, S.J., R.K. Narayanan, and S. Sarojam, *Electrically conducting silver nanoparticle–polyacrylic acid hydrogel by in situ reduction and polymerization approach.* Materials Letters, 2014. **116**: p. 135-138.
77. Jo, H., et al., *Electrically conductive graphene/polyacrylamide hydrogels produced by mild chemical reduction for enhanced myoblast growth and differentiation.* Acta Biomater, 2017. **48**: p. 100-109.
78. Yang, X., et al., *Ordered gelation of chemically converted graphene for next-generation electroconductive hydrogel films.* Angew Chem Int Ed Engl, 2011. **50**(32): p. 7325-8.
79. Gaharwar, A.K., N.A. Peppas, and A. Khademhosseini, *Nanocomposite hydrogels for biomedical applications.* Biotechnol Bioeng, 2014. **111**(3): p. 441-53.
80. Zhang, L. and G. Shi, *Preparation of highly conductive graphene hydrogels for fabricating supercapacitors with high rate capability.* The Journal of Physical Chemistry C, 2011. **115**(34): p. 17206-17212.
81. Cui, Z., et al., *A study of conductive hydrogel composites of pH-responsive microgels and carbon nanotubes.* Soft Matter, 2016. **12**(18): p. 4142-53.
82. Sang, L., et al., *Thermally sensitive conductive hydrogel using amphiphilic crosslinker self-assembled carbon nanotube to enhance neurite outgrowth and promote spinal cord regeneration.* RSC Advances, 2016. **6**(31): p. 26341-26351.
83. Li, W., et al., *Strong and Robust Polyaniline-Based Supramolecular Hydrogels for Flexible Supercapacitors.* Angew Chem Int Ed Engl, 2016. **55**(32): p. 9196-201.
84. Xia, Y. and H. Zhu, *Polyaniline nanofiber-reinforced conducting hydrogel with unique pH-sensitivity.* Soft Matter, 2011. **7**(19): p. 9388-9393.
85. Hur, J., et al., *Polypyrrole/Agarose-based electronically conductive and reversibly restorable hydrogel.* ACS Nano, 2014. **8**(10): p. 10066-76.
86. Carquigny, S., et al., *Investigation of pharmaceutically active ionic liquids as electrolyte for the electrosynthesis of polypyrrole and active component in controlled drug delivery.* Electrochimica Acta, 2016. **211**: p. 950-961.
87. Samanta, D., J.L. Meiser, and R.N. Zare, *Polypyrrole nanoparticles for tunable, pH-sensitive and sustained drug release.* Nanoscale, 2015. **7**(21): p. 9497-504.
88. Pattavarakorn, D., et al., *Electroactive performances of conductive polythiophene/hydrogel hybrid artificial muscle.* Energy Procedia, 2013. **34**: p. 673-681.
89. Chen, L., et al., *Environmental responses of polythiophene hydrogels.* Macromolecules, 2000. **33**(4): p. 1232-1236.

90. Kim, Y.S., et al., *Highly conductive and hydrated PEG-based hydrogels for the potential application of a tissue engineering scaffold.* Reactive and Functional Polymers, 2016. **109**: p. 15-22.
91. Spencer, A.R., et al., *Electroconductive Gelatin Methacryloyl-PEDOT:PSS Composite Hydrogels: Design, Synthesis, and Properties.* ACS Biomaterials Science & Engineering, 2018. **4**(5): p. 1558-1567.
92. Dai, T., et al., *Conducting hydrogels with enhanced mechanical strength.* Polymer, 2009. **50**(22): p. 5236-5241.
93. Yang, L., et al., *Boosting current generation in microbial fuel cells by an order of magnitude by coating an ionic liquid polymer on carbon anodes.* Biosens Bioelectron, 2017. **91**: p. 644-649.
94. Huang, X., et al., *Ionic liquid induced surface trap-state passivation for efficient perovskite hybrid solar cells.* Organic Electronics, 2017. **41**: p. 42-48.
95. Romann, T., et al., *Reactions at graphene|tetracyanoborate ionic liquid interface – New safety mechanisms for supercapacitors and batteries.* Electrochemistry Communications, 2017. **74**: p. 38-41.
96. Viswanathan, G., et al., *Preparation of biopolymer fibers by electrospinning from room temperature ionic liquids.* Biomacromolecules, 2006. **7**(2): p. 415-8.
97. Varaprasad, K., et al., *Hydrogel–silver nanoparticle composites: A new generation of antimicrobials.* Journal of Applied Polymer Science, 2010. **115**(2): p. 1199-1207.
98. Murthy, P.S., et al., *First successful design of semi-IPN hydrogel-silver nanocomposites: a facile approach for antibacterial application.* J Colloid Interface Sci, 2008. **318**(2): p. 217-24.
99. Bajpai, S.K., N. Chand, and M. Mahendra, *In situ formation of silver nanoparticles in poly(methacrylic acid) hydrogel for antibacterial applications.* Polymer Engineering & Science, 2013. **53**(8): p. 1751-1759.
100. Zhang, W., et al., *Photogeneration of reactive oxygen species on uncoated silver, gold, nickel, and silicon nanoparticles and their antibacterial effects.* Langmuir, 2013. **29**(15): p. 4647-51.
101. Rattanaruengsrikul, V., N. Pimpha, and P. Supaphol, *In vitro efficacy and toxicology evaluation of silver nanoparticle-loaded gelatin hydrogel pads as antibacterial wound dressings.* Journal of Applied Polymer Science, 2012. **124**(2): p. 1668-1682.
102. Grade, S., et al., *Serum albumin reduces the antibacterial and cytotoxic effects of hydrogel-embedded colloidal silver nanoparticles.* RSC Advances, 2012. **2**(18): p. 7190-7196.
103. Garcia-Astrain, C., et al., *Biocompatible hydrogel nanocomposite with covalently embedded silver nanoparticles.* Biomacromolecules, 2015. **16**(4): p. 1301-10.
104. Haider, A. and I.-K. Kang, *Preparation of silver nanoparticles and their industrial and biomedical applications: a comprehensive review.* Advances in Materials Science and Engineering, 2015.
105. Ahn, Y., et al., *Highly conductive and flexible silver nanowire-based microelectrodes on biocompatible hydrogel.* ACS Appl Mater Interfaces, 2014. **6**(21): p. 18401-7.

106. Gurunathan, S. and J.H. Kim, *Synthesis, toxicity, biocompatibility, and biomedical applications of graphene and graphene-related materials.* Int J Nanomedicine, 2016. **11**: p. 1927-45.
107. Annabi, N., et al., *Highly Elastic and Conductive Human-Based Protein Hybrid Hydrogels.* Advanced Materials, 2016. **28**(1): p. 40-+.
108. Servant, A., et al., *Graphene-based electroresponsive scaffolds as polymeric implants for on-demand drug delivery.* Adv Healthc Mater, 2014. **3**(8): p. 1334-43.
109. Yang, X., et al., *Superparamagnetic graphene oxide–Fe 3 O 4 nanoparticles hybrid for controlled targeted drug carriers.* Journal of materials chemistry, 2009. **19**(18): p. 2710-2714.
110. Chen, C., et al., *A three-dimensionally chitin nanofiber/carbon nanotube hydrogel network for foldable conductive paper.* Carbohydr Polym, 2015. **134**: p. 309-13.
111. Ahadian, S., et al., *Hybrid hydrogels containing vertically aligned carbon nanotubes with anisotropic electrical conductivity for muscle myofiber fabrication.* Sci Rep, 2014. **4**: p. 4271.
112. Chen, Z., et al., *A Three-Dimensionally Interconnected Carbon Nanotube-Conducting Polymer Hydrogel Network for High-Performance Flexible Battery Electrodes.* Advanced Energy Materials, 2014. **4**(12).
113. Ahadian, S., et al., *Hybrid hydrogel-aligned carbon nanotube scaffolds to enhance cardiac differentiation of embryoid bodies.* Acta Biomaterialia, 2016. **31**: p. 134-143.
114. Guiseppi-Elie, A., *Electroconductive hydrogels: Synthesis, characterization and biomedical applications.* Biomaterials, 2010. **31**.
115. Li, W., et al., *Strong and Robust Polyaniline-Based Supramolecular Hydrogels for Flexible Supercapacitors.* Angewandte Chemie, 2016. **128**(32): p. 9342-9347.
116. Mawad, D., A. Lauto, and G.G. Wallace, *Conductive Polymer Hydrogels*, in *Polymeric Hydrogels as Smart Biomaterials*, S. Kalia, Editor. 2016, Springer International Publishing: Cham. p. 19-44.
117. Wu, Y., et al., *Fabrication of conductive gelatin methacrylate–polyaniline hydrogels.* Acta Biomaterialia, 2016. **33**: p. 122-130.
118. Szöllősi, A., et al., *Formation of novel hydrogel bio-anode by immobilization of biocatalyst in alginate/polyaniline/titanium-dioxide/graphite composites and its electrical performance.* Chemosphere, 2017. **174**: p. 58-65.
119. Dispenza, C., et al., *Electrically conductive hydrogel composites made of polyaniline nanoparticles and poly(N-vinyl-2-pyrrolidone).* Polymer, 2006. **47**(4): p. 961-971.
120. Balint, R., N.J. Cassidy, and S.H. Cartmell, *Conductive polymers: Towards a smart biomaterial for tissue engineering.* Acta Biomaterialia, 2014. **10**(6): p. 2341-2353.
121. Zhao, X., et al., *Antibacterial and conductive injectable hydrogels based on quaternized chitosan-graft-polyaniline/oxidized dextran for tissue engineering.* Acta Biomaterialia, 2015. **26**: p. 236-248.
122. Pillay, V., et al., *A review of integrating electroactive polymers as responsive systems for specialized drug delivery applications.* J Biomed Mater Res A, 2014. **102**(6): p. 2039-54.
123. Balint, R., N.J. Cassidy, and S.H. Cartmell, *Conductive polymers: towards a smart biomaterial for tissue engineering.* Acta Biomater, 2014. **10**(6): p. 2341-53.

124. Brahim, S., D. Narinesingh, and A. Guiseppi-Elie, *Polypyrrole-hydrogel composites for the construction of clinically important biosensors.* Biosensors and Bioelectronics, 2002. **17**(1–2): p. 53-59.
125. Hur, J., et al., *Polypyrrole/Agarose-Based Electronically Conductive and Reversibly Restorable Hydrogel.* ACS Nano, 2014. **8**(10): p. 10066-10076.
126. Kim, D.-H., M. Abidian, and D.C. Martin, *Conducting polymers grown in hydrogel scaffolds coated on neural prosthetic devices.* Journal of Biomedical Materials Research Part A, 2004. **71A**(4): p. 577-585.
127. Ketabat, F., et al., *Injectable conductive collagen/alginate/polypyrrole hydrogels as a biocompatible system for biomedical applications.* Journal of Biomaterials Science-Polymer Edition, 2017. **28**(8): p. 794-805.
128. Carquigny, S., et al., *Investigation of pharmaceutically active ionic liquids as electrolyte for the electrosynthesis of polypyrrole and active component in controlled drug delivery.* Electrochimica Acta, 2016. **211**: p. 950-961.
129. Samanta, D., J.L. Meiser, and R.N. Zare, *Polypyrrole nanoparticles for tunable, pH-sensitive and sustained drug release.* Nanoscale, 2015. **7**(21): p. 9497-9504.
130. Liu, M., et al., *Polypyrrole coated PLGA core-shell nanoparticles for drug delivery and photothermal therapy.* Rsc Advances, 2016. **6**(87): p. 84269-84275.
131. Kim, S.Y. and G.T.R. Palmore, *Conductive hydrogel for bio-electrocatalytic reduction of dioxygen.* Electrochemistry Communications, 2012. **23**: p. 90-93.
132. Shi, Y., et al., *Nanostructured conductive polypyrrole hydrogels as high-performance, flexible supercapacitor electrodes.* Journal of Materials Chemistry A, 2014. **2**(17): p. 6086-6091.
133. Spearman, B.S., et al., *Conductive interpenetrating networks of polypyrrole and polycaprolactone encourage electrophysiological development of cardiac cells.* Acta Biomaterialia, 2015. **28**: p. 109-120.
134. Mihic, A., et al., *A Conductive Polymer Hydrogel Supports Cell Electrical Signaling and Improves Cardiac Function After Implantation into Myocardial Infarct.* Circulation, 2015. **132**(8): p. 772-784.
135. Ismail, Y.A., et al., *Sensing characteristics of a conducting polymer/hydrogel hybrid microfiber artificial muscle.* Sensors and Actuators B: Chemical, 2011. **160**(1): p. 1180-1190.
136. Yang, J., et al., *Polypyrrole-incorporated conductive hyaluronic acid hydrogels.* Biomaterials Research, 2016. **20**(1): p. 31.
137. Jeong, B. and A. Gutowska, *Lessons from nature: stimuli-responsive polymers and their biomedical applications.* Trends in Biotechnology, 2002. **20**(7): p. 305-311.
138. Kai, D., et al., *Polypyrrole-contained electrospun conductive nanofibrous membranes for cardiac tissue engineering.* J Biomed Mater Res A, 2011. **99**(3): p. 376-85.
139. Chen, L., et al., *Environmental Responses of Polythiophene Hydrogels.* Macromolecules, 2000. **33**(4): p. 1232-1236.
140. Mawad, D., et al., *Electroconductive Hydrogel Based on Functional Poly(Ethylenedioxy Thiophene).* Chemistry of Materials, 2016. **28**(17): p. 6080-6088.
141. Naficy, S., et al., *Electrically Conductive, Tough Hydrogels with pH Sensitivity.* Chemistry of Materials, 2012. **24**(17): p. 3425-3433.

142. Hassarati, R.T., et al., *Improving Cochlear Implant Properties Through Conductive Hydrogel Coatings.* IEEE Transactions on Neural Systems and Rehabilitation Engineering, 2014. **22**(2): p. 411-418.
143. Wu, Q., et al., *A robust, highly stretchable supramolecular polymer conductive hydrogel with self-healability and thermo-processability.* Scientific Reports, 2017. **7**: p. 41566.
144. Aouada, F.A., et al., *Electrochemical and mechanical properties of hydrogels based on conductive poly(3,4-ethylene dioxythiophene)/poly(styrenesulfonate) and PAAm.* Polymer Testing, 2006. **25**(2): p. 158-165.
145. Zhang, X., et al., *Conducting polymer aerogels from supercritical CO2 drying PEDOT-PSS hydrogels.* Journal of Materials Chemistry, 2010. **20**(24): p. 5080-5085.
146. Shin, D.S., et al., *Sensing Conductive Hydrogels for Rapid Detection of Cytokines in Blood.* Advanced Healthcare Materials, 2016. **5**(6): p. 659-664.
147. Larsson, K.C., P. Kjall, and A. Richter-Dahlfors, *Organic bioelectronics for electronic-to-chemical translation in modulation of neuronal signaling and machine-to-brain interfacing.* Biochim Biophys Acta, 2013. **1830**(9): p. 4334-44.
148. Kim, Y.S., et al., *Highly conductive and hydrated PEG-based hydrogels for the potential application of a tissue engineering scaffold.* Reactive & Functional Polymers, 2016. **109**: p. 15-22.
149. Yoon, S.G. and S.T. Chang, *Microfluidic capacitive sensors with ionic liquid electrodes and CNT/PDMS nanocomposites for simultaneous sensing of pressure and temperature.* Journal of Materials Chemistry C, 2017. **5**(8): p. 1910-1919.
150. Zhou, T., et al., *Poly(ionic liquid) hydrogels exhibiting superior mechanical and electrochemical properties as flexible electrolytes.* Journal of Materials Chemistry A, 2016. **4**(3): p. 1112-1118.
151. Huddleston, J.G., et al., *Characterization and comparison of hydrophilic and hydrophobic room temperature ionic liquids incorporating the imidazolium cation.* Green Chemistry, 2001. **3**(4): p. 156-164.
152. Chanie, Y., I. Díaz, and E. Pérez, *Kinetics and mechanisms of adsorption/desorption of the ionic liquid 1-buthyl-3-methylimidazolium bromide into mordenite.* Journal of Chemical Technology & Biotechnology, 2016. **91**(3): p. 705-710.
153. Lei, Z., et al., *Introduction: Ionic Liquids.* Chem Rev, 2017. **117**(10): p. 6633-6635.
154. Gallagher, S., et al., *Swelling and shrinking properties of thermo-responsive polymeric ionic liquid hydrogels with embedded linear pNIPAAM.* Int J Mol Sci, 2014. **15**(4): p. 5337-49.
155. Egorova, K.S., E.G. Gordeev, and V.P. Ananikov, *Biological Activity of Ionic Liquids and Their Application in Pharmaceutics and Medicine.* Chem Rev, 2017. **117**(10): p. 7132-7189.
156. Robinson, S.S., et al., *Integrated soft sensors and elastomeric actuators for tactile machines with kinesthetic sense.* Extreme Mechanics Letters, 2015. **5**: p. 47-53.
157. Liang, X., et al., *Preparation of cellulose-based conductive hydrogels with ionic liquid.* Reactive and Functional Polymers, 2015. **86**: p. 1-6.
158. Kresse, H. and E. Schonherr, *Proteoglycans of the extracellular matrix and growth control.* J Cell Physiol, 2001. **189**(3): p. 266-74.

159. Scott, J.E., *Extracellular matrix, supramolecular organisation and shape.* Journal of Anatomy, 1995. **187**(Pt 2): p. 259-269.
160. Ma, Z., et al., *Potential of nanofiber matrix as tissue-engineering scaffolds.* Tissue Eng, 2005. **11**(1-2): p. 101-9.
161. Schultz, G.S. and A. Wysocki, *Interactions between extracellular matrix and growth factors in wound healing.* Wound Repair Regen, 2009. **17**(2): p. 153-62.
162. Li, J., Y.P. Zhang, and R.S. Kirsner, *Angiogenesis in wound repair: angiogenic growth factors and the extracellular matrix.* Microsc Res Tech, 2003. **60**(1): p. 107-14.
163. Huang, Z.-M., et al., *A review on polymer nanofibers by electrospinning and their applications in nanocomposites.* Composites Science and Technology, 2003. **63**(15): p. 2223-2253.
164. Darrell, H.R. and C. Iksoo, *Nanometre diameter fibres of polymer, produced by electrospinning.* Nanotechnology, 1996. **7**(3): p. 216.
165. Agarwal, S., J.H. Wendorff, and A. Greiner, *Use of electrospinning technique for biomedical applications.* Polymer, 2008. **49**(26): p. 5603-5621.
166. Boudriot, U., et al., *Electrospinning approaches toward scaffold engineering--a brief overview.* Artif Organs, 2006. **30**(10): p. 785-92.
167. Xie, J., et al., *Electrospun nanofibers for neural tissue engineering.* Nanoscale, 2010. **2**(1): p. 35-44.
168. Jun, I., S. Jeong, and H. Shin, *The stimulation of myoblast differentiation by electrically conductive sub-micron fibers.* Biomaterials, 2009. **30**(11): p. 2038-2047.
169. Bendrea, A.D., L. Cianga, and I. Cianga, *Review paper: progress in the field of conducting polymers for tissue engineering applications.* J Biomater Appl, 2011. **26**(1): p. 3-84.
170. Chen, M.C., Y.C. Sun, and Y.H. Chen, *Electrically conductive nanofibers with highly oriented structures and their potential application in skeletal muscle tissue engineering.* Acta Biomater, 2013. **9**(3): p. 5562-72.
171. Malki, M., et al., *Gold Nanorod-Based Engineered Cardiac Patch for Suture-Free Engraftment by Near IR.* Nano Lett, 2018.
172. Raney, J.R. and J.A. Lewis, *Printing mesoscale architectures.* MRS Bulletin, 2015. **40**(11): p. 943-950.
173. Agarwala, S., et al., *A novel 3D bioprinted flexible and biocompatible hydrogel bioelectronic platform.* Biosensors & Bioelectronics, 2018. **102**: p. 365-371.
174. Leberfinger, A.N., et al., *Concise Review: Bioprinting of Stem Cells for Transplantable Tissue Fabrication.* Stem Cells Translational Medicine, 2017. **6**(10): p. 1940-1948.
175. Coburn, J.C. and G.T. Grant, *FDA Regulatory Pathways and Technical Considerations for the 3D Printing of Medical Models and Devices*, in *3D Printing in Medicine*. 2017, Springer. p. 97-111.
176. Liu, Y.Q., et al., *Nature-Inspired Structural Materials for Flexible Electronic Devices.* Chemical Reviews, 2017. **117**(20): p. 12893-12941.
177. Tai, Y.L., et al., *A highly sensitive, low-cost, wearable pressure sensor based on conductive hydrogel spheres.* Nanoscale, 2015. **7**(35): p. 14766-14773.
178. Wei, S., et al., *Scalable and Automated Fabrication of Conductive Tough-Hydrogel Microfibers with Ultrastretchability, 3D Printability, and Stress Sensitivity.* ACS Applied Materials and Interfaces, 2018. **10**(13): p. 11204-11212.

179. Tian, K., et al., *3D Printing of Transparent and Conductive Heterogeneous Hydrogel–Elastomer Systems.* Advanced Materials, 2017. **29**(10).
180. Guo, S.Z., et al., *3D Printed Stretchable Tactile Sensors.* Advanced Materials, 2017. **29**(27).
181. Li, L., et al., *All Inkjet-Printed Amperometric Multiplexed Biosensors based on Nanostructured Conductive Hydrogel Electrodes.* Nano Letters, 2018: p. acs.nanolett.8b00003-acs.nanolett.8b00003.
182. Darabi, M.A., et al., *Skin-Inspired Multifunctional Autonomic-Intrinsic Conductive Self-Healing Hydrogels with Pressure.* 2017. **1700533**: p. 1-8.
183. Odent, J., et al., *Highly Elastic, Transparent, and Conductive 3D-Printed Ionic Composite Hydrogels.* Advanced Functional Materials, 2017. **27**(33): p. 1-10.
184. Liu, X., et al., *A Compact Closed-Loop Optogenetics System Based on Artifact-Free Transparent Graphene Electrodes.* Front Neurosci, 2018. **12**: p. 132.
185. Wu, G.H. and S.H. Hsu, *Review: Polymeric-Based 3D Printing for Tissue Engineering.* J Med Biol Eng, 2015. **35**(3): p. 285-292.
186. Abidian, M.R., et al., *Hybrid conducting polymer-hydrogel conduits for axonal growth and neural tissue engineering.* Adv Healthc Mater, 2012. **1**(6): p. 762-7.
187. Lee, S.J., et al., *3D printing nano conductive multi-walled carbon nanotube scaffolds for nerve regeneration.* J Neural Eng, 2018. **15**(1): p. 016018.
188. Jung, I.Y., et al., *Hydrogel Based Biosensors for In Vitro Diagnostics of Biochemicals, Proteins, and Genes.* Advanced Healthcare Materials, 2017. **6**(12): p. 1-19.
189. Lind, J.U., et al., *Instrumented cardiac microphysiological devices via multimaterial three-dimensional printing.* Nature Materials, 2017. **16**(3): p. 303-308.
190. McKenzie, M., et al., *Hydrogel-Based Drug Delivery Systems for Poorly Water-Soluble Drugs.* Molecules, 2015. **20**(11): p. 20397-408.
191. Norouzi, M., B. Nazari, and D.W. Miller, *Injectable hydrogel-based drug delivery systems for local cancer therapy.* Drug Discov Today, 2016. **21**(11): p. 1835-1849.
192. Naderi-Meshkin, H., et al., *Chitosan-based injectable hydrogel as a promising in situ forming scaffold for cartilage tissue engineering.* Cell Biol Int, 2014. **38**(1): p. 72-84.
193. Chung, S.E., et al., *Guided and fluidic self-assembly of microstructures using railed microfluidic channels.* Nat Mater, 2008. **7**(7): p. 581-7.
194. Tasoglu, S., et al., *Magnetic Levitational Assembly for Living Material Fabrication.* Adv Healthc Mater, 2015. **4**(10): p. 1469-76, 1422.
195. Fabiilli, M.L., et al., *Acoustic droplet-hydrogel composites for spatial and temporal control of growth factor delivery and scaffold stiffness.* Acta Biomater, 2013. **9**(7): p. 7399-409.
196. Albrecht, D.R., et al., *Multiphase electropatterning of cells and biomaterials.* Lab on a Chip, 2007. **7**(6): p. 702-709.
197. Kim, D., et al., *A Facile Approach for Constructing Conductive Polymer Patterns for Application in Electrochromic Devices and Flexible Microelectrodes.* ACS Appl Mater Interfaces, 2016. **8**(48): p. 33175-33182.
198. Wu, Y., et al., *Fabrication of conductive gelatin methacrylate-polyaniline hydrogels.* Acta Biomater, 2016. **33**: p. 122-30.

199. Lee, J.M., et al., *Conductive hydrogel/nanowire micropattern-based sensor for neural stem cell differentiation.* Sensors and Actuators B: Chemical, 2018. **258**: p. 1042-1050.
200. Srinivasan, S., et al., *Carbon nanotube triggered self-assembly of oligo(p-phenylene vinylene)s to stable hybrid pi-gels.* Angew Chem Int Ed Engl, 2008. **47**(31): p. 5746-9.
201. Okesola, B.O., et al., *Selective Extraction and In Situ Reduction of Precious Metal Salts from Model Waste To Generate Hybrid Gels with Embedded Electrocatalytic Nanoparticles.* Angew Chem Int Ed Engl, 2016. **55**(1): p. 183-7.
202. Chakraborty, P., et al., *Co-assembled conductive hydrogel of N-fluorenylmethoxycarbonyl phenylalanine with polyaniline.* J Phys Chem B, 2014. **118**(48): p. 13969-80.
203. Seidlits, S.K., J.Y. Lee, and C.E. Schmidt, *Nanostructured scaffolds for neural applications.* Nanomedicine (Lond), 2008. **3**(2): p. 183-99.
204. Xu, Y., et al., *Self-assembled graphene hydrogel via a one-step hydrothermal process.* ACS Nano, 2010. **4**(7): p. 4324-30.
205. Kopeček, J. and J. Yang, *Smart self-assembled hybrid hydrogel biomaterials.* Angewandte Chemie International Edition, 2012. **51**(30): p. 7396-7417.
206. Pugliese, R., et al., *Cross-linked self-assembling peptide scaffolds.* Nano Research, 2018. **11**(1): p. 586-602.
207. Thompson, C.B. and L.T.J. Korley, *Harnessing Supramolecular and Peptidic Self-Assembly for the Construction of Reinforced Polymeric Tissue Scaffolds.* Bioconjugate chemistry, 2017. **28**(5): p. 1325-1339.
208. Cheng, Q.Y. and B.H. Han, *Supramolecular hydrogel based on graphene oxides for controlled release system.* J Nanosci Nanotechnol, 2013. **13**(2): p. 755-60.
209. Sun, Y., Q. Wu, and G. Shi, *Supercapacitors based on self-assembled graphene organogel.* Phys Chem Chem Phys, 2011. **13**(38): p. 17249-54.
210. Cai, G., et al., *Extremely Stretchable Strain Sensors Based on Conductive Self-Healing Dynamic Cross-Links Hydrogels for Human-Motion Detection.* Adv Sci (Weinh), 2017. **4**(2): p. 1600190.
211. Haraguchi, K., K. Uyama, and H. Tanimoto, *Self-healing in nanocomposite hydrogels.* Macromol Rapid Commun, 2011. **32**(16): p. 1253-8.
212. Shi, Z.J., et al., *Electroconductive natural polymer-based hydrogels.* Biomaterials, 2016. **111**: p. 40-54.
213. Liu, X., et al., *Electrical stimulation promotes nerve cell differentiation on polypyrrole/poly (2-methoxy-5 aniline sulfonic acid) composites.* J Neural Eng, 2009. **6**(6): p. 065002.
214. Ghasemi-Mobarakeh, L., et al., *Electrical stimulation of nerve cells using conductive nanofibrous scaffolds for nerve tissue engineering.* Tissue Eng Part A, 2009. **15**(11): p. 3605-19.
215. Sirivisoot, S., R. Pareta, and B.S. Harrison, *Protocol and cell responses in three-dimensional conductive collagen gel scaffolds with conductive polymer nanofibres for tissue regeneration.* Interface Focus, 2014. **4**(1): p. 20130050.
216. Weng, B., et al., *Inkjet printed polypyrrole/collagen scaffold: A combination of spatial control and electrical stimulation of PC12 cells.* Synthetic Metals, 2012. **162**(15–16): p. 1375-1380.

217. Kotwal, A. and C.E. Schmidt, *Electrical stimulation alters protein adsorption and nerve cell interactions with electrically conducting biomaterials.* Biomaterials, 2001. **22**(10): p. 1055-64.
218. Yow, S.-Z., et al., *A 3D Electroactive Polypyrrole-Collagen Fibrous Scaffold for Tissue Engineering.* Polymers, 2011. **3**(1).
219. Kim, D.H., et al., *Nanoscale cues regulate the structure and function of macroscopic cardiac tissue constructs.* Proc Natl Acad Sci U S A, 2010. **107**(2): p. 565-70.
220. Zhou, J., et al., *Engineering the heart: evaluation of conductive nanomaterials for improving implant integration and cardiac function.* Sci Rep, 2014. **4**: p. 3733.
221. Laiva, A.L., et al., *Biomimetic approaches for cell implantation to the restoration of infarcted myocardium.* Nanomedicine (Lond), 2015. **10**(18): p. 2907-30.
222. Dong, R., et al., *Self-Healing Conductive Injectable Hydrogels with Antibacterial Activity as Cell Delivery Carrier for Cardiac Cell Therapy.* ACS Appl Mater Interfaces, 2016. **8**(27): p. 17138-50.
223. Gelmi, A., et al., *Direct Mechanical Stimulation of Stem Cells: A Beating Electromechanically Active Scaffold for Cardiac Tissue Engineering.* Adv Healthc Mater, 2016. **5**(12): p. 1471-80.
224. Liu, L., et al., *Increased proliferation and differentiation of pre-osteoblasts MC3T3-E1 cells on nanostructured polypyrrole membrane under combined electrical and mechanical stimulation.* J Biomed Nanotechnol, 2013. **9**(9): p. 1532-9.
225. Wang, Y., M. Rouabhia, and Z. Zhang, *Pulsed electrical stimulation benefits wound healing by activating skin fibroblasts through the TGFbeta1/ERK/NF-kappaB axis.* Biochim Biophys Acta, 2016. **1860**(7): p. 1551-9.
226. Zhao, X., et al., *Antibacterial anti-oxidant electroactive injectable hydrogel as self-healing wound dressing with hemostasis and adhesiveness for cutaneous wound healing.* Biomaterials, 2017. **122**: p. 34-47.
227. Kaur, G., et al., *Electrically conductive polymers and composites for biomedical applications.* RSC Advances, 2015. **5**(47): p. 37553-37567.
228. Ravichandran, R., et al., *Applications of conducting polymers and their issues in biomedical engineering.* J R Soc Interface, 2010. **7 Suppl 5**: p. S559-79.
229. Sarwar, M.S., et al., *Bend, stretch, and touch: Locating a finger on an actively deformed transparent sensor array.* Sci Adv, 2017. **3**(3): p. e1602200.
230. Nichol, J.W., et al., *Cell-laden microengineered gelatin methacrylate hydrogels.* Biomaterials, 2010. **31**(21): p. 5536-44.
231. Zhang, Y.N., et al., *A Highly Elastic and Rapidly Crosslinkable Elastin-Like Polypeptide-Based Hydrogel for Biomedical Applications.* Adv Funct Mater, 2015. **25**(30): p. 4814-4826.
232. Lin, M., et al., *Functional expression of a biologically active fragment of soluble gp130 as an ELP-fusion protein in transgenic plants: purification via inverse transition cycling.* Biochem J, 2006. **398**(3): p. 577-83.
233. Nichol, J.W., et al., *Cell-laden microengineered gelatin methacrylate hydrogels.* Biomaterials, 2010. **31**(21): p. 5536-5544.

234. Noshadi, I., et al., *Engineering Biodegradable and Biocompatible Bio-ionic Liquid Conjugated Hydrogels with Tunable Conductivity and Mechanical Properties.* Sci Rep, 2017. **7**(1): p. 4345.
235. Stinstra, J.G., et al., *Modelling passive cardiac conductivity during ischaemia.* Med Biol Eng Comput, 2005. **43**(6): p. 776-82.
236. Sasaki, M., et al., *Highly conductive stretchable and biocompatible electrode-hydrogel hybrids for advanced tissue engineering.* Adv Healthc Mater, 2014. **3**(11): p. 1919-27.
237. Kim, Y., et al., *Stretchable nanoparticle conductors with self-organized conductive pathways.* Nature, 2013. **500**(7460): p. 59-63.
238. Chun, K.Y., et al., *Highly conductive, printable and stretchable composite films of carbon nanotubes and silver.* Nat Nanotechnol, 2010. **5**(12): p. 853-7.
239. Park, M., et al., *Highly stretchable electric circuits from a composite material of silver nanoparticles and elastomeric fibres.* Nat Nanotechnol, 2012. **7**(12): p. 803-9.
240. Mihic, A., et al., *A Conductive Polymer Hydrogel Supports Cell Electrical Signaling and Improves Cardiac Function After Implantation into Myocardial Infarct.* Circulation, 2015. **132**(8): p. 772-784.
241. Chicurel, M.E., C.S. Chen, and D.E. Ingber, *Cellular control lies in the balance of forces.* Curr Opin Cell Biol, 1998. **10**(2): p. 232-9.
242. Kloxin, A.M., et al., *Mechanical Properties of Cellularly Responsive Hydrogels and Their Experimental Determination.* Advanced Materials, 2010. **22**(31): p. 3484-3494.
243. Ebrahimi, A.P., *Mechanical properties of normal and diseased cerebrovascular system.* J Vasc Interv Neurol, 2009. **2**(2): p. 155-62.
244. Fioretta, E.S., et al., *Influence of substrate stiffness on circulating progenitor cell fate.* J Biomech, 2012. **45**(5): p. 736-44.
245. Annabi, N., et al., *Controlling the porosity and microarchitecture of hydrogels for tissue engineering.* Tissue Eng Part B Rev, 2010. **16**(4): p. 371-83.
246. Zeltinger, J., et al., *Effect of pore size and void fraction on cellular adhesion, proliferation, and matrix deposition.* Tissue Eng, 2001. **7**(5): p. 557-72.
247. Ganji, F., S. Vasheghani-Farahani, and E. Vasheghani-Farahani, *Theoretical Description of Hydrogel Swelling: A Review.* Iranian Polymer Journal, 2010. **19**(5): p. 375-398.
248. Feng, X., et al., *Highly Swellable, Dual-Responsive Hydrogels Based on PNIPAM and Redox Active Poly(ferrocenylsilane) Poly(ionic liquid)s: Synthesis, Structure, and Properties.* Macromol Rapid Commun, 2016. **37**(23): p. 1939-1944.
249. Silva, S.S., et al., *The use of ionic liquids in the processing of chitosan/silk hydrogels for biomedical applications.* Green Chemistry, 2012. **14**(5): p. 1463-1470.
250. Fukaya, Y., et al., *Bio ionic liquids: room temperature ionic liquids composed wholly of biomaterials.* Green Chemistry, 2007. **9**(11): p. 1155-1157.
251. Mathur, A., et al., *In vitro cardiac tissue models: Current status and future prospects.* Adv Drug Deliv Rev, 2016. **96**: p. 203-13.
252. Guan, X., et al., *Development of hydrogels for regenerative engineering.* Biotechnol J, 2017.
253. Yue, K., et al., *Synthesis, properties, and biomedical applications of gelatin methacryloyl (GelMA) hydrogels.* Biomaterials, 2015. **73**: p. 254-71.

254. Loessner, D., et al., *Functionalization, preparation and use of cell-laden gelatin methacryloyl-based hydrogels as modular tissue culture platforms.* Nat Protoc, 2016. **11**(4): p. 727-46.
255. Zhu, J., *Bioactive modification of poly(ethylene glycol) hydrogels for tissue engineering.* Biomaterials, 2010. **31**(17): p. 4639-56.
256. Ralphe, J.C. and W.J. de Lange, *3D engineered cardiac tissue models of human heart disease: learning more from our mice.* Trends Cardiovasc Med, 2013. **23**(2): p. 27-32.
257. Cicha, I., et al., *Nano-biomaterials for cardiovascular applications: Clinical perspective.* J Control Release, 2016. **229**: p. 23-36.
258. Yeo, Y., et al., *Photocrosslinkable hydrogel for myocyte cell culture and injection.* J Biomed Mater Res B Appl Biomater, 2007. **81**(2): p. 312-22.
259. Benton, J.A., B.D. Fairbanks, and K.S. Anseth, *Characterization of valvular interstitial cell function in three dimensional matrix metalloproteinase degradable PEG hydrogels.* Biomaterials, 2009. **30**(34): p. 6593-603.
260. Lutolf, M.P., et al., *Repair of bone defects using synthetic mimetics of collagenous extracellular matrices.* Nat Biotechnol, 2003. **21**(5): p. 513-8.
261. Browning, M.B., et al., *Endothelial cell response to chemical, biological, and physical cues in bioactive hydrogels.* Tissue Eng Part A, 2014. **20**(23-24): p. 3130-41.
262. Lee, S.H., et al., *Hydrogel-based three-dimensional cell culture for organ-on-a-chip applications.* Biotechnol Prog, 2017.
263. Balint, R., N.J. Cassidy, and S.H. Cartmell, *Electrical Stimulation: A Novel Tool for Tissue Engineering.* Tissue Engineering Part B-Reviews, 2013. **19**(1): p. 48-57.
264. Titushkin, I. and M. Cho, *Regulation of Cell Cytoskeleton and Membrane Mechanics by Electric Field: Role of Linker Proteins.* Biophysical Journal, 2009. **96**(2): p. 717-728.
265. Cui, H.T., et al., *In Situ Electroactive and Antioxidant Supramolecular Hydrogel Based on Cyclodextrin/Copolymer Inclusion for Tissue Engineering Repair(a).* Macromolecular Bioscience, 2014. **14**(3): p. 440-450.
266. Hussain, A., et al., *Functional 3-D cardiac co-culture model using bioactive chitosan nanofiber scaffolds.* Biotechnol Bioeng, 2013. **110**(2): p. 637-47.
267. Zuppinger, C., *3D culture for cardiac cells.* Biochim Biophys Acta, 2016. **1863**(7 Pt B): p. 1873-81.
268. van Marion, M.H., et al., *Behavior of CMPCs in unidirectional constrained and stress-free 3D hydrogels.* J Mol Cell Cardiol, 2015. **87**: p. 79-91.
269. Davis, M.E., et al., *Custom design of the cardiac microenvironment with biomaterials.* Circ Res, 2005. **97**(1): p. 8-15.
270. Sepantafar, M., et al., *Stem cells and injectable hydrogels: Synergistic therapeutics in myocardial repair.* Biotechnol Adv, 2016.
271. Pok, S., et al., *Biocompatible carbon nanotube-chitosan scaffold matching the electrical conductivity of the heart.* ACS Nano, 2014. **8**(10): p. 9822-32.
272. Koshy, S.T., et al., *Injectable, porous, and cell-responsive gelatin cryogels.* Biomaterials, 2014. **35**(8): p. 2477-87.
273. Chen, Y.C., et al., *Functional Human Vascular Network Generated in Photocrosslinkable Gelatin Methacrylate Hydrogels.* Adv Funct Mater, 2012. **22**(10): p. 2027-2039.

274. Browning, M.B., et al., *Determination of the in vivo degradation mechanism of PEGDA hydrogels.* J Biomed Mater Res A, 2014. **102**(12): p. 4244-51.
275. Dreesmann, L., M. Ahlers, and B. Schlosshauer, *The pro-angiogenic characteristics of a cross-linked gelatin matrix.* Biomaterials, 2007. **28**(36): p. 5536-43.
276. Xia, Y., et al., *Bone tissue engineering using bone marrow stromal cells and an injectable sodium alginate/gelatin scaffold.* Journal of Biomedical Materials Research Part A, 2012. **100a**(4): p. 1044-1050.
277. Yi, S., et al., *Extracellular Matrix Scaffolds for Tissue Engineering and Regenerative Medicine.* Curr Stem Cell Res Ther, 2016.
278. Sepantafar, M., et al., *Stem cells and injectable hydrogels: Synergistic therapeutics in myocardial repair.* Biotechnol Adv, 2016. **34**(4): p. 362-379.
279. Titushkin, I. and M. Cho, *Regulation of cell cytoskeleton and membrane mechanics by electric field: role of linker proteins.* Biophys J, 2009. **96**(2): p. 717-28.
280. Balint, R., N.J. Cassidy, and S.H. Cartmell, *Electrical stimulation: a novel tool for tissue engineering.* Tissue Eng Part B Rev, 2013. **19**(1): p. 48-57.
281. Dvir, T., et al., *Nanotechnological strategies for engineering complex tissues.* Nat Nanotechnol, 2011. **6**(1): p. 13-22.
282. Zhao, G., et al., *Recent Advances in Electrospun Nanofibrous Scaffolds for Cardiac Tissue Engineering.* Advanced Functional Materials, 2015. **25**(36): p. 5726-5738.
283. Martins, A.M., et al., *Electrically conductive chitosan/carbon scaffolds for cardiac tissue engineering.* Biomacromolecules, 2014. **15**(2): p. 635-43.
284. Radhakrishnan, J., U.M. Krishnan, and S. Sethuraman, *Hydrogel based injectable scaffolds for cardiac tissue regeneration.* Biotechnol Adv, 2014. **32**(2): p. 449-61.
285. Liau, B., D. Zhang, and N. Bursac, *Functional cardiac tissue engineering.* Regen Med, 2012. **7**(2): p. 187-206.
286. Wang, W., Y. Zhang, and W. Liu, *Bioinspired fabrication of high strength hydrogels from non-covalent interactions.* Progress in Polymer Science, 2017. **71**: p. 1-25.
287. Feng, G., et al., *Elastic Light Tunable Tissue Adhesive Dendrimers.* Macromol Biosci, 2016. **16**(7): p. 1072-82.
288. Annabi, N., et al., *Engineering a sprayable and elastic hydrogel adhesive with antimicrobial properties for wound healing.* Biomaterials, 2017. **139**: p. 229-243.
289. Assmann, A., et al., *A highly adhesive and naturally derived sealant.* Biomaterials, 2017. **140**: p. 115-127.
290. Cho, E., J.S. Lee, and K. Webb, *Formulation and characterization of poloxamine-based hydrogels as tissue sealants.* Acta Biomater, 2012. **8**(6): p. 2223-32.
291. Chen, Q., S. Liang, and G.A. Thouas, *Synthesis and characterisation of poly (glycerol sebacate)-co-lactic acid as surgical sealants.* Soft Matter, 2011. **7**(14): p. 6484-6492.
292. Annabi, N., et al., *Engineering a highly elastic human protein-based sealant for surgical applications.* Sci Transl Med, 2017. **9**(410).
293. Lang, N., et al., *A blood-resistant surgical glue for minimally invasive repair of vessels and heart defects.* Science translational medicine, 2014. **6**(218): p. 218ra6-218ra6.
294. Mooney, D.J. and E.A. Silva, *Tissue engineering: a glue for biomaterials.* Nat Mater, 2007. **6**(5): p. 327-8.

295. Mehdizadeh, M. and J. Yang, *Design strategies and applications of tissue bioadhesives.* Macromol Biosci, 2013. **13**(3): p. 271-88.
296. Lawrence, P.G. and Y. Lapitsky, *Ionically cross-linked poly(allylamine) as a stimulus-responsive underwater adhesive: ionic strength and pH effects.* Langmuir, 2015. **31**(4): p. 1564-74.
297. Zhu, W., Y.J. Chuah, and D.A. Wang, *Bioadhesives for internal medical applications: A review.* Acta Biomater, 2018. **74**: p. 1-16.
298. Li, J., et al., *Tough adhesives for diverse wet surfaces.* Science, 2017. **357**(6349): p. 378-381.
299. Liang, S., et al., *Paintable and Rapidly Bondable Conductive Hydrogels as Therapeutic Cardiac Patches.* Advanced Materials, 2018. **30**(23).
300. Kazemzadeh-Narbat, M., et al., *Engineering Photocrosslinkable Bicomponent Hydrogel Constructs for Creating 3D Vascularized Bone.* Adv Healthc Mater, 2017. **6**(10).
301. Cochain, C., K.M. Channon, and J.S. Silvestre, *Angiogenesis in the infarcted myocardium.* Antioxid Redox Signal, 2013. **18**(9): p. 1100-13.
302. Azevedo, P.S., et al., *Cardiac Remodeling: Concepts, Clinical Impact, Pathophysiological Mechanisms and Pharmacologic Treatment.* Arq Bras Cardiol, 2016. **106**(1): p. 62-9.
303. Stoppel, W.L., D.L. Kaplan, and L.D. Black, 3rd, *Electrical and mechanical stimulation of cardiac cells and tissue constructs.* Adv Drug Deliv Rev, 2016. **96**: p. 135-55.
304. McArthur, L., et al., *Electrical consequences of cardiac myocyte: fibroblast coupling.* Biochem Soc Trans, 2015. **43**(3): p. 513-8.
305. Kohl, P., et al., *Electrical coupling of fibroblasts and myocytes: relevance for cardiac propagation.* J Electrocardiol, 2005. **38**(4 Suppl): p. 45-50.
306. Gaudesius, G., et al., *Coupling of cardiac electrical activity over extended distances by fibroblasts of cardiac origin.* Circ Res, 2003. **93**(5): p. 421-8.
307. Struthers, A.D., *Pathophysiology of heart failure following myocardial infarction.* Heart, 2005. **91 Suppl 2**: p. ii14-6; discussion ii31, ii43-8.
308. Zhao, G., et al., *Recent Advances in Electrospun Nanofibrous Scaffolds for Cardiac Tissue Engineering.* Advanced Functional Materials, 2015. **25**(36): p. 5726-5738.
309. Prabhakaran, M.P., et al., *Electrospun biocomposite nanofibrous patch for cardiac tissue engineering.* Biomed Mater, 2011. **6**(5): p. 055001.
310. Cui, Z., B. Yang, and R.-K. Li, *Application of Biomaterials in Cardiac Repair and Regeneration.* Engineering, 2016. **2**(1): p. 141-148.
311. Capulli, A.K., et al., *Fibrous scaffolds for building hearts and heart parts.* Adv Drug Deliv Rev, 2016. **96**: p. 83-102.
312. Mauretti, A., et al., *Cardiac Progenitor Cells and the Interplay with Their Microenvironment.* Stem Cells Int, 2017. **2017**: p. 7471582.
313. Ebrahimi, B., *In vivo reprogramming for heart regeneration: A glance at efficiency, environmental impacts, challenges and future directions.* J Mol Cell Cardiol, 2017. **108**: p. 61-72.
314. Safari, S., et al., *Mesenchymal stem cell-derived exosomes: A novel potential therapeutic avenue for cardiac regeneration.* Cell Mol Biol (Noisy-le-grand), 2016. **62**(7): p. 66-73.
315. Pereira, M.J., et al., *Sensing the cardiac environment: exploiting cues for regeneration.* J Cardiovasc Transl Res, 2011. **4**(5): p. 616-30.

316. Montgomery, M., et al., *Flexible shape-memory scaffold for minimally invasive delivery of functional tissues.* Nat Mater, 2017. **16**(10): p. 1038-1046.
317. Cambria, E., et al., *Cardiac Regenerative Medicine: The Potential of a New Generation of Stem Cells.* Transfus Med Hemother, 2016. **43**(4): p. 275-281.
318. Le, T.Y., et al., *New Developments in Cardiac Regeneration.* Heart Lung Circ, 2017. **26**(4): p. 316-322.
319. Lang, N., et al., *A blood-resistant surgical glue for minimally invasive repair of vessels and heart defects.* Sci Transl Med, 2014. **6**(218): p. 218ra6.
320. Artzi, N., et al., *Aldehyde-amine chemistry enables modulated biosealants with tissue-specific adhesion.* Adv Mater, 2009. **21**(32-33): p. 3399-403.
321. Mahdavi, A., et al., *A biodegradable and biocompatible gecko-inspired tissue adhesive.* Proc Natl Acad Sci U S A, 2008. **105**(7): p. 2307-12.
322. Selvi, F., et al., *Effects of different suture materials on tissue healing.* J Istanb Univ Fac Dent, 2016. **50**(1): p. 35-42.
323. Pinnaratip, R., et al., *Multifunctional biomedical adhesives.* Advanced healthcare materials, 2019. **8**(11): p. 1801568.
324. Scognamiglio, F., et al., *Adhesive and sealant interfaces for general surgery applications.* J Biomed Mater Res B Appl Biomater, 2016. **104**(3): p. 626-39.
325. Mehdizadeh, M., et al., *Injectable citrate-based mussel-inspired tissue bioadhesives with high wet strength for sutureless wound closure.* Biomaterials, 2012. **33**(32): p. 7972-7983.
326. Henise, J., et al., *Surgical sealants with tunable swelling, burst pressures, and biodegradation rates.* J Biomed Mater Res B Appl Biomater, 2017. **105**(6): p. 1602-1611.
327. Shazly, T.M., et al., *Augmentation of postswelling surgical sealant potential of adhesive hydrogels.* J Biomed Mater Res A, 2010. **95**(4): p. 1159-69.
328. Sahithi, K., et al., *Polymeric composites containing carbon nanotubes for bone tissue engineering.* Int J Biol Macromol, 2010. **46**(3): p. 281-3.
329. Song, F., et al., *Nanocomposite hydrogels and their applications in drug delivery and tissue engineering.* Journal of biomedical nanotechnology, 2015. **11**(1): p. 40-52.
330. Moreno-Vega, A.-I., et al., *Polymeric and ceramic nanoparticles in biomedical applications.* Journal of Nanotechnology, 2012. **2012**.
331. Das, S.S., et al., *Laponite-based Nanomaterials for Biomedical Applications: A Review.* Curr Pharm Des, 2019. **25**(4): p. 424-443.
332. Golafshan, N., et al., *Nanohybrid hydrogels of laponite: PVA-Alginate as a potential wound healing material.* Carbohydrate polymers, 2017. **176**: p. 392-401.
333. Gaharwar, A.K., et al., *Shear-thinning nanocomposite hydrogels for the treatment of hemorrhage.* ACS Nano, 2014. **8**(10): p. 9833-42.
334. Shirzaei Sani, E., et al., *Engineering adhesive and antimicrobial hyaluronic acid/elastin-like polypeptide hybrid hydrogels for tissue engineering applications.* ACS Biomaterials Science & Engineering, 2018. **4**(7): p. 2528-2540.
335. Peng, H.T. and P.N. Shek, *Novel wound sealants: biomaterials and applications.* Expert Rev Med Devices, 2010. **7**(5): p. 639-59.
336. Daamen, W.F., et al., *Elastin as a biomaterial for tissue engineering.* Biomaterials, 2007. **28**(30): p. 4378-4398.

337. Hsu, S.H. and H.S. Hung, *Surface modification by nanobiomaterials for vascular tissue engineering applications.* Curr Med Chem, 2018.
338. Nettles, D.L., A. Chilkoti, and L.A. Setton, *Applications of elastin-like polypeptides in tissue engineering.* Adv Drug Deliv Rev, 2010. **62**(15): p. 1479-85.
339. Lin, R., S. Wang, and W. Liu, *Protein-derived Smart Materials for Medical Applications: Elastin-like Polypeptides.* Current pharmaceutical design, 2018. **24**(26): p. 3008-3013.
340. Seliktar, D., *Designing cell-compatible hydrogels for biomedical applications.* Science, 2012. **336**(6085): p. 1124-8.
341. Wolfenson, H., B. Yang, and M.P. Sheetz, *Steps in mechanotransduction pathways that control cell morphology.* Annual review of physiology, 2019. **81**: p. 585-605.
342. Thomas, B.H., et al., *Hydrophilic-hydrophobic hydrogels for cartilage replacement.* J Mech Behav Biomed Mater, 2009. **2**(6): p. 588-95.
343. Duan, X. and H. Sheardown, *Dendrimer crosslinked collagen as a corneal tissue engineering scaffold: mechanical properties and corneal epithelial cell interactions.* Biomaterials, 2006. **27**(26): p. 4608-17.
344. Lee, K.Y., et al., *Controlling mechanical and swelling properties of alginate hydrogels independently by cross-linker type and cross-linking density.* Macromolecules, 2000. **33**(11): p. 4291-4294.
345. Jang, J., et al., *Effects of alginate hydrogel cross-linking density on mechanical and biological behaviors for tissue engineering.* J Mech Behav Biomed Mater, 2014. **37**: p. 69-77.
346. Bhardwaj, T., et al., *Effect of material geometry on cartilagenous tissue formation in vitro.* J Biomed Mater Res, 2001. **57**(2): p. 190-9.
347. Griffon, D.J., et al., *Chitosan scaffolds: interconnective pore size and cartilage engineering.* Acta Biomater, 2006. **2**(3): p. 313-20.
348. Wu, C.-J., et al., *Mechanically tough pluronic F127/laponite nanocomposite hydrogels from covalently and physically cross-linked networks.* Macromolecules, 2011. **44**(20): p. 8215-8224.
349. Chang, C.-W., et al., *PEG/clay nanocomposite hydrogel: a mechanically robust tissue engineering scaffold.* Soft Matter, 2010. **6**(20): p. 5157-5164.
350. Shazly, T.M., et al., *Viscoelastic adhesive mechanics of aldehyde-mediated soft tissue sealants.* Biomaterials, 2008. **29**(35): p. 4584-91.
351. Shazly, T.M., et al., *Augmentation of postswelling surgical sealant potential of adhesive hydrogels.* Journal of Biomedical Materials Research Part A, 2010. **95**(4): p. 1159-1169.
352. Tan, H., et al., *A PEG-Lysozyme hydrogel harvests multiple functions as a fit-to-shape tissue sealant for internal-use of body.* Biomaterials, 2019. **192**: p. 392-404.
353. Coenen, A.M.J., et al., *Elastic materials for tissue engineering applications: Natural, synthetic, and hybrid polymers.* Acta Biomater, 2018. **79**: p. 60-82.
354. Patel, A., et al., *Highly elastomeric poly(glycerol sebacate)-co-poly(ethylene glycol) amphiphilic block copolymers.* Biomaterials, 2013. **34**(16): p. 3970-3983.
355. Zaragoza, J., et al., *Experimental Investigation of Mechanical and Thermal Properties of Silica Nanoparticle-Reinforced Poly(acrylamide) Nanocomposite Hydrogels.* PLoS One, 2015. **10**(8): p. e0136293.

356. Gaharwar, A.K., et al., *Assessment of using Laponite® cross-linked poly (ethylene oxide) for controlled cell adhesion and mineralization.* Acta biomaterialia, 2011. **7**(2): p. 568-577.
357. Ghadiri, M., et al., *Physico-chemical, mechanical and cytotoxicity characterizations of Laponite®/alginate nanocomposite.* Applied clay science, 2013. **85**: p. 64-73.
358. Wu, C.J., J.J. Wilker, and G. Schmidt, *Robust and adhesive hydrogels from cross-linked poly(ethylene glycol) and silicate for biomedical use.* Macromol Biosci, 2013. **13**(1): p. 59-66.
359. Yang, J., et al., *Keys to enhancing mechanical properties of silica nanoparticle composites hydrogels: the role of network structure and interfacial interactions.* Composites science and technology, 2014. **95**: p. 1-7.
360. Gaharwar, A.K., et al., *Transparent, elastomeric and tough hydrogels from poly(ethylene glycol) and silicate nanoparticles.* Acta Biomater, 2011. **7**(12): p. 4139-48.
361. Yin, J., et al., *3D Bioprinting of Low-Concentration Cell-Laden Gelatin Methacrylate (GelMA) Bioinks with a Two-Step Cross-linking Strategy.* ACS Appl Mater Interfaces, 2018. **10**(8): p. 6849-6857.
362. Yeboah, A., et al., *Elastin-like polypeptides: A strategic fusion partner for biologics.* Biotechnol Bioeng, 2016. **113**(8): p. 1617-27.
363. Golafshan, N., et al., *Nanohybrid hydrogels of laponite: PVA-Alginate as a potential wound healing material.* Carbohydr Polym, 2017. **176**: p. 392-401.
364. Kamata, H., et al., *Design of Hydrogels for Biomedical Applications.* Adv Healthc Mater, 2015. **4**(16): p. 2360-74.
365. Buwalda, S.J., P.J. Dijkstra, and J. Feijen, *In situ forming stereocomplexed and post-photocrosslinked acrylated star poly (ethylene glycol)-poly (lactide) hydrogels.* European polymer journal, 2017. **94**: p. 152-161.
366. Xiao, W., et al., *Synthesis and characterization of photocrosslinkable gelatin and silk fibroin interpenetrating polymer network hydrogels.* Acta Biomater, 2011. **7**(6): p. 2384-93.
367. Tao, L., et al., *In vitro and in vivo studies of a gelatin/carboxymethyl chitosan/LAPONITE® composite scaffold for bone tissue engineering.* RSC advances, 2017. **7**(85): p. 54100-54110.
368. Rajabi, N., et al., *An adhesive and injectable nanocomposite hydrogel of thiolated gelatin/gelatin methacrylate/Laponite(R) as a potential surgical sealant.* J Colloid Interface Sci, 2020. **564**: p. 155-169.
369. Lih, E., et al., *Rapidly curable chitosan–PEG hydrogels as tissue adhesives for hemostasis and wound healing.* Acta biomaterialia, 2012. **8**(9): p. 3261-3269.
370. Charron, P.N., et al., *Mechanical properties and failure analysis of visible light crosslinked alginate-based tissue sealants.* J Mech Behav Biomed Mater, 2016. **59**: p. 314-321.
371. Pinnaratip, R., et al., *Effect of incorporating clustered silica nanoparticles on the performance and biocompatibility of catechol-containing PEG-based bioadhesive.* Biomed Mater, 2018. **13**(2): p. 025003.

372. Liu, Y., et al., *Marine adhesive containing nanocomposite hydrogel with enhanced materials and bioadhesive properties.* MRS Online Proceedings Library Archive, 2013. **1569**: p. 33-38.
373. Gaharwar, A.K., et al., *2D Nanoclay for Biomedical Applications: Regenerative Medicine, Therapeutic Delivery, and Additive Manufacturing.* Adv Mater, 2019. **31**(23): p. e1900332.
374. Liu, Y. and B.P. Lee, *Recovery property of double-network hydrogel containing mussel-inspired adhesive moiety and nano-silicate.* J Mater Chem B, 2016. **4**(40): p. 6534-6540.
375. Liu, Y., et al., *A Moldable Nanocomposite Hydrogel Composed of a Mussel-Inspired Polymer and a Nanosilicate as a Fit-to-Shape Tissue Sealant.* Angew Chem Int Ed Engl, 2017. **56**(15): p. 4224-4228.
376. Li, Y. and B.P. Lee, *Biomimetic approach to designing adhesive hydrogels: from chemistry to application*, in *Carbon Nanomaterials for Biomedical Applications*. 2016, Springer. p. 481-500.
377. Lu, X., et al., *Magnesium oxide-crosslinked low-swelling citrate-based mussel-inspired tissue adhesives.* Biomaterials, 2020. **232**: p. 119719.
378. Han, L., et al., *Mussel-inspired adhesive and conductive hydrogel with long-lasting moisture and extreme temperature tolerance.* Advanced Functional Materials, 2018. **28**(3): p. 1704195.
379. Guo, J., et al., *Click chemistry improved wet adhesion strength of mussel-inspired citrate-based antimicrobial bioadhesives.* Biomaterials, 2017. **112**: p. 275-286.
380. Walker, B.W., et al., *Engineering a naturally-derived adhesive and conductive cardiopatch.* Biomaterials, 2019. **207**: p. 89-101.
381. Chandrasekharan, A., et al., *In situ photocrosslinkable hyaluronic acid-based surgical glue with tunable mechanical properties and high adhesive strength.* Journal of Polymer Science Part A: Polymer Chemistry, 2019. **57**(4): p. 522-530.
382. Smart, J.D., *The basics and underlying mechanisms of mucoadhesion.* Advanced drug delivery reviews, 2005. **57**(11): p. 1556-1568.
383. Yang, X., et al., *Design and development of polysaccharide hemostatic materials and their hemostatic mechanism.* Biomater Sci, 2017. **5**(12): p. 2357-2368.
384. Chen, Z., et al., *A rapid hemostatic sponge based on large, mesoporous silica nanoparticles and N-alkylated chitosan.* Nanoscale, 2018. **10**(43): p. 20234-20245.
385. Feng, C., et al., *Chitosan-Coated Diatom Silica as Hemostatic Agent for Hemorrhage Control.* ACS Appl Mater Interfaces, 2016. **8**(50): p. 34234-34243.
386. Dawson, J.I. and R.O.C. Oreffo, *Clay: new opportunities for tissue regeneration and biomaterial design.* Advanced Materials, 2013. **25**(30): p. 4069-4086.
387. Olson, S.T. and I. Björk. *Regulation of thrombin activity by antithrombin and heparin*. Copyright© 1994 by Thieme Medical Publishers, Inc.